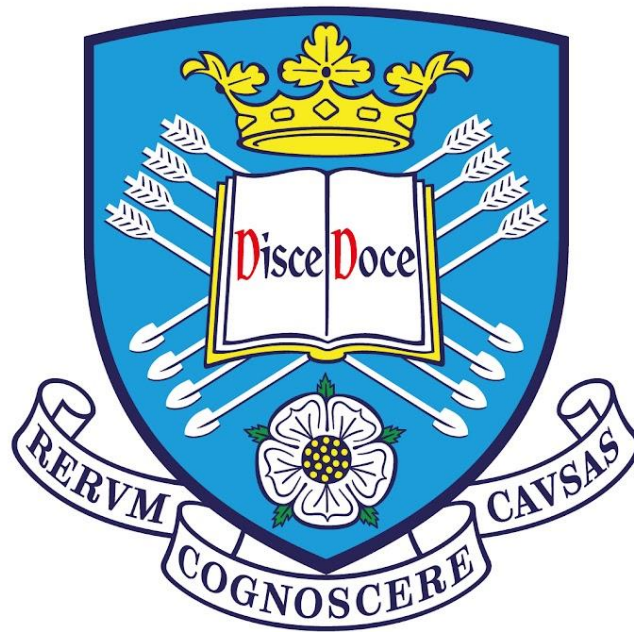# Ordering of Epitaxial Semiconductor Nanostructures Using *In Situ* Pulsed Laser Interference Patterning

Yunran Wang

The University of Sheffield

Department of Electronic and Electrical Engineering

A dissertation submitted in fulfilment of the requirements for the degree of Doctor of Philosophy

December 2021

ABSTRACT

Low-dimensional semiconductor nanostructures have received enormous research attention by virtue of their unique electronic structure and have shown major potential for applications in nanoelectronics, nanophotonics, and optoelectronics. In particular, III-V semiconductor quantum dots (QDs), quantum dot molecules (QDMs) and quantum rings (QRs) are deemed to be promising building blocks for quantum information processing and communications. Self-assembly during epitaxial growth has enabled the production of these structures with high crystalline and optical quality. However, self-assembly also comes with stochastic nucleation and size inhomogeneity, which can limit their potential for device integration where precise positioning and nanostructures with predictable and ideally identical electronic properties are demanded. Site-controlled growth of nanostructures using *ex situ* lithographic techniques presents an attractive approach; nevertheless, this involves complex fabrication processes and the resulting properties of the structures have not, in general, matched those of random self-assembled nanostructures. This dissertation seeks to develop an innovative approach to laterally align high-quality epitaxial semiconductor nanostructures using an *in situ* patterning process based on the direct application of optical methods.

In this work, an *in situ* technique combining nanosecond pulsed direct laser interference patterning (DLIP) with molecular beam epitaxy (MBE) growth is introduced, which offers a fast, high-efficiency route to realise the lateral ordering of semiconductor nanostructures. In the first part, the epitaxial growth and characterisation of Stranski-Krastanov (S-K) InAs QD and QDM arrays on GaAs substrates are investigated. The nanoisland arrays induced by single-pulse four-beam DLIP are observed to act as preferential nucleation sites for InAs QDs and result in a site occupancy dependent on the growth and interference parameters. The influences of both the DLIP conditions and the epitaxial growth parameters on the ordering of InAs/GaAs QDs are discussed. Precisely ordered arrays of single InAs QDs are fabricated for the first time using this *in situ* and non-invasive approach. The patterned QD arrays exhibit strong photoluminescence (PL) and a narrow full width at half maxima (FWHM), indicating good size uniformity and high optical quality.

The second part of the dissertation explores the fabrication of ordered GaAs/AlGaAs QD and QR arrays using the droplet epitaxy (DE) approach combined with *in situ* DLIP. The DE approach has emerged as an attractive method to create lattice-matched self-assembled QDs with certain advantages compared to strain-driven nucleation processes. Regular arrays of Ga droplets are initially formed on nanoisland-templated AlGaAs surfaces, which are subsequently crystallised into GaAs crystals under an arsenic flux. By optimising the growth parameters, including the deposited Ga amount, the growth temperature, and the arsenic beam equivalent pressure, highly ordered arrays of single GaAs QDs and QRs can be obtained. High optical quality and excellent size homogeneity are attained according to the low-temperature PL spectra, in which a record-narrow PL emission FWHM of ~17 meV from patterned GaAs QD arrays is observed.

In the final part of the dissertation, initial studies of the selective area growth (SAG) of GaAs droplets and nanocrystals on Si (100) & (111) substrates, and the growth and characterisation of type-II GaSb QDs on GaAs substrates employing *in situ* DLIP are demonstrated. These initial investigations show that DLIP is able to structure a silicon substrate to create Si nanoisland arrays. These islands can serve as preferential nucleation sites for Ga droplets, which can then be crystallised under arsenic exposure. Further deposition of GaAs results in the formation of periodic GaAs nanocrystals on the surface, with the size and site occupancy depending on the interference and growth parameters. The lateral ordering of S-K GaSb QDs on GaAs substrates has also been obtained, with the QD nucleation again subject to DLIP-induced nanoisland arrays. Low-temperature PL spectra of the patterned ordered arrays of GaSb QDs exhibit a comparably narrow FWHM of ~50 meV and reveal the characteristics of type-II band alignment.

ACKNOWLEDGEMENTS

Four years passed in the blink of an eye, leaving me with many valuable memories. Being a student in Electronic and Electrical Engineering at the University of Sheffield has been an incredible and indelible experience. I was very blessed to have met and worked with many fantastic people and benefited a lot from them. I would like to show my unfeigned gratitude to all those who have given me help, support, encouragement, and love during my PhD research and daily life.

First and foremost, I am deeply indebted to Prof. Mark Hopkinson, for being such a great supervisor, without whom I would not be here today. It was his lectures and project six years ago in the first place that opened the door for me to the world of semiconductors and I have been fascinated with it ever since. Furthermore, I am deeply grateful to Mark for offering me this precious chance to undertake my doctoral degree and participate in the NanoStencil project, and for always giving me considerable support, guidance, patience, encouragement and believing in me over the past years. Thanks for all the discussions and suggestions during my study, all the insightful comments and patient corrections of my manuscripts and dissertation, all the support and help through challenges and difficulties. I have extensively benefited from not only his wide knowledge and rich experience in MBE growth, optical characterisation, and even mechanical skills, but also his praiseworthy attitude towards research and life, particularly his constant passion and optimism has inspired me to a great extent to pursue my goals.

Also, my heartfelt thanks go to my closest colleague Dr. Im Sik Han, for staying with me in everyday lab life, without whom the MBE growth would have not been possible. He is a very calm and diligent person who has considerable expertise in MBE and always taught me patiently. I really enjoyed the daily discussion with my family-like group of Mark and Im Sik about the growth recipes and results, no matter whether there is failure or success. The achievement presented in this dissertation is indeed the outcome of teamwork and it would not be possible to accomplish my publications and dissertation without them. I wish to extend my deep acknowledgement to the current and former group members, from whom I have received a great deal of help, support and joy. Thanks to Dr. Chaoyuan Jin for his supervision and guidance on modelling and optical characterisation, his constructive discussions and practical comments for

what decision I have made. Although we have not seen each other for three years due to the pandemic, you have always been my energy, my strength, and my light in my life. Once again, I love you more than I can say.

致我最摯愛的父母、外婆、爺爺奶奶，以及我深愛的每一位家人，對你們的愛與感謝無以言表。

感恩你們一直支持我所做每一個決定，因為有你們無限的愛與陪伴，我才能如此肆意地追逐理想。

感恩擁有這樣歡聲笑語向上向善的大家庭，感恩遇見的每一個人。

我相信，我們很快會相見。

博学之，审问之，慎思之，明辨之，笃行之。有弗学，学之弗能弗措也；有弗问，问之弗知弗措也；有弗思，思之弗得弗措也；有弗辨，辨之弗明弗措也；有弗行，行之弗笃弗措也。人一能之己百之，人十能之己千之。果能此道矣，虽愚必明，虽柔必强。

录自中庸第二十章　辛丑年六月　韵兴

TABLE OF CONTENTS

LIST OF PUBLICATIONS AND PRESENTATIONS

Journal publications

YR. Wang, SM. Olaizola, IS. Han, CY. Jin, and M. Hopkinson, "Direct patterning of periodic semiconductor nanostructures using single-pulse nanosecond laser interference," *Optics Express* 28, 32529-32539 (2020)

YR. Wang, IS. Han, CY. Jin, and M. Hopkinson, "Precise Arrays of Epitaxial Quantum Dots Nucleated by In Situ Laser Interference for Quantum Information Technology Applications," *ACS Applied Nano Materials*, 3(5), 4739-4746 (2020)

YR. Wang, IS. Han, CY. Jin, and M. Hopkinson, "Formation of laterally ordered quantum dot molecules by in situ nanosecond laser interference. *Applied Physics Letters*, *116*(20), 201901 (2020)

YR. Wang, IS. Han, CY. Jin, and M. Hopkinson, "In-Situ Pulsed Laser Interference Nanostructuring of Semiconductor Surfaces. *Journal of Laser Micro Nanoengineering*, *15*(2), 139-142 (2020)

YR. Wang, CY. Jin, CH. Ho, S. Chen, H. Francis, and M. Hopkinson, "Thermodynamic processes on a semiconductor surface during in-situ multi-beam laser interference patterning". *IET Optoelectronics*, *13*(1), 7-11 (2019)

IS. Han, YR. Wang, and M. Hopkinson, "Ordered GaAs quantum dots by droplet epitaxy using in situ direct laser interference patterning". *Applied Physics Letters*, *118*(14), 142101 (2021)

LF. Wang, YR. Wang, H. Francis, R. Lu, MJ. Xia, F. Liu. F, M. Hopkinson, CY. Jin, "Theoretical modelling of single-mode lasing in microcavity lasers via optical interference injection", *Optics Express*, *28*(11), 16486-16496 (2020)

S. Chen, H. Francis, C. Ho, K. Che, YR. Wang, M. Hopkinson, S. Zhang, and C. Jin, "Control of Quality Factor in Laterally Coupled Vertical Cavities", *IET Optoelectronics*, 14(3), 100-103 (2020)

H. Francis, S. Chen, C. Ho, K. Che, <u>YR. Wang</u>, M. Hopkinson and C. Jin, "Generation of optical frequency combs using a photonic crystal cavity", *IET Optoelectronics*, *13*(1), 23-26 (2019)

Conference proceedings

<u>YR. Wang</u>, M. Hopkinson, IS. Han, S. Behera, and CY. Jin, "Directed self-assembly of InAs quantum dots using in-situ interference lithography", *Quantum Dots, Nanostructures, and Quantum Materials: Growth, Characterization, and Modeling XVII*, International Society for Optics and Photonics, 11291, 1129107 (2020)

<u>YR. Wang</u>, M. Hopkinson, IS. Han, and CY. Jin, "In-situ laser interference patterning of MBE growth surfaces", *Laser-based Micro-and Nanoprocessing XIV*. International Society for Optics and Photonics, 11268: 112680U (2020)

S. Behera, <u>YR. Wang</u>, IS. Han, CY. Jin, and M. Hopkinson, "Fabrication of sub-micrometer periodic nanostructures using pulsed laser interference for efficient light trapping in optoelectronic devices." *Laser Applications in Microelectronic and Optoelectronic Manufacturing (LAMOM) XXV*. International Society for Optics and Photonics, 11267 (2020)

H. Francis, S. Chen, C. Ho, K. Che, <u>YR. Wang</u>, M. Hopkinson and C. Jin "Modulating Photonic Crystal Structures to Generate Optical Frequency Combs", IEEE International Conference on Manipulation, Manufacturing and Measurement on the Nanoscale (3M-NANO), IEEE, 55-59, (2018)

S. Chen, H. Francis, C. Ho, K. Che, <u>YR. Wang</u>, M. Hopkinson, S. Zhang, and C. Jin "Quality Factor Control in Laterally-Coupled Vertical Cavities", 2018 IEEE International Conference on Manipulation, Manufacturing and Measurement on the Nanoscale (3M-NANO), IEEE, 60-64 (2018)

PRESENTATIONS

<u>YR. Wang</u>, IS. Han, and M. Hopkinson, "In-situ interference patterning during MBE growth", UK MBE Meeting, London, UK, 2022

<u>YR. Wang</u>, M. Hopkinson, IS. Han, and CY. Jin, "In-situ laser interference patterning of MBE growth surfaces", SPIE Photonics West, San Francisco, USA, 2020

YR. Wang, C. Jin and M. Hopkinson, "Multi-beam laser interference of semiconductors". UK Semiconductors, Sheffield, UK, 2018

YR. Wang, C. Jin and M. Hopkinson, "In-situ multi-beam laser interference patterning of semiconductors", EU Marie-Curie 'PROMIS' workshop, Windermere, UK, 2018

YR. Wang, C. Jin and M. Hopkinson, "Multi-beam laser interference patterning of semiconductors", SIOE, Cardiff, UK, 2018

LIST OF ABBREVIATIONS

As	Arsenic
AlAs	Aluminium Arsenide
AFM	Atomic Force Microscopy
BEP	Beam Equivalent Pressure
CB	Conduction Band
CBE	Chemical Beam Epitaxy
CMOS	Complementary Metal-Oxide-Semiconductor
CW	Continuous Wave
DE	Droplet Epitaxy
DLIP	Direct Laser Interference Patterning
DOE	Diffractive Optic Element
DOS	Density of States
EBL	Electron Beam Lithography
EDS	Energy-Dispersive X-ray Spectroscopy
ELOG	Epitaxial Lateral Overgrowth
ES	Excited-State
FDM	Finite Difference Method
FEG	Field Emission Electron Gun
F-M	Franck-van der Merwe
FSS	Fine-Structure Splitting
FWHM	Full Width at Half Maximum
Ga	Gallium
GaAs	Gallium Arsenide
GaN	Gallium Nitride
GaSb	Gallium Antimonide
Ge	Germanium
GS	Ground-State
In	Indium
InAs	Indium Arsenide
IBL	Ion Beam Lithography
InP	Indium Phosphide

IR	Infrared
KMC	Kinetic Monte Carlo
LED	Light-Emitting Diode
LIL	Laser Interference Lithography
LON	Local Oxidation Nanolithography
MBE	Molecular Beam Epitaxy
ML	Monolayer
MOCVD	Metal-Organic Chemical Vapour Deposition
MOSFET	Metal-Oxide-Semiconductor Field-Effect Transistor
MQW	Multiple Quantum Wells
ND	Neutral Density
Nd:YAG	Neodymium-Doped Yttrium Aluminium Garnet
NIL	Nanoimprint Lithography
NR	Nanoring
NS	Nanosecond
NW	Nanowire
OPSL	Optically Pumped Semiconductor Laser
PL	Photoluminescence
QCL	Quantum Cascade Laser
QD	Quantum Dot
QDM	Quantum Dot Molecule
QR	Quantum Ring
QW	Quantum Well
RHEED	Reflection High Energy Electron Diffraction
Sb	Antimony
Si	Silicon
SAG	Selective Area Growth
SAQD	Self-Assembled Quantum Dot
SCQD	Site-Controlled Quantum Dot
SEM	Scanning Electron Microscopy
S-K	Stranski-Krastanov
SL	Superlattice
SLM	Spatial Light Modulator
STM	Scanning Tunnelling Microscope

TE	Transverse Electric
TEM	Transmission Electron Microscopy
TM	Transverse Magnetic
UHV	Ultra-High Vacuum
UV	Ultraviolet
VB	Valence Band
VLS	Vapour-Liquid-Solid
V-W	Volmer-Weber
WL	Wetting Layer
1-D	One-Dimensional
2-D	Two-Dimensional
3-D	Three-Dimensional
0-D	Zero-Dimensional

CHAPTER *1*

INTRODUCTION

1.1 THE DRIVE TOWARDS III-V COMPOUND SEMICONDUCTORS

A vision for the miniaturisation of machinery and controlling material at the molecular or atomic level was outlined by a notable talk in 1959 given by Richard Feynman entitled "There's plenty of room at the bottom" [1]. After decades of efforts, many of Feynman's hypotheses have been verified to be technically feasible and a wealth of innovative concepts have been verified. The field of manipulating matter and devices on the scale of molecules and atoms, normally between 1 and 100 nanometres (nm), is now referred to as nanoscience and nanotechnology. In the 21st century, these concepts have evolved into one of the most important industrial technologies and are being used in an assortment of areas including information technology, chemistry, engineering, biology and medicine. The progress made in nanoscience and nanotechnology has significantly relied upon the exploitation of new nanomaterials and nanostructures with unique characteristics.

Modern society has witnessed considerable scientific and technological progress in electronic and optical communications, involving integrated circuits and semiconductor photonics. The development of semiconductor nanotechnology has been the key driving force for novel micro-, nanoelectronics, optoelectronics and quantum information science. The scaling of transistors has continued for the past 50 years as predicted by Moore's law [2]. However, conventional silicon (Si)-based transistors are approaching their technological limit and at some stage it may be necessary to look beyond the Si MOSFET for advanced computation approaches. In addition, Si has an indirect band gap therefore an inefficiency in terms of optical absorption and emission. Whilst in recent years Si-based photonics has become a compelling technology platform, the lack of an integrated light source remains a

serious limitation. In order to extend the information technology revolution, it is highly desirable to replace Si with alternative high-performance nanomaterials and systems. Hence, III-V compound semiconductors are reckoned as one of the up-and-coming alternatives attributed to their high carrier mobility and high electron drift velocity [3]. It has recently been reported that nanoscale transistors fabricated using III-V compound semiconductors yield superb performance [4][5]. III-V semiconductors also exhibit high photon conversion efficiency coupled with a range of band gaps that can map to specific applications. The exploitation of new generation quantum technologies, for instance, cavity quantum electrodynamics, quantum communication and computing systems on account of III-V semiconductors have attracted growing interest [6][7][8].

Elements listed in Group III and Group V of the periodic table can combine to form III-V compound semiconductors, e.g., InAs, InP, GaAs, GaN, AlAs, GaSb, etc., and their ternary and quaternary alloys. Figure 1.1 displays various semiconductor materials with their corresponding band gap energy and lattice constant. Since the first III-V compound was synthesised by Thiel and Koelsch in 1910 [9], III-V compound semiconductors have turned into the theme of intense research for decades in view of their wide scope of electronic and optical properties and their application potential. Many III-V semiconductors have direct band gaps that exhibit strong light absorption and high emission efficiency, which make them particularly attractive in optoelectronic applications including light-emitting diodes (LEDs) [10], solid-state lasers [11], photodetectors [12], and solar cells [13][14]. Another example of their potential is that the conversion efficiency of Si solar cells is limited to around 25%, whilst multijunction AlGaInP/AlGaAs/GaAs/InGaAs solar cells have enabled a conversion efficiency record of 47% [13].
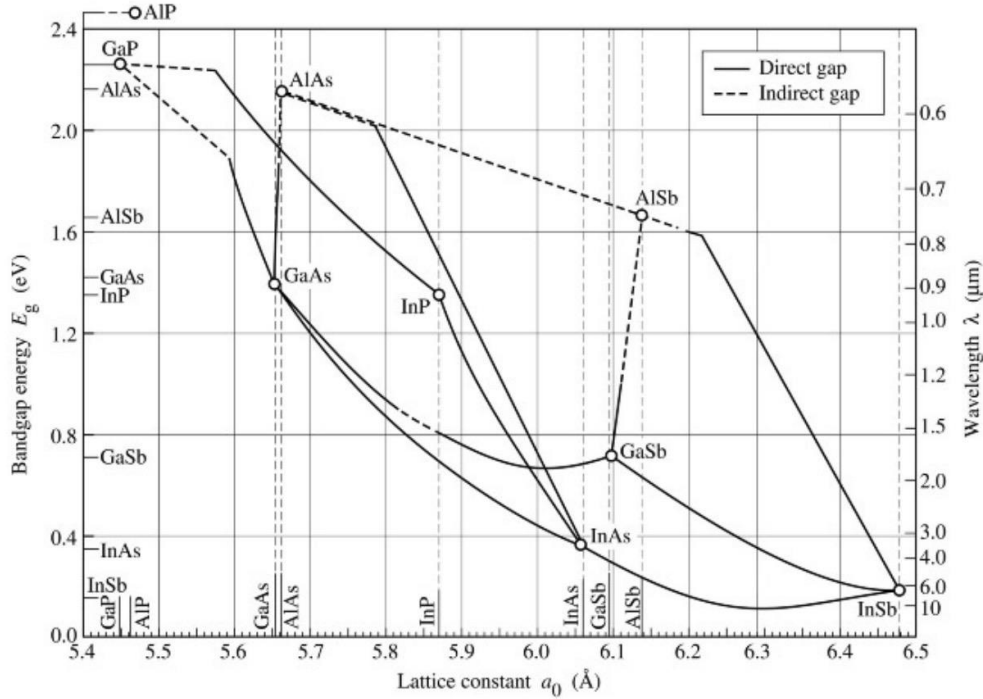
Figure 1.1 Graph of commonly used III-V compound semiconductors with their band gap energy, lattice constants, and wavelengths at room temperature (adopted from Tien, 1988).

Minimising the dimensions of semiconductor materials has been shown to alter the chemical and physical properties in a way that deviates from their bulk form. In particular, structuring on the nanoscale has been shown to considerably enhance the performance of semiconductor devices. Nowadays, the advancement in lithography and epitaxial growth techniques has taken the material size down to a few nanometres, at which scale the electronic and optical characteristics of the nanostructured materials can be governed by quantum effects. By precisely controlling the dimensions of semiconductor structures, we are able to obtain low-dimensional quantum systems for the realisation of state-of-art device technologies. In particular, III-V compound semiconductor nanostructures have aroused increasing interest on account of their intriguing physical characteristics and are at the forefront of future device innovation.

1.2 LOW-DIMENSIONAL SEMICONDUCTOR NANOSTRUCTURES

When the dimensionality of a semiconductor nanomaterial reaches the order of the de Broglie wavelength of electrons or holes, e.g., 8 nm for electrons in Si and 17 nm in GaAs at room temperature [15], quantum effects begin to take a prominent role. A

simple way to create such confinement is a semiconductor heterostructure produced by interfacing two or more semiconductor materials with distinct band gap energy. In this way, charge carriers are confined within the material and novel physical phenomena such as electrical, mechanical, magnetic, and optical properties can be introduced. According to the degrees of freedom of carrier movement in all spatial directions, semiconductor structures are classified as three-dimensional (3-D) bulk structures, two-dimensional (2-D) quantum wells (QWs), one-dimensional (1-D) nanowires (NWs) or nanotubes (NTs), and zero-dimensional (0-D) quantum dots (QDs). Additionally, quantum confinement effects in low-dimensional structures result in significant variations in the density of states (DOS) and the energy band structure in materials. The DOS stands for the number of states per unit energy per unit volume and determines the energy distributions of carriers in a semiconductor. Figure 1.2 describes that the further reduction in semiconductor dimensionality gives rise to a more discontinuous and discrete DOS function.
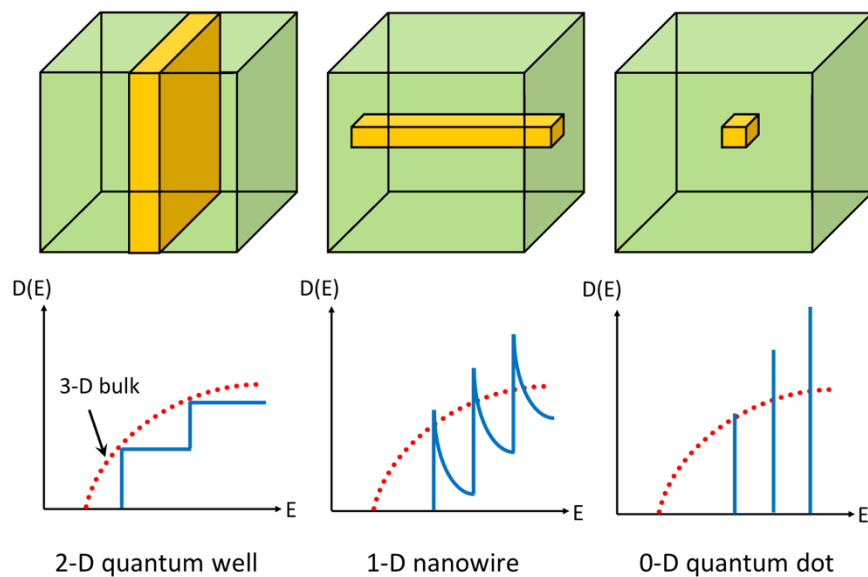
Figure 1.2 Low-dimensional quantum systems (2-D, 1-D and 0-D) and their density of states D(E). The red dotted line denotes the DOS of 3-D bulk.

The quantisation of energy levels in low-dimensional semiconductor nanostructures offers intriguing optical and electronic characteristics, which endow them with great potential in the fields of optoelectronics, electronics and photonics. A 2-D QW refers to a thin potential well layer sandwiched by barrier layers that can confine electrons and holes in one dimension. III-V compound QW-based nanostructures, for example, GaAs/AlGaAs superlattices, type-II InAs/GaSb superlattices, GaAsBi/GaAs multiple

quantum wells (MQWs), InGaN/GaN MQWs, etc have been intensively used in commercial devices such as infrared (IR) photodetectors [16][17][18], LEDs [19][20][21], and quantum cascade lasers (QCLs) [22][23][24]. A representative transmission electron microscopy (TEM) image of GaAs/AlGaAs MQWs for QCLs is shown in Figure 1.3(a). In the recent decade, 1-D III-V NWs that allow carriers to propagate freely in the longitudinal direction have drawn great attention for applications, particularly in nanoelectronics [25][26], nanophotonics [27][28] and photovoltaics [29][30]. In terms of photonics applications, semiconductor NWs can exhibit high optical absorption and strong lateral light coupling. Both the electronic and photonic properties can be manipulated by their geometry, surface-to-volume ratio, composition, doping, external electrical field, etc. NW structures have a diameter typically from a few nm to sub-micron, whilst the length can reach tens of microns. To give an instance, Figure 1.3(b) manifests a scanning electron microscopy (SEM) micrograph of hexagonal GaAs NW arrays.

(a)   (b)   (c)
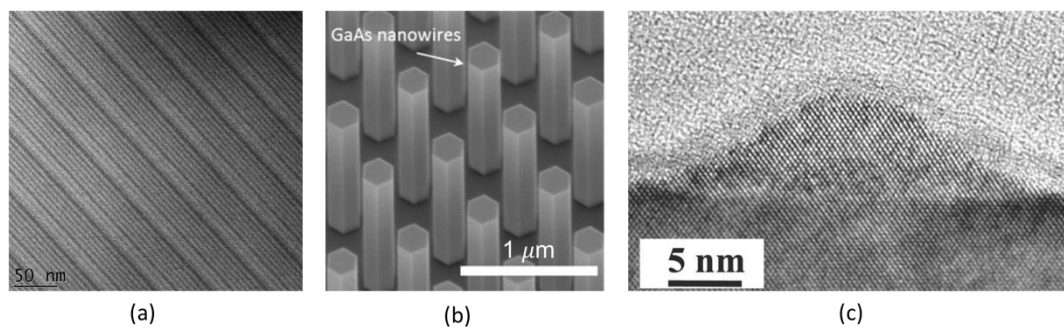
Figure 1.3 (a) TEM image of GaAs/AlGaAs MQWs [22]. (b) SEM image of GaAs NW arrays [29]. (c) TEM micrograph of an InAs/GaAs QD [31].

Semiconductor quantum dots (QDs) are 0-D nanostructures, also known as "artificial atoms", that confine carriers in all three spatial dimensions. These structures may be formed by chemical synthesis [32] or epitaxial growth methods under certain controlled conditions. Here we will focus on the epitaxial approach which offers a high degree of size control coupled with the ability to incorporate into a crystal matrix. The typical size of such a QD is a few to tens of nm and the resulting structure may therefore contain typically 10^4 - 10^5 atoms. Figure 1.3(c) displays a TEM cross-sectional image of one such QD system, that of InAs on GaAs. By reason of the strong quantum confinement and their discrete atomic-like electronic states, QDs exhibit superior electronic and optical properties that are contingent upon the dot shape, size and alloy

composition, which provide them with excellent performance in optoelectronic devices, e.g., QD lasers and LEDs. Specifically, the concept of QD lasers was first theoretically proposed by Arakawa *et al*. in 1982 [33], predicting low threshold current density and less temperature sensitivity compared with conventional QW lasers, and afterwards they have been experimentally verified to achieve high differential gain, high-speed modulation, and extremely low threshold current density [34][35][36]. III-V compound QDs also offer a wide spectral range of emission wavelengths, for example, the emission wavelengths of InAs/GaAs QDs can be tuned from 900 nm to the 1.55 μm telecom wavelength at room temperature by controlling their size and composition [37][38].

Moreover, the development of high-quality single photon sources and the manipulation of spin qubits have enabled the applications for on-chip quantum photonic circuits and novel quantum information technologies, including quantum key distribution, communication, computing, and cryptography [39][40][41][42][43]. Single semiconductor QDs appear to be excellent sources of pure, bright, indistinguishable and on-demand single photons. It has been reported that III-V self-assembled QDs can achieve high purity single photons [44]. Once a QD is filled with two electron-hole pairs, it can generate a biexciton and a radiative quantum cascade emission occurs: a single photon is emitted since the biexciton state $|XX\rangle$ decays to either of the two intermediate exciton states $|X\rangle$, and as a consequence of the transition from the exciton state to the ground state another single photon is emitted [45]. These two photons are generally with slightly different energy as a result of the Coulomb interaction. Pure single photons can be extracted by spectral filtering. An ideal QD exhibits degenerate energy of two exciton states and is able to emit a pair of polarisation-entangled photons. Specific applications have been found for highly indistinguishable entangled photon pairs, such as quantum repeaters [46]. In real QD structures, the exciton states present a fine-structure splitting (FSS) arising from an anisotropic exchange interaction, that weakens the degree of entanglement [47]. To minimise this splitting, methods including controlling the QD symmetry during growth [48], or applying electric, magnetic, or strain fields, have been employed [49][50][51].

A special case of quantum dot structures, quantum dot molecules (QDMs) are nanostructures that consist of at least two vertically or laterally coupled QDs. These have recently received great interest in quantum computing due to their unique

physical phenomena [52][53]. Electronic coupling in the molecules allows them to act as quantum gates, and qubits inside the QDMs can be adjusted by external magnetic or electric fields [54][55][56]. An atomic force microscopy (AFM) micrograph of lateral QDMs composed of two closely stacked QDs is shown in Figure 1.4(a). More complex structures e.g., semiconductor quantum rings (QRs) or nano-rings (NRs) have been explored intensively during the past years and have shown significant potential for applications in optoelectronic devices in view of their particular topology [57][58][59]. An AFM micrograph of typical GaAs/AlGaAs QRs is presented in Figure 1.4(b). It is also possible to modify the geometry of the ring structure from single rings to double rings or even concentric rings as displayed in Figure 1.4(c) and (d) through different growth conditions [60]. In QRs, as a consequence of the inimitable ring shape, quantum interference effects, particularly the Aharonov-Bohm effect, are observed under magnetic fields [61][62].
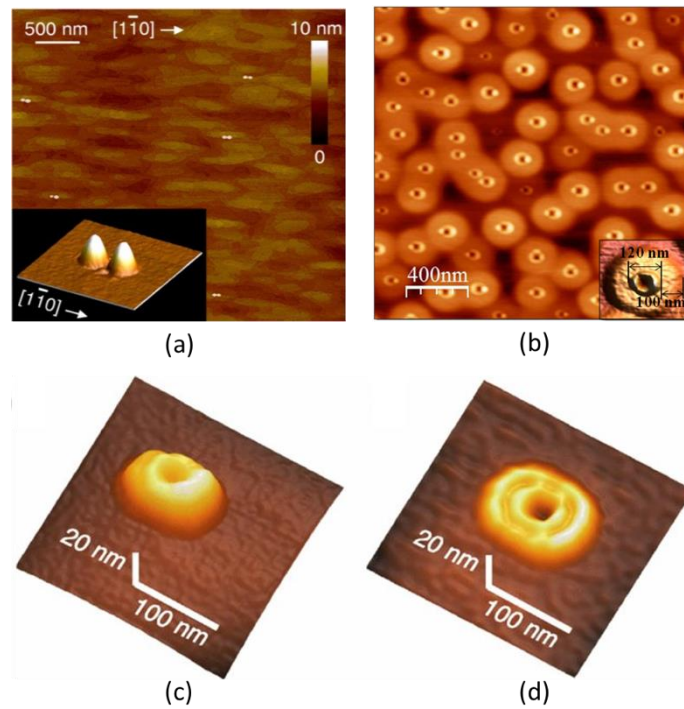
Figure 1.4 AFM micrographs of (a) lateral InAs/GaAs QDMs [56], (b) GaAs/AlGaAs QRs [57], (c) GaAs single-ring, and (d) double concentric ring [60].

These III-V compound semiconductor nanostructures offer superiority over bulk semiconductors in some applications and, in addition, provide a wealth of new quantum phenomena. Their properties however are critically dependent on their crystallinity, morphology, composition, etc. In order to implement these structures in

applications, it is of considerable importance to fabricate high-quality, defect-free and controllable nanostructures.

1.3 FABRICATION OF SEMICONDUCTOR NANOSTRUCTURES

The two major routes for fabricating semiconductor nanostructures include top-down lithographic approaches and bottom-up self-assembly routes. Regarding the top-down method, the nanostructures are produced from the bulk-like materials in a subtractive way, involving lithographic techniques such as electron beam lithography (EBL) [63], optical lithography [64], nanoimprint lithography (NIL) [65], ion beam lithography (IBL) [66], followed by an etching process, e.g., wet/dry etching, for transferring the pattern onto the material. Currently this is the dominant approach in the electronics industry. Despite the advantages the top-down method offers, such as the ability to achieve precise addressability and to form an arbitrary desired shape in specific positions, there are certain disadvantages that limit its potential for high-performance and high-efficiency devices. These include, for instance, the resolution limitation of lithographic techniques, the high cost of associated equipment, a time consuming and low throughput sequential process, etc. In addition, surface defects or contamination can easily be introduced during these processes and their minimisation requires the ultimate precautions in cleanliness and handling. For nanostructures with low dimensionality, even a single atomic scale defect or impurity in the proximity of the nanostructure may change the energetic level considerably.

As an alternative, nanofabrication by bottom-up approaches that utilise physical and chemical processes to assemble nanostructures from atoms and molecules in an additive way can allow the atomically precise control of structure dimensions, and thus, a controllable crystal structure and material composition can be attained by meticulous control of the deposition techniques. One major merit of this approach is that it overcomes the limitations of top-down techniques as it is without the need for lithographic steps and other *ex situ* processes, enabling the production of defect-free and high-quality semiconductor nanostructures. With enormous progress in both ultrahigh vacuum technology and semiconductor material science over several decades, very thin epitaxial films can be grown smoothly at atomic dimensions by modern bottom-up epitaxial growth methods. These methods include metal-organic chemical vapour deposition (MOCVD) [67], chemical beam epitaxy (CBE) [68] and molecular beam epitaxy (MBE) [69]. In this way, high crystalline quality and nearly

defect-free semiconductor materials and nanostructures can be grown with an atomic layer accuracy in a reproducible manner. For instance, III-V semiconductor NWs can be prepared with excellent dimensional control by means of the vapour-liquid-solid (VLS) growth method [70] and semiconductor QD structures can be grown by epitaxial self-assembly using MBE or MOCVD via droplet or strain-driven processes. Nevertheless, although self-assembly allows high crystalline quality nanostructures, it suffers from natural stochastic processes with an inherent disorder that results in a fluctuation in size, shape and composition. Whilst there have been significant device developments using quantum dot ensembles, the lack of precise ordering, particularly in terms of position, hinders them for device applications requiring the properties of single quantum dots rather than an ensemble. This will lead to a very low yield when we try to integrate individual QD structures into device architectures.

1.4 MOTIVATION AND OBJECTIVE

III-V semiconductor nanostructures, particularly QD structures, are of considerable interest for high performance optoelectronics, nanophononics and future quantum technologies. As ideal solid-state single photon and entangled photon sources, single QDs, QDMs and QRs have enabled a wealth of new physics and applications such as quantum emitters, quantum repeaters, and qubit gates for quantum computing [40][41][53]. Many of these applications require the incorporation of single QDs or regular arrays of QDs within device architectures such as photonic crystal microcavities or micropillar cavities to allow efficient coupling between the optical modes and the embedded QDs. The strong coupling between excitonic and photonic states enables the manipulation of quantum information [71]. Nevertheless, most of this work to date has been performed on locating randomly positioned self-assembled QDs, usually by carefully selecting an individual dot from a large number of candidates. Whilst this may be an acceptable approach for physical investigations, it would lead to a very low yield for scalable fabrication. Aside from that, lateral ordering of semiconductor nanostructures with narrow size distributions could be desirable for QD ensemble applications such as high-performance lasers, solar cells, etc. [72][73][74].

Today, it remains a challenge to engineer the size, shape, composition, position and density of self-assembled epitaxial structures accurately to exploit and fulfil their

optical and electronic potential. The capability to realise scalable and deterministic fabrication of single QD nanostructures that are laterally ordered and with identical quantum states and characteristics would constitute a key step towards future functional device applications. Therefore, an alternative nanofabrication paradigm that can both maintain the high crystalline and optical quality of materials through bottom-up natural epitaxial self-assembly, but also allows top-down lithographic positioning would be highly attractive. This would be especially true if it can be performed without the need for multi-step processing and the introduction of impurities and contamination. This could be potentially achieved through the integration of lithography and epitaxial growth in a high vacuum environment, such as that found in MBE.

Direct laser interference patterning (DLIP) has been demonstrated to be a powerful approach for fabricating large-area periodic micro- and nanoscale structures, with advantages over conventional lithographic methods. It is a mask-less approach that can be applied over a large area in a single step and is therefore highly cost effective. This dissertation seeks to establish a fast, single step and cost-effective route to produce precisely ordered arrays of high-quality III-V QD nanostructures with well-defined size and shape by combining the simplicity of *in situ* interference patterning with the advantages of MBE self-assembly.

1.5 DISSERTATION OUTLINE

This dissertation deals with the growth and characterisation of ordered arrays of III-V semiconductor nanostructures, including InAs/GaAs QDs and QDMs, GaAs/AlGaAs QDs and QRs, GaAs/Si nanocrystals and GaSb/GaAs QDs, by means of combining *in situ* direct laser interference patterning with MBE growth. The framework of this dissertation is outlined as follows.

Chapter 2 presents a succinct background and fundamentals of the epitaxy of III-V QDs, including the growth mode and growth mechanism, underlying growth thermodynamics and kinetics, S-K growth of InAs/GaAs QDs and DE growth of GaAs/AlGaAs QDs, and lastly the commonly used methods for spatial ordering or site control of III-V QDs.

Chapter 3 outlines the experimental techniques and characterisation methods involved in the dissertation work. These include MBE for the growth of

semiconductors, AFM, SEM as well as energy dispersive X-ray spectroscopy (EDS) to examine the sample surface structures and photoluminescence spectroscopy for optical characterisation.

Chapter 4 demonstrates the technique of *in situ* pulsed laser interference patterning. The principles of multi-beam interference and the simulation of the interference patterns using MATLAB are shown initially, and the innovative experimental set-up of a bench-top *ex situ* laser interference lithography for fabricating large area nanostructures on photoresist is then discussed in detail. This approach is initially used to provide important verification of the ability to perform single pulse laser exposure to produce periodic structures. Next, the integration of *in situ* DLIP with the MBE system is introduced. And then the simulation of the transient thermal effect induced by single pulse DLIP on GaAs surfaces is presented, which is critical for describing the upcoming growth of nanostructures. Last, the experimental results for single-pulse DLIP on GaAs surfaces are discussed in detail, in which regular arrays of nanoholes and nanoislands are formed.

Chapter 5 presents the growth and characterisation of ordered InAs/GaAs QD arrays, in which first a theoretical model is built to simulate the surface adatom diffusion and the initial stages of the nucleation processes. The experimental results of patterned InAs QDs and QDMs are shown. The effects of both the laser interference parameters and the epitaxial growth conditions on the formation of QD arrays are discussed. The optical characterisation of the patterned QDs is then presented.

Chapter 6 shows the growth and characterisation of ordered arrays of GaAs/AlGaAs QDs and QRs, including the results of varied growth parameters on the formation of patterned QD nanostructures and the optical characterisation of the ordered arrays of GaAs QDs and QRs.

Chapter 7 describes the initial results of *in situ* DLIP on other semiconductor materials, including the nanopatterning of Si substrates and the SAG of GaAs nanocrystals on Si, as well as their structural characterisation, and lastly the fabrication of ordered type-II GaSb/GaAs QD arrays and their structural and optical characterisation.

Chapter 8 summarises the dissertation and lays out an outlook for future work.

CHAPTER *2*

EPITAXY OF SELF-ASSEMBLED QUANTUM DOTS

Epitaxial self-assembly is one of the most important techniques for semiconductor QD fabrication. Tremendous efforts over decades have led to remarkable development in growing defect-free and high quality III-V semiconductor QDs through epitaxial self-assembly methods and then incorporating QDs into devices to fully exploit their advantageous characteristics. Nevertheless, the natural stochastic distribution and the lack of homogeneity in shape, size, and composition of the self-assembled QDs (SAQDs) hinder their performance in device applications. The reliable production of highly homogeneous and ordered QDs during epitaxy still presents a technical challenge. As a result, approaches to accurately control QDs over the size, density and spatial ordering are highly desirable. Many excellent research works have been carried out in recent years to deterministically control the QDs at defined positions and to organise SAQDs into regular arrays with homogeneous size distribution. Techniques such as strain anisotropic engineering [75] and pre-patterning the substrate prior to QD growth [76][77] are commonly involved, which will be reviewed in detail in this chapter. Amongst these approaches, the site controlled QD growth on pre-patterned substrate surfaces, typically holes or pits by lithographic methods, has been successfully demonstrated in various systems [78][79].

With the aim of achieving control over SAQD growth, it is necessary to shed light on the underlying mechanisms, since the interplay between growth thermodynamics and kinetics provides the incentive for QD self-assembly. This chapter covers the fundamental epitaxial growth processes involved in the QD formation and the current well-established approaches that have been employed for QD lateral ordering. Section 2.1 briefly introduces the growth mechanism during epitaxy, in which the S-K growth mode and the alternative droplet epitaxy (DE) growth method will be respectively

described. In Section 2.2, we will review several methods commonly used to obtain site-controlled growth and spatial ordering of QDs.

2.1 GROWTH MECHANISM OF SAQDS

In the early 90's, the spontaneous emergence of dislocation-free islands was first experimentally observed in heteroepitaxial systems of Ge/Si (100) [80][81], and thereafter the growth of InAs SAQDs on GaAs was reported [82][83]. Since then, the fundamental aspects of these heteroepitaxial growth systems have been intensively investigated and this has shown that the formation of 3-D coherent islands is directed by the elastic relaxation energy on account of the lattice mismatch between the underlying substrate and the deposited material, for instance, ~4% for Ge/Si and ~7% for InAs/GaAs. This growth technique has since also been successfully employed to other III-V heteroepitaxial systems such as GaSb/GaAs, InP/InGaP and InGaN/GaN QDs. In the meantime, epitaxial growth theories of SAQDs have been developed and continue to be debated, including thermodynamic and kinetic considerations.

The thermodynamics of self-assembly hinge on the principle of thermodynamic equilibrium in that the epitaxial system contrives to reach the minimum of the free energy by contrasting the surface energy density of the epilayer and the substrate, the interface energy between the epilayer and the substrate as well as the elastic relaxation energy. The decrease in total free energy drives the formation of self-assembled nanostructures. From the thermodynamic rationale perspective, the heteroepitaxial growth of nanostructures can be categorised into three classical growth modes [84], which are the Volmer-Weber (V-W) mode [85], the Stranski-Krastanov (S-K) growth mode [86], and the Franck-van der Merwe (F-M) mode [87]. Figure 2.1 diagrammatically depicts these three growth modes. The surface energy density of the deposited layer γ_l, the surface energy density of the substrate γ_s and the interface energy density between the deposited layer and the substrate γ_{sl} are proposed to identify the growth modes.
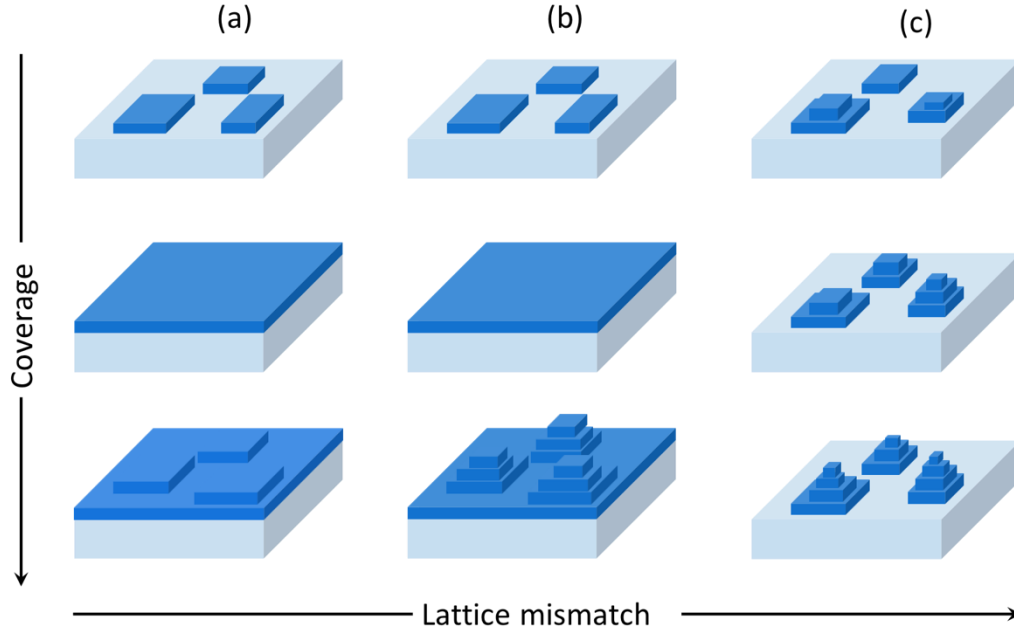
Figure 2.1 Diagrammatic representations of three kinds of heteroepitaxial growth modes. (a) the F-M mode, (b) the S-K mode and (c) the V-W mode.

In the F-M growth mode, also called the layer-by-layer mode, the crystal grows in a 2-D layer-by-layer manner, where $\gamma_s \geq \gamma_l + \gamma_{sl}$, and there is no accumulation of strain energy during the growth process by reason of a small lattice mismatch between the substrate and the deposited layer. Whereas in the case of the V-W mode, or island mode, $\gamma_s < \gamma_l + \gamma_{sl}$, 3-D islands form directly on the substrate. The driving force for island formation could be a large lattice mismatch between the substrate and the deposited layer, or the high surface energy of the deposited layer compared to that of the substrate, or the high interface energy due to the different crystallographic structures. With respect to the S-K growth mode, which lies intermediately between F-M and V-W modes and is therefore observed in intermediate strain situations, this embarks first upon the formation of a 2-D pseudomorphic layer, known as the wetting layer (WL). Then once the WL surpasses a certain critical value, the system relaxes to liberate the strain energy, forming coherent 3-D islands upon the WL. The S-K growth mode is the representative mode for many intermediately strained III-V heteroepitaxial systems such as InAs/GaAs (001) SAQDs.

Since most growth processes take place in nonequilibrium conditions, it is essential to include growth dynamic or kinetic considerations to further investigate the growth mechanisms. The surface morphology is controlled by the kinetics and interaction

between the adatoms with kinks, steps and terraces on the substrate. During MBE growth, typical kinetic events are presented schematically in Figure 2.2. Atoms from the vapour phase impinge upon the surface of the substrate at a deposition flux rate F, anterior to atom physisorption or chemisorption on the growth surface. The adatoms on the surface undergo random diffusion to favourable lattice sites overcoming local diffusion barriers. After mobile adatoms meet each other, they may form dimers or larger clusters by adatom aggregation. Nucleation and growth take place by further aggregation or attachment to existing islands. The desorption of adatoms into the gas phase may also occur during the growth process at high temperatures, or these may dissociate or detach from clusters/islands. In the conventional mean-field theory [88], the heteroepitaxial growth of QDs is generally elucidated as a process of irreversible adatom aggregation via random adatom diffusion and attachment/detachment, which is analogous to the well-known kinetic mechanism for sub-monolayer epitaxial growth of 2-D islands [89]. In the early stage of nucleation, due to the lack of existing formed 2-D islands on the surface, an adatom is prone to interact with another adatom to form a cluster rather than being captured by existing islands. As deposition continues, instead of nucleating new islands, stable 2-D islands can grow laterally by capturing adatoms to the edges, and vertically by directly depositing atoms atop the island or by atom upward hopping from the edges to the island top to nucleate a new 2-D island atop the original island. Once the 2-D island diameter is large enough, lateral growth is restrained, whilst atoms migrate from the edges of the 2-D island to its top, where the strain is released, leading to an increase in island height [88][90][91]. Typically, in MBE, which is usually far from equilibrium, growth limited by kinetics plays an important role.
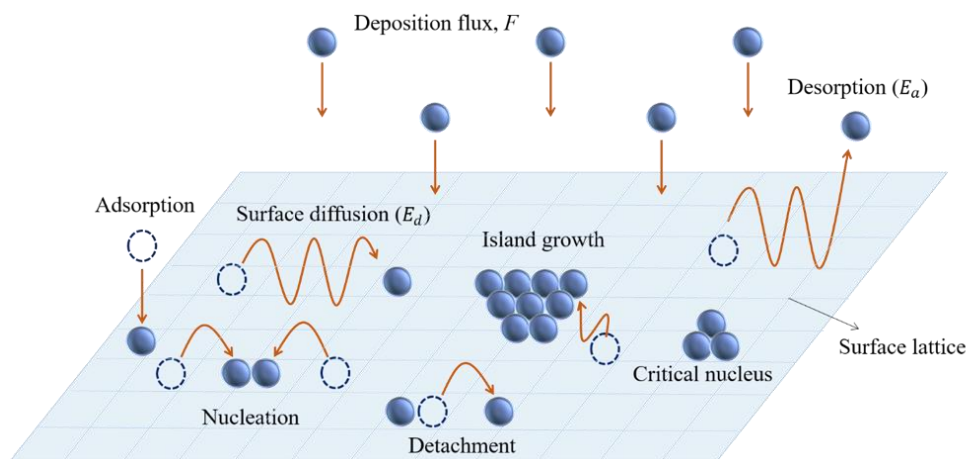
Figure 2.2 Depiction of typical kinetic atomistic processes during epitaxial growth.

Hence, the interplay between thermodynamics and kinetics is of particular significance to the epitaxial growth of nanostructures. In recent years, it has been proposed to apply both thermodynamic and kinetic models to analyse the size distributions of coherent islands and to speculate on the resulting evolution of density and size distributions which depend upon temperature and growth rate (GR), etc. For instance, Shchukin *et al*. have initiated a thermodynamic model to consider the energetics of coherent QD ensembles which involves the surface energy and strain energy [92]. A quantitative thermodynamic model has been built that can address the transition and formation of SAQDs by Li *et al*. [93][94]. Meanwhile, kinetic models which can explain the formation of coherently strained islands including the stages of island nucleation, growth and interactions have been established [95][96][97][98].

Typical epitaxial III-V SAQDs are grown via the two most prominent growth modes, which are the S-K growth mode for lattice-mismatched systems and DE for both lattice-mismatched and lattice-matched systems. In(Ga)As SAQDs grown on GaAs substrates are nowadays one of the most extensively studied prototypical III-V semiconductor QDs for optoelectronic and photonic applications. In view of the lattice mismatch, InAs SAQDs are generally grown via the S-K growth mode by MBE or MOCVD. In the forthcoming sections, the S-K and DE growth of III-V SAQDs will be demonstrated respectively.

2.1.1 STRANSKI-KRASTANOV GROWTH OF INAS/GAAS QDS

InAs QDs obtained by the S-K growth mode generally exhibit high structural and optical quality in spite of stochastic dot nucleation. With regard to the S-K growth mode, a thin 2-D layer (WL) of InAs is initially deposited upon the GaAs substrate, and as the deposition thickness increases, the strain that arises from the 7.2% compressive lattice mismatch between InAs and GaAs accumulates. As the WL thickens to a critical amount, the transition from 2-D layers to 3-D islands takes place and this so-called QDs growth takes place to liberate the elastic energy accumulated in the layer. In terms of the InAs/GaAs (001) system, the critical thickness of the WL ranges from 1.5 to 1.8 monolayer (ML) [91][99], subject to the growth temperature. The surface density of S-K InAs QDs typically ranges between 1×10^8 and 1×10^{11} cm^{-2}. A 3-D AFM image of S-K InAs/GaAs (001) SAQDs by MBE presenting a comparatively high surface density of $\sim 2.2 \times 10^{10}$ cm^{-2} is displayed in Figure 2.3(a). The typical height and width of a SAQD are 1-15 nm and 10-100 nm, respectively. It has been

demonstrated that the shape of InAs SAQDs can vary from a pyramid-like shape to a dome-like shape, with transitions in the shape resulting from an increase in the deposition amount or by ripening [100][101]. Figure 2.3(b) presents an STM image of a typical pyramid-like shape InAs/GaAs (001) QD.
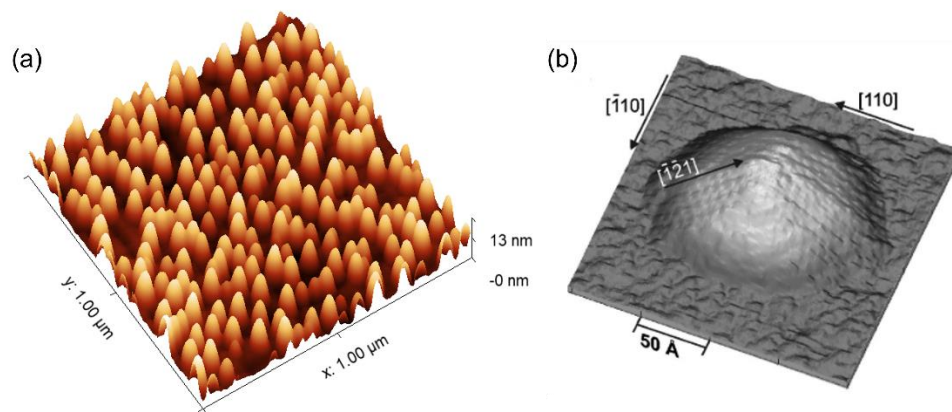
Figure 2.3 (a) 1 × 1 μm² 3-D AFM micrograph of InAs SAQDs on GaAs, (b) 3-D STM micrograph of a pyramid-shape InAs/GaAs (001) dot [102].

Figure 2.4 demonstrates the surface morphology with 1.5 ML InAs coverage on the GaAs (001) substrate [103], which is just at the point of the initial formation of SAQDs. It is possible to observe three different kinds of features on the terraces, which are, approximately 1 ML high 2-D islands, small quasi-3-D QDs at the upper edge of the islands or terraces, and larger 3-D QDs. These quasi-3-D QDs are a precursor of the large 3-D QDs and are only observable within a limited range of InAs coverage, tending to disappear after a certain coverage. It is noted that the nucleation of SAQDs is always found preferentially at the upper step edges of 2-D islands or terraces, which could be associated with the energy barrier for indium adatom diffusion and elastic energy relaxation at the step edges [104].

InAs/GaAs SAQDs grown via the S-K mode have shown advantages such as coherently stained structures (defect-free) and high optical quality. Nevertheless, owing to the natural stochastic nucleation process, the resulting fluctuations in shape, size, composition of these SAQDs and spatial randomness causes difficulties for device application. Over the past decades, there have been considerable efforts which have attempted to tune the size, density and shape as well as to homogenise the SAQD size distribution by optimising the growth parameters, e.g., the GR, the growth interruption time and the capping temperature, etc [105][106][107][108][109].
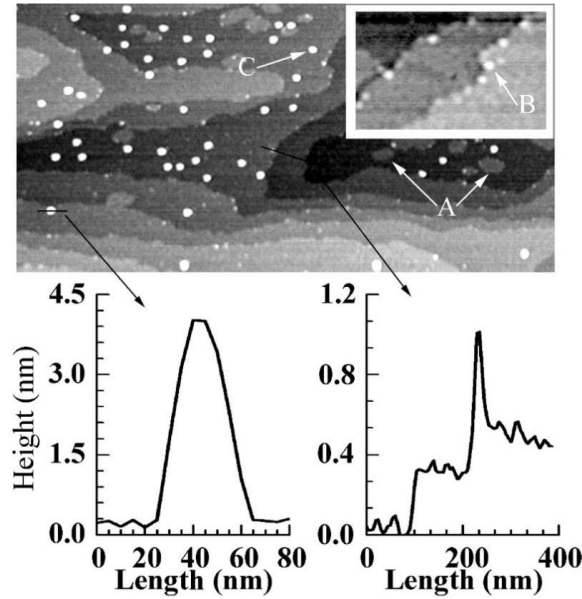
Figure 2.4 AFM micrographs of 1.5 ML InAs deposited upon a GaAs (001) surface. A: ~1 ML high 2-D islands; B: a small quasi-3-D QD showing width of ~20 nm and ~2 in height; C: a ~40 nm wide and 3-4 nm in height 3-D QD. The inset shows clearly preferred dot nucleation at the upper step edges. The cross-sections show the typical full-sized QDs (left) and quasi-3-D dots on the steps [103].

2.1.2 DROPLET EPITAXIAL APPROACH

For lattice-matched material systems that cannot be fabricated via the S-K growth mode, the DE method provides an effective alternative. The DE technique was first introduced in 1993 by Kogushi *et al*. [110]. With regard to the epitaxial growth of III-V nanostructures, the DE method has now established itself as a highly attractive alternative route. It is an epitaxial growth method that relies on the formation and manipulation of group III metallic droplets and the subsequent incorporation of group V elements to crystallise these droplets into 3-D nanocrystals on the substrate surface. III-V SAQD systems such as lattice-matched GaAs/AlGaAs QDs [87][88][113], and lattice-mismatched InGaAs/GaAs QDs [114][115], have been successfully fabricated using the DE approach. In this work, the DE growth of GaAs QDs arranged in an ordered manner on AlGaAs surfaces will be discussed.
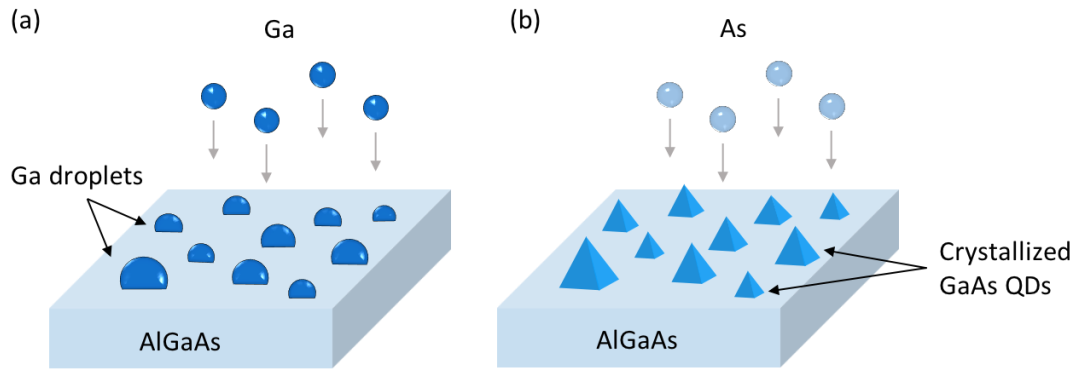
Figure 2.5 Schematic illustrations of GaAs/AlGaAs QD growth by DE (a) deposition of Ga metallic droplets and (b) GaAs QD formation by crystallisation under an arsenic flux.

The process for growing GaAs/AlGaAs QDs via the DE approach is schematically illustrated in Figure 2.5. First, Ga is deposited onto an AlGaAs surface unaccompanied by arsenic flux to create liquid Ga droplets. This approach has some similarities to the V-W growth mode. Subsequently, these droplets are crystallised under an arsenic flux to form GaAs nanocrystals (QDs). The QD density is governed by the droplet density, ranging from low (~10^8 cm^{-2}) to high density (~10^{11} cm^{-2}) [111][116], depending upon the deposition amount of Ga and the substrate temperature. The technique is relatively simple in principle, but the production of high-quality GaAs QDs through DE is challenging since it requires a system with a very low As background pressure to prevent premature crystallisation, and low deposition temperatures of about 200 °C are required, which may result in point defects. As a result, long growth interrupts to reduce the As background are a requirement and post-growth annealing is an essential procedure needed to restore the crystalline quality [117]. By controlling the substrate temperature and V/III ratio, different nanostructure morphologies including QDs and QRs can be obtained by DE [118][119]. Figure 2.6(a) displays a cross-sectional HRTEM micrograph of a GaAs/AlGaAs SAQD, and (b) and (c) reveal 3-D AFM micrographs of ~5 × 10^9 cm^{-2} density GaAs/AlGaAs QDs and QRs respectively. These QDs are typically 30-50 nm in diameter and ~10 nm high, whereas a lower height for the QRs is observed at around 2 nm.
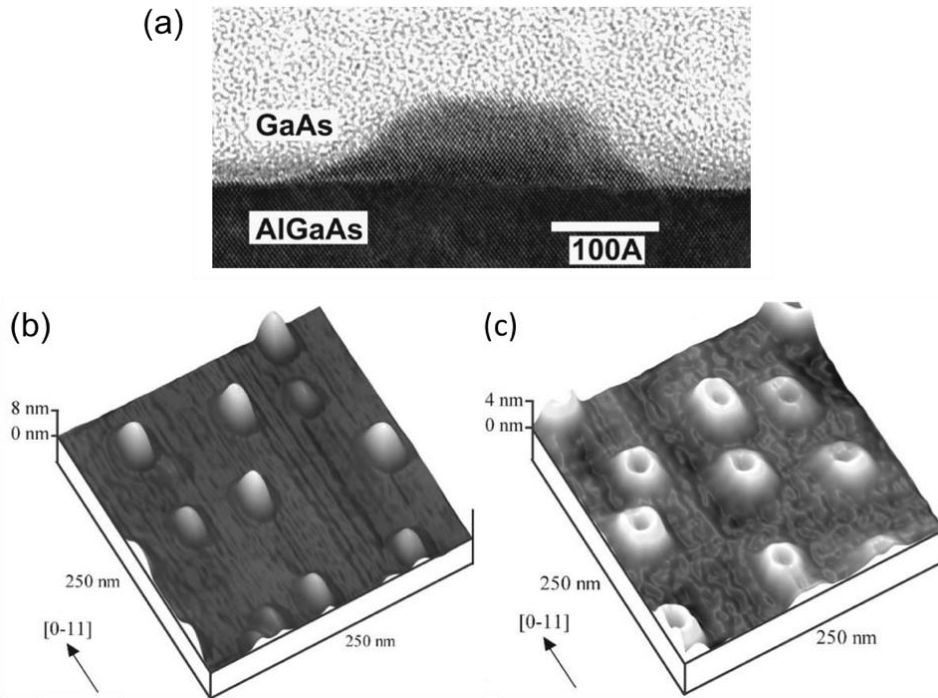
Figure 2.6 (a) Cross-sectional HRTEM micrograph of a GaAs/AlGaAs QD [113]. AFM micrographs of GaAs/AlGaAs (b) QDs and (c) QRs [118].

2.2 APPROACHES FOR THE LATERAL ORDERING OF SAQDS

The fabrication of large area and reliable high-quality SAQDs with precise control of their lateral alignment remains an obstacle owing to the random nucleation and natural inhomogeneity of epitaxial QDs. To surmount this issue, numerous efforts have been devoted to obtaining the ultimate control over the lateral positioning of SAQDs, basically relying on either structuring the growth surface directly or relying on crystallographic properties such as steps formed on high index surfaces or strain field modulation. Approaches demonstrated include the growth on multiatomic steps [120], vicinal substrates [121], high index substrates [122], cleaved-edge overgrowth [123], inverted pyramid growth [124], multilayer vertical stacking [37][125], self-organised anisotropic strain engineering [75][126], and substrate pre-patterning [127][128][129]. Amongst these approaches, the epitaxial regrowth on a pre-patterned substrate has been shown to be the most promising way to achieve precision site-controlled QD growth, with a number of results showing both precise alignment and excellent optical qualities [76][77]. In this section, a brief overview of some representative approaches to achieve the lateral ordering of SAQDs will be given.

2.2.1 MULTILAYER VERTICAL STACKING

The vertically stacking of QDs in multilayers has been shown to be an effective approach for the improvement of both QD positioning and homogeneity [37][130]. The approach relies on the seeding effect from the modulation of the strain field generated by the underlying QDs. When the spacer layer is sufficiently thin, QDs are inclined to nucleate on top of the buried dots as a result of strain-induced adatom migration. The ordering probability was found to be strongly related to the spacer layer thickness. Figure 2.7(a) illustrates the process of indium adatom diffusion on the stressed surface, and Figure 2.7(b) displays the cross-sectional TEM micrograph of vertical stacking of InAs/GaAs (100) QDs spaced by a 36 ML-thick layer.
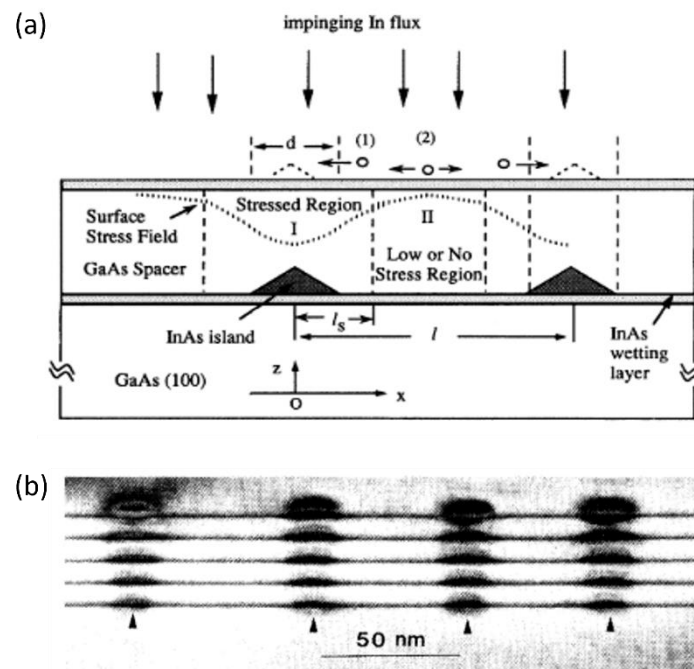
Figure 2.7 (a) Illustrative diagram of indium adatom migration on the strained surface. (b) A cross-sectional TEM micrograph displaying InAs/GaAs (100) SAQDs that are vertically stacked with 36 ML GaAs spacer layers [37].

Wang *et al*. introduced the growth of 1-D arrays of InGaAs quantum dot chains (QDCs) on GaAs (100) by stacking 17-period QD layers with the alignment attributed to the anisotropic strain field-driven self-assembly [125][131][132]. The QD alignment could be enhanced by introducing growth interruptions when growing GaAs spacer layers, and by controlling the InGaAs deposition amount, QDCs longer than 5 μm were fabricated. AFM images of the fabricated 1-D arrays of InGaAs QDCs are shown in

Figure 2.8. It was concluded that the lateral ordering of SAQDs is the result of the surface anisotropy of strain that affects adatom migration, and the repulsive interaction between adjacent QDs. The lateral ordering and QD uniformity can be improved by altering the number of multilayers, the thickness of the spacer layer and the alloy composition [132].
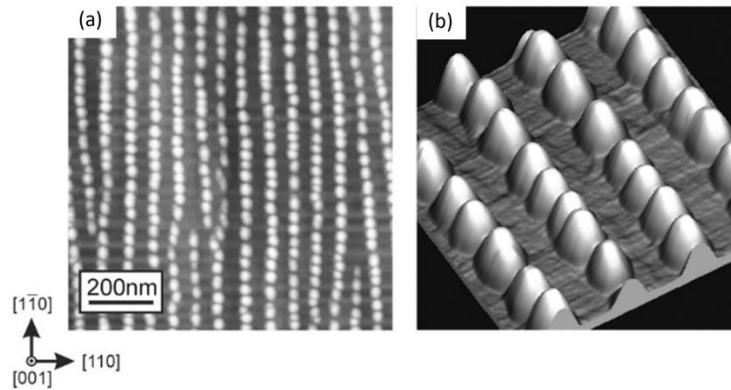
Figure 2.8 AFM micrographs of (a) 2-D and (b) 3-D InGaAs/GaAs QDC arrays by vertically stacking 17-period multilayers [125].

2.2.2 SELF-ORGANISED ANISOTROPIC STRAIN ENGINEERING

Lateral position controlled SAQDs have been attained through self-organised anisotropic strain engineering which relies upon the local anisotropic strain modulation in a grown multilayer superlattice (SL) template. It was first reported by Mano *et al.* who utilised anisotropic strain engineering to fabricate 1-D linear arrays of InAs SAQDs on GaAs (100) substrates by MBE [75]. It has also been shown as a feasible approach for InAs QDs on an InGaAsP/InP (100) SL template [126]. The growth processes include random QD formation, the deposition of a thin cap, high temperature annealing, the overgrowth of QDs and the vertical stacking of SLs, which are illustrated in Figure 2.9 [133]. Due to the adatom anisotropic diffusion and strain correlations, linear arrays of SAQDs were formed on the SL template. By controlling the deposition amount, the number of SL periods and the separation layer thickness, linear well-organised QD arrays were formed. The advantage of this technique is that it is defect-free and maintains high structural and optical properties.
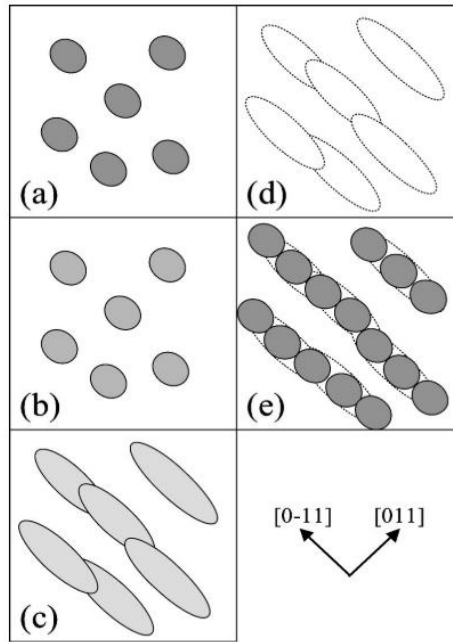
Figure 2.9 Schematic of lateral QD ordering on QW-like SL template. (a) Formation of random SAQDs, (b) deposition of a thin capping layer, (c) elongated QD formation after annealing, (d) deposition of spacing layer and (e) overgrowth of QDs [133].

Figure 2.10 exhibits AFM micrographs of 1-D arrays of InAs/GaAs SAQDs through self-organised anisotropic strain engineering with different deposition amounts (a) 2.3 nm and (b, c) 1.8 nm, and GaAs separation thicknesses (a, b) 13 nm and (c) 16 nm.
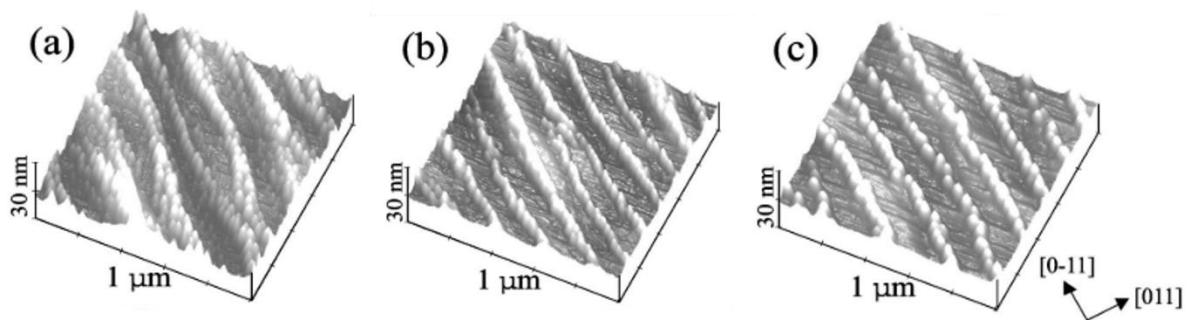
Figure 2.10 3-D AFM micrographs of InAs SAQDs upon QW-like templates (a) 2.3 nm InAs SAQDs grown at 540 °C separated by 13 nm thick GaAs layer, (b) 1.8 nm InAs SAQDs grown at 540 °C separated by 13 nm thick GaAs layer, and (c) 1.8 nm InAs SAQDs grown at 540 °C separated by 16 nm thick GaAs layer [133].

In a similar way, the MBE growth of 2-D arrays of InAs QDs or QDMs on high index GaAs (311)B substrates based upon InAs/GaAs SL templates has been presented [134][135]. Such growth results in 2-D mesoscopic modulation of the strain field as

well as the formation of InAs SAQDs atop the SL template in a periodic lateral arrangement. Figure 2.11 presents AFM images of 2-D arrays of self-organised anisotropic strain engineered InAs SAQDs using a 10-period InAs/GaAs SL template on the GaAs (311)B substrate. Connected InAs QD arrays were observed by depositing 3.3 nm InAs atop the SL template without annealing, as shown in Figure 2.11(a), and isolated QDM arrays were formed by depositing 0.6 nm InAs at 485 °C with annealing (b). Almost single InAs QD 2-D arrays were formed with 0.45 nm InAs coverage and an increased growth temperature of 510 °C.
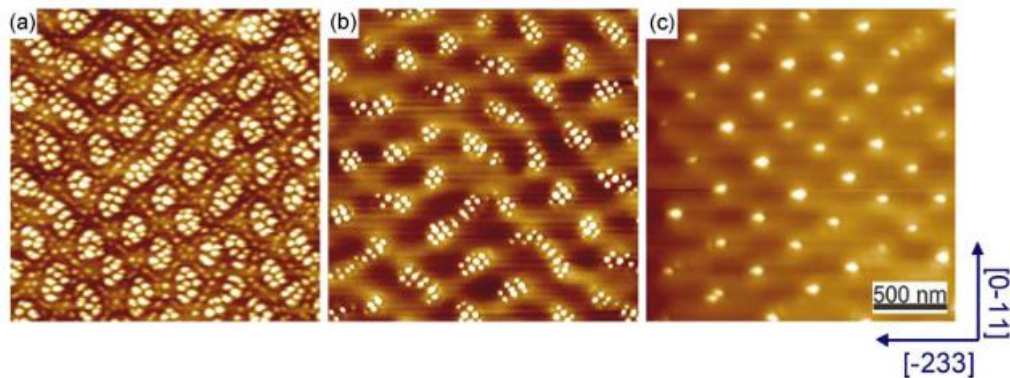
Figure 2.11 AFM micrographs demonstrating ordered arrays of InAs SAQDs transit from QDMs to single dots on InAs/GaAs SL templates utilising different growth conditions including growth temperatures, annealing temperatures, annealing time, InAs amounts [135].

2.2.3 SITE-CONTROL BY SUBSTRATE PRE-PATTERNING

Intensive research works have been carried out on the growth of site controlled QDs (SCQDs) by substrate pre-patterning and regrowth. The approach relies upon the introduction of local surface features on the substrate, such as arrays of pits, grooves, nanoholes, or trenches, that can serve as preferred nucleation sites for QDs. For regrowth on such a pre-structured surface, the diffusion of adatoms is driven by curvature-induced capillary under chemical potential gradients [136]. The tendency of SAQDs to nucleate at the step edges or kinks, on the sidewalls of ridges has been widely observed [137].

Commonly used techniques to pattern the substrate surface include EBL [76][78][129][138], IBL [139], ultraviolet (UV)-NIL [127][140][141] and AFM assisted local oxidation nanolithography (LON) [142][143], scanning tunnelling microscopy

(STM) probe-assisted lithography [144], etc. These approaches provide excellent positional control of QDs, and show high scalability and feasibility for deterministic device integration [145]. However, these are all sequential scanning approaches and as a result, the patterning process takes considerable time to complete. Whilst these are excellent research-level tools, it is worth pointing out that the semiconductor industry prefers to use optical lithography techniques in which a single exposure can pattern a large area. Also, contaminants and defects at the regrowth interface may be introduced by the use of these *ex situ* lithographic methods when combined with etching. Residual surface oxides resulting from *ex situ* processing may result in a non-negligible degradation of the optical quality [146]. Generally, this influence can be mitigated by means of state-of-the-art wafer cleaning procedures such as atomic hydrogen cleaning [143][147], introducing a thick buffer layer [77] and stacking multiple layers of QDs [76]. However, the latter approaches may also reduce the effect of site control. The growth conditions, particularly deposition amount, GR, and growth temperature, which govern the adatom migration and desorption, have shown a strong impact on the realisation of highly ordered and uniform QDs. In addition, the dimension, shape, and period of the etched holes or pits can affect the structural and optical characteristics of SCQDs [141][148].

A considerable improvement in the optical quality of SCQDs obtained by *ex situ* lithographic approaches has been reported in recent years. Some representative techniques should be highlighted. Soft UV-NIL is an emerging micro/nanopatterning technique that uses a flexible mould (stamp) to directly define the mechanical deformation of a resist layer and then transfers the pattern onto the substrate by etching or lift-off [149]. It is capable of producing nanostructures with high throughput, high resolution and low cost over a large area. Over the past years, it has shown potential to fabricate pre-patterned substrate templates for the site-controlled growth of III-V semiconductor QDs by MBE [115][116][121][123]. Tommila *et al*. illustrated the production of single InAs SCQDs in UV-NIP pre-patterned pits and showed a narrow PL emission linewidth of 41 μeV from an individual dot. The AFM micrographs of the fabricated InAs SCQDs are displayed in Figure 2.12. It appears that the height of QDs increases as the pit depth and diameter increase and that the single QD occupancy is also associated with the pit size.
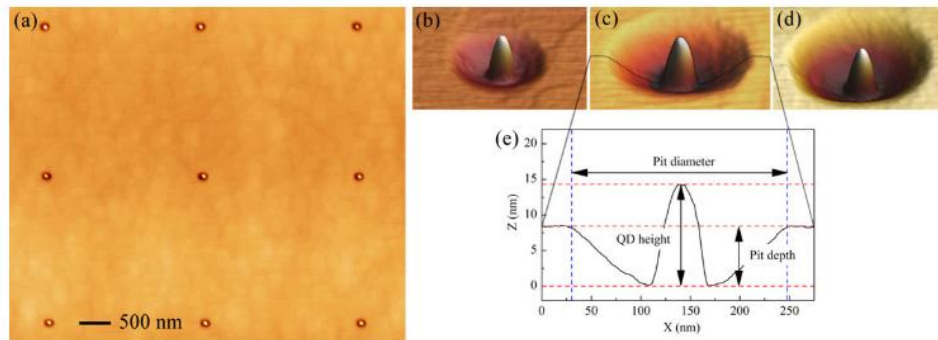
Figure 2.12 AFM micrographs of InAs SCQDs grown in pits fabricated by UV-NIL. (a-d) The pit diameter is 100 nm, 165 nm, 220 nm and 250 nm accordingly. The QD height in (b-d) increases from 13.2 nm, 14.4 nm to 15.8 nm. (e) The cross-sectional file of the QD shown is in (c) [141].

AFM-assisted LON has been widely employed to pattern metallic and semiconductor surfaces [151][152][153], which applies a voltage to an AFM tip to induce a local oxidation reaction on the sample surface in a controlled humidity atmosphere and does not require the use of resist layer and complex cleaning process. In recent years, this technique has been developed to fabricate III-V SCQDs, and high optical quality single SCQDs were demonstrated [143][153][155][156]. It starts with the creation of oxide dots on the surface, which can then be removed through wet chemical etching and/or *in situ* atomic hydrogen treatment, and hence nanoholes can be obtained on the surface. By regrowing QDs on the nanohole-templated surface, ordered arrays of SCQDs can be formed. Herranz *et al.* revealed the influences of growth parameters (growth temperature and As$_4$ overpressure) upon the fabrication of single InAs/GaAs SCQDs by AFM-assisted LON [156]. Figure 2.13 shows the fabrication procedures by LON. Initially, a square array of oxide dots was created on the GaAs surface, and then *ex situ* HF wet etching was performed to selectively remove the oxides and nanoholes were subsequently produced. Afterwards, the sample was loaded into the MBE chamber and the surface was exposed to *in situ* atomic hydrogen flux for further oxide removal. Finally, InAs was supplied onto this hole-patterned surface and nucleation occurs within those nanoholes. By optimising the substrate temperature and arsenic flux, single InAs SCQD arrays were fabricated. By means of stacking two QD layers that are spaced by a GaAs layer with 15 nm thickness, one can improve the structural and optical qualities of these SCQDs. The results presented an 89% single dot occupancy and a narrow single dot linewidth of 64 μeV (a median of 146 μeV) [155].
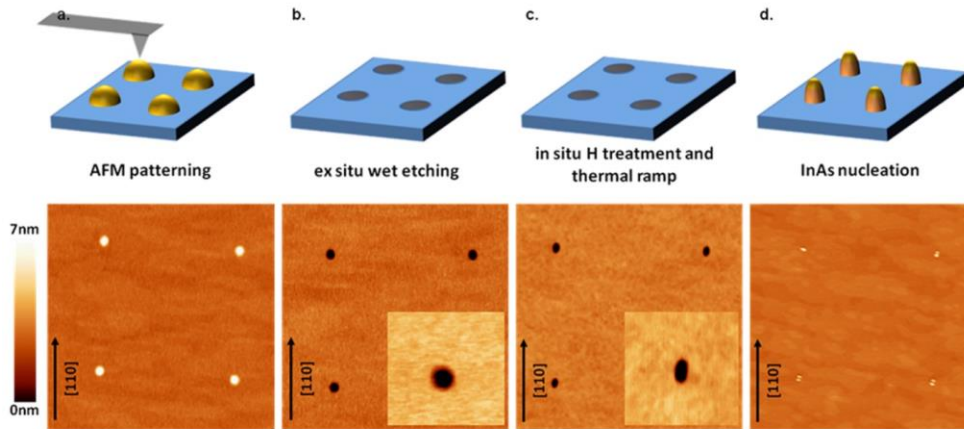
Figure 2.13 Schematic illustrations and AFM images of the procedures of SCQD growth by AFM-assisted LON. (a) Oxidation of GaAs substrate, (b) formation of nanoholes after HF wet etching, (c) surface after atomic hydrogen treatment, and (d) InAs regrowth in the holes [156].

EBL followed by the etching process has become an important technique to prepare nanohole-patterned substrates. The EBL process is capable of achieving a resolution down to a few nm and a well calibrated system can achieve excellent positional accuracy. Notable efforts have been made to grow III-V SCQDs with high quality using this approach [76][77][147]. Yakes *et al*. demonstrated the production of InAs SCQDs and QD chains on the hole and line-patterned substrates by EBL, in the absence of InAs seed QDs [77]. By virtue of growing a 90 nm thick GaAs buffer layer between the patterned substrate and the QDs, and crystal growth anisotropy, high uniformity SCQDs were obtained which show an extremely narrow optical linewidth of 6 μeV and a median of 19 μeV. The fabrication of single InAs SCQDs on GaAs substrates with prominent optical properties was revealed by Jöns *et al*. [76]. Square arrays of small pits were produced by EBL and wet etching, and InAs was deposited on the pit-patterned surface after cleaning. Two stacked QD layers were grown, with the second layer being 22 nm away from the regrowth interface. Figure 2.14(a) depicts the AFM micrograph of seed QDs on a pit-patterned substrate and Figure 2.14(b) displays the dot occupancy statistics. The micro-PL map and histogram of linewidths from single InAs SCQDs are revealed in Figure 2.14(c) and (d). The positioning probability of high-quality dots from the second QD layer was ~40%. A remarkable narrow single dot emission linewidth as low as 7 μeV and a median linewidth of 13 μeV was achieved by vertical stacking to alleviate the influence of defects at the regrowth interface.
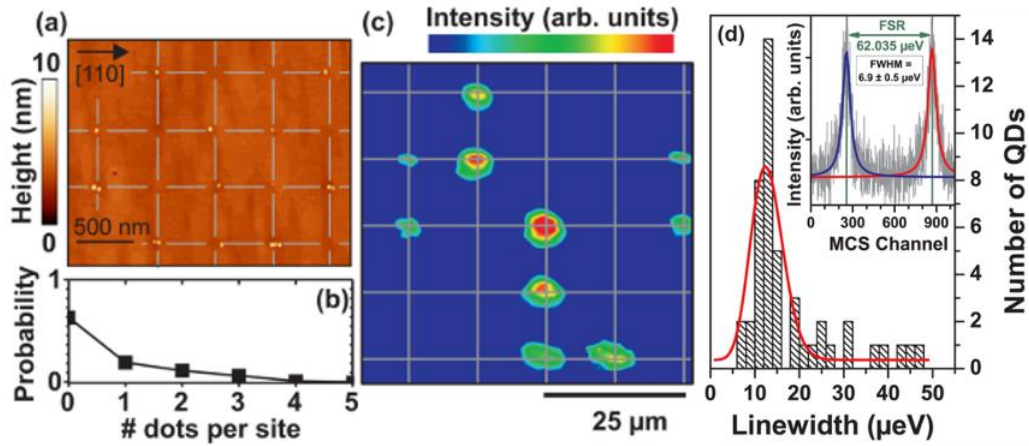
Figure 2.14 (a) AFM image of single InAs SCQDs with a period of 500 nm fabricated by EBL showing the QD occupancy. (b) Statistics of QD occupancy. (c) Micro-PL map emitted from the second layer of SCQDs. (d) Histogram of linewidths extracted from 40 SCQDs [76].

Despite the excellent achievements, these lithographic techniques such as LON and EBL are relatively low throughput, which does not lend themselves easily for mass production. Furthermore, the high yield production of ordered SCQD arrays with high structural and optical quality still remains challenging due to the potential for impurities and defects to be incorporated during the lithographic process and the possible influence of residual oxides during the re-growth step. Although the optical properties can be improved by growing a thick buffer layer or employing vertical stacking, the cost is often the loss of precise site control. Therefore, the development of defect-free nanopatterned templates for the lateral positioning of QDs is highly desirable.

CHAPTER *3*

EXPERIMENTAL METHODS AND CHARACTERISATION

In this chapter, the epitaxial growth technique as well as the characterisation routes employed to conduct the research in the dissertation will be demonstrated in detail. First of all, a general introduction to MBE will be given. And then, the structural characterisation methods including AFM, SEM and EDS will be described. Finally, optical characterisation by PL measurements will be demonstrated.

3.1 MOLECULAR BEAM EPITAXY

Based upon the reaction between atomic or molecular beam fluxes with the surface of a heated wafer within an ultra-high vacuum (UHV) environment (10^{-8}–10^{-12} mbar), MBE is a versatile epitaxy technique to grow thin films of metals, insulators and semiconductors [157][158]. In comparison to other deposition methods, MBE allows more accurate control of the beam flux and growth conditions, and an attainable low deposition rate, typically 1 ML s^{-1}, which contributes to the ability to grow accurate thicknesses and to achieve high purity and low defect films. Figure 3.1 depicts a graphic diagram of a standard solid-source MBE growth chamber. The effusion cells are utilised to generate atomic or molecular beam fluxes that are targeted to the sample surface below the substrate manipulator, where they may interact with each other. For III-V growth, Ga, In, Al, P, As and Sb, etc. elemental sources are used. In order to manipulate the reaction between atoms and the substrate, e.g., adsorption, desorption, hopping and bonding, it is necessary to control the substrate temperature. For III-V compound crystals, the adsorption coefficient of group III atoms at lower temperatures usually approaches unity. Therefore, accompanying group V atoms may incorporate into the crystal lattice on the premise that there are sufficient group III atoms available [159]. In practice, a significant excess of the group V is a requirement for high quality epitaxial growth, with typical beam equivalent V/III ratios of 15-25 in

use for GaAs-based materials. The group III atoms, such as In, Ga and Al are observed to exhibit desorption at substrate temperatures above around 500, 620, and 1000 °C respectively. Moreover, the substrate temperature will influence the migration length of surface atoms, subsequently controlling the surface morphology and the optical quality of nanostructures. Aside from substrate temperature, other MBE growth conditions such as the deposition rate, may easily bring in changes in the surface morphology [160]. Monitoring of the evolution of MBE growth can be realised through *in situ* reflection high energy electron diffraction (RHEED). Figure 3.1 denotes that high energy electrons emitted from a RHEED gun are diffracted at a superficial angle of 1-2° from atoms from the surface, and a phosphor coated screen can detect the diffracted electrons. The RHEED pattern is an indication of the real-time surface morphology, roughness, surface reconstruction state, and the GR through measuring intensity oscillations.
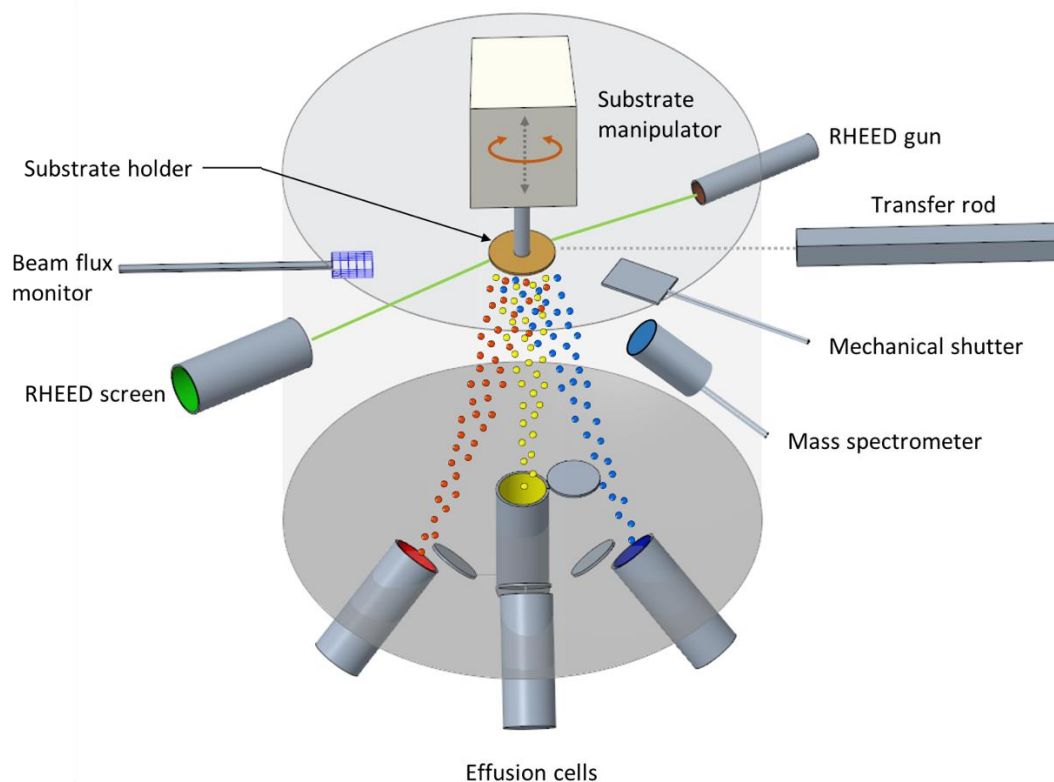
Figure 3.1 Graphic description of a typical solid-source MBE growth chamber.

As displayed in Figure 3.2, a modified solid-source MBE system (Dr. Eberl MBE-Komponenten GmbH, Germany) was employed to grow III-V materials in this dissertation. It contains three main chambers, which are the growth chamber (main chamber), the buffer chamber and the load lock chamber. Gate valves are used to

separate all these chambers. In, Al and Ga effusion cells from Group III, n:Si and p:Be dopant cells, and As and Sb valved-cracker cells from group V are fitted in the growth chamber. The system is pumped to base pressures $\ll 10^{-10}$ mbar by a cryopump and a Ti sublimation pump. Cell shutters are installed in front of each cell to interrupt the beam fluxes under automated computer control. Thermocouples in contact with the crucible provide a measurement of the temperature of the effusion cell. The beam equivalent pressure can be measured by the beam flux monitor which is an unshielded Bayard-Alpert style ionisation gauge that can be moved into position directly below the substrate. All the GaAs samples grown in this dissertation were prepared as follows. Epi-ready 2-inch wafers or quarter wafers were first loaded into the load lock chamber and pumped by a turbo pump until the pressure is ~1×10^8 mbar. Afterwards, the wafer was transferred into the buffer chamber with a transfer rod for degassing on a heater stage at 300 °C for at least half an hour. Subsequently, the wafer was transferred to the main chamber and the substrate temperature was raised to around 650 °C to remove the native oxide on GaAs. An arsenic flux was provided at temperatures above 400 °C to prevent dissociation of the substrate.
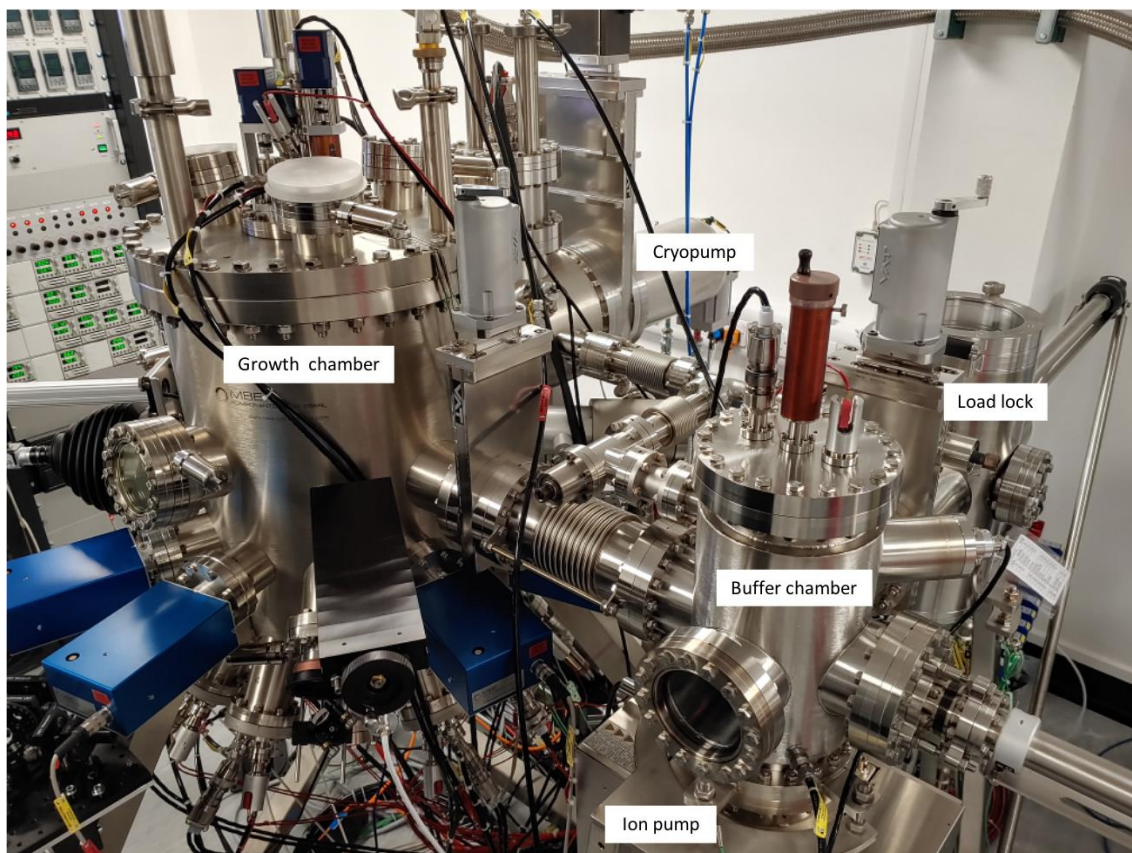
Figure 3.2 Photograph of the MBE system.

Growth then proceeds to establish a GaAs buffer layer whose purpose is to smooth the interface and bury any interfacial contamination. The growth quality can be confirmed by the observation of strong surface reconstructions in the RHEED pattern.

3.2 STRUCTURAL CHARACTERISATION METHODS

3.2.1 ATOMIC FORCE MICROSCOPY

As a surface analytical technique, AFM is capable of imaging the 3-D surface topography and the physical properties of solid materials including ceramics, polymers and semiconductors with nm resolution. It measures the surface morphology by detecting the extremely weak atomic force interaction between its tiny mechanical probe and the sample surface. An AFM consists of a sharp tip, typically <10 nm in diameter, which is attached to a microcantilever. The horizontal resolution is determined by the tip radius of curvature which ranges from 5-7 nm in our case. The cantilever is deflected as a result of the fluctuation in the surface morphology according to Hooke's law. A focused laser light reaches the back of the cantilever, and afterwards the reflected beam shifts with the deflection of the cantilever. Thus, by detecting the alterations in the light spot position through a position-sensitive photodetector, information on the surface topography can be obtained. Three basic operation modes of AFM scanning are non-contact mode, tapping mode and contact mode. The cantilever oscillates 5-10 nm in proximity to the sample surface with regard to non-contact mode. Van der Waals force governs the interaction between the surface and the tip. The advantage of this method is that it will not damage the surface and the tip. However, this mode is more suitable for use in UHV conditions, since an absorbed water layer will inevitably accumulate on the sample surface in ambient conditions to affect the measurement. On the contrary, the tip and the sample surface stay in contact in terms of contact mode, leading to a repulsive force. The imposed force on the tip by the cantilever may deface the sample surface morphology during scanning, thus, if the sample cannot bear such a force, it is not appropriate to use this mode. The most commonly used mode employed in the AFM imaging of semiconductors is the tapping mode, which is in many ways an intermediate approach. In this case, the cantilever oscillates at a pre-determined resonant frequency above the surface of the sample and the surface is detected through a small shift in the relative phase of the oscillation. With respect to the tapping mode, the tip only

periodically and gently taps the sample surface. Thus, it is suitable for measuring soft samples and, as it seems to cope better with the absorbed water layer, seems more effective in ambient conditions.

AFM is especially ideal for the surface structural characterisation of semiconductor nanostructures, particularly QDs. It is capable of gaining information including the diameter, height, shape, density and surface roughness. In this work, a tapping mode AFM (FSM NanoView-1000) in air which is shown in Figure 3.3 is used for the structural characterisation of the fabricated samples. Silicon AFM probes (NANOSENSORS) with tip radius <10 nm, a length of 100 um, and a resonance frequency of ~300 kHz were used for scanning. All the analysis was performed using Gwydion and WSxM software [161].
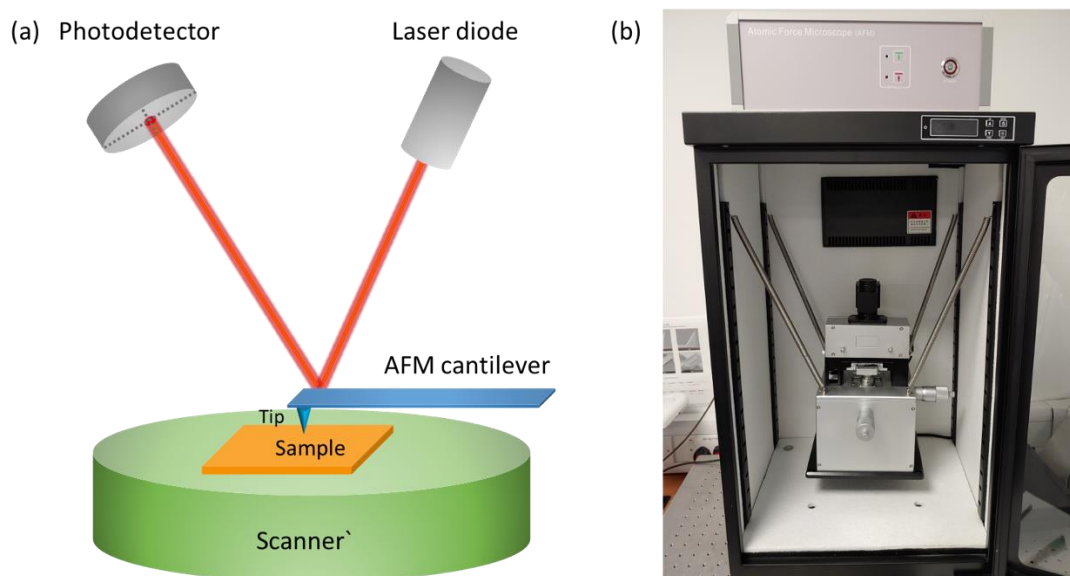
Figure 3.3 (a) Diagrammatic illustration of the principle of AFM. (b) Photograph of an AFM instrument.

3.2.2 SCANNING ELECTRON MICROSCOPY

As one of the electron microscopy techniques, SEM is utilised for morphology characterisation and is able to acquire high-resolution micrographs of the sample surface. A focused narrow high-energy electron beam is employed for scanning the surface in a raster pattern and is able to image the surface morphology and topography through secondary electrons or backscattered electrons etc. generated by the interaction between the atoms in the sample and the electrons. With additional

analytical equipment, it can also provide information such as crystal structure, orientation and the chemical composition of samples. The resolution of SEM is generally 1-20 nm and the magnification can go to 300,000 times and above and be continuously adjustable. SEM images show a large field of view and a high depth of field producing a quasi-3-D view of the sample surface owing to the narrow electron beam.

A typical SEM is composed of an electron gun, electromagnetic lenses, electron detectors and a vacuum system. The electron gun ejects electrons that are subsequently accelerated under a high voltage, and these high-energy primary electrons are focused by electromagnetic lenses towards the sample. By scanning across the sample surface, a variety of electronic signals can be excited e.g., backscattered electrons, secondary electrons, cathodoluminescence and characteristic X-rays, and then collected by specific detectors which convert them into electronic signals. Backscattered electrons and secondary electrons are mostly employed to image surface topography and morphology, and the characteristic X-rays can be used for elemental analysis. According to the type of electron sources, it can be divided into field emission electron gun (FEG), thermionic electron gun (normally a tungsten filament) and lanthanum hexaboride cathode. FEGSEM that utilises a strong electric field to emit high energy electrons shows great advantages over conventional thermionic sources due to its long service life of at least 1000 hours, small spot size, better brightness and high resolution even at low accelerating voltages, but it requires high vacuum environment which is more costly. SEM is often equipped with EDS to both image the sample surface and attain the elemental information of the sample. By detecting the characteristic X-rays stimulated from the electron beam bombardment, one can identify the local elemental composition of the sample, since different elements exhibit distinguishing emission spectra as a result of different atomic structures. In this way, EDS provides spectra that show the peaks regarding the composition of the atoms, and therefore the spatial distribution of elements present in the sample can be mapped.

In this research work, a FEGSEM operating at 10 kV accelerating voltage was employed to depict the surface morphologies of the patterned samples. Additional state-of-the-art SEM-EDS elemental analysis of the samples was accomplished at Top Analytica, Finland in cooperation with Tampere University as part of the NanoStencil project.

3.3 OPTICAL CHARACTERISATION METHODS

The optical properties of fabricated semiconductor nanostructures were characterised by photoluminescence (PL) spectroscopy, which is a contactless, non-invasive route to identify the optical quality. By analysing the PL spectra, general information on the material such as the band structures, composition, emission energy, and linewidth can be obtained. The principles of PL and the experimental setup for PL spectroscopy are included in this section.

3.3.1 PHOTOLUMINESCENCE

PL is an optical process that occurs when a material generates photon emissions by absorbing incident light, normally the photon energy exceeds the band gap of the material. Figure 3.4 displays the diagrammatic representation of the PL process within a direct band gap material. Electrons in the valence band (VB) are excited into the conduction band (CB), thereby producing free electron-hole pairs. Very rapidly, these carriers then relax to the lowest energy states and subsequently either recombine radiatively, emitting a photon, or non-radiatively by transferring the energy to impurities or defects in the crystal. The PL efficiency is subject to the competition between the non-radiative and radiative recombination. Generally, low-temperature PL is performed with the intention of suppressing the thermal non-radiative recombination and reducing peak broadening due to phonons.
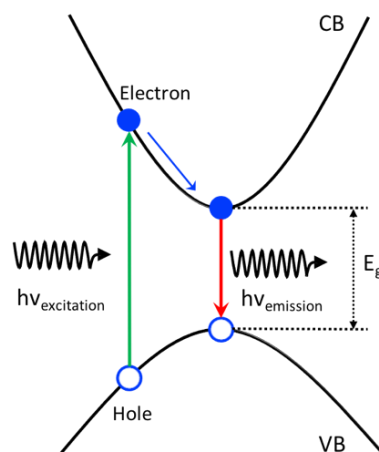
Figure 3.4 Diagrammatic representation of PL process.

Figure 3.5 depicts the schematic of a confocal PL setup utilised in this work. This includes an excitation light source, a cryostat, a monochromator and a detector. A

continuous liquid nitrogen flow cryostat and a closed cycle cryostat were employed to measure low-temperature PL. Both have high precision XYZ translation stages that either move the sample (with regard to the flow cryostat) or move the optics (with respect to the continuous flow cryostat). In terms of the excitation source, a 659 nm continuous wave (CW) pumped diode laser, or a 594 nm optically pumped semiconductor laser (OPSL) was used. As well as laser emission intensity control, neutral density (ND) filters were fixed anterior to the laser to reduce the excitation laser power to the required level. A 20× or 100× objective lens was utilised for the beam focusing on the sample surface, to obtain a spot diameter of ~12 μm or ~2 μm respectively. The same objective lens then collected the PL signal emitted from the sample and the path was then split by means of a dichroic mirror. The light is then collected by fibre and passed towards the entrance slit of a grating monochromator (Horiba FHR 1000 spectrometer) with a 1 m focal length, which offers a spectral resolution of 0.01 nm for 10 μm slits, and finally detected by a cooled InGaAs or Si detector or later in the project by InGaAs or Si detector arrays (Andor iDus).
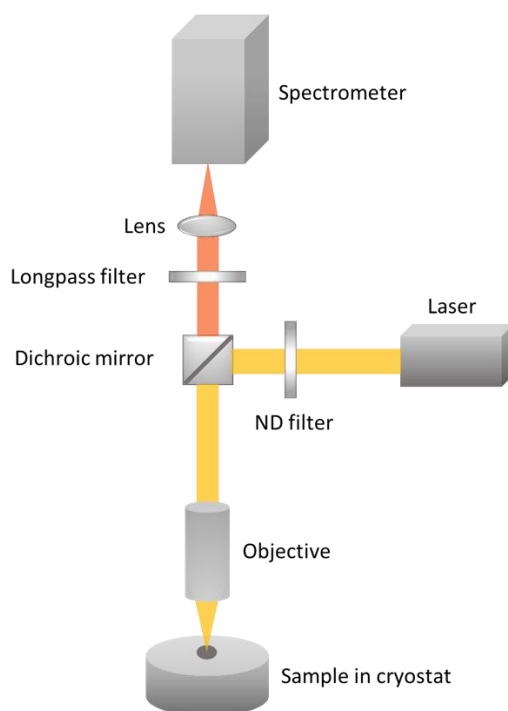
Figure 3.5 Diagrammatic depiction of the PL setup employed in this dissertation.

CHAPTER *4*

MULTIPLE BEAM LASER
INTERFERENCE PATTERNING

Nanopatterning technologies based on laser interference have emerged as promising approaches to fabricate periodic or quasi-periodic structures which can be widely employed in applications, such as nanophotonics [162], plasmonics [163], bioengineering [164], magnetic storage [165], and nanofluidics [166]. Laser interference lithography (LIL) [167][168], also referred to as holographic lithography, is a relatively facile, rapid, cost-effective and mask-less technique to fabricate one-, two-, or even three-dimensional periodic structures with a minimum resolution down to half the laser wavelength. Depending on the diameter of the laser beam and the beam energy, it can in principle pattern large areas (~cm²). The approach relies on the two or more coherent light wave interferences that can be recorded, for example on a photoresist layer. After development and pattern transfer such as etching, nanostructures on the target material can be fabricated. Figure 4.1 shows an example of fabricated Si structures by LIL followed by deep reactive ion etching [169]. This approach employed a simple Lloyd's mirror interferometer configuration to firstly produce line arrays (Figure 4.1(a)), and by rotating the substrate over 90° during the second exposure, 2-D structures such as holes and pillars as displayed in Figure 4.1(b) and (c) could be fabricated.
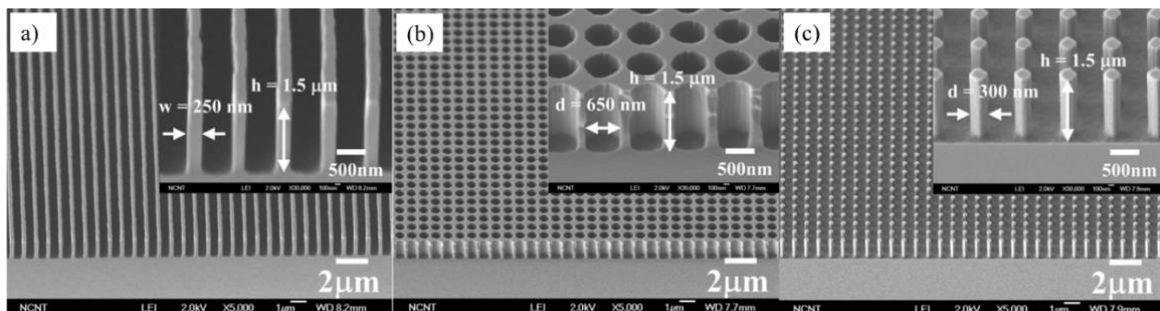
Figure 4.1 SEM micrographs of fabricated periodic silicon nanostructures of (a) lines, (b) holes and (c) pillars (λ = 405 nm, minimum exposure dose of 21.6 mJ) [169].

Lithography configurations such as diffractive optic elements (DOEs) [170][171][172], spatial light modulators (SLMs) [173][174] and the Lloyd's mirror interferometer [169][175] as depicted in Figure 4.2(a-c) have been widely employed for laser interference owing to their system compactness, simplicity and stability. However, these techniques have some limitations, for instance, the adjustment of incidence angle, polarisation dependence, the low thresholds for laser power and limited interference pattern resolution. As an alternative to these simple setups, configurations based on beam splitting and steering are more versatile for multi-beam interference lithography, particularly when different incidence angles and polarisations are required. They can also handle high-power laser intensities. Figure 4.2(d) exhibits a graphic diagram of a 3-beam LIL setup obtained by beam splitting [176].
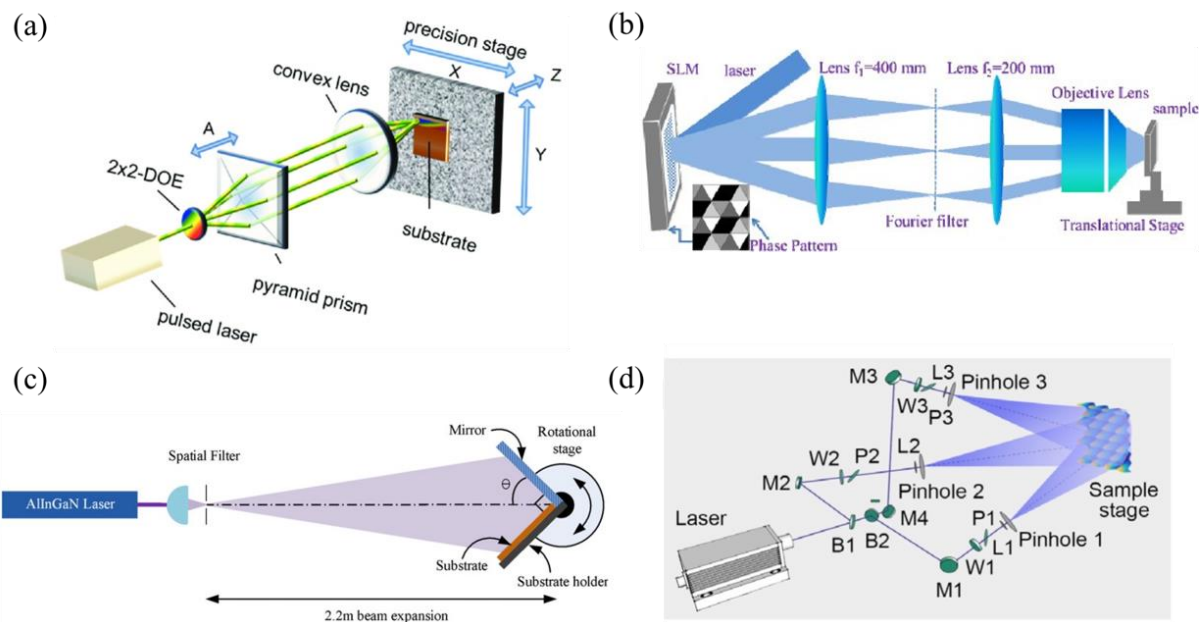
Figure 4.2 Graphic diagrams of (a) the DOE configuration, (b) SLM configuration, (c) Lloyd's mirror interferometer configuration, and (d) three-beam lithography configuration by beam splitting and beam steering [169][171][173][176].

CW lasers with timed exposures are normally used for LIL; however, in this case the interference may be disturbed by configuration vibration due to thermal instability or even airflows. Therefore, pulsed LIL is a potential alternative that can be immune from these effects as a result of a sufficiently short pulse duration. Nevertheless, there has been remarkably little work on photoresist exposure using pulsed laser interference

and no reports on 2-D periodic nanostructures with true-nm scale period by single pulse LIL [168][177].

With enough pulse energy, short-pulse lasers can enable the interference patterning of materials directly in a single step devoid of the utilisation of photoresists. In recent years, DLIP [178][179][180] has been demonstrated to be an attractive fabrication method that can structure materials directly to create periodic micro- and nano-scale surface features. Compared with the traditional LIL process, this technique can provide a high speed and high yield. The surface modification is mainly dependent on the local interaction between the laser and material, including photothermal, photochemical or photomechanical mechanisms [181][182]. Sub-micron and nanostructures such as ordered arrays of gratings, holes or pillars have been fabricated on a great variety of materials, such as polymers [178], metals [179] and ceramics [180]. Many of these structures are formed by laser ablation or deformation processes using relatively high-power single-pulse or multi-pulse nanosecond (ns), picosecond (ps) or femtosecond (fs) lasers. Figure 4.3(a-c) displays examples of patterned titanium microstructures by high power three-beam DLIP at a laser wavelength λ = 532 nm [183]. In terms of DLIP on semiconductor materials, it has also been reported that micro- and sub-micron structures can be produced on silicon surfaces using such an approach [172][184][185][186]. Figure 4.3(d) and (e) show fabricated silicon structures obtained by four-beam picosecond DLIP at a laser wavelength λ = 532 nm for the application of creating Mie-resonant metasurfaces [172]. In addition, previously published research has shown the ability to spatially arrange III-V semiconductor nanostructures using *in situ* DLIP within an MBE chamber, including the formation of InGaAs QD arrays by two-beam [187] and four-beam DLIP [188]. The significance of these works is that they show that near-surface absorption of nanosecond UV pulses of moderate laser energy (~50 mJ) is sufficient to induce surface nanostructuring during III-V epitaxy. However, the underlying mechanisms discussed in these works are somewhat unclear, with Clegg et al. [187] suggesting a surface diffusion process, while Zhang et al. [188] attributing their observations to the removal of the InGaAs WL. Most significantly, the presence of an intermediate surface structuring step before the nucleation of QDs has not been clearly demonstrated. Furthermore, precisely controlled single dot arrays were not achieved and associated optical properties have never been reported. There has been very little work on the realisation of large-area, defect-free and high-quality precisely ordered arrays of semiconductor

nanostructures by single-pulse DLIP and the investigation of the underlying structure formation mechanisms.
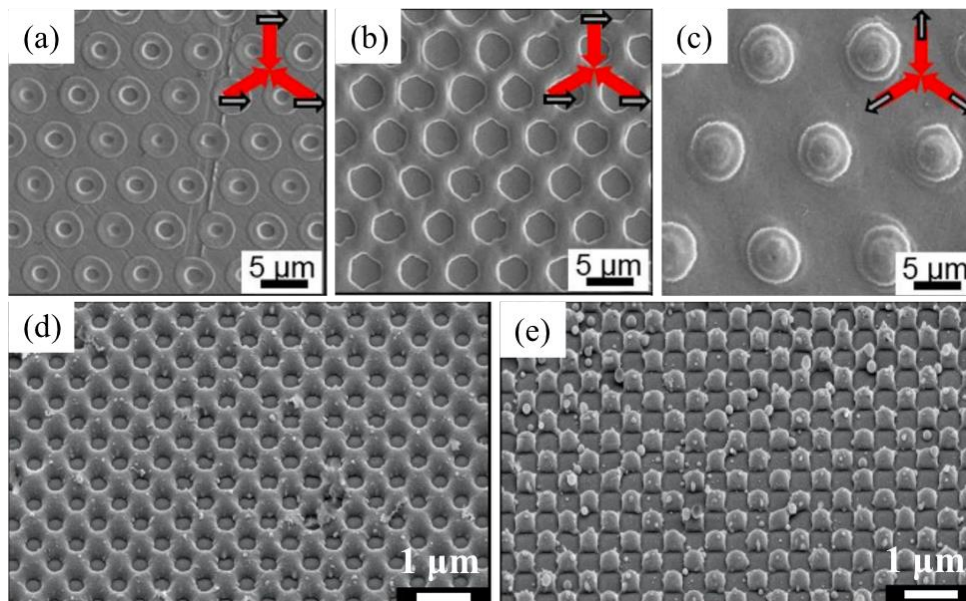
Figure 4.3 SEM micrographs of (a-c) three-beam DLIP on titanium surfaces with different laser fluences of (a) 0.6 J/cm² , (b) 1.1 J/cm² and (c) 4.0 J/cm². (d,e) Silicon nanostructures produced by four-beam DLIP with different laser fluences of around (d) 2.7 J/cm² and (e) 3.75 J/cm² [172][183].

In this chapter, the principle of multiple beam interference is demonstrated initially in Section 4.1. And then we discuss in Section 4.2 the simulation of multi-beam interference patterns with various beam parameters, for instance, the number of beams, angle of incidence, polarisation state and intensity ratio. In Section 4.3, we focus on the detailed experimental studies of *ex situ* single-pulse nanosecond four-beam LIL on photoresists, including a brief introduction of the ns-pulsed laser we used, the design of a beam-shaping LIL system, sample preparation and surface characterisation. We have achieved in this dissertation the production of large area periodic 2-D nanostructures (nanoholes and nanodots) with a period of 300 nm via a single exposure. In Section 4.4, the configuration and implementation of the integration of multi-beam DLIP with the MBE growth chamber are given. This special system is intended for the *in situ* epitaxial growth of semiconductor nanostructures by DLIP. Finally, Section 4.5 will show the simulation of DLIP-induced transient thermal effect on the GaAs surface, in which the surface temperature variations under different

parameters are discussed, and the *in situ* patterning results of periodic nanoisland and nanohole arrays on GaAs surfaces will be presented.

4.1 PRINCIPLE OF MULTIPLE BEAM INTERFERENCE

Multi-beam interference can be described as a linear superposition of multiple coherent electromagnetic waves. To simplify the theoretical analysis, the laser beam can be approximated as a uniform plane wave when both the divergence angle and interference area are small, as is usually the case with laser sources. The intensity distribution is stated as the superposition of the electric field vectors, and the electric field vector of the mth beam can be expressed as:

$$\vec{E}_m = A_m \vec{P}_m \exp\left[i(\vec{k}_m \cdot \vec{r} + \delta_m) \right] \tag{4-1}$$

where A_m is the amplitude, $\vec{P}_m$ is the unit polarisation vector, $\vec{k}_m$ is the wave vector pointing the propagation direction, $\vec{r}$ is the position vector, and δ_m is the initial phase. In Eq. (4-1) $\vec{P}_m$, $\vec{k}_m$ and $\vec{r}$ are functions of the spatial coordinate which can be respectively written as:

$$\begin{aligned}
\vec{P}_m =\ &-(\cos\theta_m \cos\varphi_m \cos\psi_m - \sin\varphi_m \sin\psi_m) \cdot \vec{i} \\
&-(\cos\theta_m \sin\varphi_m \cos\psi_m + \cos\varphi_m \sin\psi_m) \cdot \vec{j} \\
&-(\sin\theta_m \cos\psi_m) \cdot \vec{k}
\end{aligned} \tag{4-2}$$

$$\vec{k}_m = k(\sin\theta_m \cos\varphi_m \cdot \vec{i} + \sin\theta_m \sin\varphi_m \cdot \vec{j} - \cos\theta_m \cdot \vec{k}) \tag{4-3}$$

$$\vec{r} = x \cdot \vec{i} + y \cdot \vec{j} + z \cdot \vec{k} \tag{4-4}$$

where $k = 2\pi/\lambda$ denotes the wave number, λ is the laser wavelength, θ_m represents the angle of incidence, φ_m is the azimuthal angle, ψ_m is the polarisation angle. And the intensity distribution of N-beam interference intensity in the $z = 0$ plane is calculated by:

$$I = \sum_{n=1}^{N} \sum_{m=1}^{N} A_n A_m \vec{P}_n \vec{P}_m \exp\left\{ i\left[(\vec{k}_n - \vec{k}_m) \cdot \vec{r} + (\delta_n - \delta_m) \right] \right\} \tag{4-5}$$

For two-beam interference, a 1-D fringe pattern can be formed, and the schematic representation is depicted in Figure 4.4(a). The angle of incidence θ as well as the wavelength λ determine the fringe pitch P, which can be calculated by:

$$P = \frac{\lambda}{2\sin\theta} \qquad (4\text{-}6)$$

An example of a fringe pattern captured by a CMOS camera based on the well-known Mach-Zehnder interferometer setup utilising a CW laser source at λ = 532 nm is displayed in Figure 4.4(b).
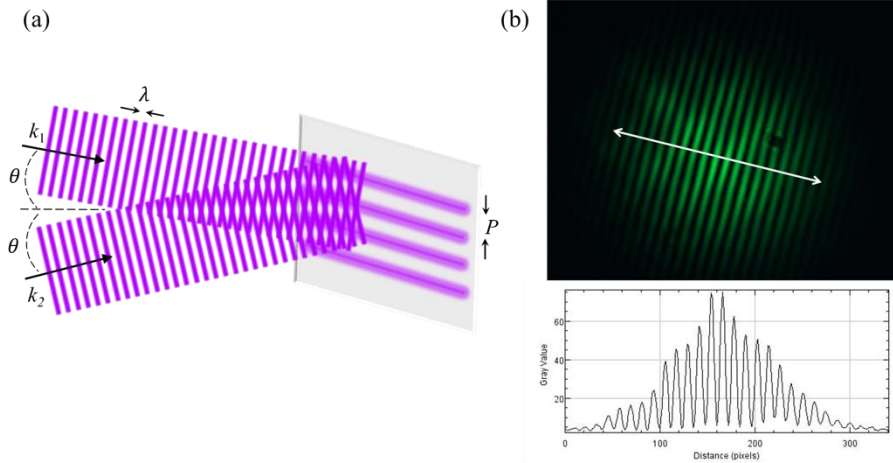
Figure 4.4 (a) Interference of two coherent plane waves incident at θ. (b) Camera image of two-beam interference pattern with its intensity profile.

In terms of interfering multiple beams, more complex periodic or quasi-periodic patterns can be generated. It can be deduced from the above equations that by adjusting the laser wavelength, incidence angle, azimuthal angle, polarisation angle, and phase difference etc., a variety of pattern periods, contrasts and shapes can be produced. For example, three- or four-beam interference forms 2-D ordered arrays of structures, and six-beam interference can create moth-eye-like structures [189]. Four-beam interference is commonly used to fabricate square arrays of structures, and a typical configuration is shown in Figure 4.5, where four symmetrically positioned beams incident on a surface at an identical incidence angle of θ.
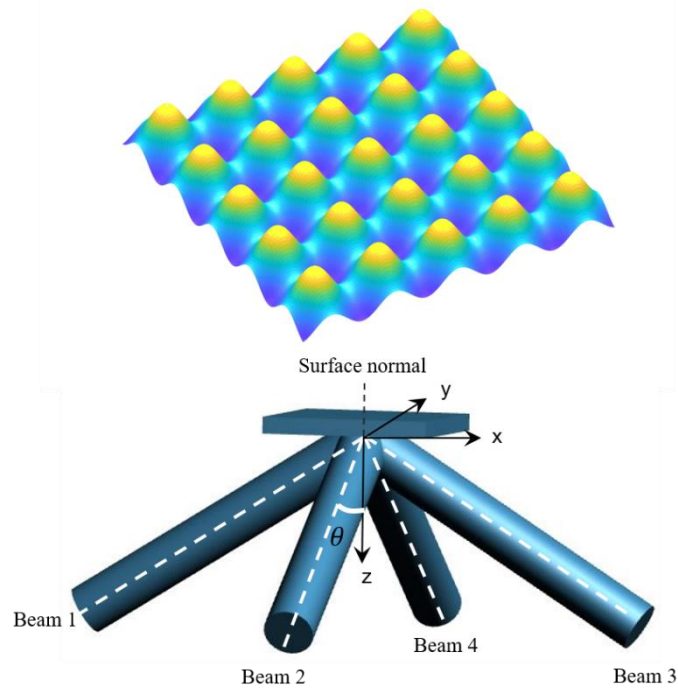
Figure 4.5 Configuration of 4-beam interference at an incidence angle of θ and equivalent azimuth angle. An example of simulated intensity distribution is shown at the top.

4.2 SIMULATION OF MULTI-BEAM LASER INTERFERENCE

To explore the influences of different beam parameters on the obtained interference patterns, theoretical simulations were performed using MATLAB. A laser wavelength of 355 nm was employed, all the amplitudes of incident beams were assumed to be the same and the initial phases were assumed to be zero.

Figure 4.6 reveals the simulated interference intensity distributions by manipulating the number of interfering beams. We assume that all interfering beams are placed symmetrically with the same incidence angles of 30° and polarisation states of transverse magnetic (TM) mode (polarisation angle of 0°). The 1-D periodic fringe-like shape can be produced by two-beam interference, 2-D arrays of circular-, square-, and hexagonal-shape patterns are created by three-, four- and six-beam interference, and more complex patterns can be formed by five-, seven- or more beams interference.
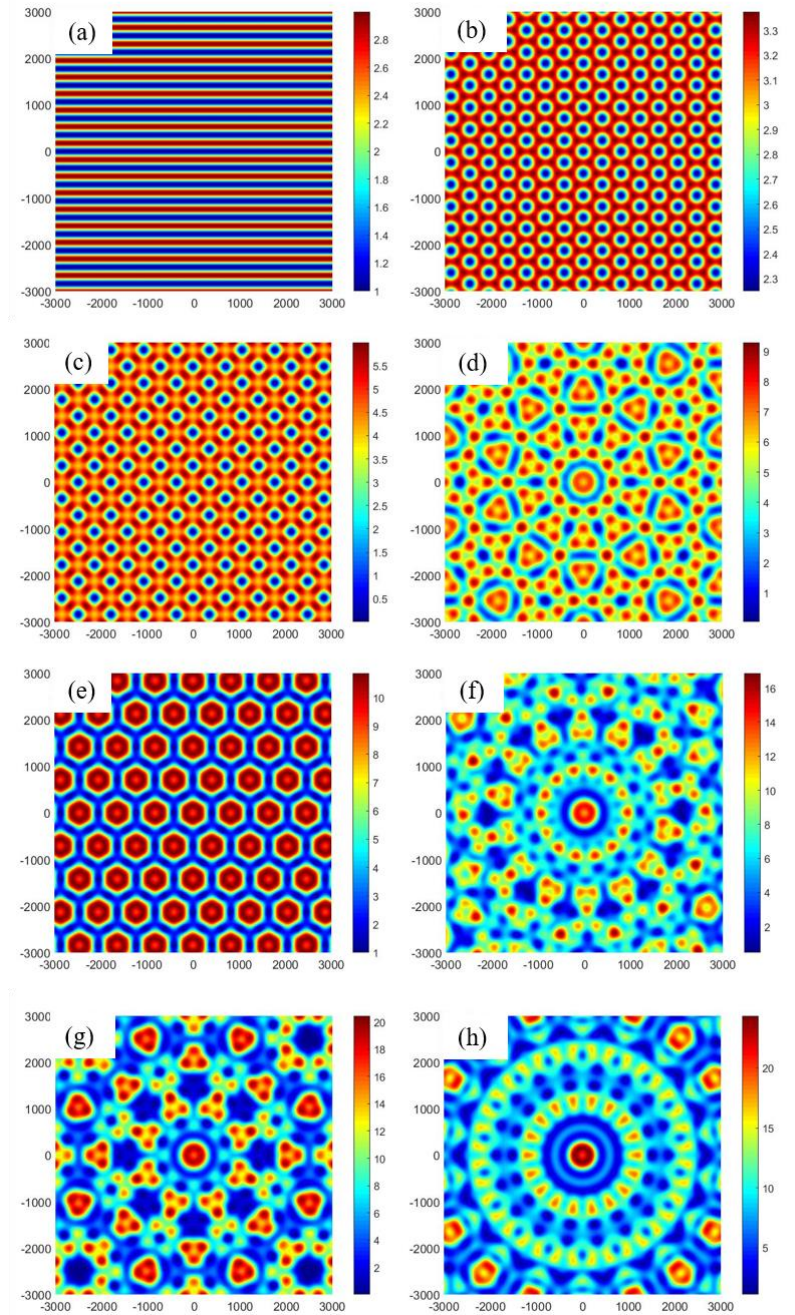
Figure 4.6 Simulation of interference patterns by (a-h) 2-, 3-, 4-, 5-, 6-, 7-, 8- and 9-beam interference, respectively. The unit of the x and y-axis is nm.

In this dissertation, 4-beam laser interference is mainly utilised to obtain square arrays of surface features with equivalent azimuthal angles of 0°, 90°, 180° and 270°. The effects of beam parameters on the resulting interference pattern including the angle of incidence and polarisation are discussed as follows. As revealed in Figure 4.7, the angle of incidence mainly determines the lattice pitch of the interference pattern, and the geometrical shape and the contrast of the pattern can be controlled by the

44

polarisation state of the interfering beams. At a laser wavelength of 355 nm, the lattice pitch is ~205 nm at an incidence angle of 60° and transverse electric (TE) polarisation (polarisation angle of 90°), while the pitch is ~290 nm at the same incidence angle but different polarisation state of TM mode. At an incidence angle of 60°, the pattern contrast in TM mode (polarisation angle of 0°, 0°, 0°, 0°) is better than that in other polarisation modes.
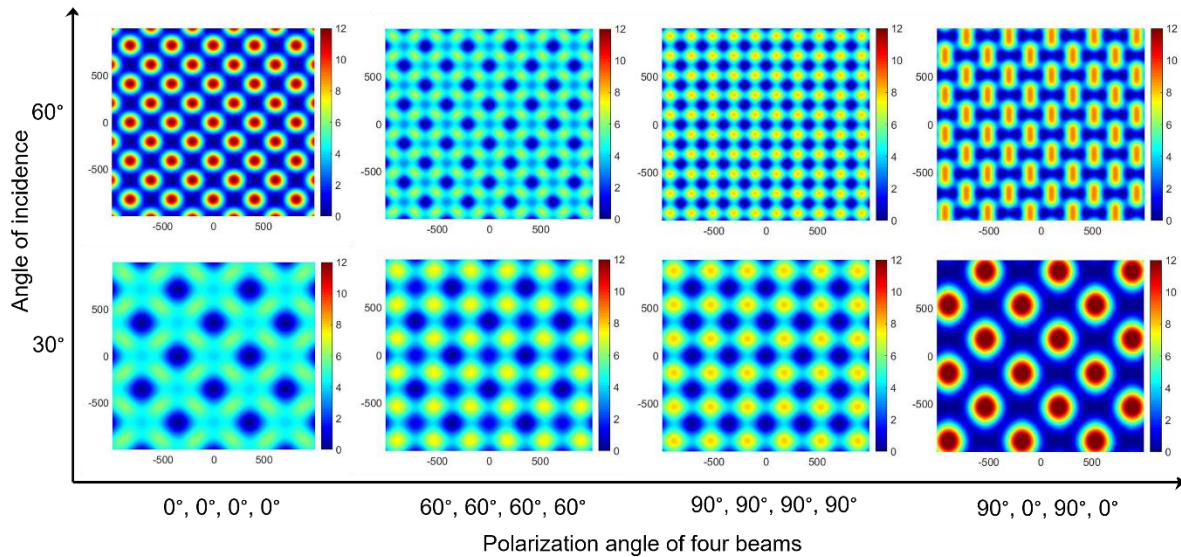
Figure 4.7 Simulation of four-beam interference intensity distributions with different combinations of incidence angle and polarisation angle. The unit of the x and y-axis is nm.

Other variations in beam parameters such as the phase and azimuthal angle also have similar effects on the interference pattern. In the case of interference experiments, another key factor that determines the shape of the pattern and the pattern homogeneity is the intensity ratio of all interfering beams. If the intensity of each beam is not identical, it leads to variations in the interference pattern, as depicted in Figure 4.8, where the angle of incidence is 60°. The interference patterns in Figure 4.8(a) and (b) show different intensity ratios of 0.3:1:0.3:1 and 1:0.1:0.1:1 with a polarisation angle of 0°, and in (c) and (d) with a polarisation angle of 60°, the intensity ratios are 0.5:1:0.5:1 and 1:0.1:0.1:1 respectively.
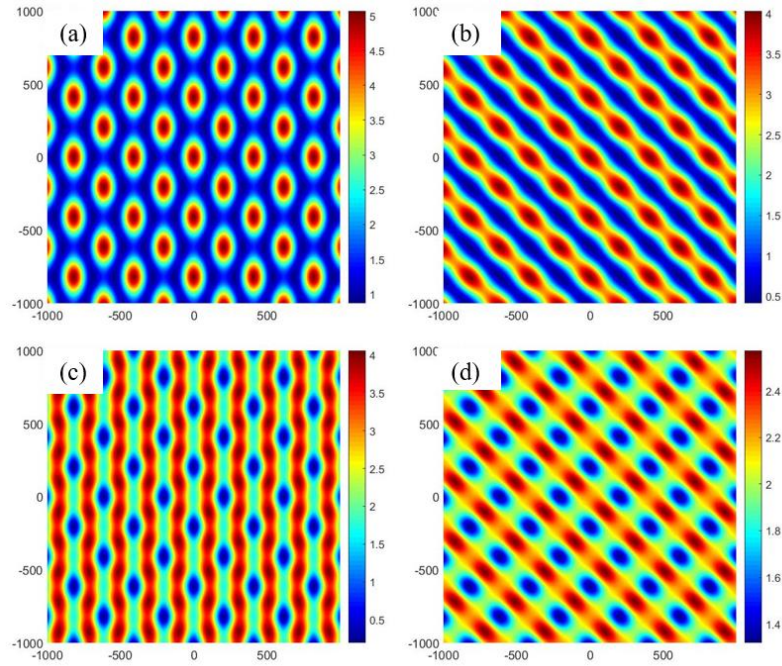
Figure 4.8 Simulation of four-beam interference intensity distributions with different combinations of beam intensity ratios and polarisations. The intensity ratio is (a) 0.3:1:0.3:1 and (b) 1:0.1:0.1:1 with a polarisation angle of 0°, (c) 0.5:1:0.5:1 and (d) 1:0.1:0.1:1 with a polarisation angle of 60°. The unit of the x and y-axis is nm.

The Moiré effect can be observed when the angles of incidence or the azimuthal angles are not identical [190][191]. Figure 4.9 reveals the simulated interference patterns with incidence angles of $\theta_1 = \theta_2 = \theta_3 = 60°$ and $\theta_4 = 55°$. The polarisation angle is 0° in Figure 4.9(a) and 60° in (b). The corresponding 3-D intensity distribution is shown in (c) and (d). Due to the problems of precisely aligning the beams, the Moiré fringe can often be seen in our experimental studies. This does not affect the local ordering of nanostructures but does introduce an undesirable long range structural variation.
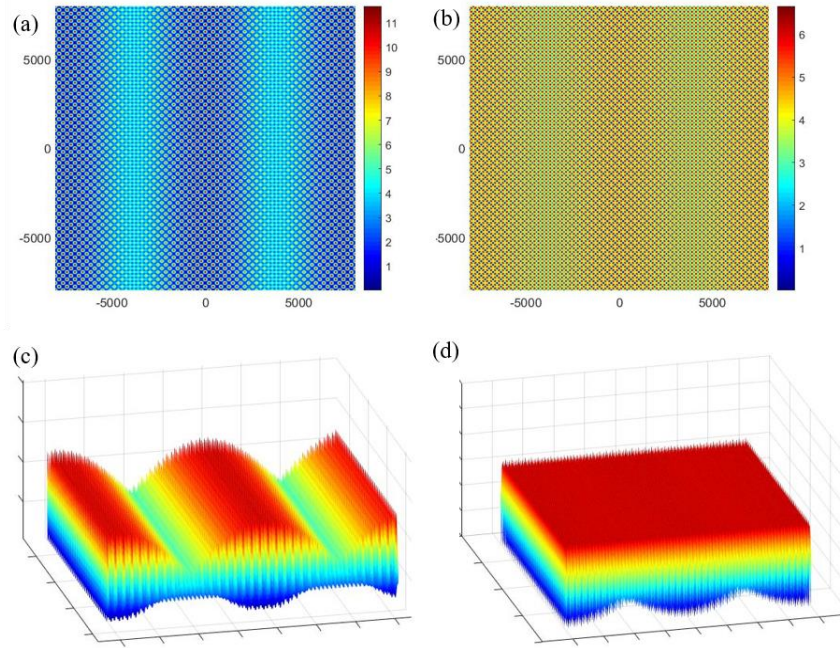
Figure 4.9 Moiré effect observed in four-beam interference with an incidence angle offset of 5°. The unit of the x and y-axis is nm.

4.3 EXPERIMENTAL STUDY OF *EX SITU* PULSED MULTI-BEAM LASER INTERFERENCE LITHOGRAPHY

4.3.1 FOUR-BEAM LIL SYSTEM

A flash-lamp pumped Neodymium-doped yttrium aluminium garnet (Nd:YAG) laser (InnoLas SpitLight 1000) which operates at λ = 355 nm was applied as the radiation source. A photograph of the laser is presented in Figure 4.10(a). A general description of the laser operation is as follows. It uses a flashlamp pumped Nd:YAG laser rod to produce a fundamental infrared laser source at 1064 nm, and using harmonic generation crystals, a second-harmonic output at 532 nm, a third-harmonic output at 355 nm and a fourth-harmonic output at 266 nm can be produced. An injection seeder in the form of a temperature stabilised single mode semiconductor fibre laser was employed to improve the output laser bandwidth and spatial profile. In order to attain high laser energy, the cavity is Q switched using an electro-optic device known as a Pockels cell. To obtain a single pulse exposure, an external shutter was used to pick a pulse from the 5 Hz laser repetition by a timed opening based on the laser Pockels cell trigger signal.
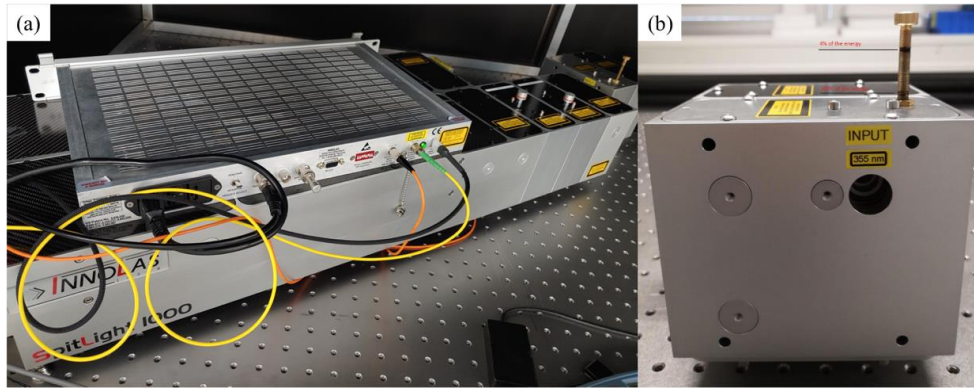
Figure 4.10 Photographs of (a) the pulsed laser with a seeder and (b) an attenuator.

The main specifications of the laser are demonstrated in Table 4.1. The laser output pulse energy reaches a maximum of ~250 mJ and thus an attenuator as shown in Figure 4.10(b) was developed and used to control the laser power, allowing a controllable low range of pulse energy down to a few mJ.

Table 4.1 Laser specifications

Wavelength (s)	Fundamental: 1064 nm, 2nd harmonic: 532 nm, 3rd harmonic: 355 nm, 4th harmonic: 266 nm
Pulse width @355 nm	7 ns
Repetition rate	5 Hz
Pulse energy @355 nm	<250 mJ
Spatial mode	TEM_{00}
Beam profile	Gaussian (far field)
Beam diameter	<5 mm
Beam divergence	<1.5 mrad

Figure 4.11 presents the four-beam LIL configuration that was utilised in the experiments. The height of the output laser beam is initially raised by the periscope assembly, and then the beam is split into four sub-laser beams with identical optical

paths by three 50:50 UV beam splitters (BS1-3). After that, these four sub-beams are reflected by four symmetrically placed UV mirrors with equivalent azimuthal angles of 0°, 90°, 180° and 270°, and then recombined on the centre of the 2-inch sample surface at an incidence angle of $\theta = 58°$. A half-wave plate and a Glan-laser polariser are applied in the path of each beam to control the pulse energy and polarisation states of the four beams. The target polarisation angle is determined by the direction of the polariser, and the half-wave plate placed before the polariser can be used to adjust the plane of linear polarisation to any arbitrary plane by rotating around its axis. In order to align these invisible UV beams at the centre of the sample, a facing down CMOS camera is used.
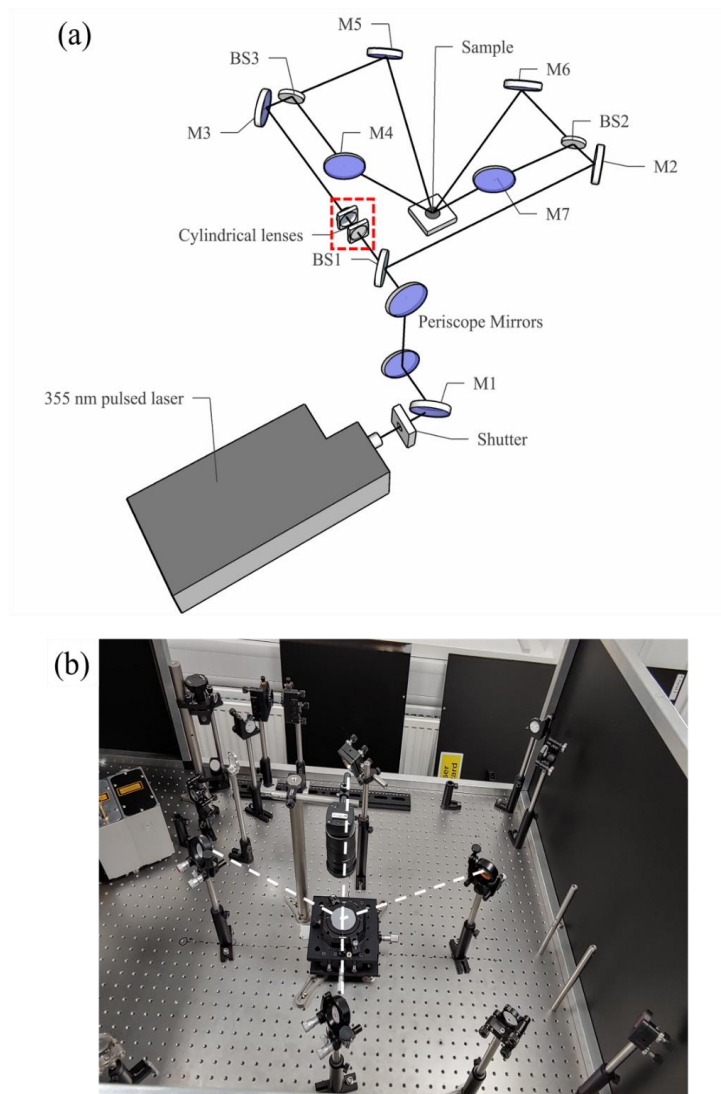
Figure 4.11 (a) Configuration of four-beam pulsed LIL at an incidence angle of 58°. BS1-BS3: 50:50 beam splitters, M1-M7: high reflective UV mirrors. (b) Photograph of the four-beam *ex situ* LIL optical setup.

A large incidence angle is generally needed to achieve a small interference period and as a result, the laser spot that is projected on the sample surface becomes an elliptical shape. This leads to more difficulties in the multi-beam alignment, and therefore results in a heterogeneous energy distribution over the interference pattern. Hence, it is of great significance to realise a large-area uniform interference pattern through optical design.

As displayed in Figure 4.12(a) in the optical path before BS1, a beam shaping system composed of two cylindrical lenses is utilised to precondition the laser beam shape. A plano-concave cylindrical lens of focal length $f = -100$ mm and a plano-convex cylindrical lens of focal length $f = 200$ mm are used to achieve a magnification of 2. This uniaxial magnification along the horizontal axis pre-compensates the spot distortion generated by the non-perpendicular incidence angle. The schematic diagram in Figure 4.12(b) illustrates the projection of the incident laser beam at an angle of 58° without the use of the beam-shaping system. The interference area of the four beams is strongly dependent on the alignment. However, four laser beams cannot completely overlap owing to their elliptical beam shape even if they are well-aligned, and there are large areas with non-desired two-beam interference. In contrast, after applying the beam shaping lenses as depicted in Figure 4.12(c), the laser beam can be initially converted into an elliptical shape at the input of the interference system, accordingly, the elliptical pre-condition offsets the ellipticity caused by the beam projection and produces a round beam shape. In this way, it enables a larger overlap area, thereby the realisation of a large area of multi-beam interference patterning.
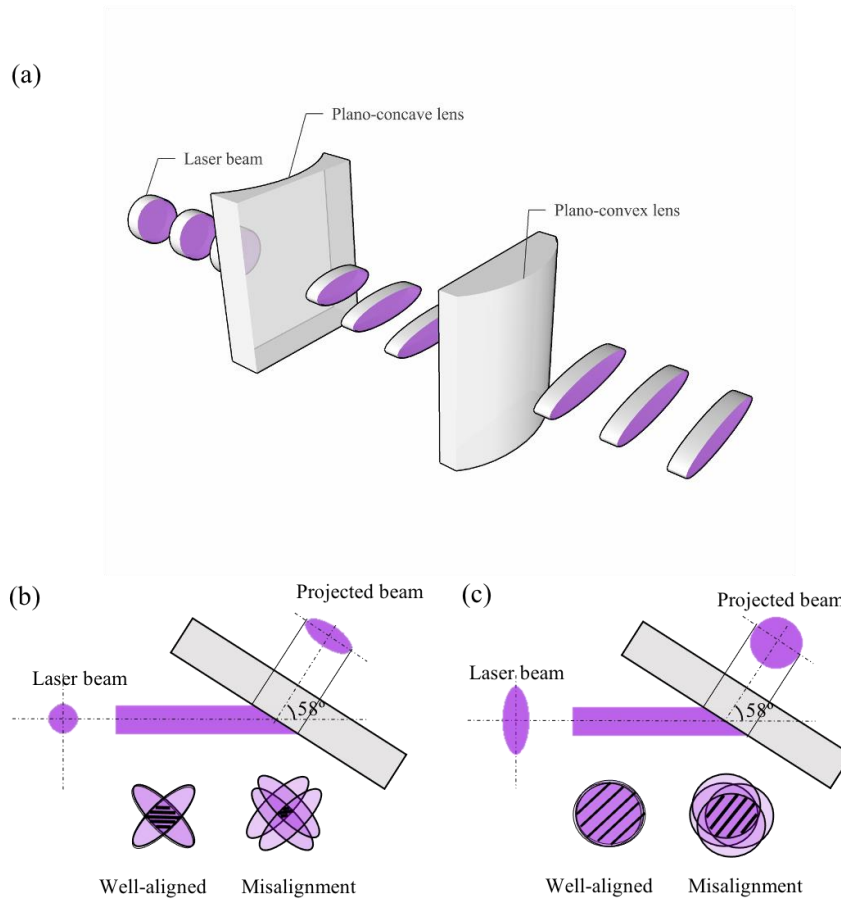
Figure 4.12 (a) Diagram of the beam-shaping system consisting of two cylindrical lenses. Schematics of the beam shape transformation due to the projection (b) without and (c) with the beam-shaping system.

4.3.2 EXPERIMENTAL DETAILS

The multi-beam LIL patterns were recorded by positive UV photoresists AZ 1514H (MicroChemicals) on 2-inch silicon wafers. The basic experimental procedure in this work can be described as follows: first, the photoresist solvent was deposited onto a clean silicon wafer by spin coating at a speed of 4000 rpm for 30 seconds which results in a resist film thickness of approximately 1.7 μm. Then this was followed by a soft bake on a hot plate for 1 min at 100 °C. After that, the photoresist layer was exposed to a single-pulse LIL in air. The optimum laser fluences were around 20-35 mJ/cm² for the exposures, and the polarisation state is TM mode. In the final step, the samples were developed using a standard AZ developer for 10-15 seconds and then rinsed with deionised water and dried with nitrogen. We have carried out the LIL experiments with and without the use of beam-shaping lenses for comparison.

4.3.3 RESULTS AND DISCUSSION

The surface morphologies of the *ex situ* LIL samples were characterised by FEGSEM and AFM. SEM micrographs of periodic line-like structures by two-beam interference and oval-shape structures by three-beam interference with the periodicity of 300 nm are shown in Figure 4.13(a, b), and (c, d) presents the corresponding simulated interference pattern. According to the simulation results, the pattern contrast of two-beam interference is poorer than that of three-beam interference. The laser fluence used for two-beam LIL was about 38 mJ/cm² and 25 mJ/cm² for three-beam LIL.
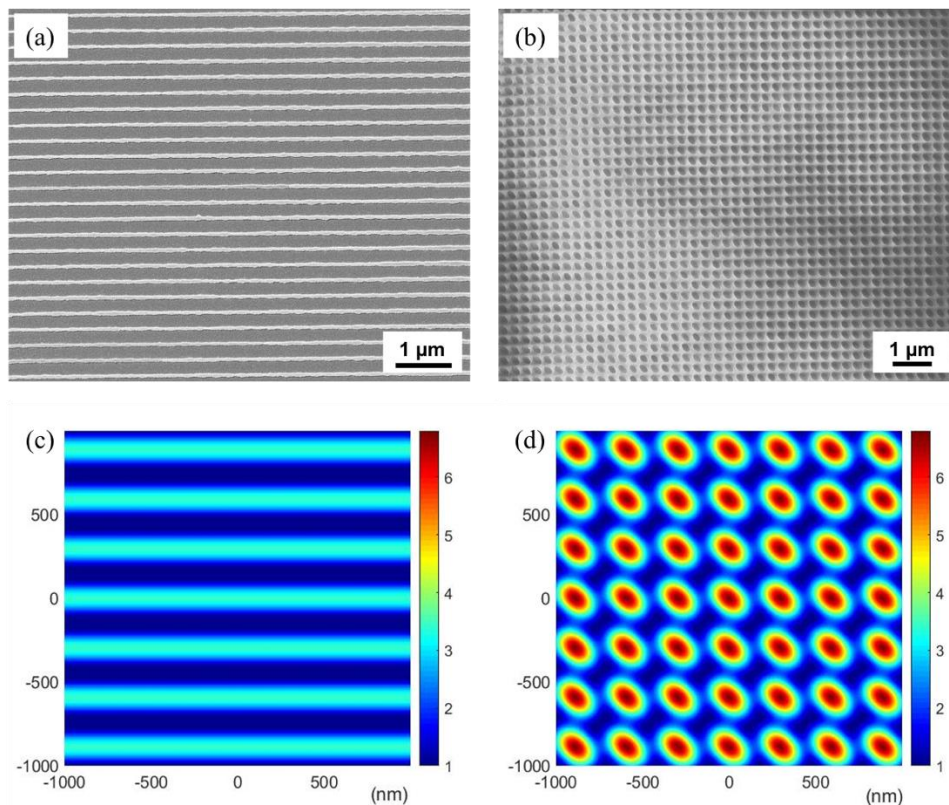
Figure 4.13 SEM micrographs of (a) 1-D arrays of gratings by two-beam interference and (b) 2-D arrays of oval-shape structures by three-beam interference. (c, d) Simulated interference patterns corresponding to (a) and (b) respectively.

As depicted in Figure 4.14(a) and (b), SEM micrographs of 2-D periodic surface features without the use of beam-shaping lenses are observed either as nanoholes or nanodots depending on the exposure and development conditions. At a laser fluence of 23 mJ/cm², the exposed regions at the interference maxima are dissolved into the developer, resulting in hole-like nanostructures on the surface (see Figure 4.14(a)). With a slightly higher laser fluence of 33 mJ/cm², as shown in Figure 4.14(b), dot-like

structures are observed since the exposed area becomes larger and connected to each other, thereby these dots are located in the interference minima regions. It is clear to see that the interference patterns displayed in Figure 4.14(a) and (b) exhibit some diversification in the shape and size of the structures over the imaging area. This might be attributed to the Gaussian beam distribution or the precise alignment issue of the four beams.
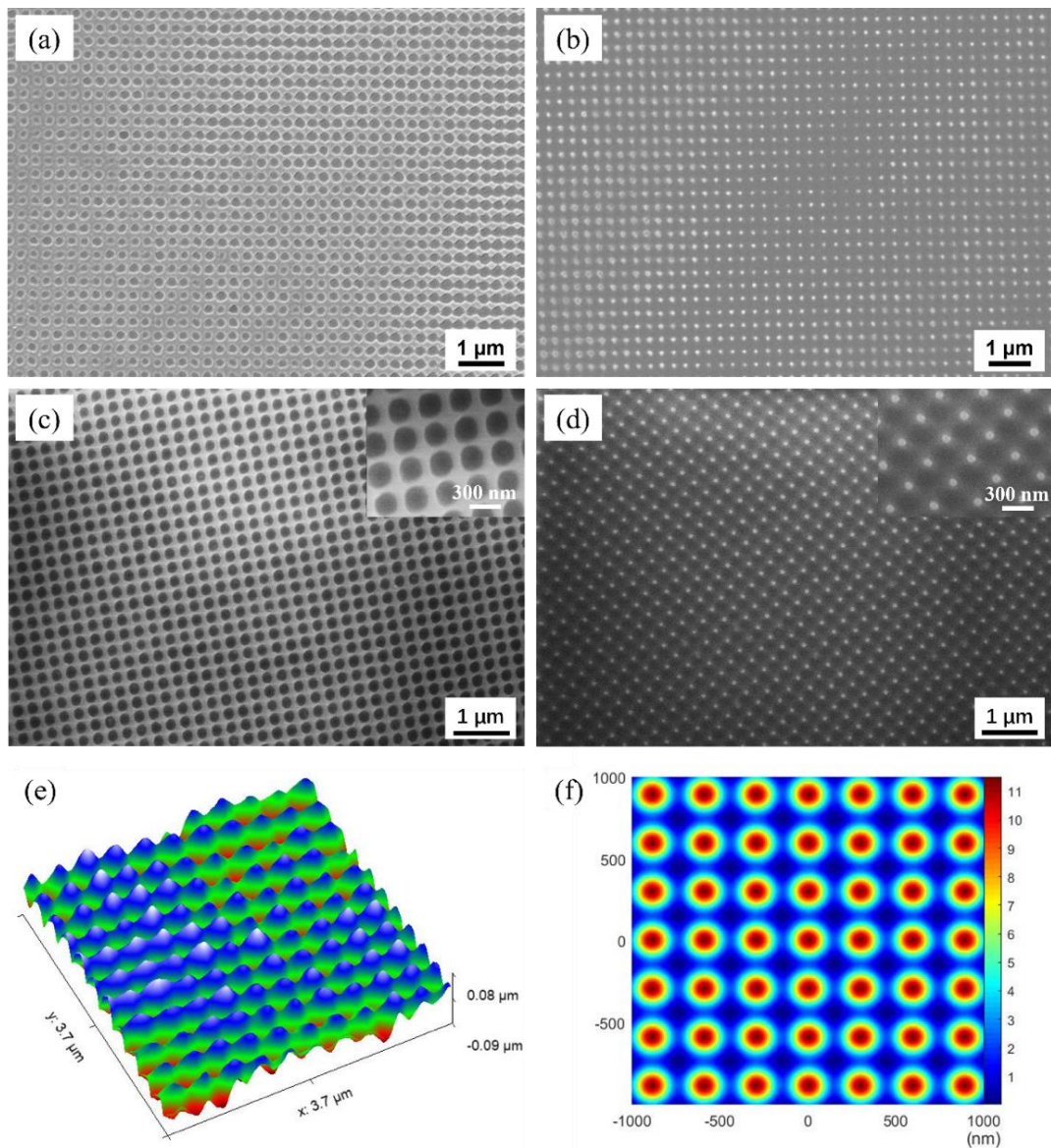
Figure 4.14 SEM micrographs of the produced 2-D nanostructures by single-pulse four-beam LIL without beam-shaping of (a) nanohole-like and (b) nanodot-like structures; with beam-shaping of (c) nanohole-like and (d) nanodot-like structures. The pattern period $\Lambda \approx 300$ nm. The insets show the corresponding magnified images. (e) 3-D AFM micrograph of the fabricated nanostructures shown in (b). (f) Simulated interference pattern.

In comparison, Figure 4.14(c) and (d) reveal SEM micrographs of produced ordered arrays of nanostructures by using beam-shaping optics with similar laser fluences of 20 mJ/cm^2 and 27 mJ/cm^2, respectively. These features are relatively homogeneous in shape and size, where the nanoholes in Figure 4.14(c) are approximately 200 nm wide and nanodots in Figure 4.14(d) are 50 nm in diameter. All the fabricated structures in the LIL experiments depict a lattice period of $\Lambda \approx 300$ nm owing to a large incidence angle of 58°, which is consistent with previous simulation results in Section 4.3. The uniform periodic nanostructures can be fabricated over the area from µm^2 to mm^2 using this approach. Figure 4.15(a) presents an SEM micrograph of the fabricated nanohole arrays over hundreds of µm^2. In terms of even larger areas, the pattern uniformity can be affected by the Moiré effect which originates from a slight misalignment of four beams such as a small offset of the incidence angles or the azimuthal angles, as illustrated in the previous simulations. An example of an SEM micrograph showing the Moiré fringe with a period of a few microns is displayed in Figure 4.15(b) which in this case is likely due to a few degrees of misalignment of the incidence angles.
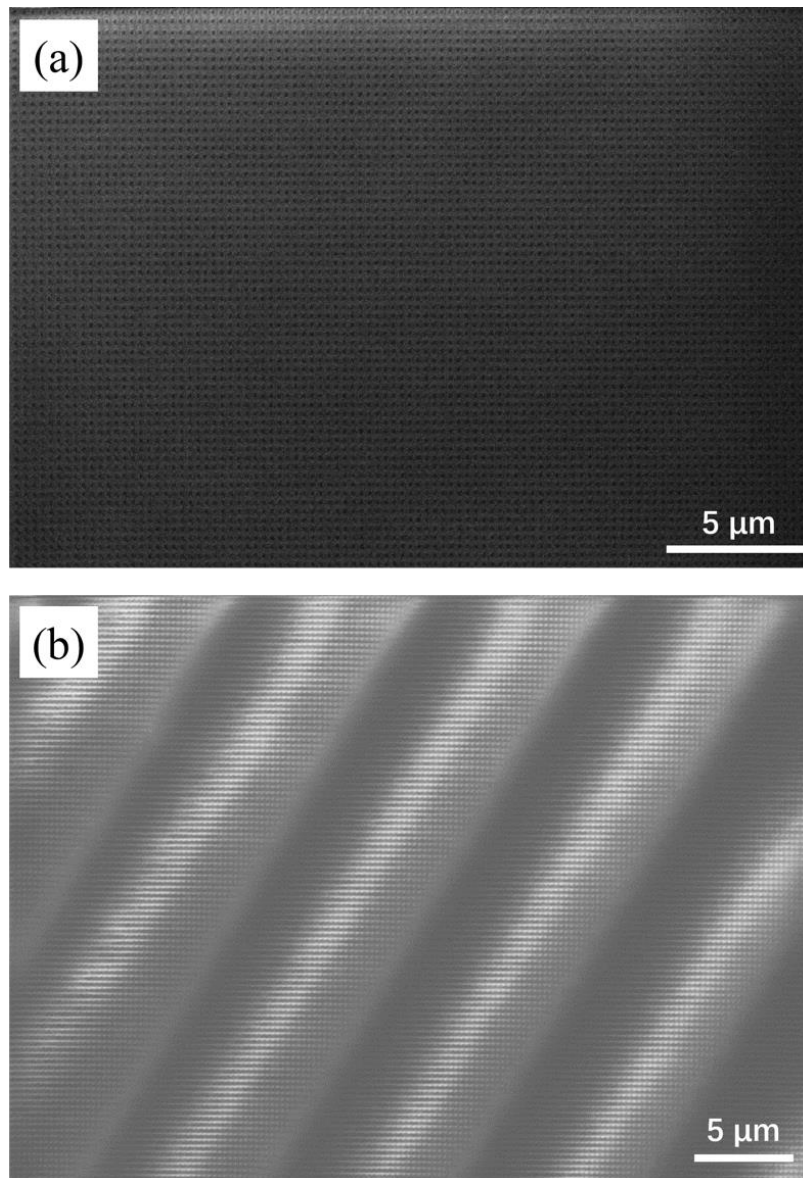
Figure 4.15 (a) SEM micrograph of fabricated homogeneous periodic nanohole structures over several hundred μm² by using the beam-shaping system. (b) SEM image of the Moiré effect due to an incidence angle offset.

The fabricated nanostructures presented in the work tend to be relatively shallow features owing to the thick photoresist (~1.7 μm). It is more desirable to have a thinner resist layer of several hundred nanometres if post pattern transfer processes such as etching are required. However, these *ex situ* four-beam LIL experiments provide important verification results of the ability to perform single shot pulsed laser exposure to generate large-area 2-D periodic nanostructures. We are not aware of any other techniques which are able to form uniform arrays of such features over hundreds of μm² with a single short (7 ns) exposure process. Larger areas of uniform

interference pattern could be realised by using additional beam expander optics, and a uniform laser beam profile, precise beam alignment and good control of the LIL parameters are also of great importance.

4.4 INTEGRATION OF DIRECT LASER INTERFERENCE PATTERNING WITH THE MOLECULAR BEAM EPITAXY SYSTEM

This section describes the laser interference setup implemented for the *in situ* growth of semiconductor nanostructures by MBE. A four-beam DLIP setup was constructed, which is very similar to our previous *ex situ* LIL setup, and the simplified configuration is shown in Figure 4.16. Since the MBE system is a large vacuum chamber in which optics cannot be placed, the laser interference setup needs to be specifically designed. The laser is placed on an optical table adjacent to the MBE chamber and a set of optical components are positioned on three sub-optical breadboards installed around the MBE system. Firstly, the output light beam is redirected to an optical sub-frame by a beam steering mirror, and periscope assembly is employed to align the height of the laser beam to the same height as the MBE optical viewports. Three 50:50 beam splitters are applied to split the beam into four sub-beams, and after reflection, these four sub-beams are directed into the MBE chamber through four symmetrically positioned UV anti-reflection coated optical viewports at 0°, 90°, 180° and 270°. The angle of incidence is 58° to the substrate, which is set by the position of the viewports and cannot be changed once welded. The optical path in the setup is approximately 3.5-4 m. Figure 4.17(a-c) presents the photographs of some of the optical setups around the MBE chamber.
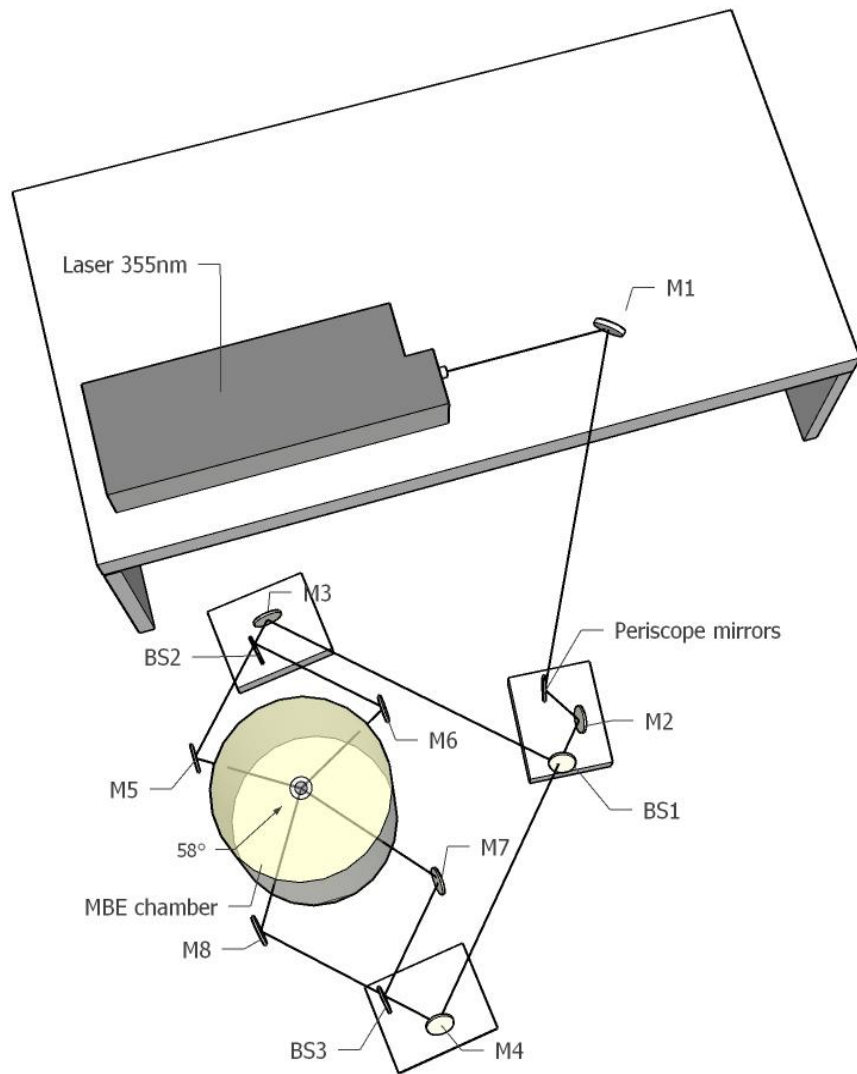
Figure 4.16 General layout of the four-beam DLIP configuration for MBE growth. BS1-BS3: 50:50 beam splitters, M1-M8: high reflective UV mirrors.

The laser beam alignment is performed by viewing the beam spots using an upward facing CMOS camera in a surface normal viewport. A 2-inch InGaN wafer that is compatible with the MBE growth environment needs to be loaded into the chamber for the beam alignment. InGaN can absorb the UV light and is able to emit blue luminescence which can be imaged by the CMOS camera. Without this, the sensitivity of the CMOS camera is poor for scattered light at 355 nm. Figure 4.17(d) presents a camera capture of the four sub-beams aligned on the centre of an InGaN wafer.
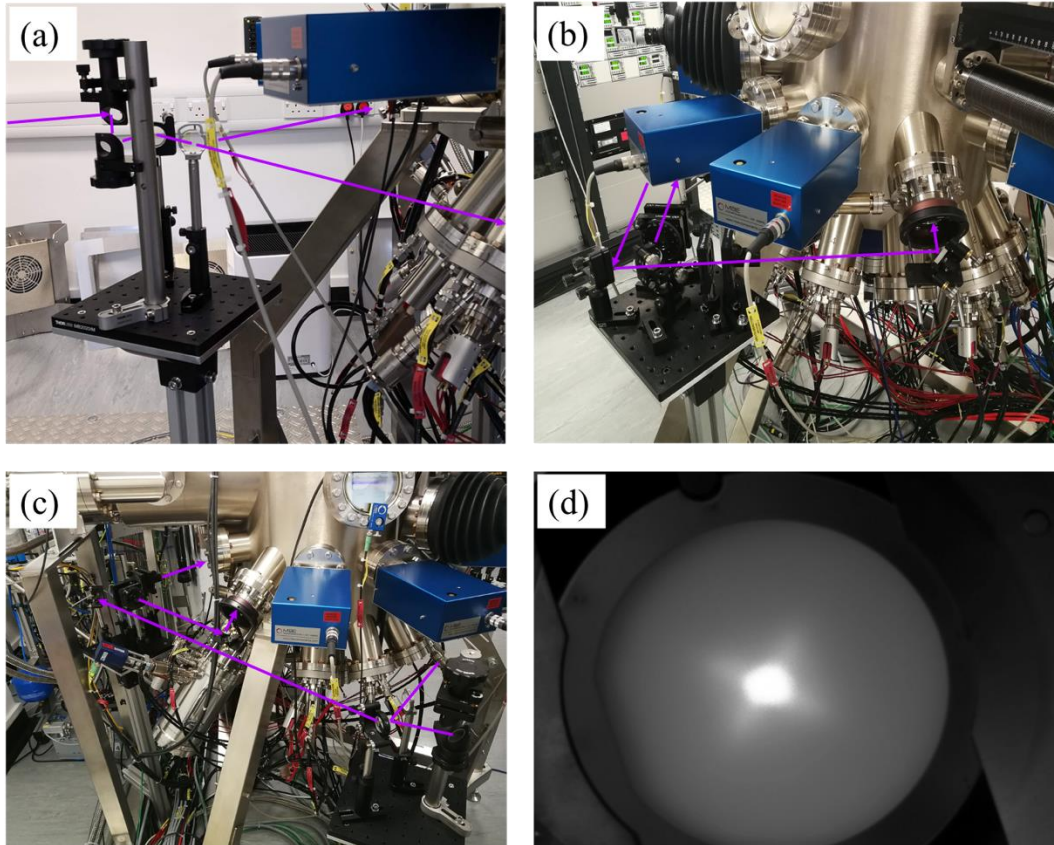
Figure 4.17 (a-c) Photographs of part of the DLIP setup around the MBE chamber. (d) Camera capture of the spot of four laser beams aligned on the centre of an InGaN wafer.

4.5 FORMATION OF PERIODIC NANOSTRUCTURES ON GAAS SURFACES BY *IN SITU* DLIP

In order to shed light on the interaction between laser pulses and III-V semiconductor materials, which may have a considerable influence on the growth mechanism of nanostructures, in this section *in situ* single pulse DLIP is applied to directly structure the epitaxial GaAs wafers. The laser-GaAs interaction starts from the incident laser being reflected and absorbed by the material. The laser enables free electrons in the material to vibrate at a high frequency, and part of the vibration energy is converted into electromagnetic waves that are reflected outward, and the rest of the energy is converted into the average kinetic energy of electrons and then transferred into heat through the relaxation process between the electrons and crystal lattice. In this section, a theoretical model is first built to analyse the laser-GaAs thermal effect. By using

different laser parameters such as the beam number, polarisation, and laser fluence, a variety of periodic nanostructures can be fabricated.

4.5.1 NUMERICAL SIMULATION OF SINGLE PULSE DLIP-INDUCED TRANSIENT THERMAL FIELD ON GAAS SURFACE

The photothermal effect is believed to be the dominant mechanism in the case of nanosecond laser irradiation processes, rather than photochemical or photomechanical mechanisms [192][193]. With nanosecond pulse duration, this is sufficient to transfer laser energy to the materials, whereas at pico- or femto- second timescales this may evolve into a more photochemical or photomechanical process. Photothermal ablation is the most common phenomenon in laser processing at nanosecond timescales on metals or semiconductors with high laser fluences. However, there has not been so much work on DLIP-induced surface modifications of III-V semiconductors in the low pulse energy regime. In this work, a thermal model of four-beam single pulse DLIP on a GaAs substrate is developed.

Heat can be generated in the irradiated material attributed to the absorption of the laser energy. The thermal fields within a GaAs substrate are governed by Fourier's law [194]. Since the 355 nm laser has a shallow penetration depth of about 1 μm in GaAs, here we only consider the 2-D heat conduction on the sample surface. Irrespective of the phase change and the exact mechanism that affects the absorption, when the material is isotropic and homogeneous, the transient thermal diffusion equation can be expressed as:

$$\rho c \frac{\partial T(x,y,t)}{\partial t} = \frac{\partial}{\partial x}\left[\kappa \frac{\partial T(x,y,t)}{\partial x}\right] + \frac{\partial}{\partial y}\left[\kappa \frac{\partial T(x,y,t)}{\partial y}\right] + Q(x,y,t) \qquad (4\text{-}7)$$

$$Q(x,y,t) = (1-R)\alpha I(x,y,t)\exp(-\alpha z) \qquad (4\text{-}8)$$

where T denotes the GaAs surface temperature at time, at the location *(x, y)*, ρ is the mass density, κ is the temperature-dependent thermal conductivity, c is temperature-dependent thermal capacity, Q is the heat source represented here by the laser energy absorbed by the material, R is the surface reflectivity of the laser light and α is the absorption coefficient, and $I(x,y,t)$ is the laser intensity distribution of 4-beam interference. The initial and boundary conditions can be expressed as:

$$T(x,y,t)\big|_{t=0} = T(x,y,t)\big|_{x,y=\infty} = T_0 \qquad (4\text{-}9)$$

where the T_0 denotes the initial substrate temperature.

Based on the above calculation model, the 2-D finite difference method (FDM) [195] is adopted to numerically solve the transient thermal distribution of a GaAs surface. The basic principle of FDM is to divide the object into small units. When the unit temperatures are not equal, the change in temperature of each node in a certain time interval can be regarded as the change caused by the heat flow through each node. Figure 4.18 illustrates a simple schematic diagram of the FDM calculation model. Take the node (i,j) as an example, where i and j denote the node in the x- and y-axis, respectively. An explicit method is used to discretize the equations on a domain and the node size is defined to be sufficiently small.
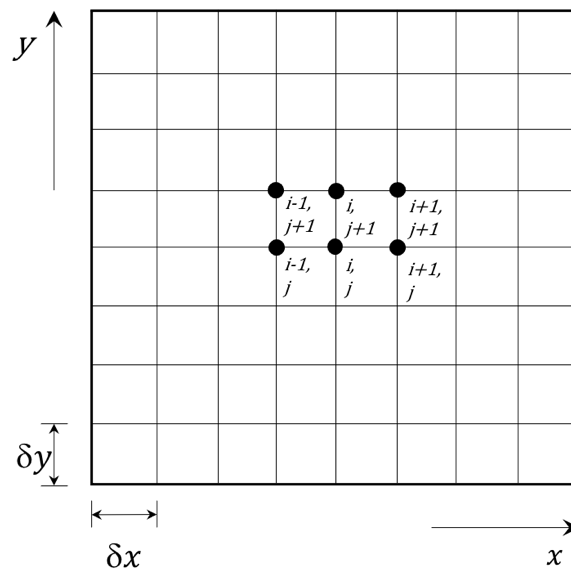
Figure 4.18 Scheme of the FDM discretisation model.

In 2-D space, Equation 4.7 exhibits:

$$\frac{T_{i,j}^{n+1}-T_{i,j}^{n}}{\Delta t} = k \left(\frac{T_{i,j+1}^{n}-2T_{i,j}^{n}+T_{i,j-1}^{n}}{\Delta x^2} + \frac{T_{i+1,j}^{n}-2T_{i,j}^{n}+T_{i-1,j}^{n}}{\Delta y^2} \right) + \frac{Q_{i,j}^{n}}{\rho c} \qquad (4\text{-}10)$$

Where $T_{i,j}$ represents the substrate temperature of node (i,j). Δt denotes the time increment.

According to the above analysis, the transient temperature gradients on a GaAs surface irradiated by single-pulse four-beam DLIP are calculated numerically using MATLAB programming. Table 4.2 shows the thermo-physical parameters of GaAs [196][197][198] and the applied simulation parameters.

Table 4.2 Thermo-physical data of GaAs and related parameters.

Parameter (unit)	Value
ρ (g/cm^3)	5.32
c (J/g $\cdot$ K)	$0.307 + 7.25 \times 10^{-5}\, T$
κ (W/cm $\cdot$ K)	$2271/T^{1.463}$
α (cm^{-1})	7×10^5
R	0.636 (s-polarisation)
	0.201 (p-polarisation)
	0.419 (mixed polarisation)
Melting point (°C)	1238
T_0 (°C)	500
θ (°)	58

Figure 4.19 presents the variation of GaAs surface temperature distribution with time. The employed parameters are 20 mJ pulse energy, 7 ns pulse duration and 0° polarisation angle. As shown in Figure 4.19(a), just after the single pulse, the interference exhibits a periodic temperature rise over the surface, and its thermal distribution is in good agreement with the four-beam laser intensity distribution. The highest temperature is positioned in the interference maxima region. The temperature at the interference maxima rises significantly over 900 °C but is still below the melting point, and the temperature at the interference minima regions increases gradually. A temperature difference of a few 100 °C exists between the maxima and minima which then slowly equilibrates to the background over a timescale of ~100 ns, as shown in Figure 4.19(b-d). Figure 4.19(e) reveals the evolution of the surface temperature at the interference maxima and minima, with the peak indicating the temperature just after the 7 ns laser pulse.
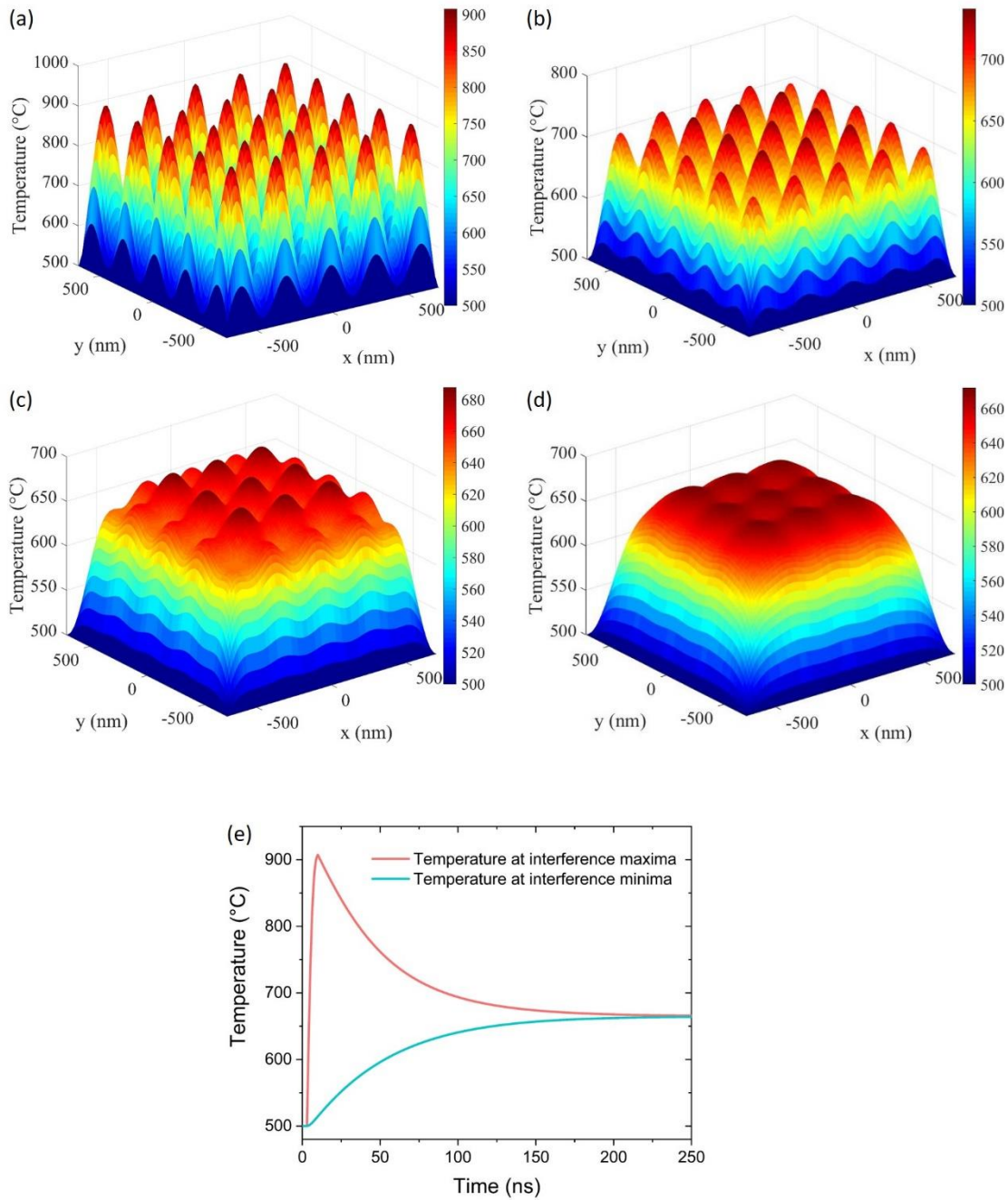
Figure 4.19 2-D surface temperature distribution on GaAs irradiated by single-pulse four-beam DLIP at different times after the pulse: (a-d) 0, 50, 100, and 150 ns. (e) Time-dependent surface temperature variation at the interference maxima and minima. The parameters used are as follows: 20 mJ pulse energy, 7 ns pulse duration, 58° incidence angle and 0° polarisation angle.

Figure 4.20 shows the simulated temporal evolution of the surface temperature at the interference maximum for different experimental parameters including the pulse energy (a), polarisation angle (b), initial substrate temperature (c), and pulse duration (d). The surface temperature rises with increasing pulse energy, and if the laser energy

is high enough, the temperature can exceed the melting point of the material, leading to localised surface melting. In terms of the different polarisation states, the simulations reveal that the surface temperature is highest at the polarisation angle of 0°, whilst lowest at the polarisation angle of 90°. For different initial substrate temperatures and pulse durations, different surface temperature evolutions can be obtained. These simulation results suggest that the material surface temperature can be modified by manipulating the laser parameters or the background substrate temperature, which provide useful guidance for the parameter selection of the following *in situ* DLIP-MBE experiments. For instance, 0° polarisation angle and pulse energy of 10-20 mJ are typically employed for the *in situ* patterning in this work, which is a much lower value than other reported DLIP pulse energy (~J).
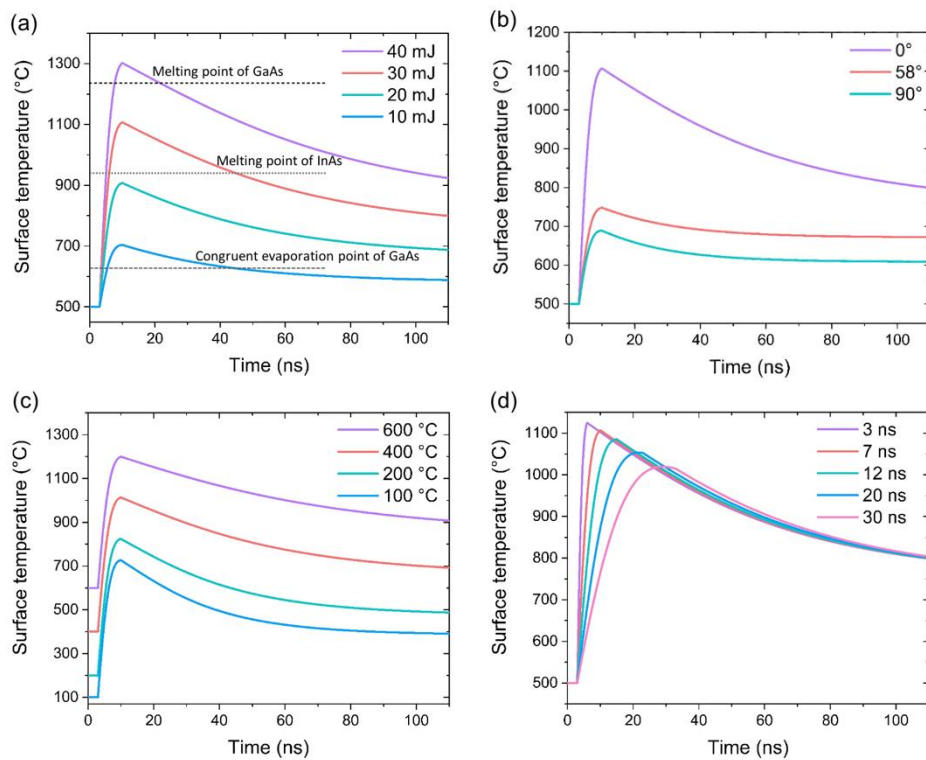
Figure 4.20 Time-dependent surface temperature at the interference maximum during and after the pulse. (a) The pulse duration of 7 ns, polarisation angle of 0°, and initial substrate temperature of 500 °C but different pulse energy. (b) The pulse energy of 20 mJ, pulse duration of 7 ns, and initial substrate temperature of 500 °C but different polarisation angles. (c) The pulse energy of 20 mJ, pulse duration of 7 ns, and polarisation angle of 0° but with different initial substrate temperatures. (d) The pulse

energy of 20 mJ, polarisation angle of 0°, and initial substrate temperature of 500 °C but different pulse durations.

According to the simulation results, the surface temperature increases rapidly even within short nanosecond laser irradiation. Since the band gap of GaAs is below the UV laser (355 nm) photon energy, high absorption efficiency leads to a significant temperature rise in the material, and due to the transient heat conduction, periodic 2-D thermal gradients can be produced over the GaAs surface. These thermal transients may modify the morphology of the GaAs surface and may also control the growth kinetics during the MBE growth, which will be discussed in the following sections.

4.5.2 EXPERIMENTAL DETAILS

The GaAs samples for DLIP were prepared as follows. Firstly, native oxide desorption was performed at a substrate temperature (T_s) of 620 °C, ahead of the growth of a 1000 nm-thick GaAs buffer at T_s = 600 °C aiming to smooth the surface. Next, T_s was decreased to 500 °C to grow a further 500 nm GaAs epilayer. In this way, the resulting surface is typically observed by AFM to be almost atomic flat with occasional meandering terraces. After the growth, the wafer was immediately irradiated by the *in situ* single-pulse DLIP inside the MBE chamber. A stabilised arsenic flux was supplied during the growth. Finally, the samples were quenched and taken out for structural characterisation by AFM.

4.5.3 POSSIBLE MECHANISMS DURING PULSED DLIP OF SEMICONDUCTOR SURFACES

There are several mechanisms that may take place during the interaction of nanosecond pulsed laser interference with materials, which can result in different surface morphologies. Mass transport appears to be the predominant mechanism. According to the aforementioned photothermal simulations, there is a 2-D thermal gradient generated on the GaAs surface due to the interference patterning. When the thermal energy exceeds the atom diffusion barrier energy, surface atoms are capable of migrating from the interference maxima (hot) regions towards the minima (cold) regions. Figure 4.21(a) shows a schematic diagram of atom migration from the hot to cold regions driven by a thermal gradient. Another well-known mechanism during laser-matter interaction is the Marangoni effect which has been widely found in the

process of laser patterning on metals [183][199][200][201]. The schematic diagram of the Marangoni flow is presented in Figure 4.21(b). If the material surface reaches its melting point under laser irradiation, the localised molten material would move either outward driven by a thermocapillary force or inward due to a chemicapillary force [200]. The resulting structure is based on the competition between the thermocapillary and chemicapillary flow. Apart from the laser melting process, thermal evaporation of the material could also be possible. Once the surface temperature exceeds a certain temperature under laser irradiation, for example, the congruent evaporation temperature of GaAs which is over 625 °C [202][203], GaAs decomposition takes place, where arsenic atoms are evaporated and free Ga atoms are left on the surface which can amalgamate to form Ga-rich metallic droplets [202]. It is well-known that Ga droplets are able to self-etch the surface to create nanoholes, and the surface mass transport occurs during the process [204][205]. Figure 4.21(c) describes the schematic processes of the Ga droplets etching and hole formation.
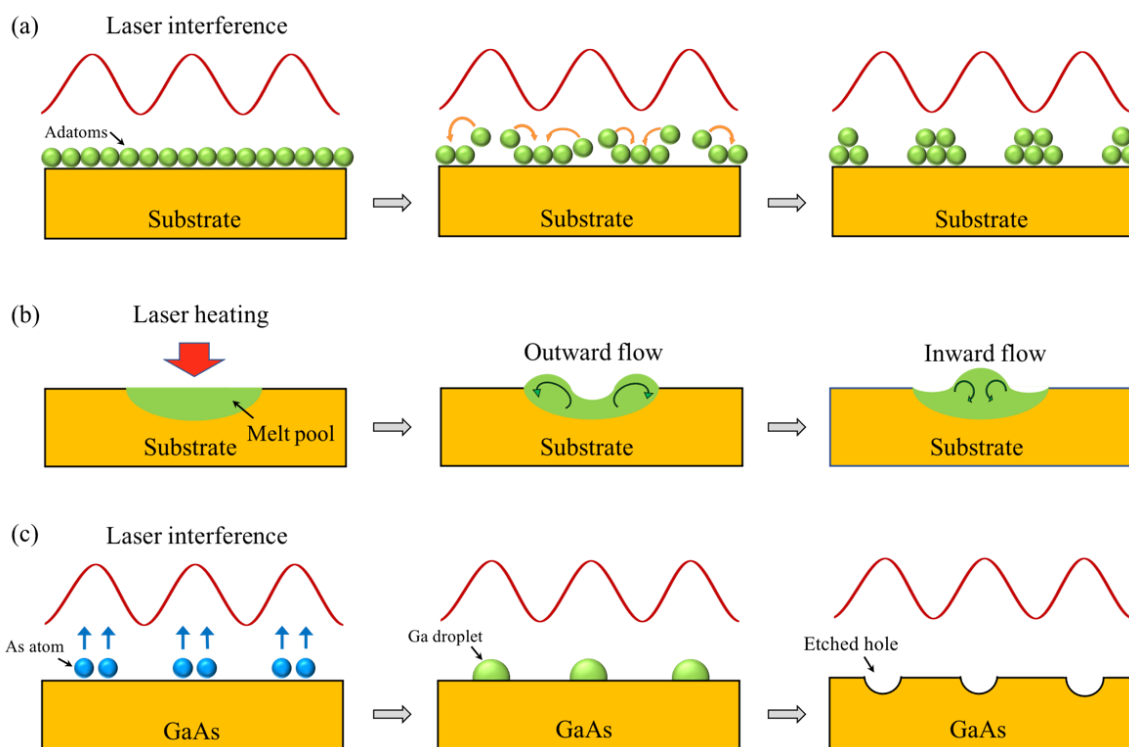
Figure 4.21 Schematic diagrams of (a) surface adatom migration driven by DLIP thermal gradients, (b) laser-induced Marangoni effect, and (c) DLIP-induced Ga droplet etching process.

4.5.4 RESULTS AND DISCUSSION

Figure 4.22 presents AFM micrographs of GaAs surfaces with (a) 1-D periodic line-like nanostructures with a pitch of 209 nm by two-beam DLIP, (b) 2-D periodic hole-like structures and (c) 2-D checkerboard gratings with a period of 209 nm by four-beam DLIP. Laser fluences of 28-45 mJ/cm^2 were used and the polarisation angle was 90°. We assume the formation of these nanostructures is attributed to surface mass transport. There are no deep hole structures observed owing to a much higher reflectance of GaAs and poorer laser intensity contrast for TE polarisation. The lattice pitch is $\Lambda = \lambda/2 \sin\theta$, which is 209 nm.
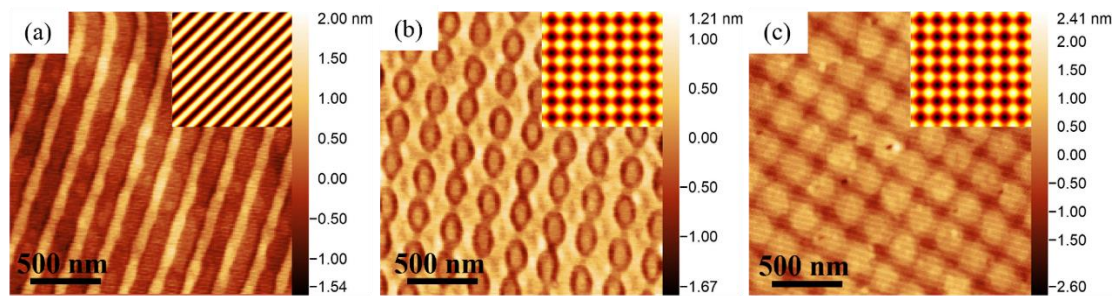
Figure 4.22 Fabricated nanostructures on GaAs surfaces with the polarisation angle of 90° (a) line-structures by 2-beam interference with a laser fluence of 28 mJ/cm^2, (b, c) 2-D structures by 4-beam interference with laser fluences of 31 mJ/cm^2 and 45 mJ/cm^2 respectively. Λ = 209 nm. The insets show the simulated interference patterns.

Figure 4.23 displays AFM images of four-beam interference patterns on GaAs in terms of 0° polarisation and with different laser fluences. A larger lattice period of $\Lambda = \lambda/\sqrt{2} \sin\theta$ = 296 nm is produced in this polarisation mode. As shown in Figure 4.23(a) with a low laser fluence of approximately 15 mJ/cm^2, a well-ordered array of nanoislands which are 80-100 nm wide and ~1 nm high on average is formed. We assume that these nanoislands result from the surface migration of atoms driven by the thermal gradient or the Marangoni effect. With an increase in the laser fluence, as revealed in Figure 4.23(b), an array of 2-D shallow holes is observed. It is clear to see that the material migrates outwards driven by the thermal gradient and accumulates around the shallow holes. With an even higher laser fluence, Figure 4.23(c) shows an array of significantly deeper nanoholes with a typical depth of 3-4 nm, and materials are also piled up on the edge of these nanoholes. The formation of nanoholes can be attributed to droplet etching and thermocapillary-driven mass transport processes. Figure 4.23(d) presents an oval-shaped hole array with monolayer height variation, which is owing to the uneven laser intensity of four beams which can be seen in some

areas of the pattern, and it shows the migration of material from interference maxima to minima areas. The results suggest that different laser fluences determine the mechanism of laser-material interaction. At low laser fluences, the formation of nanoislands dominates, while at high laser fluences nanohole formation becomes completely dominant.
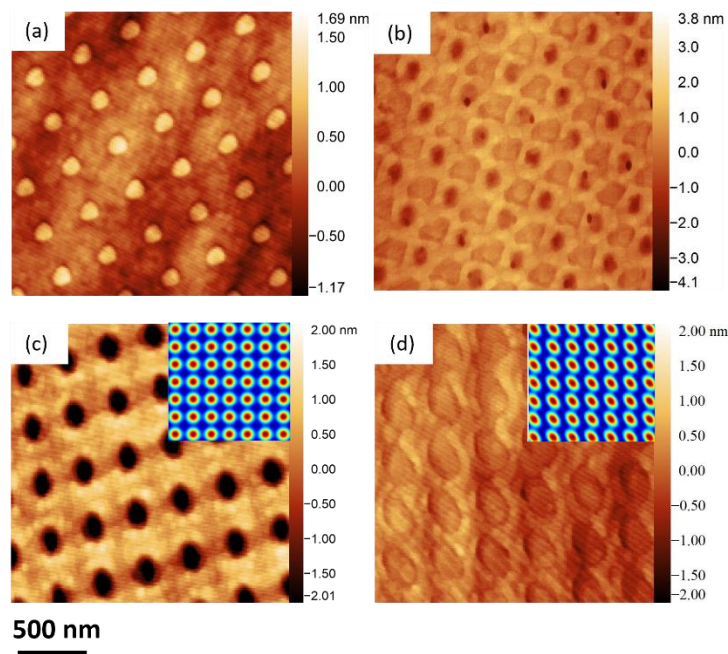
Figure 4.23 Fabricated nanostructures on GaAs surfaces with the polarisation angle of 0° at different laser fluences (a) 15 mJ/cm², (b) 22 mJ/cm², and (c, d) 38 mJ/cm². (d) presents the pattern with unequal laser intensities of four beams. The period $\Lambda \approx 300$ nm. The insets show the simulated interference patterns.

Therefore, at relatively high laser fluences, ordered arrays of nanohole structures with a period of 300 nm can be fabricated on the GaAs surface. Figure 4.24(a) and (b) depict AFM micrographs of fabricated periodic nanohole arrays, in which (a) shows a clean GaAs surface with arrays of nanoholes. The holes are ~3 nm deep and ~120 nm wide. The corresponding enlarged 3-D AFM image and cross-sectional profiles of nanoholes in Figure 4.24(a) are presented in Figure 4.24(c) and (e) respectively. As shown in Figure 4.24(b), there is not only the formation of nanohole arrays but also the formation of droplet-like structures on the interstitial planar surfaces. The holes are approximately the same size as the holes shown in Figure 4.24(a). The formation of droplets is due to a slightly higher laser fluence in these regions. A higher fluence produces a larger thermal gradient on the surface, therefore, Ga atoms in the hot regions can move out to nucleate in the cold regions, and these free Ga droplets

recrystallise as GaAs structures when the temperature is cooled down. The enlarged 3-D AFM micrograph and the corresponding cross-sectional profiles are displayed in Figure 4.24(d) and (f) respectively.
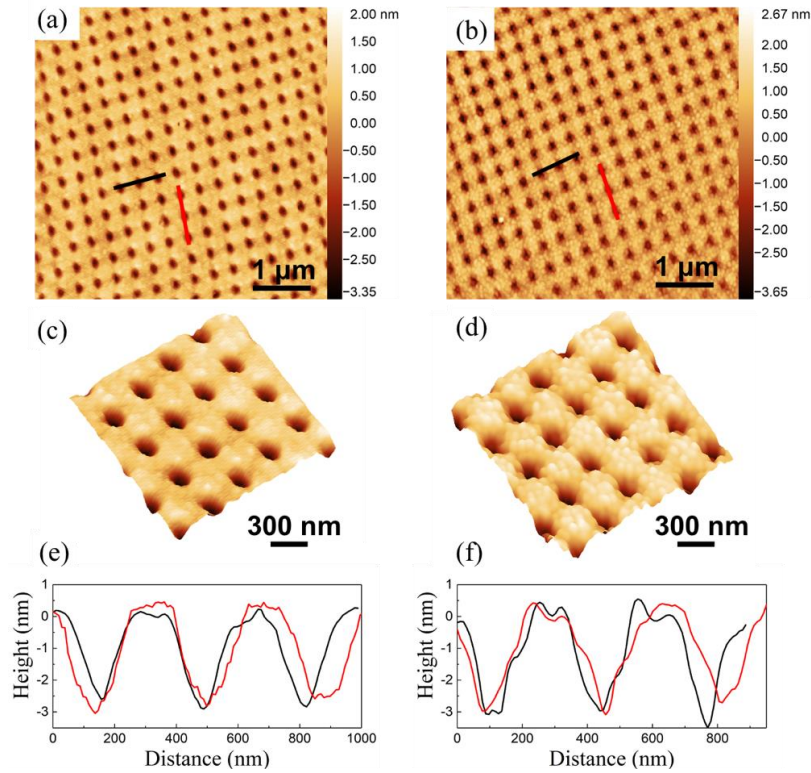
Figure 4.24 AFM micrographs of the fabricated 2-D arrays of nanoholes on GaAs surfaces with a period of 300 nm after the single-pulse four-beam DLIP. The laser fluences were (a) 35 mJ/cm² and (b) 46 mJ/cm². (c, d) The corresponding 3-D AFM micrographs. (e, f) Cross-sectional profiles of nanoholes along the directions marked in (a, b).

Compared with the fabrication of nanoholes by laser-ablation or deformation using high laser energy (~J/cm²), this *in situ* DLIP technique allows efficient and fast fabrication of ordered arrays of semiconductor nanostructures using relatively low pulse fluences (~mJ/cm²). Especially by combining the patterning with epitaxial growth in the same MBE chamber, it is very advantageous to keep the surface with atomic flatness and cleanness. Single nanosecond pulse DLIP is also favourable for the MBE growth since the growth chamber cannot maintain a low vibration level due to the use of mechanical vacuum pumps. The *in situ* direct nanopatterning technique presents advantages over conventional *ex situ* patterning technologies and is capable

of producing many varieties of surface structures by precisely controlling the laser interference parameters and the substrate growth temperature.

4.6 SUMMARY

The lithographic technique of laser interference patterning has been demonstrated in this chapter. Simulated multi-beam interference patterns are obtained. It can be concluded that a wide variety of patterns including 1-D grating shapes, 2-D square and hexagonal shapes, and more complex shapes can be realised with different interference configurations and laser parameters. Moreover, the laser-matter interaction due to a photothermal effect that induces transient temperature gradients on the GaAs surface has been simulated, which provides an early comprehension of the nanostructure formation process. Two laser interference systems consisting of (1) an *ex situ* bench-top pulsed LIL and (2) an *in situ* DLIP-MBE have been presented and implemented. Large area uniform periodic nanostructures with a small period of 300 nm are successfully obtained on conventional photoresists by using single shot LIL. It is also shown that the uniformity can be improved using a beam-shaping system. With regard to *in situ* DLIP, a wide variety of nanostructures have been obtained on GaAs substrates. The formation of diverse nanostructures results from different mechanisms such as surface mass transport, melting and etching that may occur during laser-matter interaction. According to the simulation results, the laser parameters such as the number of interfering beams and polarisation state determine the period and the contrast of the interference pattern. The 0° polarisation angle provides the highest surface temperature at the interference maxima as well as the best contrast and thus the largest thermal gradient compared to other polarisation states. The simulation suggests that a temperature difference of a few 100 °C exists between the interference maxima and minima on the GaAs surface after the pulse which then slowly equilibrates over hundreds of nanoseconds. In addition, with different laser fluences, different physical mechanisms can become dominant. Ordered arrays of shallow GaAs nanoislands (~1 nm high) have been obtained by single pulse four-beam DLIP with a polarisation angle of 0° and a relatively low laser fluence of ~15 mJ/cm². With high laser fluences of approximately 35-45 mJ/cm², nanohole arrays can be fabricated. The results presented in this chapter show that single shot laser interference provides excellent potential for rapid, highly efficient and large area fabrication of periodic and quasi-periodic surface nanostructures.

CHAPTER *5*

GROWTH AND CHARACTERISATION OF ORDERED INAS/GAAS QD NANOSTRUCTURES

This chapter concerns the *in situ* DLIP-assisted lateral ordering of InAs QDs on GaAs substrates. First of all, a theoretical model that predicts the surface adatom kinetic processes based on the photothermal effect mentioned in the previous chapter will be presented in Section 5.1. Then the growth details and results of ordered InAs/GaAs QDs will be described in Section 5.2 and 5.3, in which the influences of the DLIP parameters and the growth conditions on the ordering of InAs QDs will be investigated respectively. Lastly, Section 5.4 will reveal the optical properties of the patterned ordered arrays of InAs QDs.

5.1 THEORETICAL MODELLING OF DLIP-INDUCED SURFACE DIFFUSION AND NUCLEATION PROCESS

The goal of this section is to model the basic processes at the initial stage of SAQD formation affected by single pulse DLIP. The spontaneous formation of lattice-mismatched heterostructures via the S-K growth mode, for instance, InAs/GaAs SAQDs, occurs via the relaxation of the elastic strain energy. During the S-K growth, the process starts from initially layer-by-layer growth and once the deposited thickness exceeds a certain amount, the 2-D layer transition to 3-D island takes place. Contingent upon an understanding of the general growth mechanisms, a range of theoretical and computational models such as using kinetic Monte Carlo (KMC) [106][107][208] and continuum models [209][210][211] have been intensively exploited to investigate the atomistic processes and surface morphological evolution during the epitaxial growth. In addition, Osipov *et al*. [96][212][213] and Dubrovskii *et al*. [97][98] have constructed a thermodynamic and kinetic model which takes the variation of

free energy during the transition from 2-D WL to 3-D island into account to analyse the nucleation and growth processes.

A fundamental step in understanding the nucleation mechanism of SAQDs is to explore the mass transport that occurs during the transition to 3-D island growth. MBE growth can be generally elucidated as a process of atomic kinetics including adsorption, desorption, diffusion, aggregation, and nucleation, etc. on the growing surface. After deposition, adatoms undergo either re-evaporation or migration stochastically on the surface to the neighbouring sites attempting to reach energetically favourable positions. The movement of adatoms is the major driving force of the self-assembly process. Here we address the typical S-K InAs/GaAs (100) QD growth system. Since the growth is usually under arsenic-rich conditions and the GaAs surface is terminated with arsenic, the kinetics of group III atoms particularly the surface migration play a dominant role in the growth process. The diffusion of indium adatoms is known to be very mobile compared with Ga adatoms on As-terminated GaAs (100) surface [214][215]. Thus, in this work, we mainly address the surface diffusion of indium adatoms which we assume is critical during the formation of InAs QDs.

We present here numerical studies of the initial stage of InAs/GaAs (100) SAQDs nucleated by DLIP with the aim to unveil the impact of laser interference on the spatial positioning of nanostructures. A qualitative thermodynamic and kinetic model based on the surface diffusion process and classical nucleation theory was developed. The model begins with the assumption that 1.0 ML of InAs has been uniformly deposited onto a flat GaAs surface under sufficiently arsenic-rich conditions, acting as a precursor for quantum dot nucleation. This layer can be described as the 2-D WL which occurs before the transition to 3-D islands. It is assumed that all the indium adatoms adsorbed evenly on the surface have an equal probability to hop from an adsorption site to adjacent sites. Due to an adequate residence time of indium adatoms on the GaAs, the desorption of indium atoms during the nanosecond laser irradiation is ignored.

In accordance with Fick's first law, the driving force for atom migration is the gradient of the chemical potential of the atoms [216]. Thus, the diffusion flux of atoms driven by the chemical potential gradient is expressed as:

$$J = -\frac{n}{RT} \cdot D \cdot \nabla\mu \qquad (5\text{-}1)$$

where n is the atom concentration, R is Boltzmann's constant, T is the absolute temperature, μ is the chemical potential, D denotes the diffusion coefficient of atoms defined by Arrhenius law:

$$D = D_0 exp^{\frac{-E_d}{RT}} \qquad (5\text{-}2)$$

D_0 is the pre-exponential factor of the diffusivity related to the hopping distance between sites and the vibrational frequency of the diffusing material. E_d is the energy barrier required to overcome during the diffusion process. The chemical potential μ on the surface can be expressed as:

$$\mu = \mu^0 + RT\ln(n) \qquad (5\text{-}3)$$

The flux J is attained when substituting Eq. (5-2) and (5-3) into Eq. (5-1):

$$J = -D_0 exp^{\frac{-E_d}{RT}} \cdot \nabla n \qquad (5\text{-}4)$$

On the basis of Fick's second law [216], the density of the diffusive adatoms at location (x,y) and time t, obeys the equation:

$$\frac{\partial n(x,y,t)}{\partial t} = \nabla \cdot \left(D_0 exp^{\frac{-E_d}{RT}} \nabla n(x,y,t) \right) \qquad (5\text{-}5)$$

The diffusion equation is numerically resolved using FDM. In a 2-D FDM scheme, the equation (5-5) can be written as:

$$\frac{n_{i,j}^{m+1} - n_{i,j}^m}{\Delta t} = D_0 exp^{\frac{-E_d}{RT}} \left(\frac{n_{i+1,j}^m - 2n_{i,j}^m + n_{i-1,j}^m}{\Delta x^2} + \frac{n_{i,j+1}^m - 2n_{i,j}^m + n_{i,j-1}^m}{\Delta y^2} \right) \qquad (5\text{-}6)$$

The value of $D_0 = 10^{-2}$ cm^{2}s^{-1}, $E_d = 0.5$ eV [217] and an initial indium adatom concentration $n_0 = 5.45 \times 10^{14}$ cm^{-2} are employed. For simplicity, we assume the surface diffusion process is 2-D isotropic and there is no detachment taking place during the process. Thus, the transient evolution of the surface morphology was simulated and after single-pulse DLIP, the indium adatom density distributions on the GaAs surface can be estimated numerically.

To theoretically describe the process of nucleation of QDs, we introduce the capillary model of S-K InAs/GaAs nucleation according to the Muller-Kern criterion [90]. The nucleation occurs once the supersaturation of adatoms surpasses a critical amount. The transition from 2-D metastable layers to the spontaneous formation of 3-D islands is considered to be a competition between an increase in surface energy and strain

energy, and the alteration in wetting potential. The total free energy of 3-D InAs island formation in the case of S-K mode can be expressed as [95]:

$$F = \Delta F_{surf} + \Delta F_{elas} - i\Delta\mu - \Delta F_{att} \tag{5-7}$$

where ΔF_{surf} denotes the increase in surface energy, ΔF_{elas} represents the elastic energy, ΔF_{att} is the attraction energy of atoms from island to substrate, i represents the number of atoms, and $\Delta\mu$ represents the chemical potential difference of atoms on the WL and island.

$$\Delta\mu = RT\,ln\left(\frac{n}{n_e}\right) \tag{5-8}$$

where T represents the surface temperature, R denotes Boltzmann's constant, n indicates the surface adatom density, and n_e is the equilibrium density of adatoms which is temperature dependent.

$$n_e = n_0 exp^{\frac{-E_a}{RT}} \tag{5-9}$$

where n_0 is the adatom density of a monolayer InAs, and E_a is the adatom formation energy. Here the 3-D InAs island is deemed to be a lens-shaped island with a contact angle $\vartheta = 20°$ and a base diameter of L. The aspect ratio of the island $\beta = (1 - cos\vartheta)/2sin\vartheta$. The surface energy is assumed to be isotropic, which can be calculated as follows:

$$\Delta F_{surf} = 4\pi\left(\frac{L}{2}\right)^2 \beta^2\gamma \tag{5-10}$$

where γ is the island-gas interface energy required to form an island. The elastic energy during the formation of island is:

$$\Delta F_{elas} = Z(\beta)\lambda_e\varepsilon_0^2 l_0^2 d_0 i \tag{5-11}$$

where $Z(\beta)$ denotes the coefficient of strain relaxation estimated by Ratsch-Zangwill approximation [218], λ_e is the elastic modulus of InAs, for isotropic approximation [219] $\lambda_e = C_{44}(3C_{12} + 2C_{44})/(C_{12} + C_{44})$, ε_0 represents the lattice mismatch between InAs and GaAs, l_0 denotes the average interatomic distance on the surface, d_0 is the height of a monolayer InAs. The attraction energy of atoms to the substrate is related to the wetting energy on the substrate $\Psi = \gamma_s - \gamma_f - \gamma_{sf}$, where γ_s represents surface energy of GaAs substrate, γ_f denotes the surface energy of InAs layer, γ_{sf} is the interfacial energy which is too small to be considerable. It gives:

$$\Delta F_{att} = \Psi e^{\left(-\frac{m}{k_0}\right)}(1 + k_0)\pi\left(\frac{L}{2}\right)^2 \tag{5-12}$$

where m is the number of MLs in WL, and k_0 is the coefficient of relaxation. Therefore, the total free energy in Eq. (5-7) can be written as:

$$F = 4\pi\beta^2\gamma_{ef}\left(\frac{L}{2}\right)^2 - iRTln\left(\frac{n}{n_{ef}}\right) \tag{5-13}$$

where γ_{ef} can be considered as the effective surface energy, and n_{ef} is the effective equilibrium concentration of adatoms.

$$\gamma_{ef} = \gamma - \frac{\Psi e^{\left(-\frac{m}{k_0}\right)}(1+k_0)}{4\beta^2} \tag{5-14}$$

$$n_{ef} = n_e exp^{\left[\frac{\lambda_e\varepsilon_0^2 l_0^2 d_0 Z(\beta)}{RT}\right]} \tag{5-15}$$

The parameter $\xi \equiv n/n_{ef} - 1$ is introduced as the supersaturation representing the system metastability [220][221]. At high supersaturation ξ, the growth system enters a metastable state. Nucleation occurs as supersaturation increases and nuclei grow by attaching new adatoms, and the supersaturation decreases after stable nuclei are formed. A higher ξ is expected to result in a higher density and a smaller critical size of nuclei [221]. When the formation free energy F reaches its maximum value, the critical number of atoms i_c within an island is obtained, where F_{i_c} can also be considered as the nucleation barrier, which present:

$$i_c = \frac{2c}{ln^3(1+\xi)} \tag{5-16}$$

$$c = \frac{\pi}{3}\frac{\gamma_{ef}^3(l_0^2 d_0)^2}{(RT)^3}\left(\frac{1-cos\vartheta}{1+\frac{cos\vartheta}{2}}\right)^2 \tag{5-17}$$

In this model, the surface is assumed to be defect-free and isotropic for nucleation so that each surface site has an equal nucleation rate I, which represents the number of emerging irreversibly nuclei in the unit area per unit time. The nucleation rate in the Zeldovich formula [213][221] is given by:

$$I = nW^+(i_c)\sqrt{\frac{|F''(i_c)|}{2\pi}}e^{-F(i_c)} \tag{5-18}$$

$W^+(i_c)$ represents the attachment rate of atoms to the critical nuclei:

$$W^+(i_c) = \frac{n\pi L_{i_c} D_e i_c}{l_0} \tag{5-19}$$

where L_{i_c} is the diameter of critical nucleus, D_e is the diffusion coefficient of adatoms on the WL. With respect to supersaturation, one can express the nucleation rate as:

$$I(\xi) = n_{ef}^2 D_e (1+\xi)^2 \ln(1+\xi) \sqrt{\frac{n_0 RT}{\gamma_{ef}}} \frac{1}{2\beta} exp^{\left(-\frac{c}{\ln^2(1+\xi)}\right)} \qquad (5\text{-}20)$$

The following values used in the model of InAs/GaAs (100) system are [95][218][222][223]: $E_a = 0.2$ eV , $\gamma \approx \gamma_f = 44$ meV/Å^2 , $\gamma_s = 45$ meV/Å^2 , $C_{12} = 45.26$ Gpa, $C_{44} = 39.59$ Gpa, $\varepsilon_0 = 0.07$, $l_0 = 0.429$ nm, $d_0 = 0.303$ nm, $\beta = 0.088$, $k_0 = 1$, $Z(\beta) = 0.6$, and $L(i_c) = 4$ nm. Equations (16-23) are solved numerically with MATLAB to obtain the indium adatom concentration distribution and the nucleation rate of InAs QDs on GaAs (100) substrates after single pulse DLIP.

Figure 5.1(a) and (b) depict respectively the four-beam interference pattern and the temperature distribution just after the 7 ns pulse, with 20 mJ pulse energy and 0° polarisation angle, and Figure 5.1(c-f) show the calculated density distributions of indium adatoms on the GaAs surface as the laser pulse energy increases. Note that the calculation is based on the initial condition of a 1 ML flat InAs layer on GaAs surface with an indium adatom concentration of 5.45×10^{14} cm^{-2}. It is clear to see that adatoms follow the same 2-D periodic distribution as the thermal distribution. Indium adatoms migrate out from the interference maxima hot regions towards the interference minima cold regions. Therefore, the surface morphology as demonstrated in Figure 5.1(c) presents a ring shape around the hot area, where the adatoms are piled up. Also, the diffusion length increases with the increase of pulse energy owing to a larger thermal gradient. Figure 5.1(c-f) reveals this trend where the adatoms gradually move towards the centre of the cold area, and Figure 5.1(f) presents the surface morphology that the indium adatoms are mainly located in the cold areas and therefore small clusters are formed. In this way, indium adatoms are arranged in good order on the surface. The distributions of the calculated nucleation rate of InAs QDs under the influence of laser interference with respect to different pulse energy are revealed in Figure 5.1(g) and (h), which correspond to Figure 5.1(e) and (f) respectively. The increment in the number of adatoms in a cluster introduces a high supersaturation that precipitates the nucleation process. The nucleation rate is much higher in the interference minima region compared with other areas, and the preferred position for nucleation is determined by the adatom diffusion length which is related to the laser pulse energy.
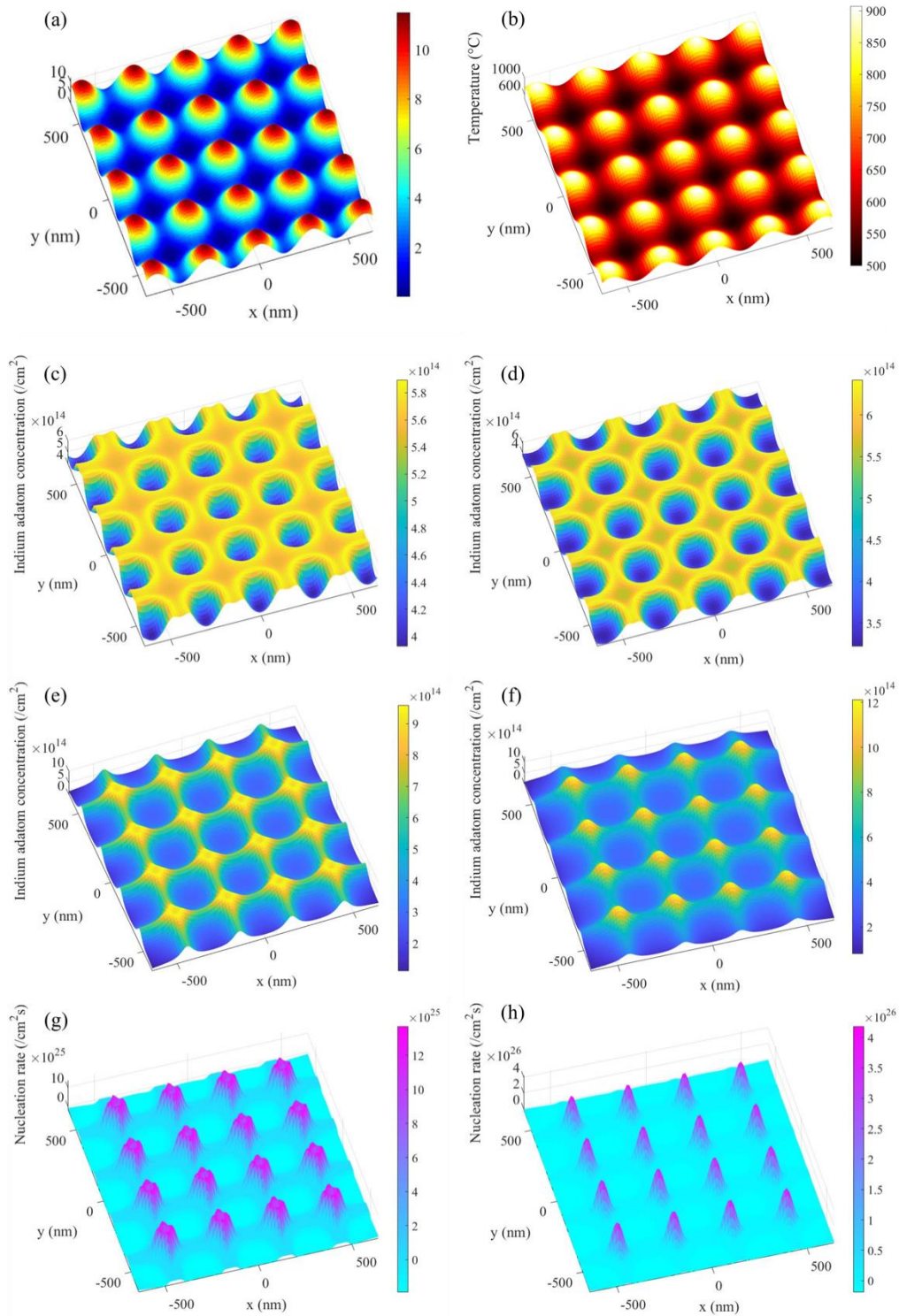
Figure 5.1 (a) Simulated four-beam interference pattern with a polarisation angle of 0°. (b) Simulated temperature distribution just after the 7 ns pulse with 20 mJ pulse energy. (c-f) Calculated distribution of indium adatom concentration just after the pulse with different pulse energy (a-d) 10 mJ, 20 mJ, 40 mJ and 50 mJ, respectively. The initial indium adatom concentration is assumed to be 5.45×10^{14} cm^{-2}. (g, h)

Calculated distribution of nucleation rate of InAs QDs with pulse energy of 40 mJ and 50 mJ.

Figure 5.2 displays the calculated adatom distribution and the nucleation rate with a polarisation angle of 58° which is a mixed polarisation state, and it is set by the DLIP optical configuration. The simulated interference pattern and temperature distribution just after the pulse are shown in Figure 5.2(a) and (b) accordingly. Compared with the results of 0° polarisation angle under the same laser energy, the surface morphologies in Figure 5.2(c) and (d) exhibit more concentrated doughnut or ring structures, which are associated with the difference in the interference pattern in these two polarisation states. For the 58° polarisation angle, the interference minima area is surrounded by four interference maxima areas and the distance between the minima area and maxima area is shorter than that of the 0° polarisation angle. Accordingly, the diffusion length is shorter for indium adatoms and these adatoms that migrate out from hot areas can be concentrated in the cold areas. In Figure 5.2(d) with slightly higher pulse energy of 20 mJ, more adatoms are mobile to diffuse to form narrow ring structures. At even higher energy as depicted in Figure 5.2(e) and (f), indium atoms are almost accumulated and concentrated in the cold areas and quasi-2-D island or cluster structures can be formed. It is noted that there is the formation of side small clusters adjacent to the main rings or islands, which is due to the interference pattern under this polarisation state. The distance between the small island and the main island is around 200 nm. Thus, based on these quasi-2-D ring or island surface structures, the nucleation of InAs QDs can also be concentrated around or located within the island areas, as displayed in Figure 5.2(g) and (h).
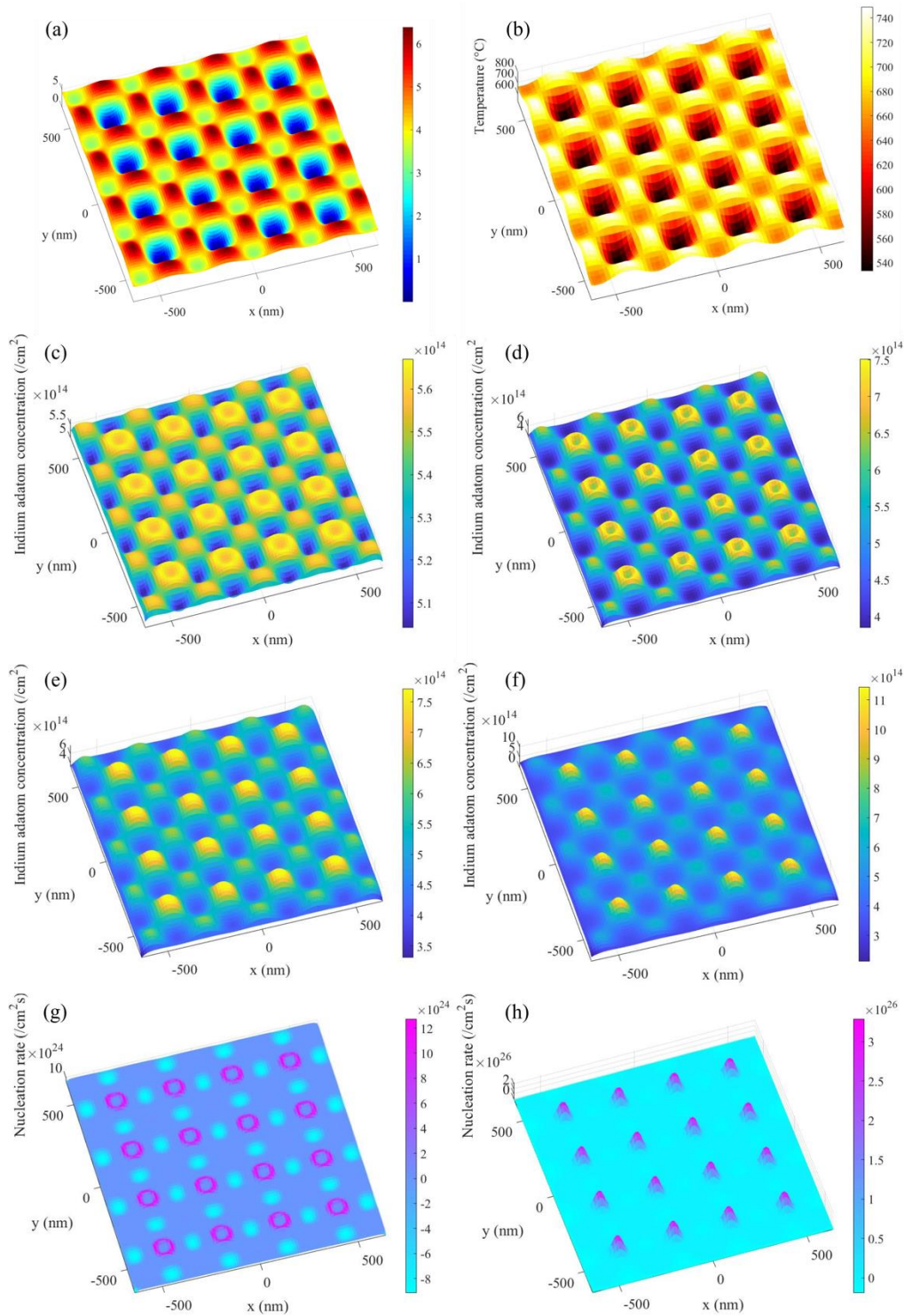
Figure 5.2 (a) Simulated four-beam interference pattern with a polarisation angle of 58°. (b) Simulated temperature distribution just after the 7 ns pulse with 20 mJ pulse energy. (c-f) Calculated distribution of indium adatom density just after the pulse with increasing pulse energy (a-d) 10 mJ, 20 mJ, 30 mJ and 40 mJ, respectively. (g, h) Calculated distribution of nucleation rate of InAs QDs with pulse energy of 20 mJ and 40 mJ.

The modelling results suggest that indium adatoms are able to migrate from the interference maxima regions towards interference minima regions driven by the 2-D thermal gradients. Due to the accumulation of adatoms, quasi-2-D clusters or islands can be formed on the surface. The shape of the island is determined by the diffusion length that is relevant to the interference pattern, the pulse energy and the magnitude of the thermal gradients. At a polarisation angle of 0°, it needs higher thermal energy for adatoms to move to the interference minima areas compared with that at the polarisation angle of 58°. Moreover, it is easier to form concentrated nanostructures including ring-shaped and small island structures at a polarisation angle of 58° owing to the pattern difference. The high concentration of indium adatoms at the interference minima areas facilitates the nucleation of 3-D InAs QDs in these areas as a result of strain accumulation.

As discussed in Chapter 4, the laser-matter interaction is a far more complex process in real experiments, for instance, the dominant mechanisms can be laser melting, ablation or evaporation in the high laser fluence regime, and the atom dynamics can be controlled by the competition between thermocapillary and chemicapillary effects, which are not taken into consideration in this modelling. However, this work provides preliminary modelling of interference-induced thermocapillary effect on the modification of the surface morphology, basically with regard to the surface mass transport. The simulation results show the influence of direct laser interference at least qualitatively on the spatial ordering of nanostructure formation and the QD nucleation, which were observed in the upcoming experimental results. In conclusion, a theoretical model was developed to analyse the kinetic behaviour including surface diffusion and nucleation of the initial stage of InAs/GaAs QD growth during the DLIP process. It suggests that the laser interference patterning enables deterministic surface diffusion of adatoms rather than a stochastic process, and therefore contributes to the spatial ordering of the nucleation process, where QDs tend to nucleate at the quasi-2-D nanoisland sites.

5.2 SAMPLE GROWTH

The samples were fabricated on 2-inch epi-ready (100) GaAs wafers by MBE. Prior to the growth, surface native oxides from the GaAs substrate were removed at a T_s about 630 °C under As$_2$ supply, after which a 500 nm GaAs buffer was grown at T_s = 600 °C at a GR of 3.0 Å s^{-1}, which was derived from the RHEED oscillation period, and then

T_s was cooled to 500 °C for InAs QD growth. 1.0 ML InAs was then supplied at a GR of 0.079 ML s^{-1}, and immediately *in situ* single-pulse DLIP was applied onto the surface. Laser fluences in the range of 12-25 mJ/cm^2 were typically utilised. Subsequently, further deposition of InAs was supplied to form S-K QDs. During DLIP, the substrate rotation was momentarily stopped at the indexing position, and the growth of InAs was not interrupted. For optical characterisation, a double-layer structure that consists of two layers of InAs QDs was fabricated. In this structure, an additional 300 nm layer of AlGaAs layer was grown prior to the GaAs buffer to enhance the PL signal, and after the first layer of QD growth, a 200 nm GaAs spacer was deposited. After 10 seconds of growth interruption, the uncapped top layer of InAs QDs guided by DLIP was grown for structural characterisation, which is under identical laser and growth conditions as the buried layer. The surface morphologies of the samples were characterised by AFM *ex situ*. Figure 5.3 states a diagrammatic representation of the grown heterostructure.
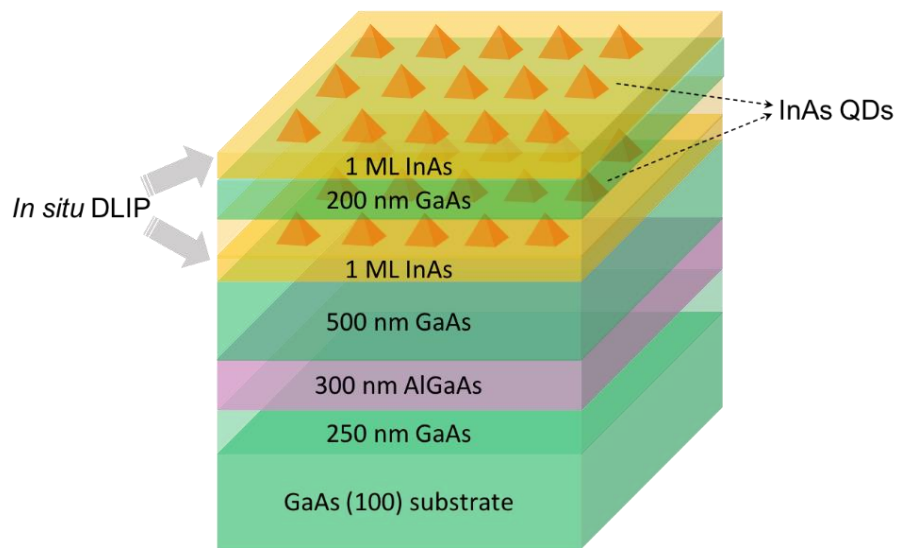
Figure 5.3 Diagrammatic representation of grown InAs QDs on a GaAs (100) substrate.

To conduct investigations upon the influence of DLIP and growth parameters on the ordering of InAs QDs, the laser interference parameters such as the pulse energy, polarisation state, number of the interfering beams, and the exposure-growth sequence, as well as the growth conditions including the InAs deposition amount, GR and substrate temperature were manipulated. In the upcoming section the detailed experimental results are discussed.

5.3 RESULTS AND DISCUSSION

5.3.1 NANOISLAND FORMATION AND QD NUCLEATION

After the initial deposition of 1 ML InAs, single pulse four-beam DLIP with a laser fluence of approximately 15 mJ/cm² was applied *in situ* on the centre of the surface. The 1 ML thickness of InAs was selected as it is below the critical thickness, and it would be expected to remain at this stage a relatively smooth surface characterised by ML terraces. Figure 5.4(a) shows a 5 × 5 µm² AFM micrograph of the sample surface with 1 ML InAs after the exposure of DLIP. The surface presents an ordered square array of quasi-2-D nanoislands with a pattern period of ~300 nm. These nanoislands are typically ~120 nm in diameter and 1.8 ± 0.2 nm in height. Based on the simulation results (see Section 4.5.1 in Chapter 4 and Section 5.1 in Chapter 5), a temperature difference of a few 100 °C exists between the interference maxima and minima after the pulse, and it is able to induce surface migration of adatoms. Figure 5.4(b) depicts an enlarged 3-D AFM micrograph of an individual nanoisland. The corresponding line scan of nanoislands along the direction as marked with the blue dotted line in (a) is depicted in Figure 5.4(c). The nanoislands appear with a central shallow pit of 0.3 ± 0.1 nm in depth, and at the edge of the nanoislands, small dips of ~0.9 nm as shown as dark rings were observed.
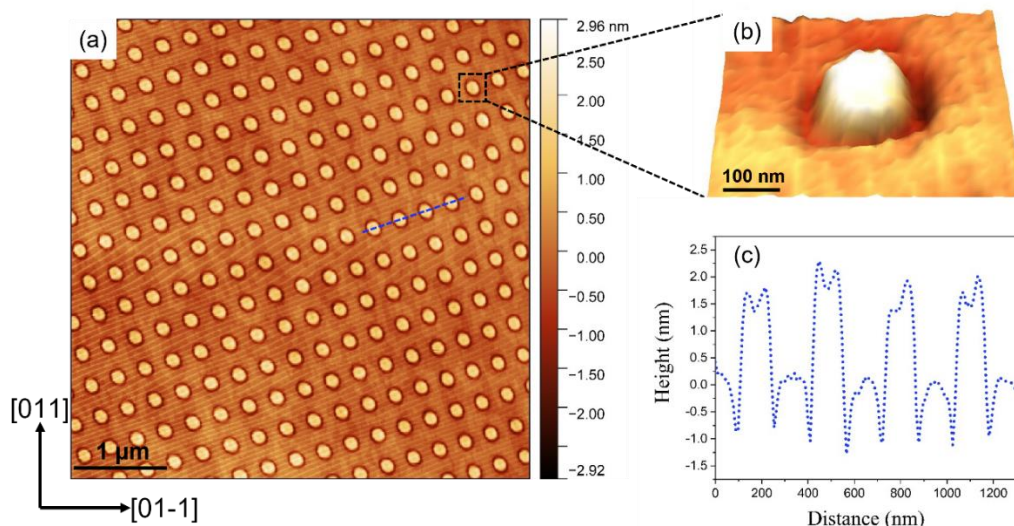
Figure 5.4 (a) 5 × 5 µm² AFM micrographs of a square array of quasi-2-D nanoislands with a period of 300 nm induced by *in situ* DLIP. (b) The magnified 3-D AFM image of a single nanoisland. (c) Line scan across four nanoislands as marked in (a).

The exact mechanism underlying the formation of these surface nanoislands is not thoroughly understood. As discussed in Chapter 4, different mechanisms may occur during the interaction between laser and materials. The formation of these nanoisland arrays may result from the surface migration of adatoms driven by the thermocapillary effect as the modelling shows. Another possible formation mechanism could be the Marangoni effect. It is feasible to melt the material surface, but maybe only a few monolayers deep, at the peak intensity interference maxima areas. Therefore, the molten material can flow inward toward the centre, which is induced by the chemicapillary effect, and consequently sombrero-shape structures could be formed.

Thus, under the effect of DLIP, the surface morphology of the initial 1 ML InAs, which would otherwise grow in the form of monolayer platelets, turns into a square array of small quasi-2-D nanoislands with a period corresponding to the size of the pattern pitch. The size of these islands seems remarkably consistent at 1-2 nm in height and 50-100 nm wide, with the width strongly relying upon the interference parameters, which will be stated later in Section 5.3.2 in detail.
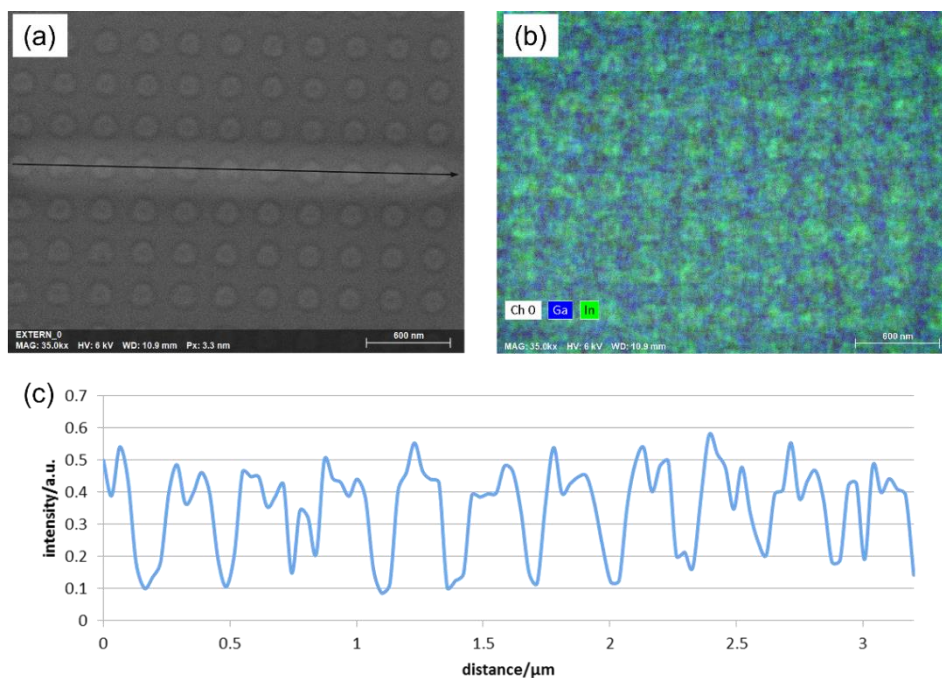
Figure 5.5 (a) SEM image of the nanoisland arrays induced by *in situ* DLIP. (b) Ga and In EDS maps of these nanoislands. (c) Line profile of the nanoislands along the line in (a).

In order to validate the assumption of surface diffusion, EDS mapping was performed for the elemental analysis using facilities provided by the project partner Tampere University. An SEM micrograph of the surface morphology of the initial 1 ML InAs after *in situ* DLIP was shown in Figure 5.5(a), in which a square array of nanoislands were imaged. Figure 5.5(b) presents the X-ray maps of Ga and In elements and Figure 5.5(c) depicts the line scan for indium along the line in (a). In the map, it is clear to see that the amount of indium is highest in the area of nanoislands and lowest between the islands. It suggests that indium atoms are mainly accumulated in the island areas which we believe is in consequence of the surface migration of indium atoms towards the nanoislands.

After the patterning, further 0.7 ML of InAs were deposited upon the growing surface with nanoisland arrays at the same GR. Overgrowth of QDs on such a nanoisland-featured surface leads to S-K InAs QDs to be formed on the pre-patterned surface. Figure 5.6(a) presents an AFM micrograph of InAs QDs on the DLIP-structured surface. It is observed that InAs QDs are preferentially nucleated at the edge of the nanoislands as a result of the small dips around the islands, and the nucleation of interstitial QDs on the planar areas between the island sites is completely suppressed. The negative surface curvature present in the dips can provide energetically favourable positions for the nucleation of QDs, since the driving force of adatom migration is always the gradient of chemical potential [136]. This phenomenon has been widely reported when QDs are overgrown on prepatterned surfaces with nanoholes or grooves [76][224]. The size distribution of these nucleated QDs exhibits a large fluctuation varying from 1 to 10 nm in height. The typical size is ~50 nm wide and ~8 nm high, whereas ~20 nm wide and ~several MLs in height small QDs are also observed. The nucleation sites of QDs at the edge of islands and the occupancy of QDs at each island site are randomly distributed, since the edges of these islands still present large areas for nucleation. In expectation of attaining uniform dot occupancy and size distribution, the growth conditions as well as the nanoisland size need to be optimised.
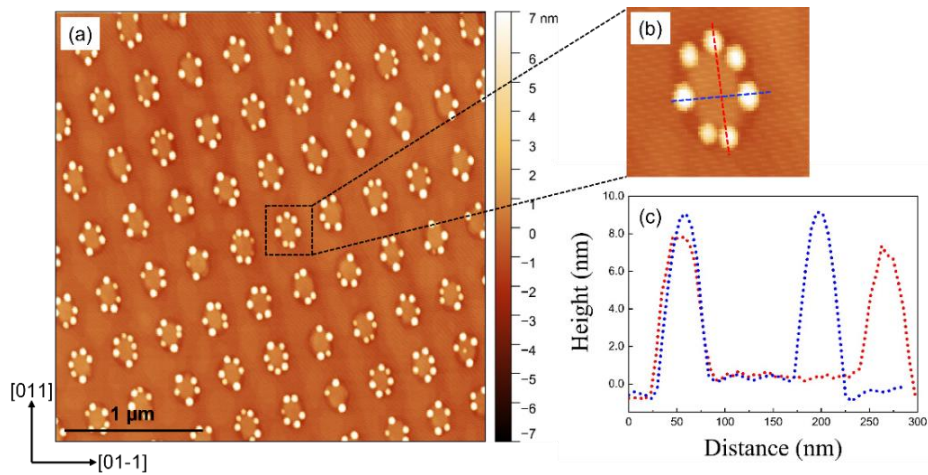
Figure 5.6 (a) 3 × 3 μm² AFM micrograph of InAs QD on the nanoisland-templated surface. (b) The magnified AFM image of a single nanoisland site. (c) Line scans across the direction as marked in (b).

5.3.2 INFLUENCE OF THE LASER INTERFERENCE PARAMETERS ON QD GROWTH

5.3.2.1 LASER INTENSITY

Due to the superposition of four coherent incident laser beams with the identical Gaussian beam profile, the resulting interference area also follows a Gaussian intensity distribution. The laser beam spot incident onto the sample surface is approximately 5 mm in diameter. Figure 5.7(a) depicts a diagram of the Gaussian intensity distribution where the energy intensity decreases from A to F with the radial distance. Hence, the morphology of the growth surface varies with the laser intensity.
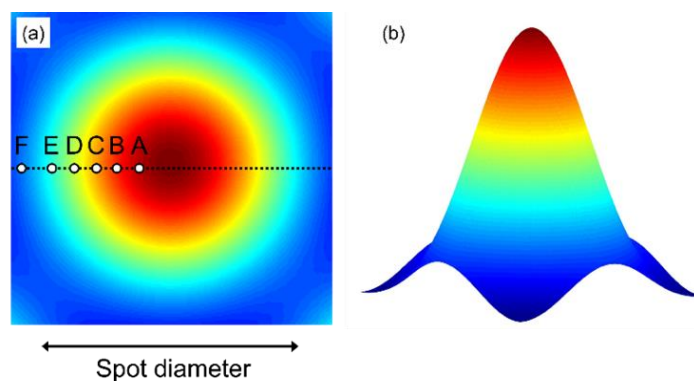
Figure 5.7 (a) 2-D and (b) 3-D illustrations of the Gaussian intensity distribution of the beam spot.

Figure 5.8 presents AFM micrographs of a GaAs (100) substrate with 1.55 ML InAs deposition in total. An output laser fluence of ~25 mJ/cm^2 and a polarisation angle of 58° were utilised. The evolution of the pattern from (a) to (f), corresponding to A to F as shown in Figure 5.7(a), represents the effect of laser intensity variations that is the consequence of a typical Gaussian beam profile. The profiles of the nanoislands as marked in dotted lines in (a-c) are shown in (g-i) respectively. Figure 5.8(a) shows the surface morphology with relatively high laser intensity, in which large star-shaped nanoisland arrays with a shallow pit of 0.7 ± 0.1 nm in depth in the centre are formed, which may be ascribed to an insufficient diffusion length of adatoms. The pattern agrees well with the modelled results shown in Figure 5.2, and according to the simulated temperature distribution, there is a temperature difference of over 100 °C on the GaAs surface. With the decrease of the laser intensity, quasi-square-shaped islands with a reduced central pit depth of 0.4 ± 0.1 nm are presented in Figure 5.8(b). And in (c) which has lower energy, the nanoislands are smaller without the central pit, typically 100-150 nm wide and 2-3 ML high.
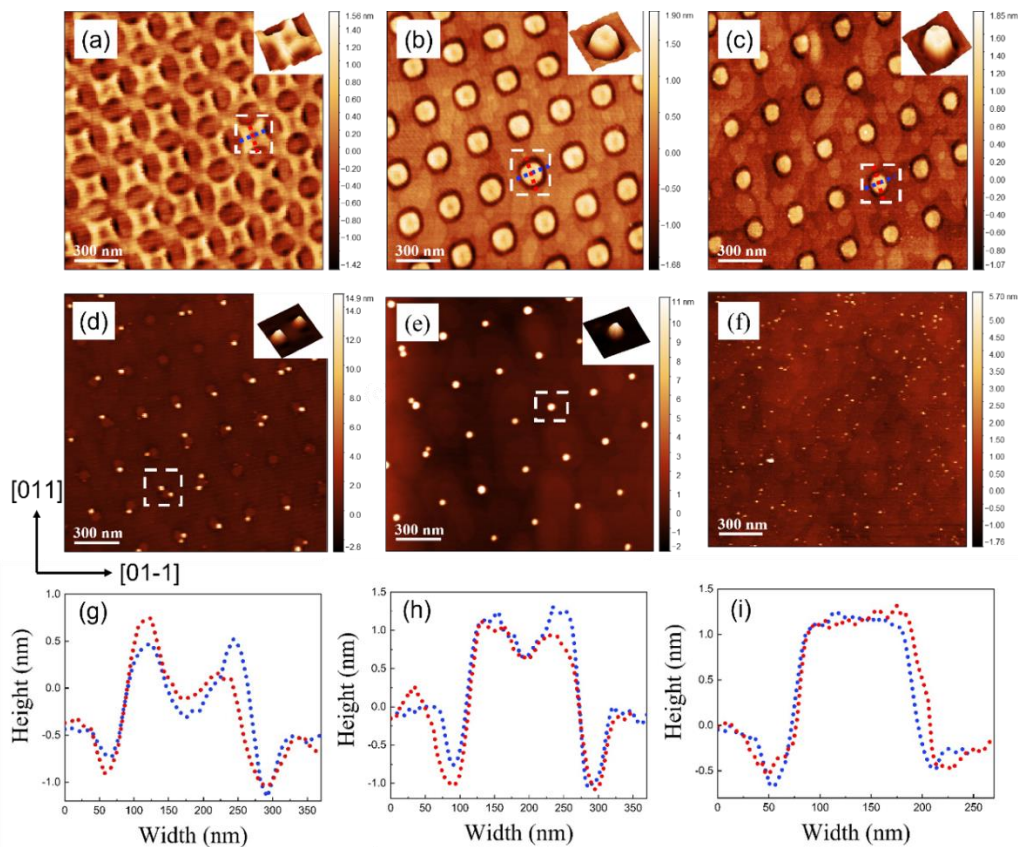
Figure 5.8 AFM micrographs (2 × 2 μm^2) of the evolution of surface morphologies as laser intensity decreases from (a) to (f). (g-i) show the corresponding line scan across the nanoislands as marked in (a-c) respectively.

Far away from the centre, the smallest island size is observed with a width of ~70 nm. It indicates that the size of the nanoisland is associated with the laser energy. As the energy reduces with the radial distance, the island size also reduces, which is attributed to the weaker thermal effect and therefore fewer surface adatoms can diffuse.

It is observed that there is no clear formation of QDs in the areas of (a-c), whereas in (d) QDs begin to nucleate at the edges of the nanoislands and some very small interstitial QDs were found between the island sites. As depicted in Figure 5.8(e), arrays of large single or pair dots with a width of 40-50 nm and height of 12-15 nm are formed, and the islands are then too small to see. Moreover, in the area between adjacent islands, there is no formation of small QDs. The growth of large QDs may be at the expense of materials from the nanoislands and the coalescence of small dots. Therefore, the probability of finding a dot is inversely proportional to the size of the nanoisland. Figure 5.8(f) shows the sample surface of random distributed InAs QDs far away from the pattern region. The small random QDs reach a density of 1×10^{10} cm^{-2} and exhibit a bimodal size distribution, indicating that the coverage of 1.55 ML in non-patterned areas is below the optimal value for a homogeneous distribution, however, the patterned QDs show a much lower QD density of $\sim 2 \times 10^9$ cm^{-2} and better size homogeneity. The results suggest that with small island size, more indium atoms can accumulate within a relatively concentrated area, giving rise to a high nucleation rate for QDs as the coverage of InAs can easily reach the critical amount for the transition from 2-D layers to 3-D dots. The existence of nanoislands lowers the critical thickness for QD formation since it promotes the surface migration of indium adatoms and enhances the nucleation rate.

Since small nanoislands are always formed at the edge of the beam overlap where the intensity is weaker, we usually reduce the laser fluence to around 12 mJ/cm^2 to produce small islands and thereby grow single QD arrays.

5.3.2.2 POLARISATION STATE

The variety of multi-beam interference patterns is strongly dependent upon the interfering beam parameters, including the incidence angle, azimuth, phase and polarisation [225][226]. Since the incidence and azimuth angles are fixed in our setup, the polarisation controlled nanopatterning for InAs QD growth was investigated in

this section. Figure 5.9(a) displays a periodic array of quasi-2-D nanoislands formed by *in situ* DLIP with the interfering beam polarisation angle of 90°, and (b) shows the magnified 3-D AFM micrograph of a single island. The line scan along nanoislands is presented in (c). The period of these nanoislands is reduced to ~200 nm due to the change of polarisation, which has been simulated in Chapter 4. Compared with the aforementioned polarisation state, these nanoislands are relatively larger in width (~150 nm) and lower in height (~2 ML). In addition, the formation of surface dips is not observed since the thermal effect is lowered in this case.
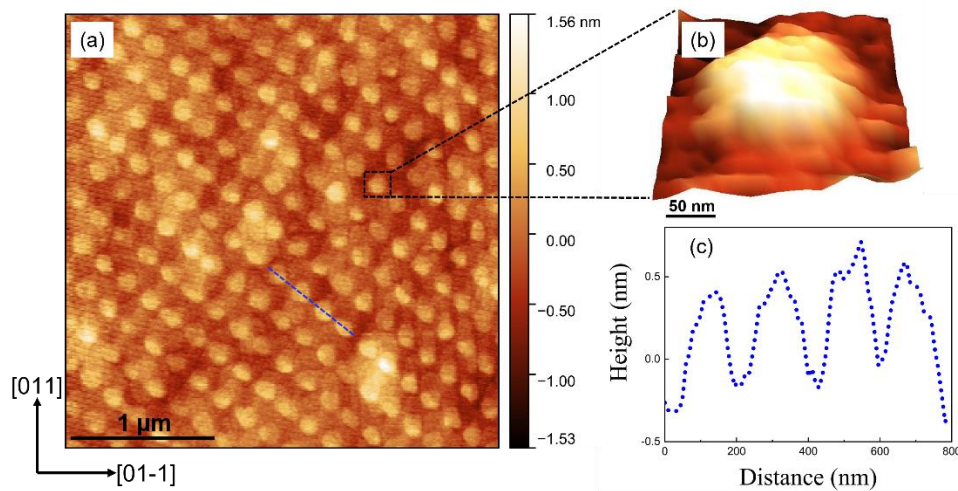
Figure 5.9 (a) 3 × 3 μm² AFM micrograph of a square array of quasi-2-D nanoislands with a period of 200 nm induced by *in situ* DLIP with the polarisation angle of 90°. (b) The magnified 3-D AFM image of a single nanoisland. (c) Line scan across four nanoislands as marked in (a).

Figure 5.10 compares the sample surface morphology of InAs QD formation in two different polarisation states, in which (a) and (e) show the QD nucleation on both nanoisland-structured surfaces. The difference is attributed to the variation in interference patterns. The interference pattern with the polarisation angle of 90° is a checkerboard-like pattern, and the size of the interference maxima and minima area are identical, resulting in an unconfined region where indium adatoms can accumulate. Furthermore, the 90° polarisation angle leads to higher reflection of the laser from the substrate than the 58° polarisation angle [198]. Thus, a reduced thermal effect and less diffusion are produced in this case. Figure 5.10(b) and (f) show the InAs QDs formed in both situations, in which the lack of good nucleation sites in the 90° polarisation state leads to a higher QD density of ~5 × 10⁹ cm⁻² and dispersed

distribution of dots with large size fluctuation from 4 to 16 nm in height. By contrast, highly ordered arrays of nearly single dots with a lower density of 1×10^9 cm^{-2} are obtained in (f). This exhibits better size uniformity and the QDs are typically 10-16 nm high. The QD occupancy and height statistic distribution of both cases are displayed in Figure 5.10(c, d, g, h), respectively.
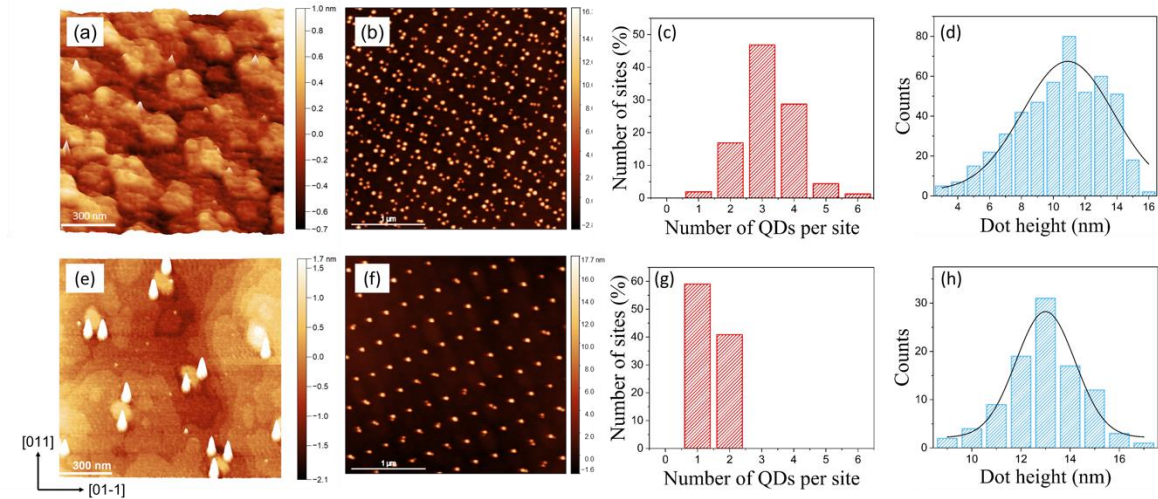
Figure 5.10 1×1 μm^2 AFM images of nanoislands formed by different polarisation angles (a) 90° and (e) 58°. (b, f) 3×3 μm^2 AFM images of InAs QDs on patterned surfaces corresponding to (a) and (e) respectively. Corresponding statistical distributions of (c, g) the QD occupation and (d, h) the QD height.

5.3.2.3 NUMBER OF INTERFERING BEAMS

The number of interfering laser beams can also determine the geometrical shape of the interference pattern. Two-beam interference results in a 1-D grating-like shape, and a number of 2-D patterns such as hexagons and ellipses can be created by three-beam interference, depending on the configuration arrangement of three beams. Figure 5.11 presents the effect of the number of interfering beams on the distribution of the patterned InAs QDs. The general features are similar to that observed for four-beam DLIP.
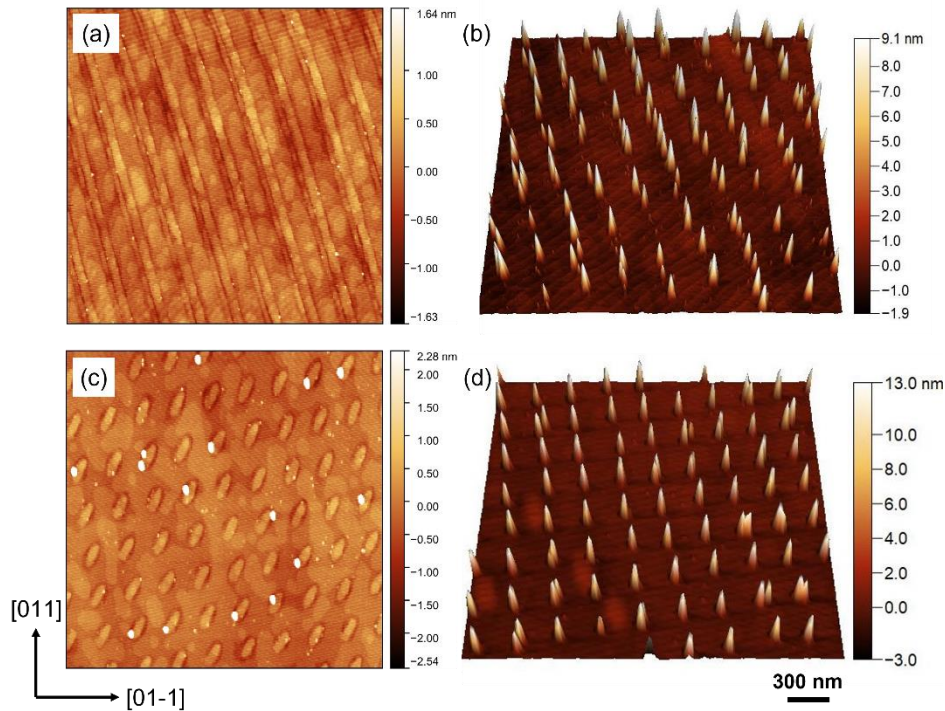
Figure 5.11 3 × 3 μm² AFM micrographs of periodic (a) 1-D gratings and (b) 1-D arrays of InAs QDs by 2-beam interference. (c) Arrays of elliptical nanoislands and (d) 2-D arrays of InAs QDs induced by 3-beam interference.

After 1 ML deposition of InAs, *in situ* DLIP was applied onto the growing surface, and the quasi line-like nanoislands (~2 ML high) were then formed by two-beam interference, and elliptical nanoisland arrays were produced by three-beam interference. By supplying further 0.6 ML InAs, QDs were grown on these island-templated surfaces. Figure 5.11(a) and (c) reveal the nucleation of a few QDs at the edge of nanoislands, and as the size of nanoislands reduces, arrays of QDs can be formed at the nanoisland sites, as depicted in Figure 5.11(b) and (d). However, the ordering of InAs QDs by 2-beam interference is not in good control, since the nucleation area for QDs is not confined, QDs can distribute more randomly on the surface. Also, this sample exhibits a QD density of ~4 × 10⁹ cm⁻² and a broad size distribution, in which ~12 nm high large dots and small dots with a height of ~3 nm were observed. In terms of 3-beam DLIP, a lower QD density can be seen of ~1.1 × 10⁹ cm⁻², and the dot size distribution is more uniform with a typical height of ~14 nm. This is owing to a higher nucleation rate at the edge of 2-D nanoisland arrays.

Compared with four-beam DLIP, the laser fluences used for two- and three-beam patterning need to be much higher, owing to a reduced intensity contrast. Moreover,

since the shape of the created nanoislands is elongated in a certain direction, the distribution of resulting QDs may be decentralised. However, the advantage of three-beam interference is that it does not produce the Moiré effect, therefore it shows potential to be applied to large-area patterning.

5.3.3 INFLUENCE OF THE GROWTH CONDITIONS ON INAS QD ORDERING

5.3.3.1 GROWTH TEMPERATURE

During the MBE growth, the length of adatom migration, the nucleation and thereby the growth of QDs are significantly different at different growth temperatures, giving rise to distinct surface morphologies and optical properties [153][154]. The influence of T_s on the formation of *in situ* patterned InAs QD arrays was explored. Figure 5.12 displays the surface morphologies of four samples with the same 1.6 ML InAs deposition thickness but at different temperatures.
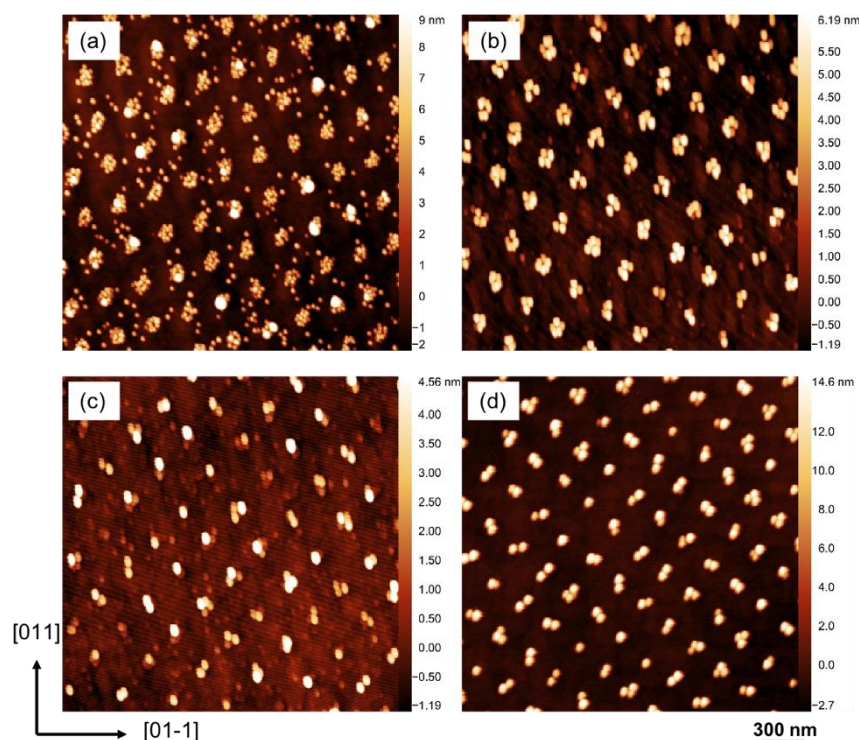
Figure 5.12 AFM micrographs of QD arrays grown with an InAs coverage of ~1.6 ML but at different substrate temperatures (a-d) T_s = 450 °C, 480 °C, 490 °C, and 500 °C.

At a low T_s of 450 °C, we can see that many small QDs around 6 nm high are nucleated at the nanoisland sites, meanwhile, big ~20 nm high clusters are also formed by reason

of the coalescence of small dots. As T_s increases to 480 °C, big clusters disappear, and the occupancy reduces to about 5 QDs per site. At 490 °C, it is clear to see the QD density decreases, and the nucleation of 1-3 QDs takes place at each site. However, these three samples exhibit large QD size fluctuations, and (b, c) also present very small QDs of a height of 1-2 nm grown on the planar surface. With the increase of T_s to 500 °C, the size uniformity is significantly improved and the size of QDs becomes larger (12-15 nm in height). Furthermore, the growth of interstitial QDs on the planar areas between sites is completely suppressed at a higher T_s. The InAs QD densities of four samples are 1.2×10^{10} cm^{-2}, 5.4×10^{9} cm^{-2}, 4.6×10^{9} cm^{-2} and 1.7×10^{9} cm^{-2} sequentially. Enhanced migration of indium adatoms at higher temperatures enables the assembly of atoms into one large dot instead of forming small new dots; therefore, a lower density of larger size QDs with better uniformity is obtained.

5.3.3.2 INAS COVERAGE

With different InAs deposition amounts, a noticeable influence of the coverage on the occupancy of QDs per site was observed. Figure 5.13 demonstrates the surface evolution of three samples in which InAs QDs are formed as InAs coverage increases from (a) 1.55 ML, (b) 1.65 ML to (c) 1.75 ML. At a subcritical InAs coverage (a), single or pair QD occupancy per site is dominant. The height of these single dots is in the range of 12-15 nm, and Figure 5.13(d) shows the 3-D AFM micrograph of an individual dot. By increasing the deposition amount of InAs to 1.65 ML (b), it clearly shows that 1-5 dots can be formed at each nanoisland site. A large fluctuation in the QD size and occupancy is observed in this sample, indicating that the InAs coverage is not the optimum value for the particular island geometry. However, some identical bi-QDMs can be seen. Figure 5.13(e) displays a typical bi-QDM consisting of two closely spaced QDs with identical dot width and height of ~50 nm and ~15 nm respectively, and with a separation between the two QDs equivalent to the nanoisland size of ~100 nm. With more deposition amounts of InAs (as seen in Figure 5.13(c)), QD occupancy can reach 6-8 dots per site. Since more indium adatoms can nucleate close to each other at the edge of the nanoislands, the density of dots is increased and QDMs which are almost symmetrically arranged around the islands can be formed. A typical symmetric hexa-QDM consisting of six QDs in a radial molecule is shown in Figure 5.13(f). The interdot distance of this molecule is greatly reduced, which makes strong coupling possible [229]. The individual QDs in this case are generally 40–50 nm in width and 12–15 nm

in height. In all three samples, the original quasi-2-D nanoislands are no longer visible, which probably results from consumption by the growth of the larger QDs.
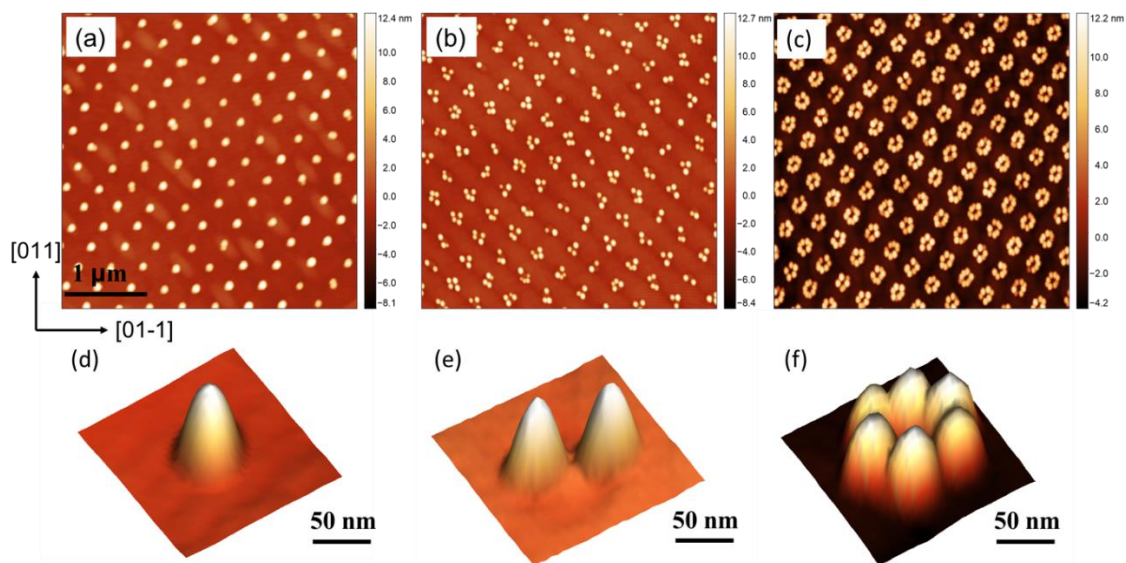
Figure 5.13 AFM micrographs of sample surface morphologies of total deposition of (a) 1.55 ML, (b) 1.65 ML, and (c) 1.75 ML InAs on the quasi-2-D nanoisland templated surfaces. (d)–(f) Corresponding 3-D AFM images of magnified single structures.

Therefore, the QD occupancy per site varies according to slightly different InAs amounts onto the initial nanoisland-templated surface. Figure 5.14(a-d) depicts the comparison of surface morphologies between different InAs coverages and non-DLIP patterned grown QDs. The corresponding statistics of the QD occupancy and QD height distribution are depicted in Figure 5.14(e-h). In Figure 5.14(a), the InAs coverage which is close to the critical thickness for 2-D to 3-D transition (~1.6 ML) results in the nucleation of one to three QDs per site, of which 75% are bi-molecules and 20% are single QDs. This shows a substantial increase in height and a narrower size distribution than that in the non-patterned case. As the total InAs coverage increases to 1.7 ML, tri-QDM and quad-QDM are formed also showing good size uniformity. The average height of these QDMs is around 15 nm. When the InAs amount is increased to 1.75 ML as shown in (c), the formation of penta- and hexa-QDMs with an average height of ~12 nm, and a QD density of ~4×10^9 cm^{-2}. In contrast, the non-patterned QDs have a relatively broader size distribution centred at ~8.5 nm and with a few large clusters formed by coalescence. These results are typical of what we would expect for random QDs using this (non-optimum) InAs deposition amount.

All the patterned InAs QDs grown have larger sizes and exhibit better homogeneity compared to the non-patterned QDs.
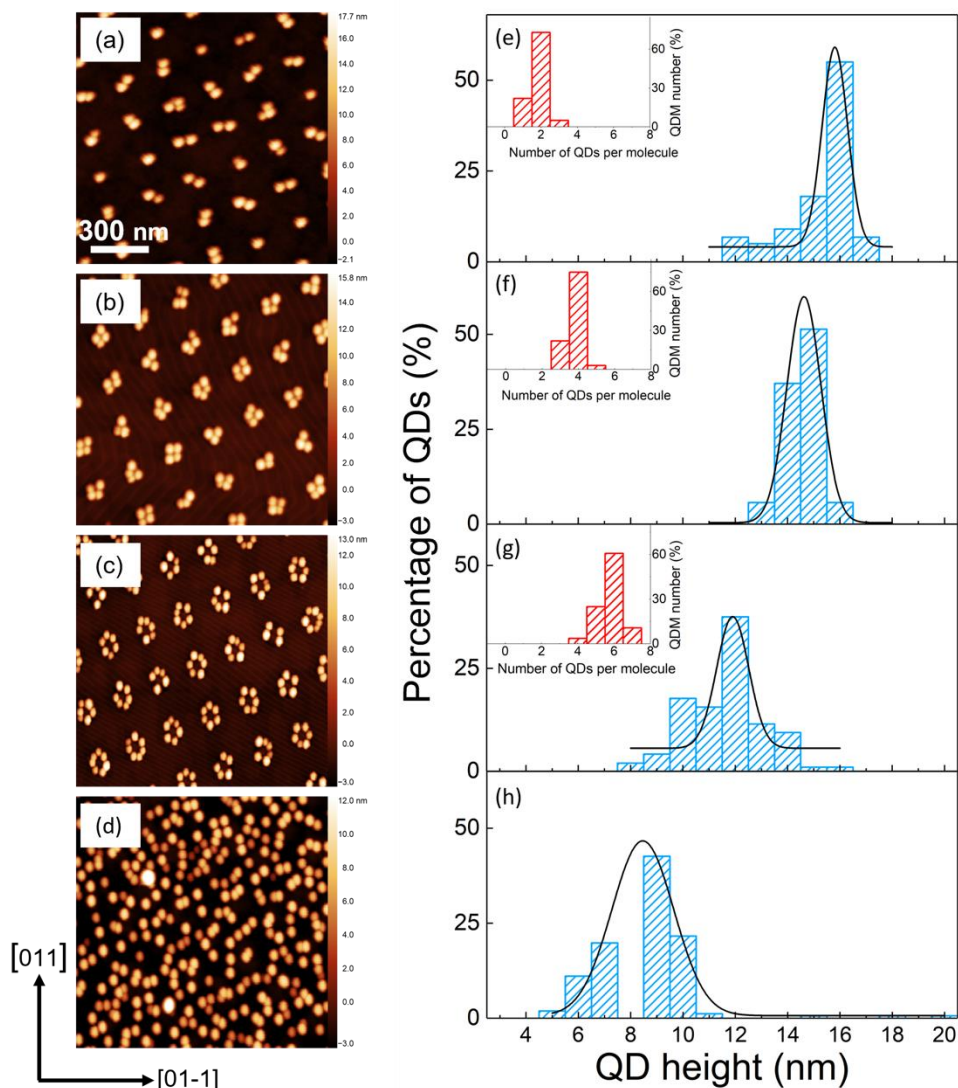
Figure 5.14. 2 × 2 μm² AFM images of sample surfaces with various InAs coverages (a) 1.6 ML, (b) 1.7 ML, and (c) 1.75 ML. (d) Non-DLIP patterned surface area with 1.75 ML InAs coverage. (e-h) Histograms of InAs QD height distribution corresponding to (a-d) respectively, and the insets show the corresponding QD occupancy per molecule.

In addition, the effect of anisotropic surface diffusion during the formation of these QDMs is not observed, which suggests that DLIP enables an almost symmetric diffusion for surface atoms. Hence, with the yield controlled by the InAs coverage, arrays of QDs and QDMs ranging from single dots, bi-, quad-, to hexa-QDMs or even more with improved size uniformity can be fabricated.

5.3.3.3 GROWTH RATE

A low GR is commonly employed in order to obtain better QD size homogeneity [105]. The impact of the GR on the DLIP-induced formation of InAs QDs was investigated in this section. Three QD samples were grown at the same T_s = 500 °C and InAs deposition thickness of 1.5 ML, but with different GRs (0.079 ML s^{-1}, 0.04 ML s^{-1}, and 0.026 ML s^{-1}). Figure 5.15(a-c) compares the surface morphologies of three samples, and the statistical distributions are depicted in Figure 5.15(d-f), respectively.
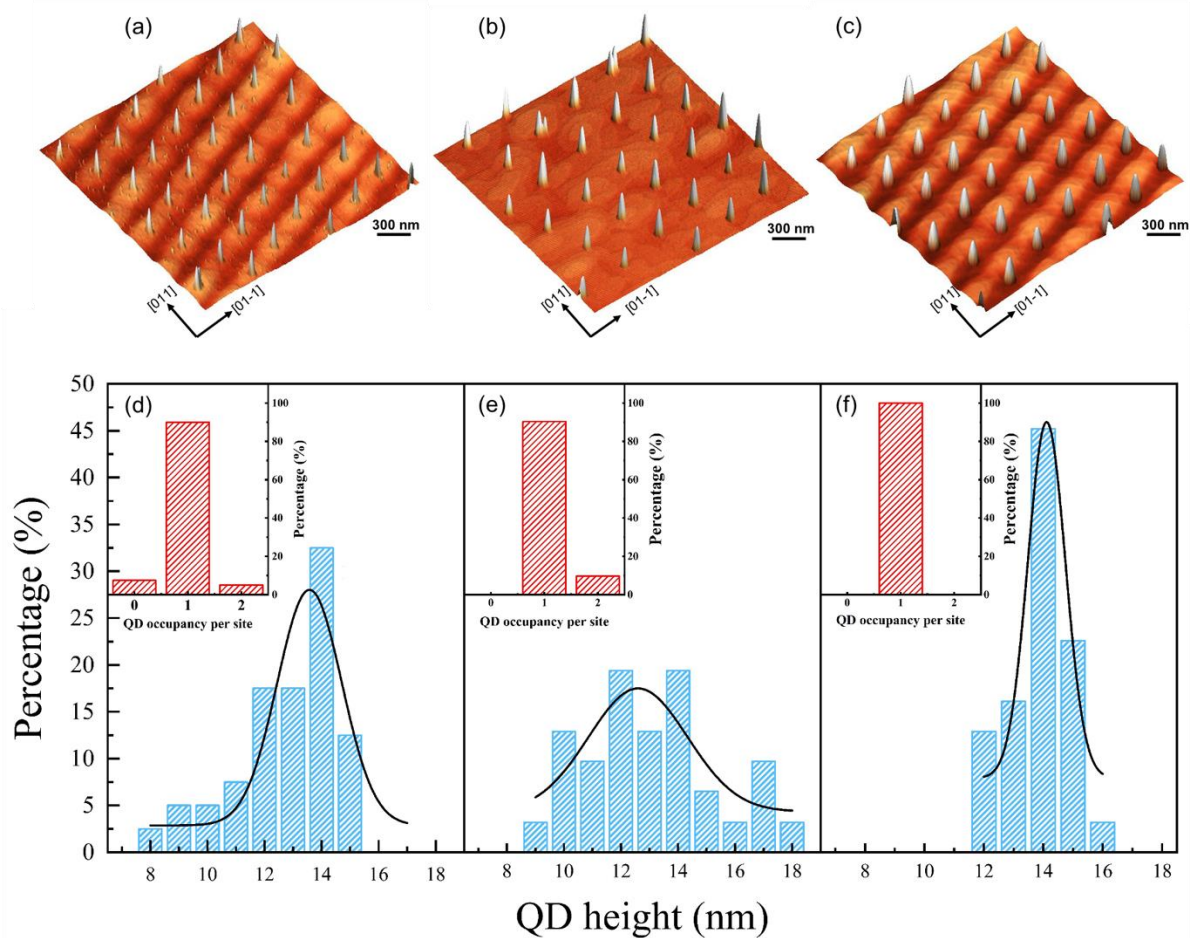
Figure 5.15 2 × 2 μm² 3-D AFM micrographs of *in situ* DLIP induced ordered arrays of InAs/GaAs QDs fabricated at different GRs (a-c) 0.079 ML s^{-1}, 0.04 ML s^{-1}, and 0.026 ML s^{-1}, respectively. (d-f) Corresponding QD height histograms. The insets display the dot occupancy per site.

As demonstrated in Figure 5.15(a, d) at a relatively higher GR of 0.079 ML s^{-1}, the sample exhibits a broad size distribution with both ~13 nm high ordered large QDs and many 1-2 nm high small QDs on the planar areas, of which the height histogram

of these small QDs is not shown in (d). Additionally, the QD occupancy per site ranges from 0 to 2, but almost 90% single dot occupancy was observed in this 2 × 2 μm^2 area. As revealed in Figure 5.15(b), the GR was reduced to 0.04 ML s^{-1}, leading to a clean surface without any interstitial small dots between the sites. In this case every island has been occupied by single or pairs of QDs, with single dot occupancy dominating (~90%). Nevertheless, the QD size distribution is broader in this case with the height ranging from 9 nm to 18 nm. In Figure 5.15(c) and (f), by further lowering the GR to 0.026 ML s^{-1}, excellent single QDs per site were achieved with heights from 12-16 nm centred at ~14 nm and exhibiting the best size homogeneity compared with the other two samples. It appears that after the DLIP process, InAs atoms need sufficient surface migration to obtain the uniform growth of individual QDs.

According to the results, it is clear to notice that a lower GR results in a larger QD size and better size homogeneity. This is attributed to different migration lengths of indium adatoms. The diffusion length of indium adatoms is longer at a lower GR, thereby atoms tend to incorporate into existing big dots instead of forming new nuclei [230]. Thus, by precisely controlling the InAs coverage just below the critical thickness and using a lower GR, precisely ordered arrays of single QDs with a narrow size distribution can be obtained.

5.3.3.4 DLIP-GROWTH SEQUENCE

Generally, *in situ* DLIP was applied after 1 ML deposition of InAs, however, if we apply the laser pulse earlier or later in the deposition cycle, qualitatively similar results were observed. Figure 5.16 compares the surface morphologies of four samples (A-D) deposited with the total InAs coverage of 1.5 ML and at a low GR of 0.026 ML s^{-1} on GaAs substrates, but with different DLIP-growth sequences. The QD height statistical distributions of samples A-D are depicted in Figure 5.17.
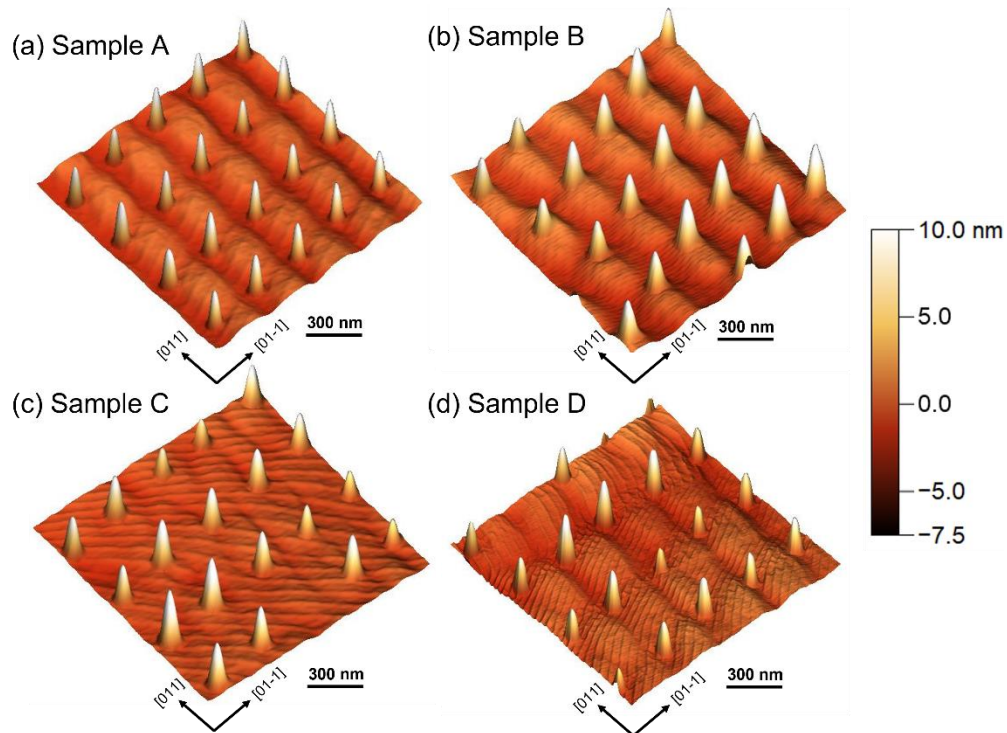
Figure 5.16 3-D AFM micrographs of the ordered InAs QD arrays of four samples with different DLIP-growth sequences (a) 0.5 ML InAs + DLIP +1.0 ML InAs, (b) 1.0 ML InAs + DLIP +0.5 ML InAs, (c) 1.2 ML InAs + DLIP +0.3 ML InAs, and (d) 1.5 ML InAs + DLIP.

For sample A (see (a)), DLIP was immediately applied after 0.5 ML deposition of InAs, and additional 1 ML InAs were supplied after the pulse. Figure 5.16(b) represents the sample B of introducing DLIP between 1 ML and 0.5 ML InAs. In terms of sample C, we applied DLIP after the growth of 1.2 ML InAs and further 0.3 ML InAs was deposited just after the single pulse. While for sample D, DLIP was applied after the total deposition of 1.5 ML InAs. It is clear that all four samples were capable of producing single QD arrays whenever DLIP was applied, albeit with different QD size fluctuations. Sample A exhibits the best size homogeneity, whereas large size inhomogeneity is shown in samples C and D. The single QDs of sample A owing to a low GR are relatively large in size with a height of ~14 nm on average. Dot heights ranging from 9 nm to 14 nm can be seen in sample B, while in samples C and D, smaller QDs with a height of 7 and 6 nm are observed. These results indicate that after the DLIP more indium atoms are needed for sufficient migration to each site to obtain the uniform growth of individual QDs.
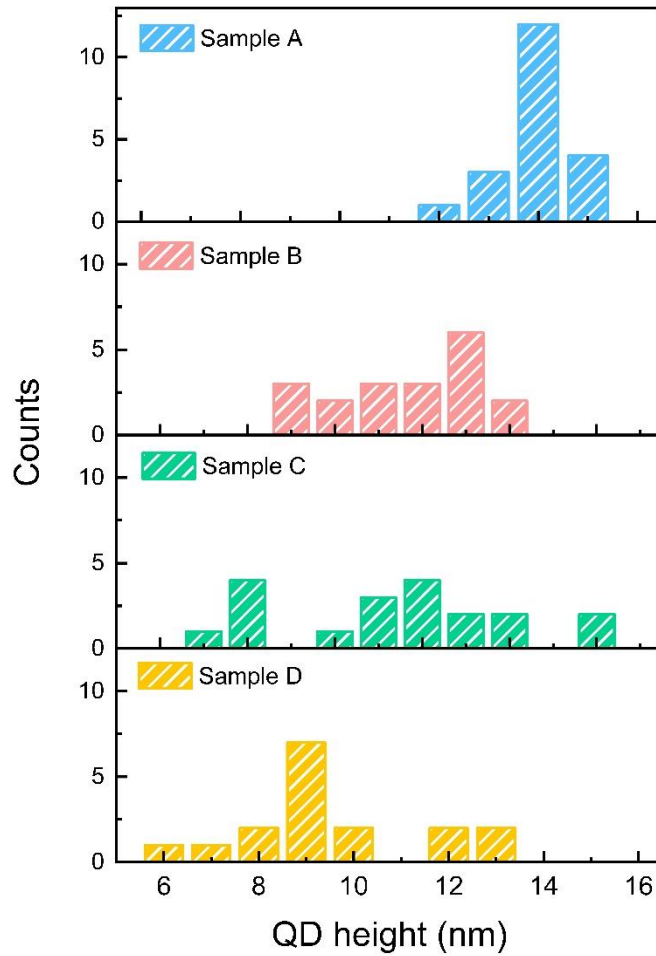
Figure 5.17 Histogram of QD height distributions for samples A-D.

In this section, precisely ordered arrays of both single InAs QDs and QDMs are obtained on nanoisland-structured GaAs (100) surfaces using *in situ* DLIP. The nanoisland array acts as preferential nucleation sites for QDs, resulting in site occupation that mainly depends on the size of the nanoisland and the InAs coverage. We assume that the formation of nanoislands is due to the surface migration of adatoms under the thermocapillary or chemicapillary effect, and we have observed small islands located in regions with low laser intensity. These observations are contrary to the work reported by Zhang *et al.* on *in situ* laser patterning for InAs QD growth [188], where they attributed the formation of nanoislands to the desorption of InGaAs WLs under laser irradiation and thus small nanoislands appeared in high laser intensity regions. In addition, in this dissertation, growth and DLIP conditions such as GR, coverage and polarisation have been optimised to achieve high quality single InAs QD arrays with good size homogeneity.

5.4 OPTICAL CHARACTERISATION

The optical quality of the patterned ordered arrays of InAs QDs assisted by *in situ* DLIP as displayed in Figure 5.16(a) was investigated by low-temperature ensemble-PL spectroscopy. The samples were mounted in a continuous flow cryostat cooled to around 88 K with liquid nitrogen. A 659 nm CW pump laser was focused through a 20× objective to a ~12 μm spot on the sample. The PL signal was spectrally resolved by a spectrometer and a liquid nitrogen cooled InGaAs detector. Figure 5.18 depicts the excitation power-dependent PL spectra of sample A at 88 K. Strong PL signals at the ground-state (GS), first excited-state (1ES), and second excited-state (2ES) emissions are clearly observed, where the peaks are at 1.05, 1.12 and 1.17 eV, accordingly. The inset of Figure 5.18 presents the logarithm plot of integrated PL (I_{PL}) intensity of the GS emission as a function of excitation power density (Pd). The fitting slope ($k = 0.95$) is close to unity (~1) at 88 K; according to the power law [231], the integrated PL intensity increases with the excitation power density, indicating that radiative recombination dominates the recombination process. These results are comparable to those reported results of high-quality self-assembled InAs QDs with a low GR [107]. A very narrow full width at half maximum (FWHM) of 22 meV for the GS peak is observed at low power, which is smaller than most values previously reported by using other nanopatterning technologies [127][139][232][233][234]. It appears that the size variation in these QDs is reasonably small, suggesting their good crystalline quality. This indicates that DLIP does not degrade the optical quality of the QDs, and this observation may enable the implementation of optically efficient quantum devices using this scheme.
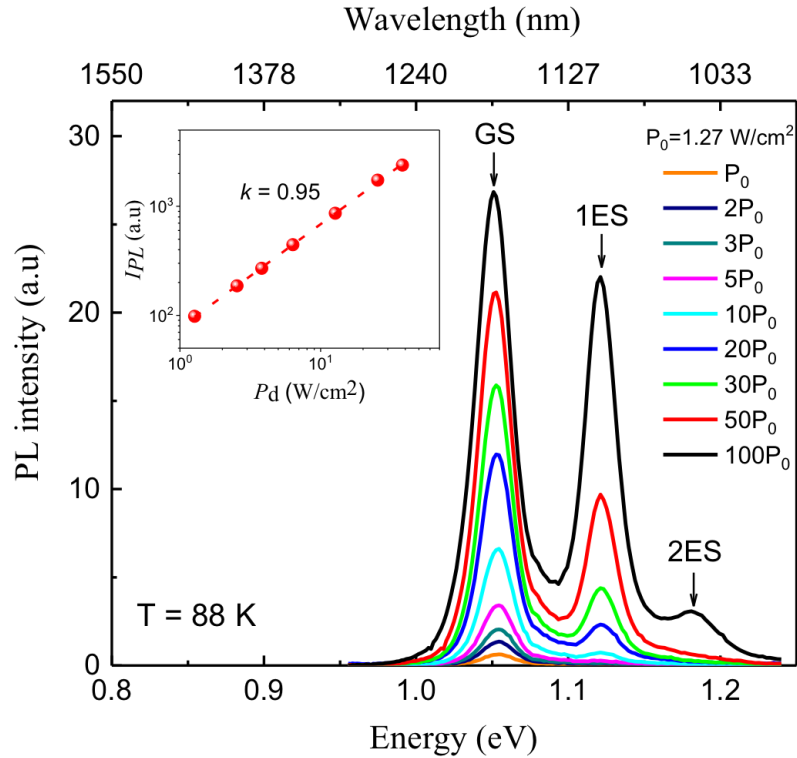
Figure 5.18. Excitation power-dependent PL spectra of an InAs QD array at 88 K. The inset shows the logarithm plot of I_{PL} as a function of Pd. The slope $k = 0.95$ reflects a linear dependence.

5.5 SUMMARY

Theoretical modelling and experimental results have been demonstrated in this chapter to explore the lateral ordering of InAs QD nanostructures on GaAs substrates during MBE growth. The modelling results, based on the study of atomic diffusion processes, suggest that DLIP is capable of inducing spatially ordered island nucleation, and thereby the ordering of the growing structures. Uniform arrays of ordered S-K InAs/GaAs QDs with a period of ~300 nm have been fabricated using *in situ* DLIP. Quasi-2-D regular arrays of nanoislands formed by DLIP act as preferential nucleation sites for InAs QDs and result in site occupation dependent on the DLIP and growth parameters, e.g., laser intensity, polarisation, DLIP-growth sequence, GR, coverage, and growth temperature. By optimising these conditions, QD and QDM arrays ranging from single QDs, bi-, quad-, up to hexa-QDMs are obtained. The PL spectra of the resulting single QD arrays show good optical quality and size uniformity.

CHAPTER *6*

GROWTH AND CHARACTERISATION OF ORDERED GAAS/ALGAAS QD STRUCTURES BY DROPLET EPITAXY

The ordering of lattice-matched GaAs QD/QR arrays on AlGaAs surfaces by DE growth in combination with *in situ* DLIP is investigated in this chapter. The description of the sample preparation procedure is shown in Section 6.1. The experimental results of fabricated GaAs QDs are presented in Section 6.2, in which the dependence of dot ordering on the deposition amount, growth temperature and arsenic flux will be discussed separately. Section 6.3 describes the optical analysis of the patterned GaAs/AlGaAs QD and QR arrays.

6.1 SAMPLE GROWTH

The samples were fabricated on 2-inch semi-insulating GaAs (100) wafers by DE using MBE. A 300 nm thick GaAs buffer and a 100 nm $Al_{0.3}Ga_{0.7}As$ barrier were grown at T_s = 630 °C on GaAs substrates after the oxide removal. Then, for the formation of Ga droplets, T_s was dropped to 100 °C and the arsenic valve was closed until the background pressure inside the chamber was decreased below 3×10^{-10} mbar. Subsequently, *in situ* single pulse DLIP with a laser fluence in the range of 40-50 mJ/cm^2 was introduced on the AlGaAs surface. After a growth interruption of 20 s, an amount equivalent to 2 ML Ga was supplied at a GR of 0.25 ML s^{-1} to form Ga droplets. These droplets were subsequently crystallised into GaAs nanocrystals under an As$_4$ flux at T_s = 200 °C for 5 min. For the PL measurement, the QDs were annealed at a T_s of 400 °C for 10 min under an As$_4$ flux to improve the crystalline quality and then covered with a 10 nm $Al_{0.3}Ga_{0.7}As$ capping layer which should be sufficient to planarize the surface and prevent the dissolution the GaAs DE quantum dots, otherwise at high temperatures these may transition to 2-D GaAs nanocrystals. After this initial low temperature capping, T_s was raised to a high temperature of 630 °C and

an additional 90 nm $Al_{0.3}Ga_{0.7}As$ barrier and a final 10 nm GaAs capping layer were grown. After the entire growth, thermal annealing of the entire structure was performed at $T_s = 750$ °C for 30 min with an arsenic flux to improve the optical quality. A schematic diagram of the grown capped GaAs/AlGaAs structures is demonstrated in Figure 6.1. The surface structural characterisation of the uncapped samples was undertaken by AFM.
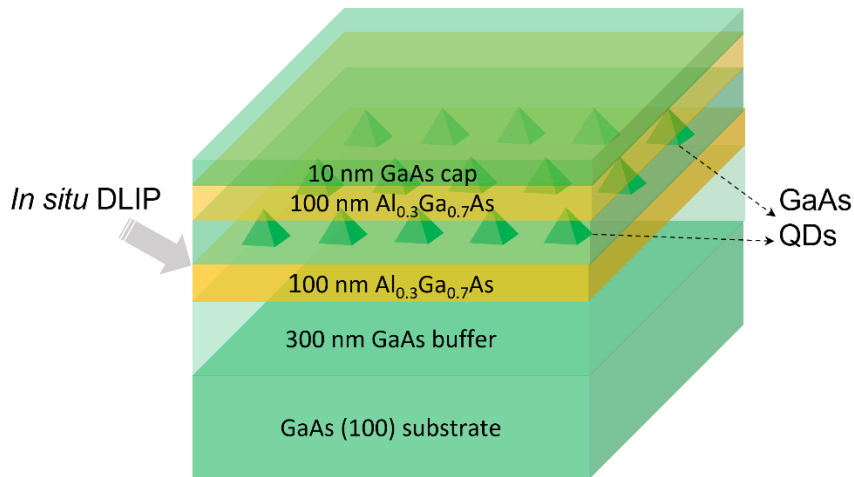
Figure 6.1 Graphic representation of grown capped GaAs/AlGaAs QDs.

6.2 RESULTS AND DISCUSSION

6.2.1 ORDERING OF GA DROPLET NUCLEATION ON ALGAAS SURFACES

In situ single pulse four-beam DLIP was applied to the sample surface once the lower 100 nm $Al_{0.3}Ga_{0.7}As$ barrier was grown with the objective to induce a spatial array of quasi-2-D nanoislands due to the thermocapillary effect. In the experimental observations, square arrays of nanoislands with a ~300 nm pitch were observed to form on the AlGaAs surface as shown in Figure 6.2(a) and (b), in which the size difference is owing to the variation of laser intensity. The nanoislands in (a) are larger where the laser intensity is higher, with a typical height of 1 nm, whilst the islands in (b) are relatively small where the laser intensity is lower, with a typical height of 0.5 nm. The smallest islands shown in Figure 6.2(b) are approximately 0.3 nm (~1 ML) high and 20 nm wide. By supplying Ga onto this surface, Ga metallic droplets were formed on or near the island sites. The formation of Ga droplets initiates only on Ga-rich surfaces. Figure 6.2(c) and (d) show the AFM micrographs of 2.5 ML Ga deposited onto the patterned surface, for which multiple droplets nucleate on relatively large

nanoislands, and single or pair of droplets can be formed on extremely small islands as displayed in Figure 6.2(b). In Figure 6.2(c), high density Ga droplets nucleate on the islands with an average occupancy of ~7 droplets per island site. These exhibit a relatively large size fluctuation ranging from 2-4 nm in height. For comparison, it is hard to observe the small islands in Figure 6.2(d), and 1 to 2 Ga droplet occupancy is achieved. The typical height of droplets in this case is ~4 nm and they show better size uniformity than that on larger islands. In both cases, the nucleation of Ga droplets on the planar area between the nanoislands is totally suppressed. The results indicate that excellent control of droplet nucleation can be obtained by introducing nanoisland sites on the surface, where the capillary-driven Ga diffusion is greatly enhanced by the presence of the nanoislands, and very small islands around 1-2 ML high are sufficient to drive preferential nucleation.
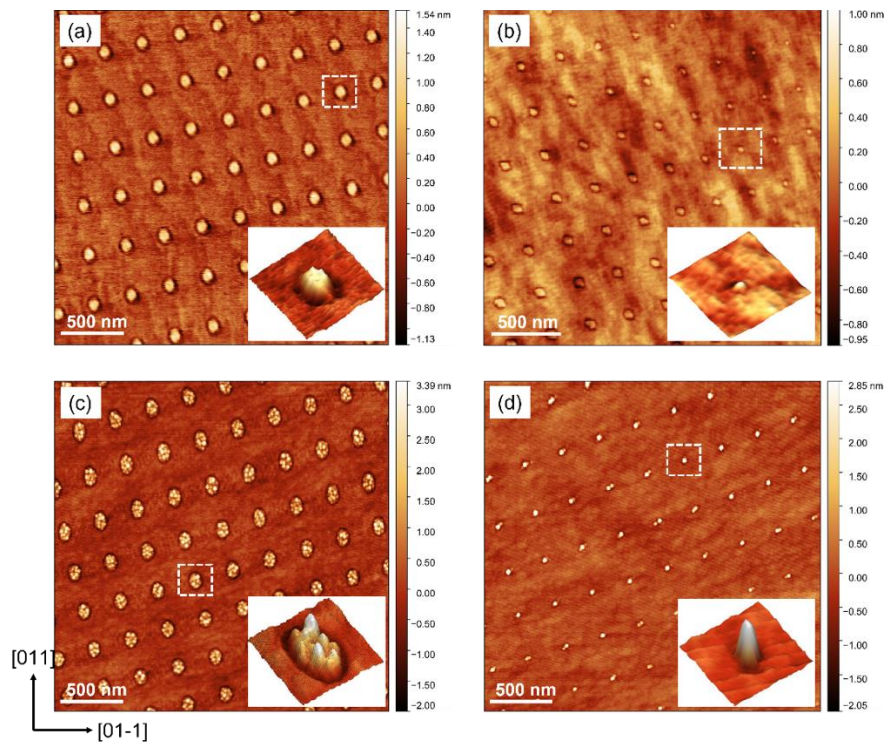
Figure 6.2 3 × 3 μm² AFM micrographs of (a, b) square arrays of nanoislands with different sizes on AlGaAs surface induced by *in situ* four-beam DLIP. (c) Multiple Ga droplets nucleate at large nanoislands. (d) Single Ga droplets nucleate at small nanoislands. The insets display the enlarged 3-D AFM images.

Our DE results exhibit qualitatively similar behaviour to the patterning of InAs/GaAs QDs in that the formation of nanoislands on the underlying planar surface by DLIP is critical for controlling the nucleation of QDs/droplets. DLIP is able to modify both

GaAs and AlGaAs surfaces, albeit with slightly higher laser energy for the AlGaAs case due to larger activation energy for diffusion and higher reflection coefficient of the laser light. Ga droplets are nucleated on the nanoislands as a result of enhanced Ga adatom diffusion towards the islands. Regarding the InAs/GaAs system, indium adatom diffusion on an arsenic terminated GaAs surface is responsible for dot nucleation. In this case, we must have an order of magnitude similar diffusion rates for Ga adatoms when unaccompanied by arsenic in order to form droplets in Ga-rich areas. Note that a very low arsenic system pressure is essential to achieve this. The droplet density and the occupancy are governed by the size of the nanoislands. Single droplets per site with good size homogeneity can be formed on small nanoislands produced using low laser energy.

6.2.2 FORMATION OF GAAS QDS

Ga droplets formed on the AlGaAs surface were subsequently crystallised into GaAs crystals under an arsenic flux. The position of GaAs QDs is predominantly dictated by the position of Ga droplets, which has been manifested by the formation of DLIP-induced nanoislands. Figure 6.3 presents the surface morphologies for 2 ML equivalent Ga droplets after the crystallisation and with a beam equivalent pressure (BEP) As_4 flux of ~2.4×10^{-4} mbar and $T_s = 200$ °C at the crystallisation stage.
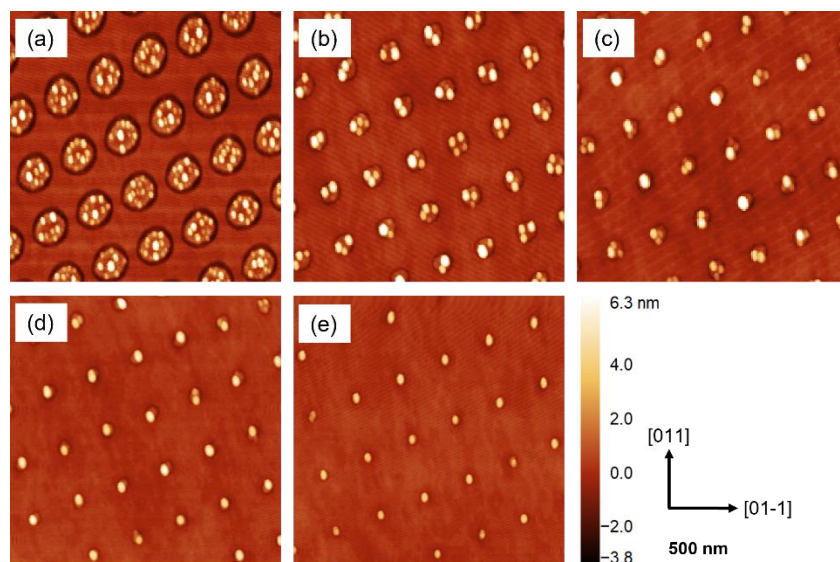
Figure 6.3 2×2 μm^2 AFM image of crystallised 2 ML GaAs QDs grown at nanoisland-templated surfaces with different diameters of nanoislands (a-e) 250, 150, 100, 80 and 50 nm accordingly.

It is observed that the surface density of the GaAs QDs is proportional to the size of nanoislands, which is comparable to that of initial Ga droplets. Many QDs (>10) were formed on larger nanoislands as shown in Figure 6.3(a), whereas with a reduction of nanoisland size from 250 nm to 50 nm (a-e), the QD occupancy per site also decreases. In Figure 6.3(e), we can observe a well-ordered array of single GaAs QDs on the surface.

Figure 6.4 reveals the statistics of these GaAs QDs. The dependence of the average dot occupancy and dot height on the diameter of nanoislands is shown in (a) and the dot height distribution of each case is displayed in (b-f) respectively. The dot occupancy on each site rises as the nanoisland size increases. Meanwhile, the dot enlarges with the increment in occupancy. Large nanoislands are able to accommodate many QDs (3-5 nm high), and due to the coalescence of these QDs, large dots or clusters can be formed with a height of ~10 nm. As the island size reduces to below 80 nm, which is comparable with the size of QDs, only one or two QDs with a dominant height of 4-5 nm were formed and this exhibits a relatively narrower height distribution. Large ~10 nm high QDs were not observed on small nanoislands. It appears that larger nanoislands can attract more Ga atoms to nucleate droplets and this effect weakens as the island size reduces. It is noted that there is no observation of QDs outside the pattern area, implying that the deposition of 2 ML Ga on the planar surface is insufficient for QD formation. However, in the laser-patterned region, the critical thickness seems to be locally reduced for droplet formation and thereby we achieve QD growth mainly on the pattern. This shows a slightly different behaviour compared with InAs/GaAs S-K grown QDs, where the formation of InAs QDs is facilitated at small nanoislands and is suppressed at large nanoislands. For the DE grown QDs, the Ga atoms appear relatively more mobile allowing a longer diffusion length and more effective nucleation at the nanoisland site.
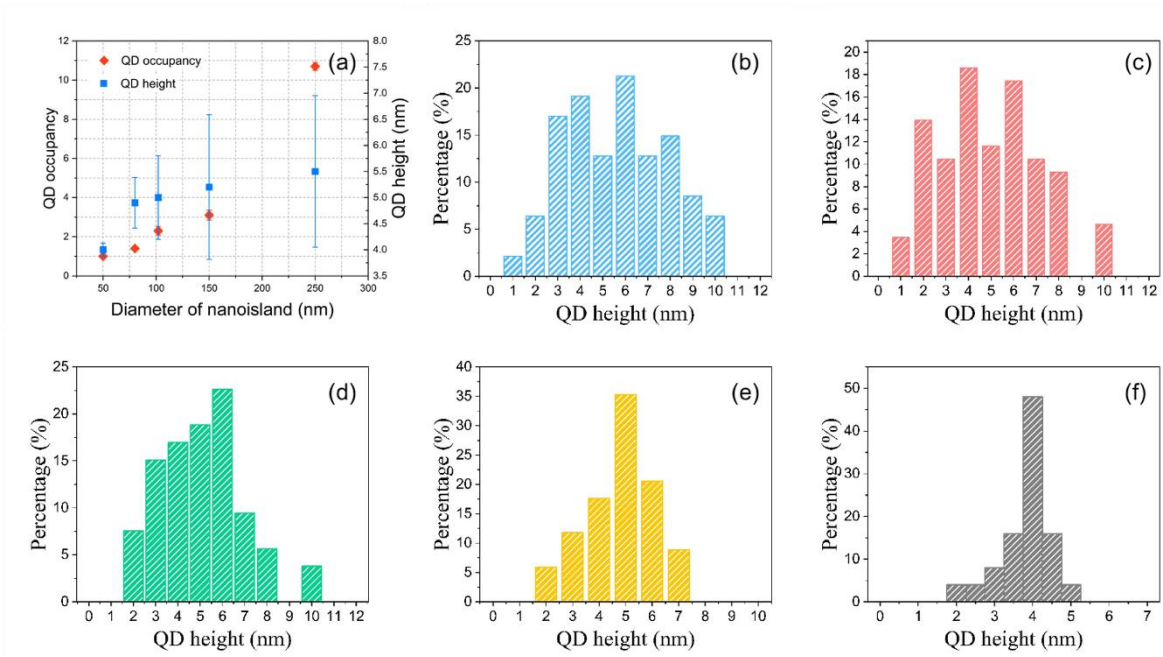
Figure 6.4 (a) Average QD occupancy per nanoisland and QD height in response to nanoisland diameter. (b-f) Histograms of QD height distribution with different diameters of nanoislands from 250, 150, 100, 80 to 50 nm accordingly.

6.2.3 INFLUENCE OF THE GROWTH CONDITIONS ON GaAs QD ORDERING

6.2.3.1 AMOUNT OF Ga DEPOSITION

Figure 6.5(a-d) displays the AFM micrographs of GaAs QDs with a Ga deposition T_s of 100 °C, a Ga GR of 0.25 ML s^{-1}, an As BEP of ~4.9 × 10^{-5} mbar and a temperature T_s of 200 °C for crystallisation, but with an increased amount of deposited Ga from (a-d) 1.85 ML, 2 ML, 2.25 ML to 2.75 ML accordingly. The relationship between the average QD height/density and the Ga amount is revealed in Figure 6.5(e). For the GaAs QDs shown in Figure 6.5(a), the average dot height is 2.14 nm and the QD density is low at ~8 × 10^8 cm^{-2}, but zero-occupancy of QDs on some nanoislands is observed. When supplying 2 ML Ga, Figure 6.5(b) shows that the average height and the density are slightly increased to 2.5 nm and ~1 × 10^9 cm^{-2}, respectively. In this case, every site is occupied by 1 or 2 QDs. The density increases to ~1.8 × 10^9 cm^{-2} as the Ga amount rises to 2.25 ML, and the mean QD height also increases to 3.2 nm. Attributed to the coalescence of small dots, some large QDs or clusters are formed. Although 1-3 QD occupancy is observed at each site, the spatial ordering is still very good. Nevertheless, when we increase the Ga amount to 2.75 ML, the average height and density of QDs

change to 3.5 nm and ~2.9×10^9 cm^{-2}, respectively. In addition, small QDs begin to form on the planar areas between the pattern sites, which suggests that the adatom density on the non-patterned area has reached the critical density for nucleation. The results show that the precise control of Ga deposition amount is critical to achieve good ordering and single QD occupancy. By reducing the amount of Ga, the coalescence of droplets can be suppressed. From the results, the optimum deposition amount of Ga for this DLIP-induced growth of a single GaAs QD array is around 2 ML equivalent at a Ga deposition T_s of 100 °C.
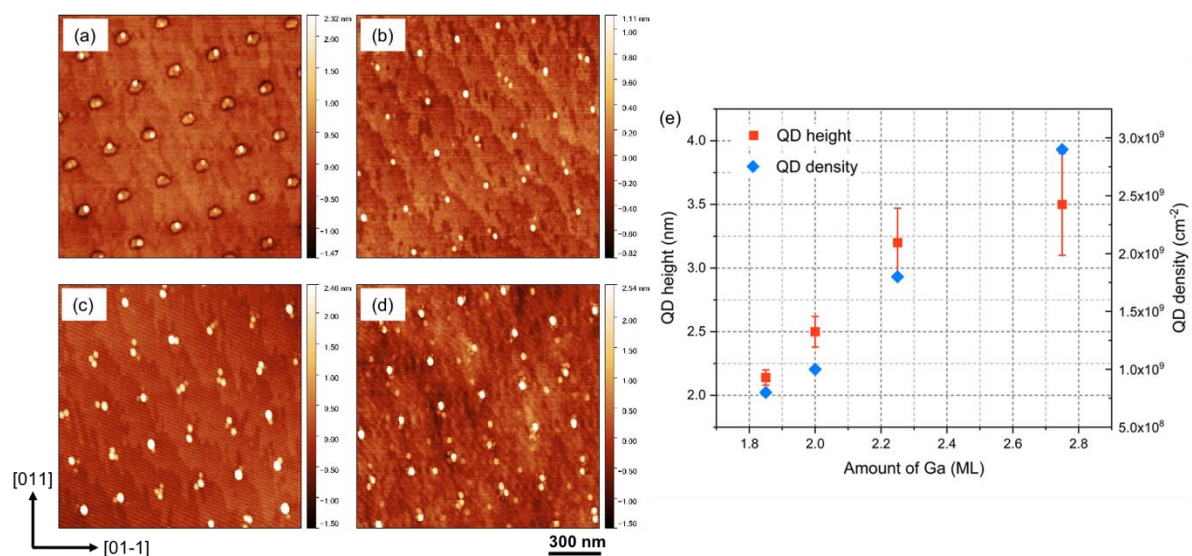
Figure 6.5 AFM micrographs of GaAs/AlGaAs QDs as the supplied amount of Ga increases (a-d) from 1.85 ML, 2 ML, 2.25 ML to 2.75 ML sequentially. (e) Graph of average QD height and density vs. amount of deposited Ga.

6.2.3.2 GROWTH TEMPERATURE

The formation of Ga droplets is contingent on the Ga adatom diffusion and the diffusion length is greatly associated with T_s. Generally, the areal density of QDs decreases with increasing T_s. By depositing Ga at different T_s, different morphologies of patterned GaAs QDs were obtained. Figure 6.6(a-c) depicts the AFM micrographs of patterned GaAs QDs with the identical 2 ML Ga deposition, As BEP of 2.4×10^{-4} mbar, and crystallisation temperature of 200 °C, but at different T_s during *in situ* DLIP and Ga droplet deposition: (a-c) 400 °C, 300 °C, and 100 °C accordingly. Figure 6.6(d-f) presents magnified 3-D images of single features in (a-c) respectively, and Figure 6.6(g-h) shows the corresponding cross-sectional profiles.
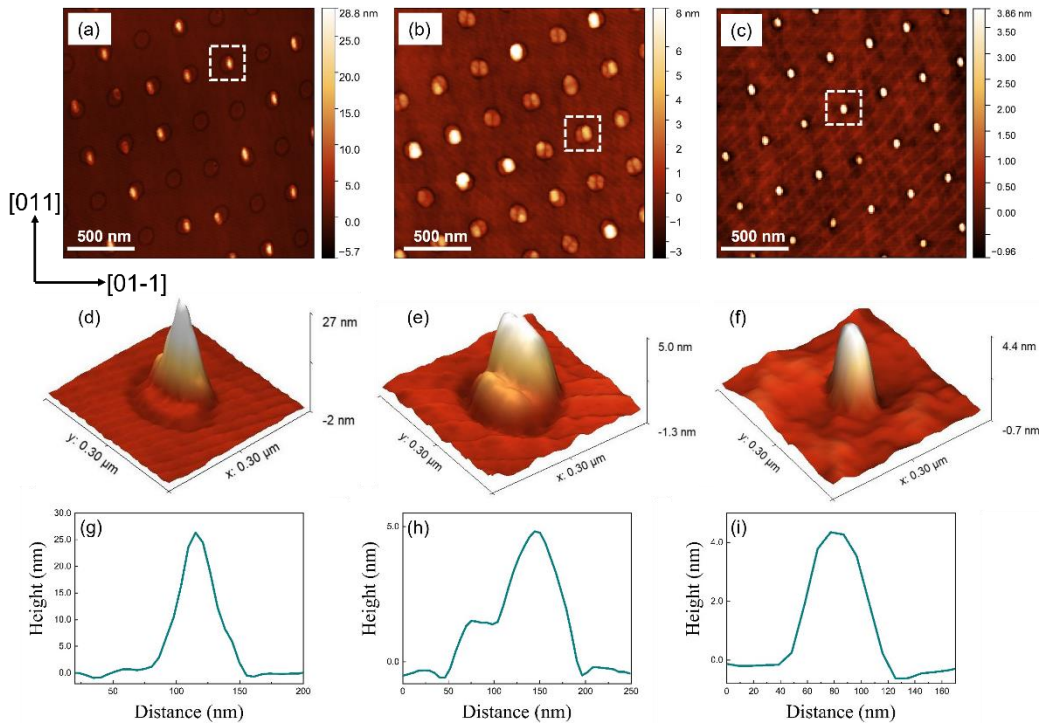
Figure 6.6 AFM micrographs of 2 ML GaAs QDs grown at different substrate temperatures during Ga droplet deposition: (a-c) T_s = 400 °C, 300 °C, and 100 °C sequentially. (d-f) The corresponding enlarged 3-D AFM images of single features as marked in (a-c) respectively. (g-i) Line scans of each QD feature.

For the GaAs QDs grown at a relatively higher T_s of 400 °C, as shown in (a), the surface density of QDs is the lowest, with single dot occupancy at some nanoisland sites but also many empty sites. Additionally, relatively large elongated QDs were formed, with a dot height ranging from 8 to 25 nm, which is on account of the enhanced migration of Ga at high temperatures and anisotropic diffusion along different orientations. Strong coalescence occurs resulting in the formation of large clusters and ascribed to the small amount of 2 ML Ga deposition, and it is not enough to obtain single QD occupancy at each site. It is noted that in addition to the formation of large QDs, we also observed small rings about 2 nm high on some islands with a 1-2 nm deep etched hole in the centre. The formation of ring structures is attributed to the dissolution of As atoms from the substrate into the droplet during and after the Ga deposition, and then crystallisation of Ga at the droplet edge [235]. The diameter of the ring is related to the original droplet size. Owing to a low T_s and no annealing process, the central nanohole is much shallower than that of other reported works using local droplet etching (over 500 °C)[236][237]. When T_s is decreased to 300 °C as revealed in Figure 6.6(b), the dot height is greatly reduced, to around ~4 nm for small

QDs and ~10 nm for big QDs, and these QDs are roughly evenly distributed on each nanoisland. Also, 1 or 2 QDs per site were obtained. By contrast, at a T_s of 100 °C, as presented in Figure 6.6(c), the height of QDs continues to decrease to 3-4 nm and shows better size homogeneity. At lower temperatures, the migration length of Ga adatoms is shorter, enabling more uniform surface diffusion and nucleation rate at each site, thus, 100% single QD occupancy per site was observed in the 2×2 μm^2 areas. In order to fabricate well-ordered arrays of single GaAs QDs with good size uniformity, a low T_s during Ga droplet deposition appears of great importance.

6.2.3.3 ARSENIC FLUX

The As flux during the crystallisation is of critical importance in controlling the shape of QD structures grown using DE method. As well as QDs, it has been demonstrated that it is possible to fabricate single QRs or NRs, double QRs or even multiple rings by carefully tuning the As flux intensity during the droplet crystallisation [118][235]. Figure 6.7 reveals the AFM micrographs of four GaAs QD sample surfaces with the same 2 ML equivalent Ga deposition at 100 °C and subsequently crystallised by As_4 without annealing, but with different crystallisation temperatures of (a) 200 °C, (b-d) 400 °C and reducing As BEPs: (a) 2.4×10^{-4} mbar, (b) 1×10^{-4} mbar, (c) 2.3×10^{-5} mbar and (d) 1.4×10^{-6} mbar. In terms of a higher As BEP as shown in Figure 6.7(a), an array of ~4 nm high single GaAs QDs with a typical base of ~80 nm was formed. The dot-like shape is comparable with that of the original Ga droplet. When the As BEP was decreased to 1×10^{-4} mbar, the shape of GaAs nanostructures was transformed to elongated rings, in which two QDs were laterally coupled, as displayed in Figure 6.7(b). These asymmetric rings have a height of around 2-3 nm and with a ~70 nm separation. With a further decrease in As BEP, these asymmetric GaAs QRs were transformed to symmetric QRs which contain quasi-2-D disks in their outer region as shown in Figure 6.7(c). The ring disks are 300 nm wide and 1 ML high on average, and the inner rings are ~1 nm high and with a width of ~80 nm approximately. The base size of the inner rings is similar to that of the QDs shown in Figure 6.7(a), which corresponds to the size of the original Ga droplets. At an even lower As BEP of 1.4×10^{-6} mbar as displayed in Figure 6.7(d), symmetric QRs without disks were formed. The size of these rings is similar to that of inner rings in (c), which is associated with the original droplet size. The enlarged AFM images of each representative structure are shown in Figure 6.7(e-h), and the corresponding cross-sectional profiles along the

directions marked as red and blue lines are presented in Figure 6.7(i-l), respectively. It is noticed that the height of GaAs structures also decreases with the reduction in As flux BEP.
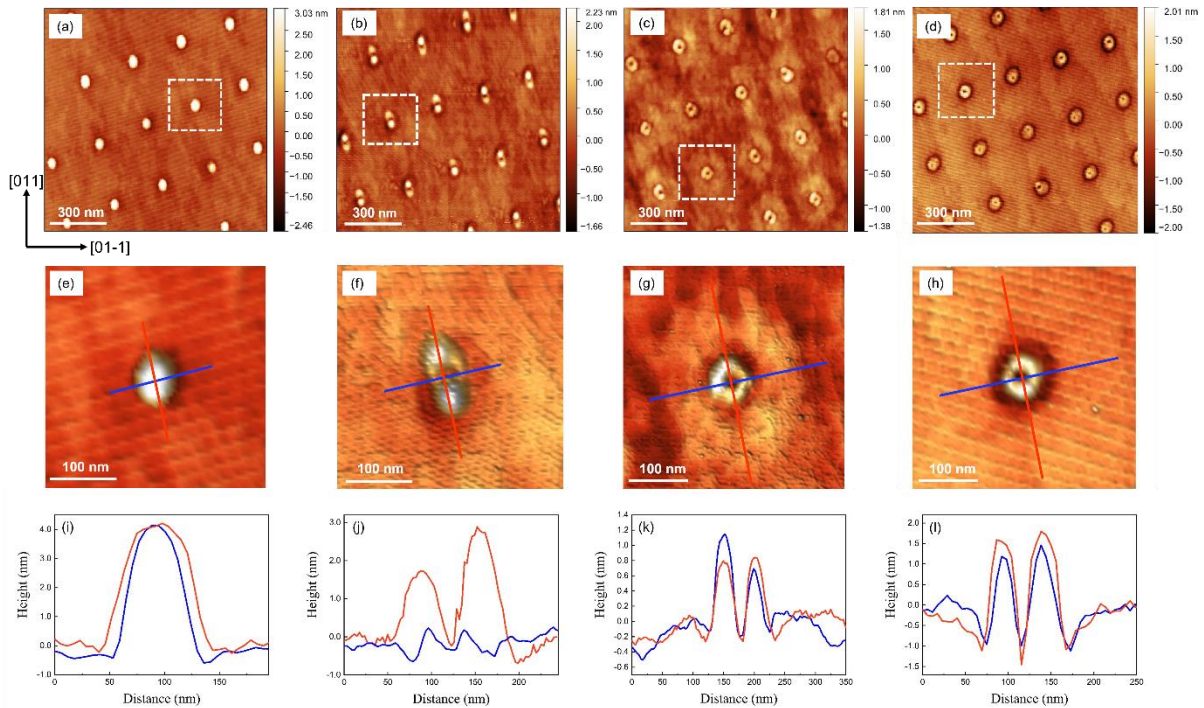
Figure 6.7 AFM micrographs of 2 ML GaAs QD nanostructure arrays grown at different T_s and As BEPs for crystallisation of (a) T_s = 200 °C, BEP = 2.4 × 10^{-4} mbar, (b) T_s = 400 °C, BEP = 1 × 10^{-4} mbar, (c) T_s = 400 °C, BEP = 2.3 × 10^{-5} mbar, and (d) T_s = 400 °C, BEP = 1.4 × 10^{-6} mbar. (e-h) The corresponding enlarged AFM images of single QD structures as marked in (a-d) respectively. (i-l) Line scans of each QD structure.

The shape evolution of GaAs nanostructures is ascribed to the competition of different incorporation procedures during the As flux irradiation [114][235][238]. It was reported that the inner QR structure is already formed at the edge of the droplet just after Ga droplet formation, due to residual As atoms from the underlying substrate or the chamber [235]. These As atoms can become dissolved beneath the droplets and then diffuse to the droplet edge driven by an internal convection flux. Thus, the size of inner rings is consistent with that of the original Ga droplets. The final shape of the GaAs nanostructures is governed by the counter-diffusion process of Ga atom diffusion from the droplets and As atom diffusion towards the droplets. When an arsenic impinging flux is supplied onto the surface, atoms from the droplets are able to diffuse towards the As-stabilised surfaces and result in crystallisation at a relatively

large distance from the Ga droplets. Through such a mechanism the outer disks can be formed. The diameter of the outer disk is controlled by the Ga diffusion length. By either increasing the T_s or reducing the As BEP, it is possible to increase the diameter of the outer disk. 2-D growth of GaAs thin layers is expected in the case of an extremely low arsenic flux. Generally, resulting from the shape of the Ga droplet, the nanostructure formed at a low As BEP is reasonably isotropic. At a relatively high As BEP, elongated structures can be formed by virtue of the anisotropic diffusion length of Ga atoms. With a further increase in the As flux intensity, the Ga diffusion is restrained whilst crystallisation is favoured, which enhances the 3-D QD growth.

6.3 OPTICAL CHARACTERISATION

After the optimisation of growth conditions, ordered arrays of single GaAs QDs can be produced with a relatively narrow size distribution at $T_s = 100\,°C$ during the droplet deposition, a Ga amount of 2 ML, $T_s = 200\,°C$ during crystallisation, and ~$2.4 × 10^{-4}$ mbar As BEP. A 3-D AFM micrograph is depicted in Figure 6.8(a) and the dot height histogram is presented in (b). Areas of the wafer outside of the laser spot do not show the formation of QDs and instead only 2-D monolayer GaAs terraces appear.
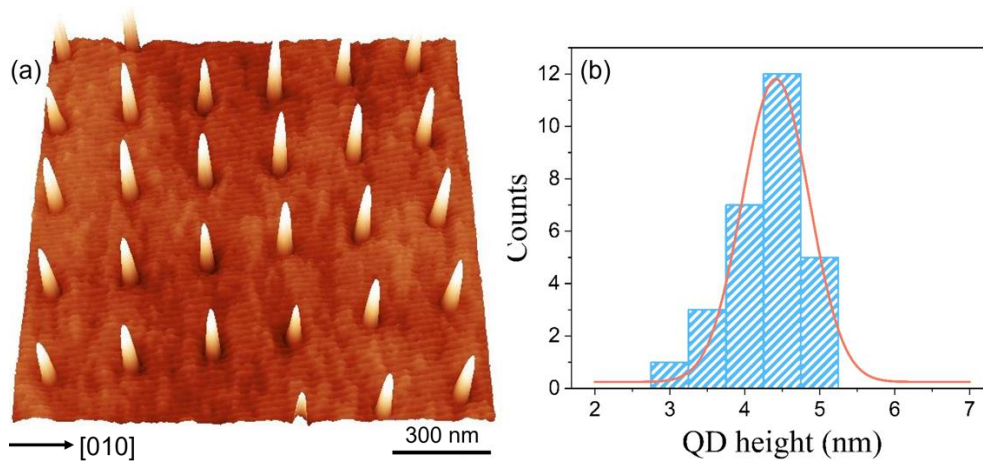
Figure 6.8 (a) 3-D AFM micrographs of the patterned array of single GaAs QDs on the AlGaAs surface with a period of 300 nm. (b) Corresponding QD height histogram.

The PL measurement of the samples was carried out at a closed cycle cryostat and excited utilising a 594 nm laser, and a 100× objective was used to collect the PL. The laser spot size in these conditions was 2-3 µm. The actual sample temperature was measured at around 60 K derived from the GaAs emission. Figure 6.9(a) manifests the

PL spectrum of the emission from an ensemble of patterned GaAs QD array at low excitation power and (b) depicts the normalised excitation-power-dependent PL spectra with an increment of excitation power from 10 µW to 10 mW.
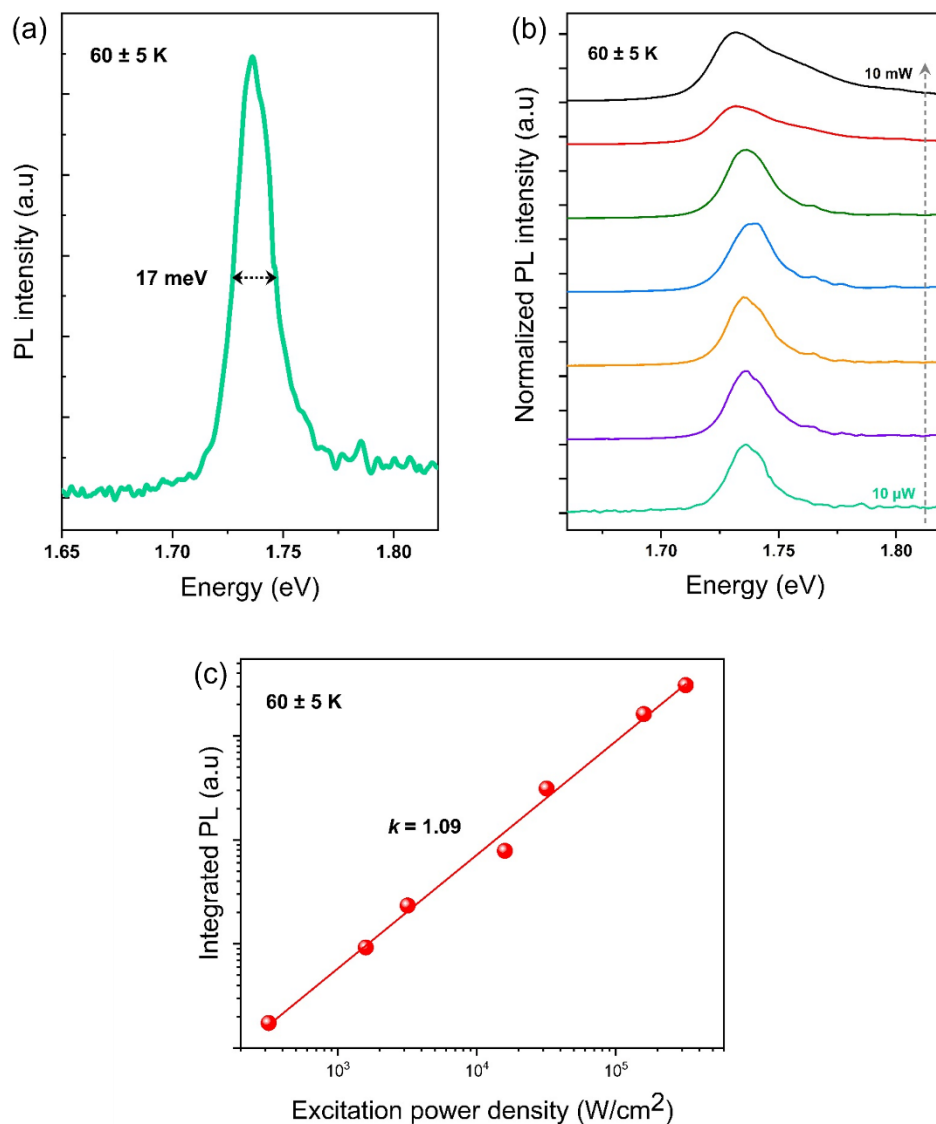
Figure 6.9 (a) Ensemble-PL spectrum of ordered arrays of GaAs QDs with low excitation power at 60 ± 5 K. (b) Normalised excitation power-dependent PL spectra. (c) Integrated PL intensity depending upon the excitation power density at 60 K. The solid line defines the slope $k = 1.09$.

A 1.74 eV PL emission peak with a record narrow FWHM of approximately 17 meV was observed at low excitation power. At relatively low excitation power, there is no considerable alteration in the shape of the spectrum or shift of the peak energy. The

PL peak was slightly red shifted by 5 meV at higher excitation power of 5-10 mW, which may be due to the local heating. The separation of the ground and excited states in this QD system is too small to be resolved, with only 15 meV calculated by Nextnano software. Figure 6.9(c) presents the integrated PL intensity of the patterned GaAs QDs as a function of the excitation power density at 60 K. The slope $k \approx 1$ reveals a linear dependence, suggesting excitonic recombination is dominant.

Figure 6.10 exhibits the PL spectrum of the patterned arrays of GaAs QRs displayed in Figure 6.7(c), regarding the low excitation power of 10 μW, the PL peak emission was at 1.78 eV, and the FWHM was approximately 41 meV. Compared with the GaAs QDs, QRs have a smaller dot size of ~1 nm in height, giving rise to larger emission energy, and the relatively broader linewidth results from greater size inhomogeneity.
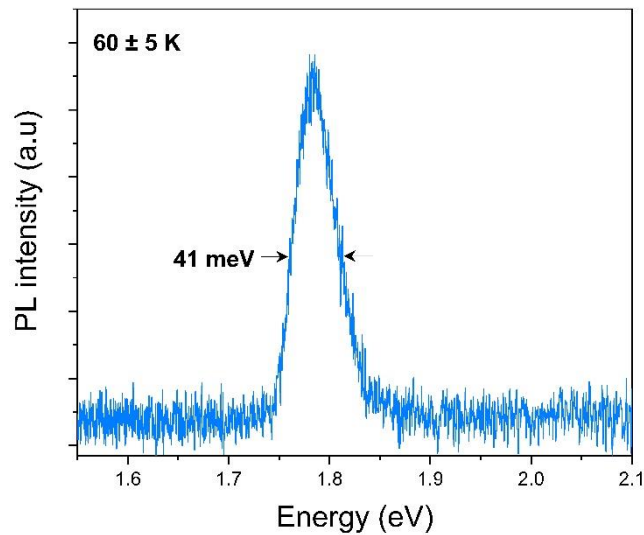
Figure 6.10 PL spectrum of patterned GaAs QRs at 60 K with the excitation power of 10 μW.

6.4 SUMMARY

This chapter demonstrates the fabrication of ordered arrays of GaAs/AlGaAs QDs and QRs by combining DE with *in situ* DLIP. Regular arrays of Ga droplets with a period of 300 nm are initially formed on nanoisland-templated AlGaAs surfaces. At an optimised deposition amount of 2 ML equivalent Ga, we are able to form Ga droplets on the patterned area, but not on the planar area. After crystallisation under an arsenic flux, dense ordered arrays of GaAs QDs with good uniformity are obtained. Various

shapes, sizes and densities of GaAs QD structures can be produced under different growth conditions. The Ga deposition and the arsenic crystallisation conditions are of critical importance. By optimising the growth temperature, Ga deposition amount and As BEP, ordered arrays of single GaAs QDs and QRs are formed. A record-narrow PL linewidth of 17 meV from the patterned GaAs QD arrays at 60 K has been achieved.

CHAPTER 7

IN SITU DLIP OF OTHER SEMICONDUCTOR MATERIALS AND SYSTEMS

In this chapter, *in situ* DLIP has been successfully applied to other semiconductor materials for the production of ordered arrays of nanostructures. Si is the most extensively utilised material in the semiconductor industry, particularly for omnipresent CMOS technology. In addition, Si periodic surface nanostructures have shown excellent properties such as light trapping and antireflection [220][221]. However, the major limitation of Si material is the indirect band gap, which results in low light emission efficiency. The monolithic integration of III-V devices on Si-based platforms has aroused tremendous technical and economic interest with respect to the future implementation of high-performance electronic and photonic devices. Nevertheless, the effective heteroepitaxial growth of III-V materials directly onto Si substrates still remains difficult after many years of study owing to material defects that arise from the large thermal and lattice mismatch [241][242]. It will be of considerable interest to explore the lateral ordering of III-V/Si nanostructures by *in situ* DLIP, which may serve as a potential platform for future SAG of III-V materials on silicon substrates.

There has also been a growing interest in type-II QDs due to their band alignment and attractive characteristics in comparison to type-I QDs, such as longer carrier lifetime and lower recombination rate [243][244]. In particular, type-II GaSb/GaAs QDs [245] are interesting in terms of a large valence band offset, which leads to highly confined holes, whilst there is only weak electron confinement on account of Coulomb attraction. Such structures could be promising candidates for applications such as memory devices [246][247]. In order to achieve precise device function, the fabrication of precisely ordered GaSb QDs with good size uniformity is an essential requirement. S-K growth is the common way to grow GaSb QDs on GaAs substrates by virtue of

the large lattice mismatch of 7.8% between GaAs and GaSb. However, so far, the realisation of the lateral ordering of GaSb/GaAs QDs has not been reported.

In this chapter, Section 7.1 describes the nanopatterning of Si substrates and the initial results of heteroepitaxial growth of GaAs nanocrystals on *in situ* DLIP-induced Si substrates. The growth and characterisation of ordered arrays of GaSb QDs on GaAs substrates by *in situ* DLIP are demonstrated in Section 7.2.

7.1 GROWTH OF GaAs/Si NANOSTRUCTURES

7.1.1 SAMPLE GROWTH

The samples were fabricated on 2-inch Si (100) or Si (111) substrates by MBE. The substrates were loaded directly with no prior chemical cleaning or deoxidation, due to the lack of facilities for HF etching. Initially, the surface oxide removal was conducted *in situ* through Ga-assisted deoxidation [129] at T_s = 800 °C for 20 min. After that, T_s was reduced to ~600 °C and *in situ* single pulse four-beam DLIP was applied to the sample surface with the pulse energy of ~60 mJ. Subsequently, Ga was deposited at a GR of 1 Å/s without arsenic to form Ga droplets, and then these Ga droplets were crystallised into GaAs nanocrystals under arsenic supply at T_s = 400 °C for 2 min. The DE process is therefore similar to that used for GaAs substrates. The surface morphologies of the samples were characterised by AFM and SEM.

7.1.2 STRUCTURAL CHARACTERISATION

Figure 7.1 presents the surface morphology of the Si (100) substrate after single pulse DLIP with relatively high pulse energy without any deposition. Remarkably, an ordered square array of nanoislands was created on Si with a period of 300 nm. These Si nanoislands are ~150 nm in width and ~9 nm high typically. The formation mechanism of the nanoislands is suggested to be attributed to the Marangoni effect [248]. The surface temperature at the interference maxima of Si substrates can, we believe, reach its melting point (1410 °C) after the high energy laser pulse, and hence local melting followed by rapid resolidification takes place. According to the Marangoni effect, the materials in the molten pool undergo inward flow due to the surface tension gradient, and this forms bumps/nanoislands. Similar experimental

results have been observed on metal and Si surfaces using high-power DLIP [199][249][250][251].
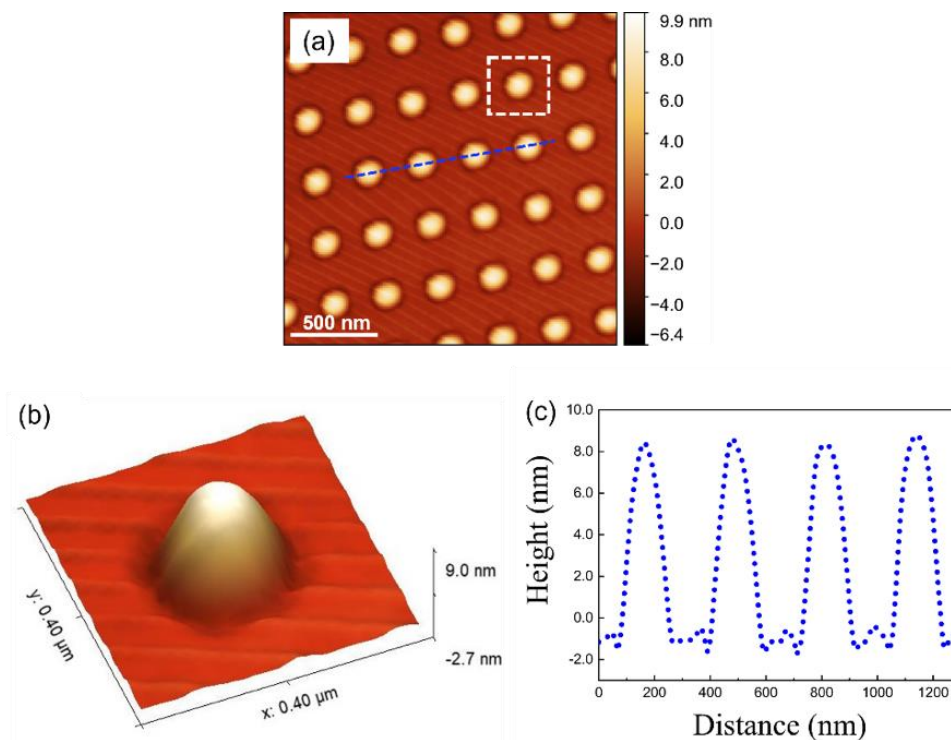
Figure 7.1 (a) 2 × 2 µm² AFM micrograph of a square array of Si nanoislands with a periodicity of 300 nm. (b) 3-D AFM image of an individual Si nanoisland. (c) Line scan of four nanoislands as marked in (a).

The shape and size of Si nanoislands vary with different laser pulse energy, as shown in Figure 7.2. Large ~280 nm wide and averagely ~10 nm in height square-like nanoislands were observed in Figure 7.2(a), under pulse energy of ~80 mJ. These islands are connected to each other indicating larger melting areas, where the shape corresponds to the interference pattern. As the pulse energy decreases to 70 mJ, the islands are less connected and with a slightly reduced ~9 nm height and ~250 nm diameter. At even lower pulse energy of 50 mJ, smaller ~140 nm wide and ~6.5 nm high round-shape nanoislands were formed. The size evolution is due to the reduction of the localised heating area as the laser energy decreases, for a smaller area of material is molten. A similar trend was observed when we decreased the substrate temperature for the DLIP. For instance, at a T_s of 100 °C, only very small size islands were formed, which suggests the surface temperature of a small area at the maximum laser intensity exceeds the melting point.
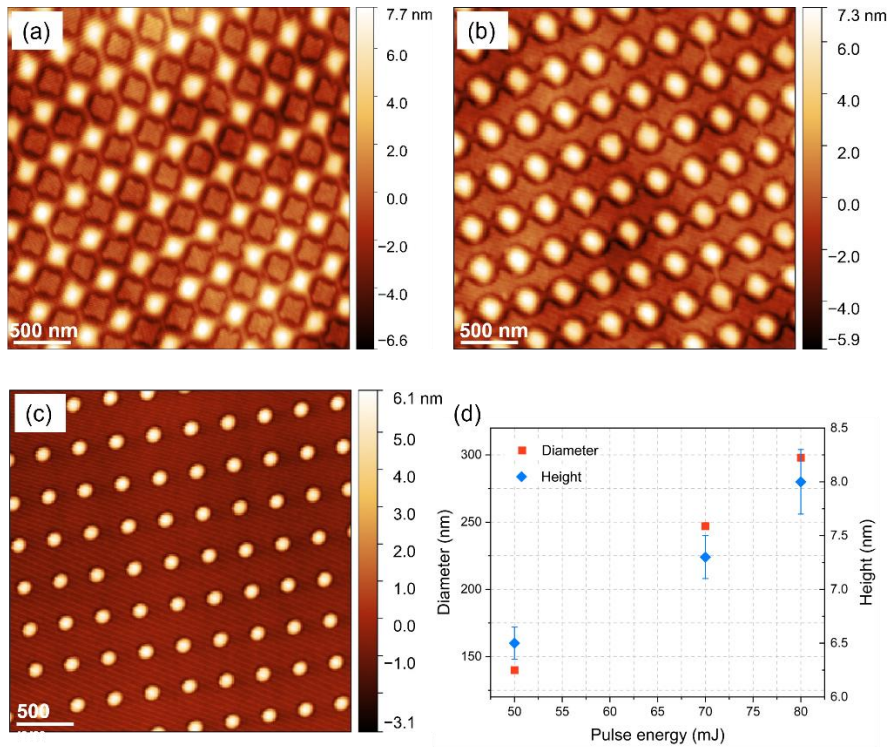
Figure 7.2 3 × 3 μm² AFM micrographs of Si nanoisland arrays at reduced energy (a-c) 80 mJ, 70 mJ and 50 mJ. (d) Average diameter and height of Si nanoislands in response to pulse energy.

After the laser patterning of Si surfaces, Ga was deposited in the absence of arsenic to form Ga liquid droplets. Figure 7.3 shows the surface morphologies of Ga droplets formed on Si-patterned surfaces with different amounts of Ga ranging from 1 nm to 20 nm (a-d) and different T_s for droplet formation. As shown in Figure 7.3(a) with 1 nm Ga deposition, it is clear that we observe Ga droplets begin to nucleate at the edge of the Si nanoislands, which is analogous to the behaviour of aforementioned InAs/GaAs QD nucleation. The Ga droplet surface density is relatively low at ~2.8 × 10^8 cm⁻² and these Ga droplets have a median height of ~15 nm and ~50 nm in diameter. By increasing the Ga deposition to 5 nm, as presented in Figure 7.3(b), the droplet density increases to ~1.7 × 10^9 cm⁻² and 1-3 droplets were observed per island site. The droplet size also becomes larger with a width of 110 nm and 30 nm in height. As the Ga amount is further increased to 10 nm, as depicted in Figure 7.3(c), big 1-3 Ga droplets occupy the site and the underlying Si nanoislands are almost covered. The size of the droplets is typically ~50 nm high and ~170 nm wide, and the density reduces to ~1 × 10^9 cm⁻². With a 20 nm amount of Ga deposition as seen in Figure 7.3(d), extremely large ~70 nm high Ga droplets were formed with a median base of ~200 nm,

117

showing a steady droplet density of ~1 × 10^9 cm^{-2}. Figure 7.4 plots the average height and diameter of Ga droplets on patterned Si (100) substrates with varied deposition amounts of Ga. The surface migration of Ga is enhanced by the presence of Si nanoislands and the preferential nucleation site is at the edge of islands. The formation of big Ga droplets is due to the coalescence of small droplets. As the Ga amount increases, the number of small droplets is reduced due to coalescence into large single droplets. In all of the samples, the formation of interstitial Ga droplets between the Si islands is completely suppressed.
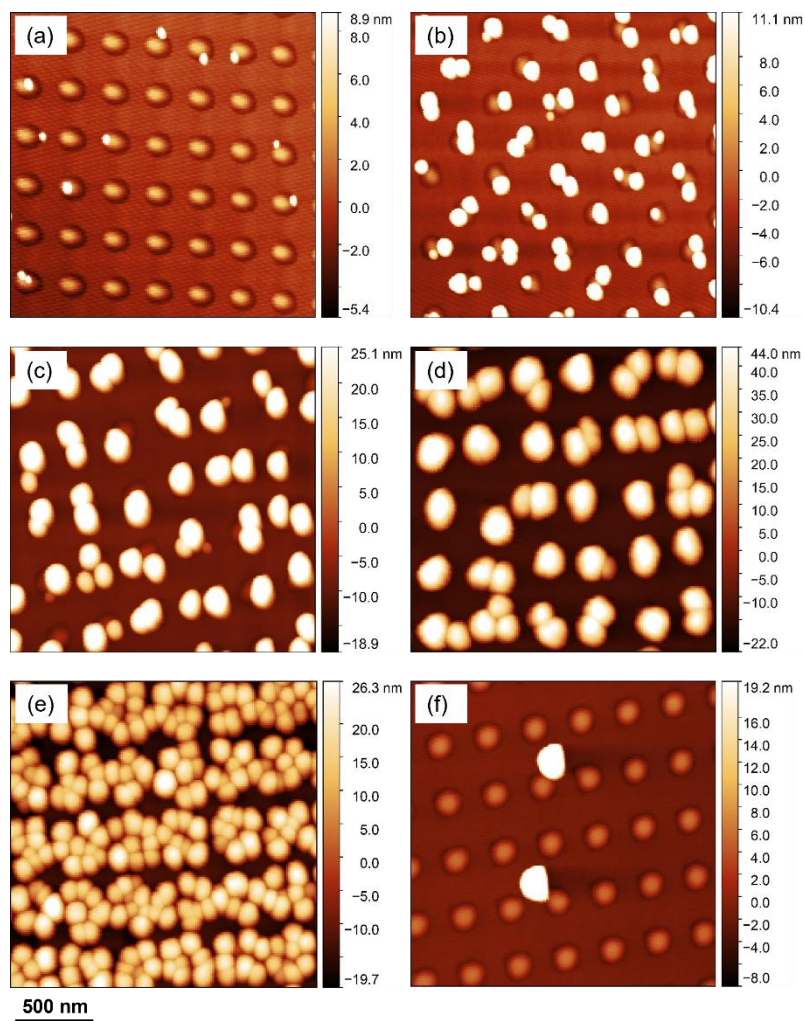
Figure 7.3 2 × 2 μm² AFM micrographs of Ga droplets on patterned Si (100) surfaces differ in Ga deposition amounts and T_s for droplet formation (a-d) T_s = 625 °C and Ga deposition amounts of (a-d) 1 nm, 5 nm, 10 nm, and 20 nm sequentially. (e) T_s = 600 °C and Ga amount of 10 nm. (f) T_s = 650 °C and Ga amount of 20 nm.

When the substrate temperature T_s was changed for Ga droplet formation, as revealed in Figure 7.3(e) and (f), different surface morphologies were observed. Figure 7.3 (e) presents the AFM image of Ga droplets at T_s = 600 °C and Ga amount of 10 nm, in which many Ga droplets with a typical height of ~30 nm were formed at the island sites. Over 7 droplet occupancies per site were obtained. This results from a shorter surface migration length of Ga atoms at a lower T_s. By contrast, when the T_s was increased to 650 °C, as shown in Figure 7.3(f), there is no droplet nucleation at nanoisland sites, whereas very few ~70 nm high droplets were formed on the surface without ordering, suggesting the Ga adatom mobility is too high at this temperature to nucleate at each Si nanoisland. Hence, the droplet size and the occupancy per site are governed by the Ga deposition amount and T_s. Under optimum conditions, the Ga adatoms are able to reach and nucleate at each island site, and ideally, single droplet nucleation per Si island can be achieved. According to the experimental data, the optimum T_s for Ga droplets to reach each Si island is about 625 °C.
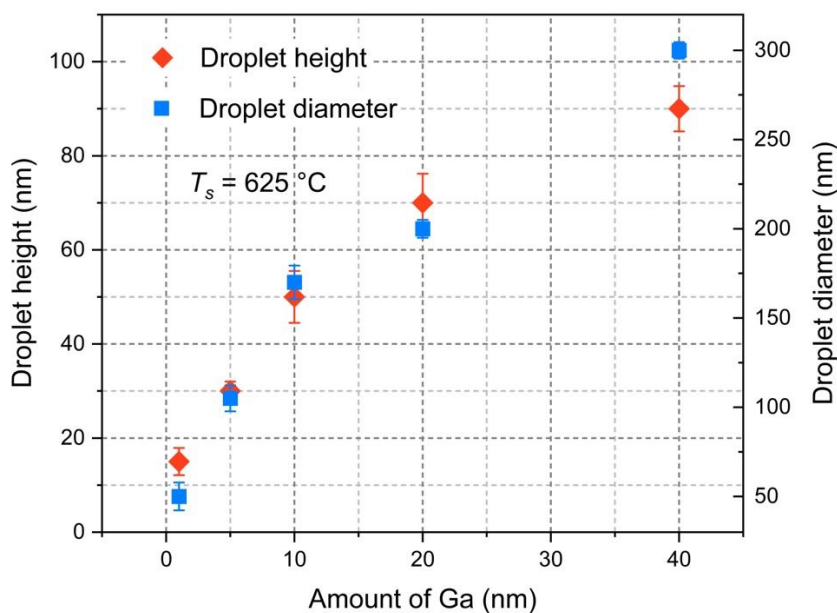
Figure 7.4 The average height and diameter variation of Ga droplets as a function of deposition amount of Ga at T_s = 625 °C.

The same patterning and Ga droplet formation processes have been applied to Si (111) substrates, and similar results were observed. Figure 7.5 displays the AFM and SEM images of 2 nm equivalent Ga droplets formed on DLIP-patterned Si (111) substrates at T_s = 600 °C. Multiple Ga droplets were nucleated at the Si nanoisland sites, and the

droplet occupancy per site relies on the size of the islands. On both Si (100) and (111) substrates, it should be mentioned that almost none or ultra-low-density droplets were formed outside the laser patterning area. We believe Ga in these regions exists as a thin uniform layer or as extremely small droplets that cannot be clearly imaged by microscopy; however, obviously it is unable to form larger droplet structures being limited by the adatom migration, which could result from residual native oxides on the non-patterned surfaces. Contrarily, Si nanoislands can be induced by DLIP whilst oxides can be removed from these areas due to the high local temperature. Whatever happens in the non-patterned regions it is clear that the existence of patterned Si nanoislands greatly enhances Ga atoms to migrate towards them to form droplets.
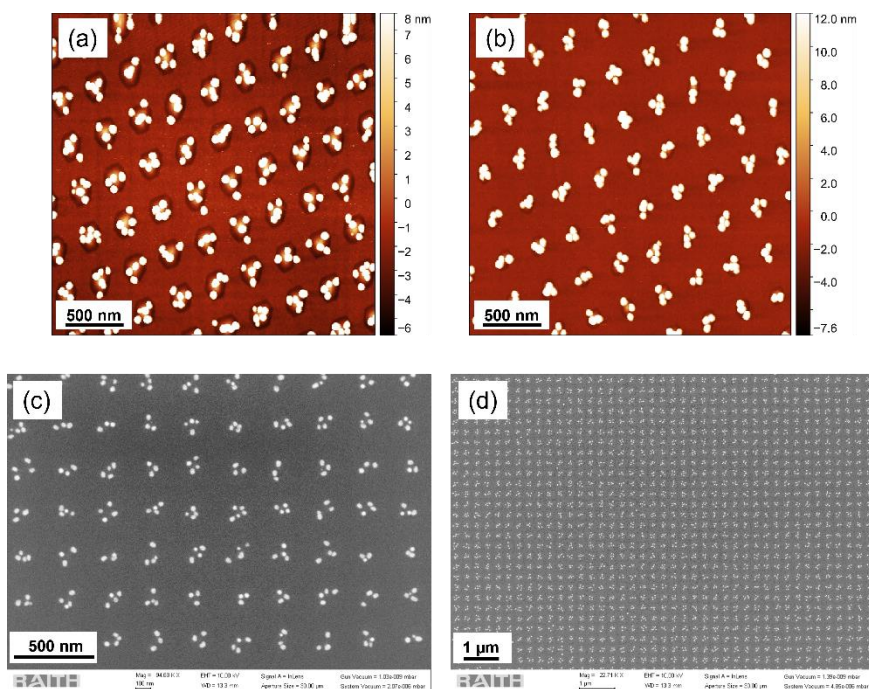
Figure 7.5 3 × 3 μm² AFM micrographs of 2 nm equivalent Ga droplets on patterned Si (111) surfaces differ in pulse energy: (a) 60 mJ and (b) 50 mJ. (c, d) Plan view SEM images at different scales.

After crystallising 20 nm-equivalent Ga droplets on patterned Si (100) substrates as shown in Figure 7.3(d), additional GaAs ranging from 30 to 150 nm were deposited on the surfaces, and arrays of 3-D GaAs nanocrystals were formed. Figure 7.6 displays arrays of GaAs nanocrystals grown on the Si nanoislands by depositing GaAs in the range of 30-150 nm at the same GR and T_s = 625 °C on Si (100) substrates. With small amounts of GaAs as depicted in Figure 7.6(a) and (b), 150-200 nm wide nanocrystal arrays were observed with considerable inhomogeneity in their shape, although some

of them develop clear rectangular facets. The non-uniformity in shape and size of GaAs nanocrystals results from the difference in the initial occupancy and position of GaAs nucleation on Si islands. Figure 7.6(c) and (e) show ~250 nm wide nanocrystals and some coalescence when the deposition thickness reaches 100 nm. The width of GaAs nanocrystals increases with the increase of deposition amount and they can become connected once a certain deposition thickness is reached. Figure 7.6(d) shows the surface morphology with 150 nm GaAs, and strong coalescence of adjacent crystals occurs, while the lateral orderliness is weakened. For comparison, the non-patterned area of the GaAs crystals on the Si (100) substrate of the same sample as (e) is presented in Figure 7.6(f), where the GaAs nanocrystals were randomly distributed.
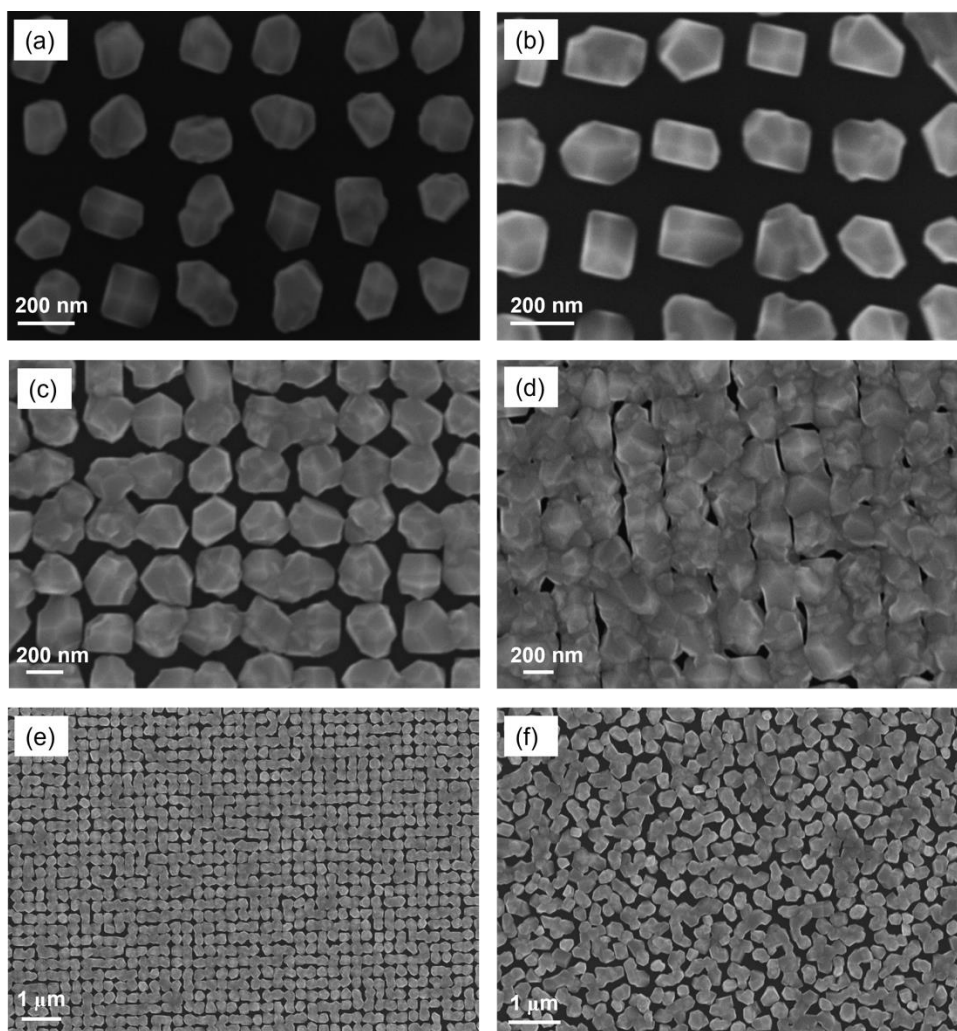
Figure 7.6 Plan-view SEM micrographs of GaAs nanocrystals fabricated on patterned Si (100) substrates with different deposition thicknesses of GaAs (a-d) 30 nm, 60 nm, 100 nm, and 150 nm respectively at T_s = 625 °C. (e) Low magnification image of the GaAs nanocrystals of (c). (f) GaAs nanocrystals in the non-patterned area.

The SAG of GaAs on DLIP-induced Si substrates involves the process of nucleation of GaAs on Si nanoislands, the subsequent lateral growth of nanocrystals and the coalescence of neighbouring crystals. T_s determines the surface migration of Ga adatoms and thereby the occupancy of GaAs on Si nanoislands. By growing thick GaAs, GaAs nanocrystals were formed upon Si islands and widened as the deposition thickness increased. Good spatial ordering can be maintained within a certain deposition thickness. SAG by defect-free DLIP technique is a useful mechanism to incorporate III-V nanostructures on silicon and the coalescence of crystals could provide a mechanism for the crystal quality improvement of bulk-like III-V semiconductors on silicon substrates. It is expected that the defects could be trapped by the sidewalls of III-V crystals or columns in a similar mechanism to that of aspect ratio trapping seen in the growth on etched trenches or with some similarities to the epitaxial lateral overgrowth (ELOG) method [252][253].

These results form only an initial study of the growth of GaAs DE on silicon, but it is clear that this presents some interesting opportunities for III-V SAG on silicon. Further studies will be needed, but this is beyond the scope of this dissertation.

7.2 GROWTH AND CHARACTERISATION OF ORDERED GaSb/GaAs QDs

7.2.1 SAMPLE GROWTH

The samples were grown on 2-inch epi-ready GaAs (100) substrates via S-K mode. A 500 nm thick GaAs buffer was grown at 630 °C following the native oxide removal. Then the T_s was reduced to 420 °C, and the arsenic valve was closed whilst the Sb valve was opened. Thus, the samples were pre-soaked under an Sb flux BEP = 1.35 × 10^{-6} mbar for 20 s before the QD growth. For QD growth, 1 ML GaSb was supplied at a GR of 0.06 ML s^{-1}, and immediately single pulse four-beam DLIP with a laser fluence of 50-60 mJ/cm^2 on the sample surfaces was applied, and subsequently further 1.5-1.7 ML of GaSb was grown. After a 20 s interruption with Sb post-soaking, the GaSb QDs were capped with a 200 nm-thick GaAs layer at 420 °C. Subsequently, the second layer of GaSb QDs was grown with the same procedure, but without capping, for surface structural characterisation by AFM.

7.2.2 STRUCTURAL CHARACTERISATION

Figure 7.7 reveals the AFM micrographs of the surface morphologies (a) after the DLIP and (b) GaSb QD nucleation around the nanoislands. After single pulse DLIP on the 1 ML GaSb layer, regular arrays of nanoislands about 1.5 nm in height which are composed of GaAsSb were formed. By depositing additional 1.5 ML GaSb on these nanoisland-templated surfaces, some GaSb QDs start to nucleate around the nanoislands, but these dots express significant size inhomogeneity varying from 2 to 5 nm in height.
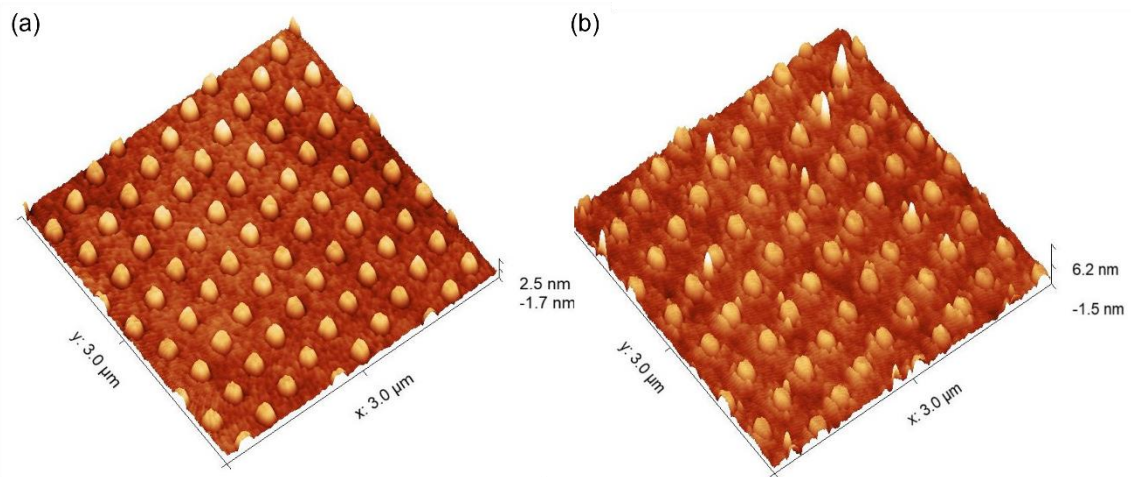
Figure 7.7 3 × 3 μm² AFM micrographs of (a) nanoisland arrays formed after DLIP and (b) GaSb QD nucleation around the nanoislands.

In the same manner as the patterned InAs QD structures, the size of nanoislands is related to the laser intensity and the surface diffusion of Ga adatoms is driven by the gradients of the chemical potential, leading to the preferential nucleation site of QDs at the edge of nanoislands. With different GaSb coverages and nanoisland sizes, the QD occupancy per site can be manipulated. For GaSb QDs grown upon small islands, one can achieve 1 or 2 dots per site. By slightly increasing the deposition amount, >3 QDs per site were observed. Figure 7.8 presents the AFM images of patterned GaSb QDs grown with different GaSb coverages of (a) 2.5 ML and (b) 2.7 ML. The ordered GaSb QDs as shown in Figure 7.8(a) have a median dot height of 2.1 ± 0.4 nm, while the height as presented in Figure 7.8(b) is around 3.2 ± 0.7 nm. The size of the patterned GaSb QDs ranges from 1 nm to 6 nm, consistent with other reports [254][255]. As the GaSb coverage increases, the QD size enlarges and the QD density rises from (a) ~1 × 10^9 cm^{-2} to (b) ~2.3 × 10^9 cm^{-2}, but at the cost of size uniformity.
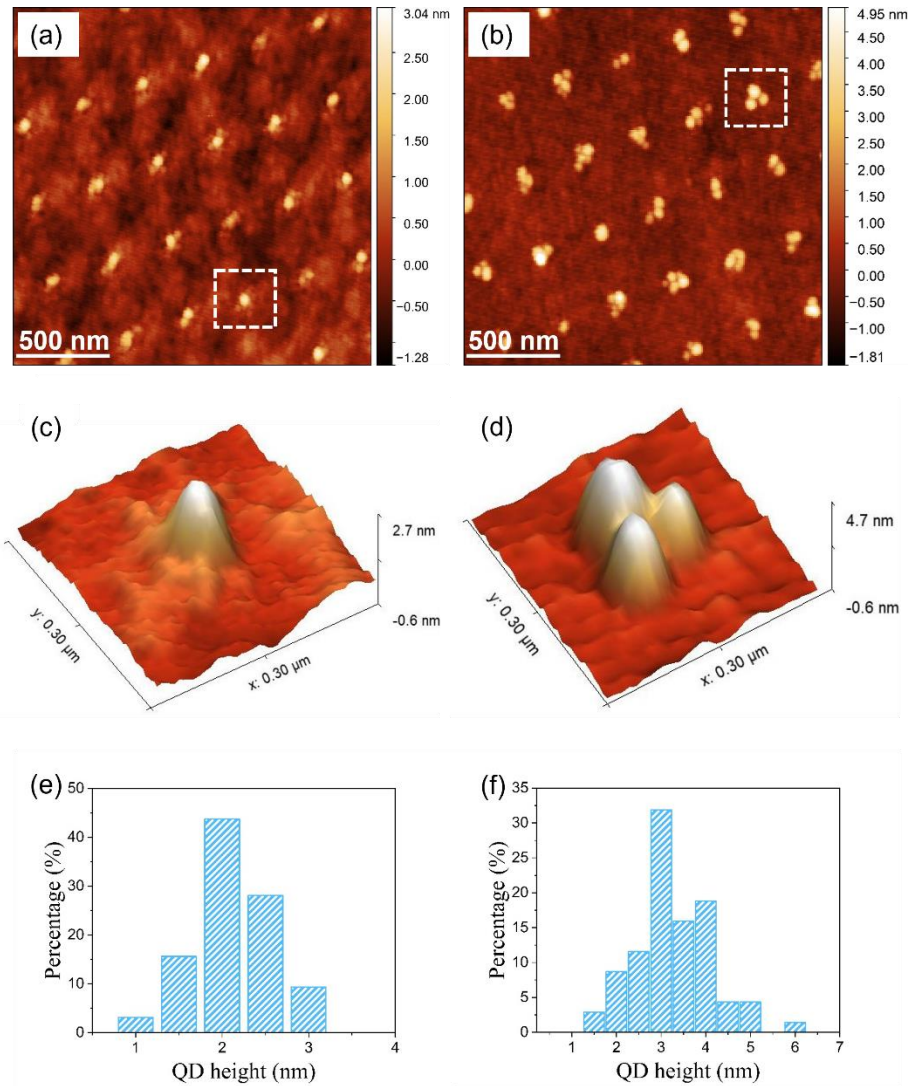
Figure 7.8 2 × 2 μm² AFM micrographs of ordered GaSb QDs with GaSb coverage of (a, b) 2.5 and 2.7 ML. (c, d) 3-D AFM micrographs of individual single and multiple QDs. (e, f) Corresponding QD height distributions.

7.2.3 OPTICAL CHARACTERISATION

Low-temperature PL measurements were undertaken to examine the optical quality of DLIP-induced GaSb/GaAs QDs. The sample was situated in a closed cycle cryostat, an optically pumped laser of 594 nm in wavelength was employed as the excitation source and a 100× objective was utilised to collect the signal. Figure 7.9(a) reveals the low-temperature PL spectra of patterned ordered GaSb QDs according to excitation power between 0.1 mW and 5 mW, and Figure 7.9(b) reveals the linear dependence between the peak energy with the cubic root of the excitation power. As shown in the

insert, the QD PL peak around ~1.1 eV and a narrow ~50 meV FWHM comparable to reported values [256][257][258] was noted utilising 0.1 mW low excitation power.
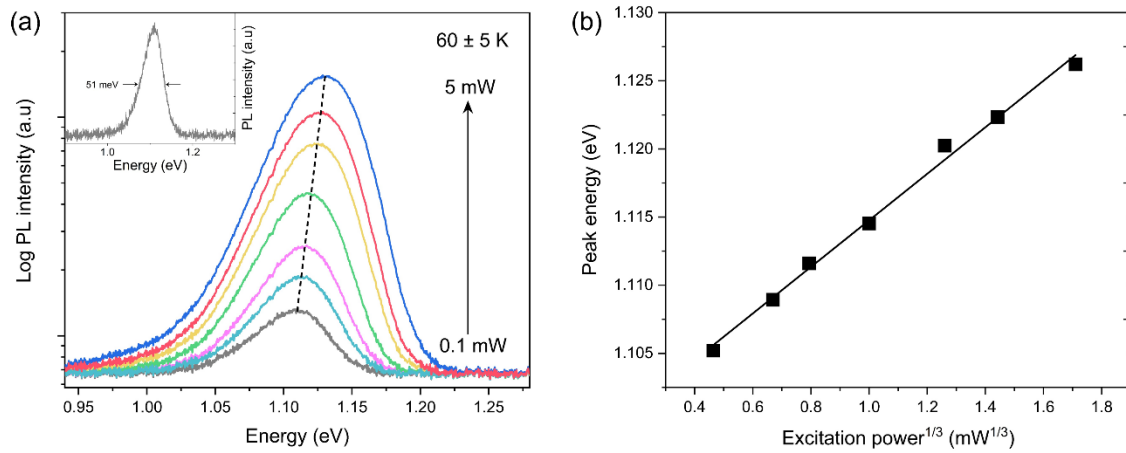
Figure 7.9 (a) Excitation power-dependent PL spectra of patterned GaSb QD arrays at 60 K. The insert shows the PL spectrum at low excitation power with a linewidth of 51 meV. (b) The QD peak energy positions are dependent upon the cube root of the excitation power.

The PL peak shifts towards higher energy by about 21 meV as the excitation power increases from 0.1 mW to 5 mW, exhibiting a typical feature of type-II band alignment [259][260][261]. The blue shift of the QD peak energy can be explained by band bending on grounds of the internal electric field generated from the spatially separated carriers that cause the conduction band to be a triangular well-shape, leading to the rise in the quantized energy levels [243][260]. The QD peak energy follows the third root of the excitation power which quantitatively confirms the band alignment behaviour typical of type-II systems, which can be expressed as $E_{PL} \propto P^{1/3}$ [262]. As revealed in Figure 7.9(b), the peak energy increases proportionally to the cube root of the excitation power, conforming to previously published results of type-II structures [262][263].

7.3 SUMMARY

This chapter explores other possibilities for *in situ* DLIP fabrication of semiconductor nanostructures. In the first part, it is concluded that single pulse DLIP is capable of structuring Si surfaces to form periodic arrays of Si nanoislands and that these Si islands perform as favoured nucleation sites for SAG of GaAs. Thus, dense ordered

arrays of GaAs droplets and nanocrystals are obtained, where the size and shape of these GaAs nanocrystals depend on the crystal orientation, deposition amount, growth temperature, etc. The results exhibit great potential for the future integration of III-V/Si materials. The production of type-II GaSb/GaAs QDs is concerned in the second part of this chapter. It is revealed that GaSb QDs prefer to nucleate at the patterned nanoisland sites, and the QD size, density and site occupancy rely on the growth parameters such as the GaSb coverage. Initial results of laterally ordered GaSb QDs on GaAs substrates are successfully obtained. The low temperature PL spectra of the patterned GaSb QD arrays indicate the unique band alignment with respect to type-II systems and show a narrow FWHM of ~50 meV.

CHAPTER *8*

CONCLUSION AND OUTLOOK

8.1 CONCLUSION

This dissertation confirms that *in situ* DLIP can provide a rapid, single step and defect-free pathway for the realisation of two-dimensional laterally ordered III-V semiconductor nanostructures with good uniformity and high optical quality. The resulting ordered arrays of QDs can constitute an appealing platform for future quantum applications. The lateral ordering was achieved by combining the MBE self-assembly (S-K or DE growth) with *in situ* pulsed direct laser interference patterning. In this dissertation, a variety of ordered III-V nanostructures including InAs/GaAs QD/QDM arrays, GaAs/AlGaAs QD/QR arrays, GaSb/GaAs QD arrays, and GaAs/Si nanocrystals have been successfully obtained. In this approach, UV nanosecond single pulse DLIP was applied to the MBE system to directly pattern the surface of the growing sample, in which it induces local laser-matter reaction processes which can modify surface diffusion processes due to a transient photothermal effect. Periodic arrays of monolayers-high nanoislands were initially created on the surface, which yield energetically preferential nucleation sites for QDs or droplets. Thus, precise ordering of QD nanostructures with a small period of ~300 nm has been obtained.

The details of the optical setup, implementation, simulation, sample preparation, growth processes, structural and optical characterisation were demonstrated. It is concluded that single pulse DLIP on the growing surface is capable of manipulating the atomic kinetics to promote the island nucleation in conformity with the theoretical modelling and experimental results, Both the DLIP parameters and the MBE growth conditions play important roles in the formation of nanostructure arrays. With optimum parameters, ordered arrays of single InAs QDs on GaAs, single GaAs QDs and QRs on AlGaAs have been obtained, the PL spectra of which show high optical quality and uniformity with record narrow linewidths. Aside from these, arrays of

type-II GaSb/GaAs QDs were successfully grown and exhibit high optical quality. Also, SAG of GaAs/Si nanocrystals was demonstrated using this *in situ* approach.

Apart from the *in situ* ordering of III-V QD nanostructures, the realisation of 2-D periodic nanoholes on both photoresist and GaAs wafers through single pulse exposure from four-beam interference with a beam-shaping system was achieved for the first time in this dissertation. The pre-conditioning of the beam shape prior to the interference compensates for the ellipticity caused by the beam projection and therefore created an improved beam spot, contributing to realising a more uniform interference pattern area. Although not the main focus of our work, the fabrication of nano-periodic surface structures through a photoresist transfer and etching process can be attractive for a range of applications and be applied to diverse materials, not just semiconductors.

To summarise, this dissertation work has addressed the lateral alignment of semiconductor nanostructures using a novel *in situ* optical technique. The results lay the foundation for fabricating ordered arrays of single QDs, QDMs or QRs in a highly efficient and large area manner to enable future quantum functional device platforms.

8.2 OUTLOOK

The follow-up work of this dissertation would include the following aspects: the improvement of laser and DLIP conditions for large-area uniform nanofabrication, the further investigation of the underlying laser-matter interaction processes during MBE, the optical characterisation of patterned single QDs/QRs and the implementation of potential single QD devices, and other possible applications of patterned nanostructures. In addition, our silicon work can only be viewed as initial investigations and is worthy of further studies.

8.2.1 IMPROVING DLIP PRODUCTION THROUGHPUT AND EXPLORATION OF PARAMETER INFLUENCE

The uniformity of interference patterns can be improved. The laser beam used in this work has a Gaussian profile which is a tendency in the far-field even if the initial profile is uniform (flat top). This leads to uneven intensity distribution in the interference pattern. As discussed in the dissertation, single QD nanostructures can be formed on the smallest nanoislands, which correspond to a lower intensity area. In

order to enable large scale fabrication of uniform single QD arrays, it would be desirable to create uniform small islands over a larger area, which would benefit from the laser beam with a uniform flat-top profile. This is certainly possible with beam shaping optics, but at present we have not been able to find such optics compatible with high energy UV pulses due to optical damage thresholds.

In the present work, the laser beam diameter is ~5 mm. When four beams are overlapped, the central area is only a few mm. Therefore, optimum patterning only exists on a small part of the central portion of the wafer. It would be useful to expand this area to cm dimensions or even the whole wafer. This could be achieved by beam expansion optics. The beam intensity will reduce with expansion, but we have excess energy available from the laser. However, there is a further problem which is that we do not have full optical path access to the whole wafer through the existing viewports. Some system redesign would be required.

A further issue is that the Moiré effect can be frequently observed in four-beam interference patterns. This results when the angles of incidence or azimuth are not identical. It introduces long range quasi-period patterns and thereby reduces the large area uniformity. Precision alignment to less than 0.1 degrees would be required, and methods would have to be developed to achieve this. Some other beam configurations could be further investigated such as three-beam interference which is known to suppress this effect.

A nanosecond pulsed laser at $\lambda = 355$ nm was utilised in this dissertation, which leads to an interference period of 200-300 nm. For some specific applications, one may require a larger or smaller period. Thus, either using a different wavelength laser or changing the incidence angle can tune the pattern period. For instance, a period of around 450 nm can be obtained using the second-harmonic 532 nm laser and 890 nm period from the fundamental 1064 nm laser with the same interference configuration. Such larger periods would have been more useful in terms of isolating QDs for single QD spectroscopy. However, such longer wavelengths will lead to a lower absorption efficiency than that of the 355 nm laser and greater surface penetration and so the laser conditions may have to be modified. Also, in practical terms, although it is easy to remove the harmonic crystals from the laser to change the wavelength, all the beam optics would have to be changed as these are wavelength specific. For these reasons, the simplest way to modify the interference periodicity is to change the incidence

angle. Some further lower ports are available on the MBE machine which could be used to achieve this. However, they have not yet been configured with viewports.

Aside from these modifications, it would be interesting to fabricate more complex patterns using multiple beam interference, such as five, six or more beams, and to perform multiple exposures by rotating the substrate.

Moreover, the underlying laser-semiconductor interaction process during the MBE growth is still not completely clear ascribed to a lack of direct evidence. The real-time surface modification such as the temperature change is difficult to monitor since the pulse duration is only a few nanoseconds and the interference maximum area is only a few 100 nm. The actual process may also involve photochemical or photomechanical effects during the laser-matter interaction. Other interesting work which would be useful to perform is to compare longer or shorter nanosecond, picosecond and femtosecond pulse DLIP on semiconductor materials, which may provide further information. Further theoretical modelling and experimental investigations on the laser-induced surface modification would be useful to progress in this area.

8.2.2 SINGLE QD PROPERTIES AND DEVICE APPLICATIONS

Since pure, bright and indistinguishable single photons are of vital importance for quantum technologies, it would be valuable to investigate the single dot optical properties of the DLIP-patterned QD arrays, e.g., single QD emission linewidth, FSS, the second order correlation function and photon indistinguishability utilising micro-PL and related measurements. Our measurements of single dot properties are compromised by the small periodicity, which is below the diffraction limit for optical investigations. Our colleagues at Zhejiang University are currently working on a near field imaging technique that can achieve imaging lower than the diffraction limit and some encouraging initial results have been demonstrated.

Otherwise, the micro-PL measurement of single-photon emission would benefit from a low-density QD array with larger spacing, hence, a small angle of incidence for interference is demanded. Moreover, it is of great interest to compare the optical properties between QDs, QDMs and QRs, for which an external magnetic or electric field could be applied for fine-tuning.

Another important direction would be towards device fabrication based upon the patterned single QD nanostructures or QD arrays, for instance, single-photon or

entangled-photon emitters. The deterministic integration of single QDs that emit controlled spectra within optical cavities leads to the implementation of quantum devices. It has always been difficult to position QDs at predefined locations, moreover, in the case of DLIP-induced QD arrays without any alignment markers, it may need more effort to pre-locate the QDs. Micro-PL in combination with *in situ* optical lithography or EBL could be a promising route for deterministic nanofabrication. Furthermore, these single QDs ultimately need to be embedded within a diode structure that performs as a single photon emitting diode with an electrical injection which is demanded with respect to the integration with photonic circuits.

8.2.3 OTHER POSSIBLE DIRECTIONS

Further work can be continued for the fabrication of III-V/Si nanostructures, such as the study of III-V columns, QDs, and NWs on both Si (100) and (111) substrates, and their structural and optical characterisation. Type II Sb-based QDs are also an interesting area for further study. The *in situ* DLIP technique could also be applied to other materials and growth technologies. For example, periodic or quasi-periodic semiconductor nanopatterned semiconductors are known to exhibit improved broadband antireflection and light-trapping properties that can be applied to improve the efficiency of solar cells, or conversely for improved light extraction in LEDs. In addition, periodic structures can be used to form surfaces that exhibit superhydrophobicity, leading to self-cleaning and anisotropic wetting surfaces on which unwanted liquid, ice or contaminants are repelled or flow in certain directions. Many other industrial or biological applications could also benefit from this relatively simple and rapid nanopatterning process to achieve structured surfaces for diverse applications such as wind turbines, aircraft surfaces and bionics.

BIBLIOGRAPHY

[1]   R. Feynman, "Conclusion : ' Plenty of Room at the Bottom,'" 1959.

[2]   R. R. Schaller, "Moore's law: past, present, and future," *IEEE Spectr.*, 1997, doi: 10.1109/6.591665.

[3]   J. A. Del Alamo, "Nanometre-scale electronics with III-V compound semiconductors," *Nature*. 2011, doi: 10.1038/nature10677.

[4]   C. Convertino *et al.*, "A hybrid III–V tunnel FET and MOSFET technology platform integrated on silicon," *Nat. Electron.*, vol. 4, no. February, 2021, doi: 10.1038/s41928-020-00531-3.

[5]   C. Navarro *et al.*, "Capacitor-less dynamic random access memory based on a III–V transistor with a gate length of 14 nm," *Nat. Electron.*, 2019, doi: 10.1038/s41928-019-0282-6.

[6]   K. Hennessy *et al.*, "Quantum nature of a strongly coupled single quantum dot-cavity system," *Nature*, 2007, doi: 10.1038/nature05586.

[7]   P. Zoller *et al.*, "Quantum information processing and communication," *Eur. Phys. J. D*, 2005, doi: 10.1140/epjd/e2005-00251-1.

[8]   M. Kroutvar *et al.*, "Optically programmable electron spin memory using semiconductor quantum dots," *Nature*, 2004, doi: 10.1038/nature03008.

[9]   A. Thiel and H. Koelsch, "Studien über das Indium," *Zeitschrift für Anorg. Chemie*, 1910, doi: 10.1002/zaac.19100660119.

[10]   Y. Kobayashi, K. Kumakura, T. Akasaka, and T. Makimoto, "Layered boron nitride as a release layer for mechanical transfer of GaN-based devices," *Nature*, 2012, doi: 10.1038/nature10970.

[11]   G. Zhang, M. Takiguchi, K. Tateno, T. Tawara, M. Notomi, and H. Gotoh, "Telecom-band lasing in single InP/InAs heterostructure nanowires at room temperature," *Sci. Adv.*, vol. 5, no. 2, pp. 1–9, 2019, doi: 10.1126/sciadv.aat8896.

[12]   S. Mauthe *et al.*, "High-speed III-V nanowire photodetector monolithically integrated on Si," *Nat. Commun.*, 2020, doi: 10.1038/s41467-020-18374-z.

[13]   J. F. Geisz *et al.*, "Six-junction III–V solar cells with 47.1% conversion efficiency under 143 Suns concentration," *Nat. Energy*, 2020, doi: 10.1038/s41560-020-0598-5.

[14]   F. Dimroth *et al.*, "Wafer bonded four-junction GaInP/GaAs//GaInAsP/GaInAs concentrator solar cells with 44.7% efficiency," *Prog. Photovoltaics Res. Appl.*, 2014, doi: 10.1002/pip.2475.

[15]   A. Jüngel, *Transport Equations for Semiconductors*. Springer, 2009.

[16] A. Kastalsky, T. Duffield, S. J. Allen, and J. Harbison, "Photovoltaic detection of infrared light in a GaAs/AlGaAs superlattice," *Appl. Phys. Lett.*, vol. 52, no. 16, pp. 1320–1322, 1988, doi: 10.1063/1.99147.

[17] A. Rogalski, "Recent progress in infrared detector technologies," 2011, doi: 10.1016/j.infrared.2010.12.003.

[18] A. Rogalski, P. Martyniuk, and M. Kopytko, "InAs/GaSb type-II superlattice infrared detectors: Future prospect," *Applied Physics Reviews*. 2017, doi: 10.1063/1.4999077.

[19] R. J. Ricker, S. R. Provence, D. T. Norton, T. F. Boggess, and J. P. Prineas, "Broadband mid-infrared superlattice light-emitting diodes," *J. Appl. Phys.*, 2017, doi: 10.1063/1.4983023.

[20] P. K. Patil *et al.*, "GaAsBi/GaAs multi-quantum well LED grown by molecular beam epitaxy using a two-substrate-temperature technique," *Nanotechnology*, 2017, doi: 10.1088/1361-6528/aa596c.

[21] Y. H. Ra, R. Navamathavan, H. Il Yoo, and C. R. Lee, "Single nanowire light-emitting diodes using uniaxial and coaxial InGaN/GaN multiple quantum wells synthesized by metalorganic chemical vapor deposition," *Nano Lett.*, 2014, doi: 10.1021/nl404794v.

[22] T. Walther and A. B. Krysa, "Transmission electron microscopy of AlGaAs/GaAs quantum cascade laser structures," *J. Microsc.*, vol. 268, no. 3, pp. 298–304, 2017, doi: 10.1111/jmi.12655.

[23] D. Botez *et al.*, "High-Power Mid-Infrared Quantum Cascade Semiconductor Lasers," 2019, doi: 10.1109/IPCon.2019.8908354.

[24] S. Kumar, "Recent progress in terahertz quantum cascade lasers," *IEEE J. Sel. Top. Quantum Electron.*, 2011, doi: 10.1109/JSTQE.2010.2049735.

[25] K. Tomioka, M. Yoshimura, and T. Fukui, "A III-V nanowire channel on silicon for high-performance vertical transistors," *Nature*, 2012, doi: 10.1038/nature11293.

[26] A. Konar *et al.*, "Carrier transport in high mobility InAs nanowire junctionless transistors," *Nano Lett.*, 2015, doi: 10.1021/nl5043165.

[27] R. Yan, D. Gargas, and P. Yang, "Nanowire photonics," *Nature Photonics*. 2009, doi: 10.1038/nphoton.2009.184.

[28] D. Saxena *et al.*, "Optically pumped room-temperature GaAs nanowire lasers," *Nat. Photonics*, 2013, doi: 10.1038/nphoton.2013.303.

[29] M. Yao *et al.*, "GaAs nanowire array solar cells with axial p-i-n junctions," *Nano Lett.*, 2014, doi: 10.1021/nl500704r.

[30] G. Mariani, A. C. Scofield, C. H. Hung, and D. L. Huffaker, "GaAs nanopillar-array solar cells employing in situ surface passivation," *Nat. Commun.*, 2013, doi: 10.1038/ncomms2509.

[31] P. Bhattacharya and Z. Mi, "Quantum-dot optoelectronic devices," *Proc. IEEE*, 2007, doi: 10.1109/JPROC.2007.900897.

[32] J. Owen and L. Brus, "Chemical synthesis and luminescence applications of colloidal semiconductor quantum dots," *J. Am. Chem. Soc.*, vol. 139, no. 32, pp. 10939–10943, 2017.

[33] Y. Arakawa and H. Sakaki, "Multidimensional quantum well laser and temperature dependence of its threshold current," *Appl. Phys. Lett.*, vol. 40, no. 11, pp. 939–941, 1982.

[34] N. Kirstaedter *et al.*, "Low threshold, large T/sub o/injection laser emission from (InGa) As quantum dots," *Electron. Lett.*, vol. 30, no. 17, pp. 1416–1417, 1994.

[35] P. G. Eliseev *et al.*, "Ground-state emission and gain in ultralow-threshold InAs-InGaAs Quantum-dot lasers," *IEEE J. Sel. Top. Quantum Electron.*, 2001, doi: 10.1109/2944.954121.

[36] S. Fathpour *et al.*, "The role of Auger recombination in the temperature-dependent output characteristics (T 0 = ∞) of p-doped 1.3 µm quantum dot lasers," *Appl. Phys. Lett.*, 2004, doi: 10.1063/1.1829158.

[37] Q. Xie, A. Madhukar, P. Chen, and N. P. Kobayashi, "Vertically self-organized InAs quantum box islands on GaAs(100)," *Phys. Rev. Lett.*, vol. 75, no. 13, pp. 2542–2545, 1995, doi: 10.1103/PhysRevLett.75.2542.

[38] J. Tatebayashi, M. Nishioka, and Y. Arakawa, "Over 1.5 µm light emission from InAs quantum dots embedded in InGaAs strain-reducing layer grown by metalorganic chemical vapor deposition," *Appl. Phys. Lett.*, 2001, doi: 10.1063/1.1375842.

[39] R. J. Warburton, "Single spins in self-assembled quantum dots," *Nature Materials*. 2013, doi: 10.1038/nmat3585.

[40] M. Davanco *et al.*, "Heterogeneous integration for on-chip quantum photonic circuits with single quantum dot devices," *Nat. Commun.*, 2017, doi: 10.1038/s41467-017-00987-6.

[41] P. Senellart, G. Solomon, and A. White, "High-performance semiconductor quantum-dot single-photon sources," *Nat. Nanotechnol.*, vol. 12, no. 11, pp. 1026–1039, 2017, doi: 10.1038/nnano.2017.218.

[42] E. Knill, R. Laflamme, and G. J. Milburn, "A scheme for efficient quantum computation with linear optics," *Nature*, 2001, doi: 10.1038/35051009.

[43] A. Beveratos, R. Brouri, T. Gacoin, A. Villing, J. P. Poizat, and P. Grangier, "Single Photon Quantum Cryptography," *Phys. Rev. Lett.*, 2002, doi: 10.1103/PhysRevLett.89.187901.

[44] L. Hanschke *et al.*, "Quantum dot single-photon sources with ultra-low multi-photon probability," *npj Quantum Inf.*, 2018, doi: 10.1038/s41534-018-0092-0.

[45] E. Moreau, I. Robert, L. Manin, V. Thierry-Mieg, J. M. Gérard, and I. Abram, "Quantum cascade of photons in semiconductor quantum dots," *Phys. Rev. Lett.*, vol. 87, no. 18, pp. 183601-1-183601–4, 2001, doi: 10.1103/PhysRevLett.87.183601.

[46] H. J. Briegel, W. Dür, J. I. Cirac, and P. Zoller, "Quantum repeaters: The role of imperfect local operations in quantum communication," *Phys. Rev. Lett.*, vol. 81, no. 26, pp. 5932–5935, 1998, doi: 10.1103/PhysRevLett.81.5932.

[47] M. Bayer *et al.*, "Fine structure of neutral and charged excitons in self-assembled In(Ga)As/(Al) GaAs quantum dots," *Phys. Rev. B - Condens. Matter Mater. Phys.*, vol. 65, no. 19, pp. 1953151–19531523, 2002, doi: 10.1103/PhysRevB.65.195315.

[48] G. Juska, V. Dimastrodonato, L. O. Mereni, A. Gocalinska, and E. Pelucchi, "Towards quantum-dot arrays of entangled photon emitters," *Nat. Photonics*, vol. 7, no. 7, pp. 527–531, 2013, doi: 10.1038/nphoton.2013.128.

[49] A. J. Bennett *et al.*, "Electric-field-induced coherent coupling of the exciton states in a single quantum dot," *Nat. Phys.*, vol. 6, no. 12, pp. 947–950, 2010, doi: 10.1038/nphys1780.

[50] J. Zhang *et al.*, "High yield and ultrafast sources of electrically triggered entangled-photon pairs based on strain-tunable quantum dots," *Nat. Commun.*, vol. 6, 2015, doi: 10.1038/ncomms10067.

[51] R. M. Stevenson *et al.*, "Magnetic-field-induced reduction of the exciton polarization splitting in InAs quantum dots," *Phys. Rev. B - Condens. Matter Mater. Phys.*, vol. 73, no. 3, pp. 1–4, 2006, doi: 10.1103/PhysRevB.73.033306.

[52] L. Wang, A. Rastelli, S. Kiravittaya, M. Benyoucef, and O. G. Schmidt, "Self-assembled quantum dot molecules," *Advanced Materials*. 2009, doi: 10.1002/adma.200803109.

[53] M. L. Kerfoot *et al.*, "Optophononics with coupled quantum dots," *Nat. Commun.*, 2014, doi: 10.1038/ncomms4299.

[54] M. Khoshnegar *et al.*, "A solid state source of photon triplets based on quantum dot molecules," *Nat. Commun.*, 2017, doi: 10.1038/ncomms15716.

[55] M. Bayer *et al.*, "Coupling and entangling of quantum states in quantum dot molecules," *Science (80-.).*, 2001, doi: 10.1126/science.291.5503.451.

[56] G. J. Beirne, C. Hermannstädter, L. Wang, A. Rastelli, O. G. Schmidt, and P. Michler, "Quantum light emission of two lateral tunnel-coupled (In,Ga)As/GaAs quantum dots controlled by a tunable static electric field," *Phys. Rev. Lett.*, vol. 96, no. 13, pp. 2–5, 2006, doi: 10.1103/PhysRevLett.96.137401.

[57] J. Wu *et al.*, "Multicolor photodetector based on GaAs quantum rings grown by droplet epitaxy," *Appl. Phys. Lett.*, 2009, doi: 10.1063/1.3126644.

[58] T. Mano, T. Kuroda, M. Yamagiwa, G. Kido, K. Sakoda, and N. Koguchi, "Lasing in GaAs/AlGaAs self-assembled quantum dots," *Appl. Phys. Lett.*, 2006, doi: 10.1063/1.2372448.

[59] F. Suárez, D. Granados, M. L. Dotor, and J. M. García, "Laser devices with stacked layers of InGaAs/GaAs quantum rings," 2004, doi: 10.1088/0957-4484/15/4/003.

[60] T. Kuroda *et al.*, "Optical transitions in quantum ring complexes," *Phys. Rev. B - Condens. Matter Mater. Phys.*, vol. 72, no. 20, pp. 1–8, 2005, doi: 10.1103/PhysRevB.72.205301.

[61] F. Ding *et al.*, "Gate controlled Aharonov-Bohm-type oscillations from single neutral excitons in quantum rings," *Phys. Rev. B - Condens. Matter Mater. Phys.*, 2010, doi: 10.1103/PhysRevB.82.075309.

[62] V. V. Arsoski, M. Ž. Tadić, and F. M. Peeters, "Strain and band-mixing effects on the excitonic Aharonov-Bohm effect in In(Ga)As/GaAs ringlike quantum dots," *Phys. Rev. B - Condens. Matter Mater. Phys.*, 2013, doi: 10.1103/PhysRevB.87.085314.

[63] C. Vieu *et al.*, "Electron beam lithography: Resolution limits and applications," *Appl. Surf. Sci.*, vol. 164, no. 1–4, pp. 111–117, 2000, doi: 10.1016/S0169-4332(00)00352-4.

[64] F. H. Dill, "Optical lithography," *IEEE Trans. Electron Devices*, vol. 22, no. 7, pp. 440–444, 1975.

[65] S. Y. Chou, P. R. Krauss, and P. J. Renstrom, "Nanoimprint lithography," *J. Vac. Sci. Technol. B Microelectron. Nanom. Struct. Process. Meas. Phenom.*, vol. 14, no. 6, pp. 4129–4133, 1996.

[66] W. L. Brown, T. Venkatesan, and A. Wagner, "Ion beam lithography," *Nucl. Instruments Methods Phys. Res.*, vol. 191, no. 1–3, pp. 157–168, 1981.

[67] A. G. Thompson, "MOCVD technology for semiconductors," *Mater. Lett.*, vol. 30, no. 4, pp. 255–263, 1997.

[68] W. T. Tsang, "Chemical beam epitaxy of InP and GaAs," *Appl. Phys. Lett.*, vol. 45, no. 11, pp. 1234–1236, 1984.

[69] A. Y. Cho and J. R. Arthur, "Molecular beam epitaxy," *Prog. solid state Chem.*, vol. 10, pp. 157–191, 1975.

[70] R. S. Wagner and W. C. Ellis, "Vapor-liquid-solid mechanism of single crystal growth," *Appl. Phys. Lett.*, 1964, doi: 10.1063/1.1753975.

[71] J. L. O'Brien, A. Furusawa, and J. Vučković, "Photonic quantum technologies," *Nat. Photonics*, vol. 3, no. 12, pp. 687–695, 2009, doi: 10.1038/nphoton.2009.229.

[72] N. N. Ledentsov *et al.*, "Three-dimensional arrays of self-ordered quantum dots for laser applications," *Microelectronics J.*, vol. 28, no. 8–10, pp. 915–931, 1997, doi: 10.1016/s0026-2692(96)00131-0.

[73] G. Wei and S. R. Forrest, "Intermediate-band solar cells employing quantum dots embedded in an energy fence barrier," *Nano Lett.*, vol. 7, no. 1, pp. 218–222, 2007, doi: 10.1021/nl062564s.

[74] O. G. Schmidt, *Lateral alignment of epitaxial quantum dots*. Springer Science & Business Media, 2007.

[75] T. Mano, R. Nötzel, G. J. Hamhuis, T. J. Eijkemans, and J. H. Wolter, "Formation of InAs quantum dot arrays on GaAs (100) by self-organized anisotropic strain engineering of a (In,Ga)As superlattice template," *Appl. Phys. Lett.*, vol. 81, no. 9, pp. 1705–1707, 2002, doi: 10.1063/1.1503872.

[76] K. D. Jöns *et al.*, "Triggered indistinguishable single photons with narrow line widths from site-controlled quantum dots," *Nano Lett.*, vol. 13, no. 1, pp. 126–130, 2013, doi: 10.1021/nl303668z.

[77] M. K. Yakes *et al.*, "Leveraging crystal anisotropy for deterministic growth of inas quantum dots with narrow optical linewidths," *Nano Lett.*, vol. 13, no. 10, pp. 4870–4875, 2013, doi: 10.1021/nl402744s.

[78] V. Baumann *et al.*, "Site-controlled growth of InP/GaInP quantum dots on GaAs substrates," *Nanotechnology*, vol. 23, no. 37, 2012, doi: 10.1088/0957-4484/23/37/375301.

[79] P. Atkinson, S. P. Bremner, D. Anderson, G. A. C. Jones, and D. A. Ritchie, "Size evolution of site-controlled InAs quantum dots grown by molecular beam epitaxy on prepatterned GaAs substrates," *J. Vac. Sci. Technol. B Microelectron. Nanom. Struct.*, vol. 24, no. 3, p. 1523, 2006, doi: 10.1116/1.2190674.

[80] D. J. Eaglesham and M. Cerullo, "Dislocation-free Stranski-Krastanow growth of Ge on Si (100)," *Phys. Rev. Lett.*, vol. 64, no. 16, p. 1943, 1990.

[81] Y. W. Mo, D. E. Savage, B. S. Swartzentruber, and M. G. Lagally, "Kinetic pathway in Stranski-Krastanov growth of Ge on Si (001)," *Phys. Rev. Lett.*, vol. 65, no. 8, p. 1020, 1990.

[82] C. W. Snyder, B. G. Orr, D. Kessler, and L. M. Sander, "Effect of strain on surface morphology in highly strained InGaAs films," *Phys. Rev. Lett.,* vol. 66, no. 23, p. 3032, 1991.

[83] D. Leonard, M. Krishnamurthy, C. Reaves, S. P. DenBaars, and P. M. Petroff, "Direct formation of quantum-sized dots from uniform coherent islands of InGaAs on GaAs surfaces," *Appl. Phys. Lett.,* vol. 63, no. 23, pp. 3203–3205, 1993.

[84] E. Bauer, "Phänomenologische theorie der kristallabscheidung an oberflächen. i.," *Zeitschrift für Krist. Mater.,* vol. 110, no. 1–6, pp. 372–394, 1958.

[85] M. Volmer and A. Weber, "Keimbildung in übersättigten Gebilden," *Zeitschrift für Phys. Chemie*, vol. 119U, no. 1, pp. 277–301, 1926.

[86] I. N. Stranski and L. Krastanow, "Berichtigung zur Arbeit - 'Zur Theorie der orientierten Ausscheidung von Ionenkristallen aufeinander,'" *Monatshefte für Chemie,* vol. 71, pp. 351–364, 1937, doi: 10.1007/BF02716117.

[87] F. FC and J. van der Merwe, "One-dimensional dislocations. I. Static theory," *Proc. R. Soc. London. Ser. A. Math. Phys. Sci.,* vol. 198, no. 1053, pp. 205–216, 1949.

[88] H. T. Dobbs, D. D. Vvedensky, A. Zangwill, J. Johansson, N. Carlsson, and W. Seifert, "Mean-field theory of quantum dot formation," *Phys. Rev. Lett.,* vol. 79, no. 5, pp. 897–900, 1997, doi: 10.1103/PhysRevLett.79.897.

[89] G. S. Bales and D. C. Chrzan, "Dynamics of irreversible island growth during submonolayer epitaxy," *Phys. Rev. B*, vol. 50, no. 9, pp. 6057–6067, 1994, doi: 10.1103/PhysRevB.50.6057.

[90] P. Müller and R. Kern, "The physical origin of the two-dimensional towards three-dimensional coherent epitaxial Stranski-Krastanov transition," *Appl. Surf. Sci.,* vol. 102, no. i, pp. 6–11, 1996, doi: 10.1016/0169-4332(96)00009-8.

[91] C. Heyn, "Critical coverage for strain-induced formation of InAs quantum dots," *Phys. Rev. B,* vol. 64, no. 16, p. 165306, 2001.

[92] V. A. Shchukin, N. N. Ledentsov, and D. Bimberg, "Spontaneous formation of nanostructures on crystal surfaces," *Phys. E Low-Dimensional Syst. Nanostructures,* vol. 9, no. 1, pp. 140–148, 2001, doi: 10.1016/S1386-9477(00)00188-0.

[93] X. L. Li, G. Ouyang, and G. W. Yang, "A thermodynamic theory of the self-assembly of quantum dots," *New J. Phys.,* vol. 10, 2008, doi: 10.1088/1367-2630/10/4/043007.

[94] X. Li, Y. Cao, and G. Yang, "Thermodynamic theory of two-dimensional to three-dimensional growth transition in quantum dots self-assembly," *Phys. Chem. Chem. Phys.,* vol. 12, no. 18, pp. 4768–4772, 2010, doi: 10.1039/b927189a.

[95] A. V. Osipov, S. A. Kukushkin, F. Schmitt, and P. Hess, "Kinetic model of coherent island formation in the case of self-limiting growth," *Phys. Rev. B - Condens. Matter Mater. Phys.*, vol. 64, no. 20, pp. 2054211–2054216, 2001, doi: 10.1103/physrevb.64.205421.

[96] A. V. Osipov, F. Schmitt, S. A. Kukushkin, and P. Hess, "Stress-driven nucleation of coherent islands: Theory and experiment," *Appl. Surf. Sci.*, vol. 188, no. 1–2, pp. 156–162, 2002, doi: 10.1016/S0169-4332(01)00727-9.

[97] G. Dubrovskii, E. Cirlin, and M. Ustinov, "Kinetics of the initial stage of coherent island formation in heteroepitaxial systems," *Phys. Rev. B - Condens. Matter Mater. Phys.*, vol. 68, no. 7, pp. 1–9, 2003, doi: 10.1103/PhysRevB.68.075409.

[98] V. G. Dubrovskiĭ, "Calculation of the size-distribution function for quantum dots at the kinetic stage of growth," *Semiconductors*, vol. 40, no. 10, pp. 1123–1130, 2006, doi: 10.1134/S1063782606100010.

[99] J. M. Moison, F. Houzay, F. Barthe, L. Leprince, E. Andre, and O. Vatel, "Self-organized growth of regular nanometer-scale InAs dots on GaAs," *Appl. Phys. Lett.*, vol. 64, no. 2, pp. 196–198, 1994.

[100] G. Costantini *et al.*, "Pyramids and domes in the InAs/GaAs(0 0 1) and Ge/Si(0 0 1) systems," *J. Cryst. Growth*, vol. 278, no. 1–4, pp. 38–45, 2005, doi: 10.1016/j.jcrysgro.2004.12.047.

[101] M. C. Xu, Y. Temko, T. Suzuki, and K. Jacobi, "Shape transition of InAs quantum dots on GaAs(001)," *J. Appl. Phys.*, vol. 98, no. 8, 2005, doi: 10.1063/1.2076431.

[102] J. Marquez, L. Geelhaar, and K. Jacobi, "Atomically resolved structure of InAs quantum dots," *Appl. Phys. Lett.*, vol. 78, no. 16, pp. 2309–2311, 2001, doi: 10.1063/1.1365101.

[103] F. Patella *et al.*, "Tracing the two- to three-dimensional transition in the InAs/GaAs(001) heteroepitaxial growth," *Phys. Rev. B - Condens. Matter Mater. Phys.*, vol. 67, no. 20, pp. 1–5, 2003, doi: 10.1103/PhysRevB.67.205308.

[104] F. Patella *et al.*, "Morphological instabilities of the InAs/GaAs(001) interface and their effect on the self-assembling of InAs quantum-dot arrays," *Appl. Phys. Lett.*, vol. 81, no. 12, pp. 2270–2272, 2002, doi: 10.1063/1.1508416.

[105] P. B. Joyce *et al.*, "Effect of growth rate on the size, composition, and optical properties of InAs/GaAs quantum dots grown by molecular-beam epitaxy," *Phys. Rev. B - Condens. Matter Mater. Phys.*, vol. 62, no. 16, pp. 10891–10895, 2000, doi: 10.1103/PhysRevB.62.10891.

[106] S. Kiravittaya, Y. Nakamura, and O. G. Schmidt, "Photoluminescence linewidth narrowing of InAs/GaAs self-assembled quantum dots," *Phys. E*

Low-Dimensional Syst. Nanostructures, vol. 13, no. 2–4, pp. 224–228, 2002, doi: 10.1016/S1386-9477(01)00525-2.

[107] K. Yamaguchi, K. Yujobo, and T. Kaizu, "Stranski-Krastanov growth of InAs quantum dots with narrow size distribution," *Jpn. J. Appl. Phys.*, vol. 39, no. 12 A, pp. 8–12, 2000, doi: 10.1143/jjap.39.l1245.

[108] Y. Nakata, K. Mukai, M. Sugawara, K. Ohtsubo, H. Ishikawa, and N. Yokoyama, "Molecular beam epitaxial growth of InAs self-assembled quantum dots with light-emission at 1.3 µm," *J. Cryst. Growth*, vol. 208, no. 1, pp. 93–99, 2000, doi: 10.1016/S0022-0248(99)00466-2.

[109] O. G. Schmidt *et al.*, "Self-assembled semiconductor nanostructures: Climbing up the ladder of order," *Surf. Sci.*, vol. 514, no. 1–3, pp. 10–18, 2002, doi: 10.1016/S0039-6028(02)01601-1.

[110] N. Koguchi and K. Ishige, "Growth of gaas epitaxial microcrystals on an s-terminated gaas substrate by successive irradiation of ga and as molecular beams," *Jpn. J. Appl. Phys.*, vol. 32, no. 5 R, pp. 2052–2058, 1993, doi: 10.1143/JJAP.32.2052.

[111] K. Watanabe *et al.*, "Fabrication of GaAs quantum dots by modified droplet epitaxy," *Japanese J. Appl. Physics, Part 2 Lett.*, vol. 39, no. 2, pp. 79–81, 2000, doi: 10.1143/jjap.39.l79.

[112] K. Watanabe, S. Tsukamoto, Y. Gotoh, and N. Koguchi, "Photoluminescence studies of GaAs quantum dots grown by droplet epitaxy," *J. Cryst. Growth*, vol. 227–228, pp. 1073–1077, 2001, doi: 10.1016/S0022-0248(01)00991-5.

[113] C. D. Lee, C. Park, H. J. Lee, S. K. Noh, K. S. Lee, and S. J. Park, "Formation of self-assembled GaAs/AlGaAs quantum dots by low-temperature epitaxy," *Appl. Phys. Lett.*, vol. 73, no. 18, pp. 2615–2617, 1998, doi: 10.1063/1.122523.

[114] T. Mano, K. Watanabe, S. Tsukamoto, H. Fujioka, M. Oshima, and N. Koguchi, "Fabrication of InGaAs quantum dots on GaAs(0 0 1) by droplet epitaxy," *J. Cryst. Growth*, vol. 209, no. 2–3, pp. 504–508, 2000, doi: 10.1016/S0022-0248(99)00606-5.

[115] Z.-M. W. Liang, Bao-Lai, "Energy Transfer within Ultralow Density twin InAs quantum dots grown by droplet epitaxy.pdf," *ACS Nano*.

[116] M. Jo, T. Mano, Y. Sakuma, and K. Sakoda, "Extremely high-density GaAs quantum dots grown by droplet epitaxy," *Appl. Phys. Lett.*, vol. 100, no. 21, pp. 1–4, 2012, doi: 10.1063/1.4721663.

[117] S. Sanguinetti, K. Watanabe, T. Kuroda, F. Minami, Y. Gotoh, and N. Koguchi, "Effects of post-growth annealing on the optical properties of self-assembled GaAs/AlGaAs quantum dots," *J. Cryst. Growth*, vol. 242, no. 3–4, pp. 321–331, 2002, doi: 10.1016/S0022-0248(02)01434-3.

[118] T. Mano and N. Koguchi, "Nanometer-scale GaAs ring structure grown by droplet epitaxy," *J. Cryst. Growth*, vol. 278, no. 1–4, pp. 108–112, 2005, doi: 10.1016/j.jcrysgro.2004.12.119.

[119] T. Mano *et al.*, "Self-assembly of concentric quantum double rings," *Nano Lett.*, vol. 5, no. 3, pp. 425–428, 2005, doi: 10.1021/nl048192.

[120] M. Kitamura, M. Nishioka, J. Oshinowo, and Y. Arakawa, "In situ fabrication of self-aligned InGaAs quantum dots on GaAs multiatomic steps by metalorganic chemical vapor deposition," *Appl. Phys. Lett.*, vol. 3663, no. December 1994, p. 3663, 1995, doi: 10.1063/1.114133.

[121] F. Poser, A. Bhattacharya, S. Weeke, and W. Richter, "Growth of spatially ordered InAs quantum dots on step-bunched vicinal GaAs (1 0 0) substrates," *J. Cryst. Growth*, vol. 248, no. SUPPL., pp. 317–321, 2003, doi: 10.1016/S0022-0248(02)01886-9.

[122] R. Notzel, J. Temmyo, and T. Tamamura, "Self-organized growth of strained lnGaAs quantum disks," *Nature*, vol. 369, no. 6476, pp. 131–133, 1994.

[123] J. Bauer *et al.*, "Long-range ordered self-assembled InAs quantum dots epitaxially grown on (110) GaAs," *Appl. Phys. Lett.*, vol. 85, no. 20, pp. 4750–4752, 2004, doi: 10.1063/1.1819987.

[124] A. Mohan *et al.*, "Polarization-entangled photons produced with high-symmetry site-controlled quantum dots," *Nat. Photonics*, vol. 4, no. 5, pp. 302–306, 2010, doi: 10.1038/nphoton.2010.2.

[125] D. Grigoriev *et al.*, "Three-dimensional self-ordering in an InGaAs/GaAs multilayered quantum dot structure investigated by x-ray diffuse scattering," *J. Phys. D. Appl. Phys.*, vol. 38, no. 10 A, 2005, doi: 10.1088/0022-3727/38/10A/029.

[126] N. Sritirawisarn, F. W. M. Van Otten, T. J. Eijkemans, and R. Nötzel, "Formation of linear InAs quantum dot arrays on InGaAsP/InP (100) by self-organized anisotropic strain engineering and their optical properties," *J. Appl. Phys.*, vol. 102, no. 5, 2007, doi: 10.1063/1.2777198.

[127] J. Tommila *et al.*, "Nanoimprint lithography patterned GaAs templates for site-controlled InAs quantum dots," *J. Cryst. Growth*, vol. 323, no. 1, pp. 183–186, 2011, doi: 10.1016/j.jcrysgro.2010.11.165.

[128] K. M. Cha, K. Shibata, and K. Hirakawa, "Single electron transport through site-controlled InAs quantum dots," *Appl. Phys. Lett.*, vol. 101, no. 22, 2012, doi: 10.1063/1.4769039.

[129] P. Atkinson, S. Kiravittaya, M. Benyoucef, A. Rastelli, and O. G. Schmidt, "Site-controlled growth and luminescence of InAs quantum dots using in situ Ga-assisted deoxidation of patterned substrates," *Appl. Phys. Lett.*, vol. 93, no. 10, pp. 1–4, 2008, doi: 10.1063/1.2980445.

[130] Y. I. Mazur *et al.*, "InGaAs/GaAs three-dimensionally-ordered array of quantum dots," *Appl. Phys. Lett.*, vol. 83, no. 5, pp. 987–989, 2003, doi: 10.1063/1.1596712.

[131] Z. M. Wang, K. Holmes, Y. I. Mazur, and G. J. Salamo, "Fabrication of (in,Ga)As quantum-dot chains on GaAs(100)," *Appl. Phys. Lett.*, vol. 84, no. 11, pp. 1931–1933, 2004, doi: 10.1063/1.1669064.

[132] V. V. Strel'chuk *et al.*, "Lateral ordering of quantum dots and wires in the (In,Ga)As/GaAs(100) multilayer structures," *Semiconductors*, vol. 41, no. 1, pp. 73–80, 2007, doi: 10.1134/S1063782607010150.

[133] T. Mano, R. Nötzel, G. J. Hamhuis, T. J. Eijkemans, and J. H. Wolter, "Direct imaging of self-organized anisotropic strain engineering for improved one-dimensional ordering of (In,Ga)As quantum dot arrays," *J. Appl. Phys.*, vol. 95, no. 1, pp. 109–114, 2004, doi: 10.1063/1.1631069.

[134] T. Van Lippen, R. Nötzel, G. J. Hamhuis, and J. H. Wolter, "Ordered quantum dot molecules and single quantum dots formed by self-organized anisotropic strain engineering," *J. Appl. Phys.*, vol. 97, no. 4, 2005, doi: 10.1063/1.1840098.

[135] E. Seḷuk, A. Y. Silov, and R. Nötzel, "Single InAs quantum dot arrays and directed self-organization on patterned GaAs (311)B substrates," *Appl. Phys. Lett.*, vol. 94, no. 26, pp. 2–5, 2009, doi: 10.1063/1.3167813.

[136] G. Biasiol and E. Kapon, "Mechanisms of self-ordering of quantum nanostructures grown on nonplanar surfaces," *Phys. Rev. Lett.*, vol. 81, no. 14, pp. 2962–2965, 1998, doi: 10.1103/PhysRevLett.81.2962.

[137] E. Placidi, F. Arciprete, V. Sessi, M. Fanfoni, F. Patella, and A. Balzarotti, "Step erosion during nucleation of InAsGaAs (001) quantum dots," *Appl. Phys. Lett.*, vol. 86, no. 24, pp. 1–3, 2005, doi: 10.1063/1.1946181.

[138] T. Ishikawa, T. Nishimura, S. Kohmoto, and K. Asakawa, "Site-controlled InAs single quantum-dot structures on GaAs surfaces patterned by in situ electron-beam lithography," *Appl. Phys. Lett.*, vol. 76, no. 2, pp. 167–169, 2000, doi: 10.1063/1.125691.

[139] J. Y. Lee, M. J. Noordhoek, P. Smereka, H. McKay, and J. M. Millunchick, "Filling of hole arrays with InAs quantum dots," *Nanotechnology*, vol. 20, no. 28, 2009, doi: 10.1088/0957-4484/20/28/285305.

[140] T. V. Hakkarainen *et al.*, "Structural characterization of InAs quantum dot chains grown by molecular beam epitaxy on nanoimprint lithography patterned GaAs(100)," *Nanotechnology*, vol. 22, no. 29, 2011, doi: 10.1088/0957-4484/22/29/295604.

[141] J. Tommila, A. Schramm, T. V. Hakkarainen, M. Dumitrescu, and M. Guina, "Size-dependent properties of single InAs quantum dots grown in

nanoimprint lithography patterned GaAs pits," *Nanotechnology*, vol. 24, no. 23, 2013, doi: 10.1088/0957-4484/24/23/235204.

[142] J. S. Kim, M. Kawabe, and N. Koguchi, "Ordering of high-quality InAs quantum dots on defect-free nanoholes," *Appl. Phys. Lett.*, vol. 88, no. 7, pp. 86–89, 2006, doi: 10.1063/1.2174097.

[143] J. Martín-Sánchez *et al.*, "Single photon emission from site-controlled InAs quantum dots grown on GaAs(001) patterned substrates," *ACS Nano*, vol. 3, no. 6, pp. 1513–1517, 2009, doi: 10.1021/nn9001566.

[144] S. Kohmoto, H. Nakamura, S. Nishikawa, and K. Asakawa, "Three-dimensional site control of self-organized InAs quantum dots by in situ scanning tunneling probe-assisted nanolithography and molecular beam epitaxy," *J. Vac. Sci. Technol. B Microelectron. Nanom. Struct.*, vol. 20, no. 3, p. 762, 2002, doi: 10.1116/1.1467662.

[145] C. Schneider *et al.*, "Lithographic alignment to site-controlled quantum dots for device integration," *Appl. Phys. Lett.*, vol. 92, no. 18, pp. 1–4, 2008, doi: 10.1063/1.2920189.

[146] F. Albert *et al.*, "Quantum efficiency and oscillator strength of site-controlled InAs quantum dots," *Appl. Phys. Lett.*, vol. 96, no. 15, pp. 2008–2011, 2010, doi: 10.1063/1.3393988.

[147] J. Skiba-Szymanska *et al.*, "Narrow emission linewidths of positioned InAs quantum dots grown on pre-patterned GaAs(100) substrates," *Nanotechnology*, vol. 22, no. 6, 2011, doi: 10.1088/0957-4484/22/6/065302.

[148] C. J. Mayer, M. F. Helfrich, and D. M. Schaadt, "Influence of hole shape/size on the growth of site-selective quantum dots," *Nanoscale Res. Lett.*, vol. 8, no. 1, pp. 1–7, 2013, doi: 10.1186/1556-276X-8-504.

[149] J. Viheriälä *et al.*, "Applications of UV-nanoimprint soft stamps in fabrication of single-frequency diode lasers," *Microelectron. Eng.*, vol. 86, no. 3, pp. 321–324, 2009, doi: 10.1016/j.mee.2008.10.010.

[150] A. Schramm *et al.*, "Large array of single, site-controlled InAs quantum dots fabricated by UV-nanoimprint lithography and molecular beam epitaxy," *Nanotechnology*, vol. 23, no. 17, 2012, doi: 10.1088/0957-4484/23/17/175701.

[151] R. García, M. Calleja, and F. Pérez-Murano, "Local oxidation of silicon surfaces by dynamic force microscopy: Nanofabrication and water bridge formation," *Appl. Phys. Lett.*, vol. 72, no. 18, pp. 2295–2297, 1998, doi: 10.1063/1.121340.

[152] S. Masubuchi, M. Ono, K. Yoshida, K. Hirakawa, and T. MacHida, "Fabrication of graphene nanoribbon by local anodic oxidation lithography using atomic force microscope," *Appl. Phys. Lett.*, vol. 94, no. 8, pp. 2007–2010, 2009, doi: 10.1063/1.3089693.

[153] R. Held, T. Heinzel, P. Studerus, and K. Ensslin, "Nanolithography by local anodic oxidation of metal films using an atomic force microscope," *Phys. E Low-Dimensional Syst. Nanostructures*, vol. 2, no. 1–4, pp. 748–752, 1998, doi: 10.1016/S1386-9477(98)00153-2.

[154] J. Canet-Ferrer *et al.*, "Exciton and multiexciton optical properties of single InAs/GaAs site-controlled quantum dots," *Appl. Phys. Lett.*, vol. 103, no. 18, 2013, doi: 10.1063/1.4828352.

[155] J. Herranz, L. Wewior, B. Alen, D. Fuster, L. Gonzalez, and Y. Gonzalez, "Role of re-growth interface preparation process for spectral line-width reduction of single InAs site-controlled quantum dots," *Nanotechnology*, vol. 26, no. 19, 2015, doi: 10.1088/0957-4484/26/19/195301.

[156] J. Herranz, L. González, L. Wewior, B. Alén, D. Fuster, and Y. González, "Study of growth parameters for single InAs QD formation on GaAs(001) patterned substrates by local oxidation lithography," *Cryst. Growth Des.*, vol. 15, no. 2, pp. 666–672, 2015, doi: 10.1021/cg5013632.

[157] S. I. Stenin and A. I. Toropov, "Molecular beam epitaxy of semiconductor films and modulated structures," *Cryst. Res. Technol.*, vol. 24, no. 8, pp. 735–744, 1989, doi: 10.1002/crat.2170240802.

[158] R. F. Farrow, *Molecular beam epitaxy: applications to key materials*. Elsevier, 1995.

[159] T. Nishinaga, *Handbook of crystal growth: fundamentals*. Elsevier, 2014.

[160] N. N. Ledentsov *et al.*, "Reversibility of the island shape, volume and density in Stranski-Krastanow growth," *Semicond. Sci. Technol.*, vol. 16, no. 6, pp. 502–506, 2001, doi: 10.1088/0268-1242/16/6/316.

[161] I. Horcas, R. Fernández, J. . Gomez-Rodriguez, J. W. S. . Colchero, J. W. S. X. . Gómez-Herrero, and A. . Baro, "WSXM: a software for scanning probe microscopy and a tool for nanotechnology. Review of scientific instruments," *Rev. Sci. Instrum.*, vol. 78, no. 1, p. 013705, 2007.

[162] G. Von Freymann *et al.*, "Three-dimensional nanostructures for photonics," *Adv. Funct. Mater.*, 2010, doi: 10.1002/adfm.200901838.

[163] M. E. Stewart *et al.*, "Nanostructured plasmonic sensors," *Chemical Reviews*. 2008, doi: 10.1021/cr068126n.

[164] Q. Luo, C. Hou, Y. Bai, R. Wang, and J. Liu, "Protein Assembly: Versatile Approaches to Construct Highly Ordered Nanostructures," *Chemical Reviews*. 2016, doi: 10.1021/acs.chemrev.6b00228.

[165] M. Albrecht *et al.*, "Magnetic multilayers on nanospheres," *Nat. Mater.*, 2005, doi: 10.1038/nmat1324.

[166] S. Jeon, V. Malyarchuk, J. O. White, and J. A. Rogere, "Optically Fabricated Three Dimensional Nanofluidic Mixers for Microfluidic Devices," *Nano Lett.*, 2005, doi: 10.1021/nl050606r.

[167] A. Rodriguez *et al.*, "Laser interference lithography for nanoscale structuring of materials: From laboratory to industry," *Microelectron. Eng.*, 2009, doi: 10.1016/j.mee.2008.12.043.

[168] M. Ellman *et al.*, "High-power laser interference lithography process on photoresist: Effect of laser fluence and polarisation," *Appl. Surf. Sci.*, vol. 255, no. 10, pp. 5537–5541, 2009, doi: 10.1016/j.apsusc.2008.07.201.

[169] I. Byun and J. Kim, "Cost-effective laser interference lithography using a 405 nm AlInGaN semiconductor laser," *J. Micromechanics Microengineering*, vol. 20, no. 5, 2010, doi: 10.1088/0960-1317/20/5/055024.

[170] T. Kondo, S. Matsuo, S. Juodkazis, and H. Misawa, "Femtosecond laser interference technique with diffractive beam splitter for fabrication of three-dimensional photonic crystals," *Appl. Phys. Lett.*, 2001, doi: 10.1063/1.1391232.

[171] S. Eckhardt, L. Müller-Meskamp, M. Loeser, M. Siebold, and A. F. Lasagni, "Fabrication of highly efficient transparent metal thin film electrodes using Direct Laser Interference Patterning," 2015, doi: 10.1117/12.2082537.

[172] J. Berzinš *et al.*, "Direct and High-Throughput Fabrication of Mie-Resonant Metasurfaces via Single-Pulse Laser Interference," *ACS Nano*, vol. 14, no. 5. pp. 6138–6149, 2020, doi: 10.1021/acsnano.0c01993.

[173] J. Lutkenhaus, D. George, M. Moazzezi, U. Philipose, and Y. Lin, "Digitally tunable holographic lithography using a spatial light modulator as a programmable phase mask," *Opt. Express*, vol. 21, no. 22, p. 26227, 2013, doi: 10.1364/oe.21.026227.

[174] S. Behera, M. Kumar, and J. Joseph, "Submicrometer photonic structure fabrication by phase spatial-light-modulator-based interference lithography," *Opt. Lett.*, vol. 41, no. 8, p. 1893, 2016, doi: 10.1364/ol.41.001893.

[175] J. de Boor, N. Geyer, U. Gösele, and V. Schmidt, "Three-beam interference lithography: upgrading a Lloyd's interferometer for single-exposure hexagonal patterning," *Opt. Lett.*, 2009, doi: 10.1364/ol.34.001783.

[176] L. Dong, Z. Zhang, Z. Wang, D. Li, and M. Liu, "Design an asymmetrical three-beam laser interference lithography for fabricating micro- and nano-structures," *J. Laser Micro Nanoeng.*, vol. 15, no. 2, pp. 85–91, 2020, doi: 10.2961/jlmn.2020.02.2002.

[177] M. Campbell, D. N. Sharp, M. T. Harrison, R. G. Denning, and A. J. Turberfield, "Fabrication of photonic crystals for the visible spectrum by holographic lithography," *Nature*, 2000, doi: 10.1038/35003523.

[178] S. Alamri and A. F. Lasagni, "Development of a general model for direct laser interference patterning of polymers," *Opt. Express*, 2017, doi: 10.1364/oe.25.009603.

[179] M. Bieda, M. Siebold, and A. F. Lasagni, "Fabrication of sub-micron surface structures on copper, stainless steel and titanium using picosecond laser interference patterning," *Appl. Surf. Sci.*, 2016, doi: 10.1016/j.apsusc.2016.06.100.

[180] J. Berger, M. Grosse Holthaus, N. Pistillo, T. Roch, K. Rezwan, and A. F. Lasagni, "Ultraviolet laser interference patterning of hydroxyapatite surfaces," *Appl. Surf. Sci.*, 2011, doi: 10.1016/j.apsusc.2010.10.120.

[181] M. Sadoqi, S. Kumar, and Y. Yamada, "Photochemical and photothermal model for pulsed-laser ablation," *J. Thermophys. Heat Transf.*, 2002, doi: 10.2514/2.6684.

[182] G. Paltauf and P. E. Dyer, "Photomechanical processes and effects in ablation," *Chemical Reviews*. 2003, doi: 10.1021/cr010436c.

[183] C. Zwahr, B. Voisiat, A. Welle, D. Günther, and A. F. Lasagni, "One-Step Fabrication of Pillar and Crater-Like Structures on Titanium Using Direct Laser Interference Patterning," *Adv. Eng. Mater.*, vol. 20, no. 7, pp. 1–9, 2018, doi: 10.1002/adem.201800160.

[184] D. Wang, Z. Wang, Z. Zhang, Y. Yue, D. Li, and C. Maple, "Direct modification of silicon surface by nanosecond laser interference lithography," *Appl. Surf. Sci.*, vol. 282, pp. 67–72, 2013, doi: 10.1016/j.apsusc.2013.05.042.

[185] V. Oliveira, R. Vilar, R. Serra, J. C. Oliveira, N. I. Polushkin, and O. Conde, "Sub-micron structuring of silicon using femtosecond laser interferometry," *Opt. Laser Technol.*, 2013, doi: 10.1016/j.optlastec.2013.06.031.

[186] M. Gedvilas, S. Indrišiunas, B. Voisiat, E. Stankevičius, A. Selskis, and G. Račiukaitis, "Nanoscale thermal diffusion during the laser interference ablation using femto-, pico-, and nanosecond pulses in silicon," *Phys. Chem. Chem. Phys.*, 2018, doi: 10.1039/c7cp08458g.

[187] C. M. Clegg and H. Yang, "Guided assembly of quantum dots through selective laser heating," *Sol. Energy Mater. Sol. Cells*, vol. 108, pp. 252–255, 2013, doi: 10.1016/j.solmat.2012.09.011.

[188] W. Zhang *et al.*, "In-situ laser nano-patterning for ordered InAs/GaAs(001) quantum dot growth," *Appl. Phys. Lett.*, vol. 112, no. 15, pp. 1–5, 2018, doi: 10.1063/1.5016096.

[189] J. Xu, Z. Wang, Z. Zhang, D. Wang, and Z. Weng, "Fabrication of moth-eye structures on silicon by direct six-beam laser interference lithography," *J. Appl. Phys.*, vol. 115, no. 20, p. 203101, 2014.

[190] O. Bryngdahl, "Moire: Formation and Interpretation.," *J Opt Soc Am*, vol. 64, no. 10, pp. 1287–1294, 1974, doi: 10.1364/JOSA.64.001287.

[191] Z. Zhang, L. Dong, Y. Ding, L. Li, Z. Weng, and Z. Wang, "Micro and nano dual-scale structures fabricated by amplitude modulation in multi-beam laser interference lithography," *Opt. Express*, vol. 25, no. 23, p. 29135, 2017, doi: 10.1364/oe.25.029135.

[192] T.-C. Chen and R. B. Darling, "Laser micromachining of the materials using in microfluidics by high precision pulsed near and mid-ultraviolet Nd: YAG lasers," *J. Mater. Process. Technol.*, vol. 198, no. 1–3, pp. 248–253, 2008.

[193] D. Werner, S. Hashimoto, and T. Uwada, "Remarkable photothermal effect of interband excitation on nanosecond laser-induced reshaping and size reduction of pseudospherical gold nanoparticles in aqueous solution," *Langmuir*, vol. 26, no. 12, pp. 9956–9963, 2010.

[194] T. Sobota, "Fourier's Law of Heat Conduction," in *Encyclopedia of Thermal Stresses*, Dordrecht: Springer Netherlands, 2014, pp. 1769–1778.

[195] A. Iserles and G. D. Smith, "Numerical Solution of Partial Differential Equations: Finite Difference Methods," *Math. Gaz.*, 1986, doi: 10.2307/3616228.

[196] V. Craciun and D. Craciun, "Thermal mechanisms in laser ablation of GaAs," *Appl. Surf. Sci.*, 1997, doi: 10.1016/S0169-4332(96)00740-4.

[197] S. Adachi, *Optical constants of crystalline and amorphous semiconductors*. Springer Science & Business Media, 1999.

[198] D. E. . R. P. H. C. J. B. Theeten, Aspnes, "Filmetrics Spectral Reflectance Calculator for Thin-Film Stack," *J. Appl. Phys.*, 1978. https://www.filmetrics.com/reflectance-calculator.

[199] B. Voisiat, C. Zwahr, and A. F. Lasagni, "Growth of regular micro-pillar arrays on steel by polarization-controlled laser interference patterning," *Appl. Surf. Sci.*, vol. 471, no. September 2018, pp. 1065–1071, 2019, doi: 10.1016/j.apsusc.2018.12.083.

[200] A. C. Tarn, I. K. Pour, T. Nguyen, D. Krajnovich, and P. Baumgart, "Experimental and theoretical studies of bump formation during laser texturing of ni-p disk substrates," *IEEE Trans. Magn.*, vol. 32, no. 5 PART 1, pp. 3771–3773, 1996, doi: 10.1109/20.538831.

[201] M. D'Alessandria, A. Lasagni, and F. Mücklich, "Direct micro-patterning of aluminum substrates via laser interference metallurgy," *Appl. Surf. Sci.*, vol. 255, no. 5 PART 2, pp. 3210–3216, 2008, doi: 10.1016/j.apsusc.2008.09.018.

[202] C. T. Foxon, J. A. Harvey, and B. A. Joyce, "The evaporation of GaAs under equilibrium and non-equilibrium conditions using a modulated beam

technique," *J. Phys. Chem. Solids*, vol. 34, no. 10, pp. 1693–1701, 1973, doi: 10.1016/S0022-3697(73)80135-0.

[203] J. Y. Tsao, *Material Fundamentals of Molecular Beam Epitaxy*. San Diego: Academic Press, 1993.

[204] C. Heyn, S. Schnüll, D. E. Jesson, and W. Hansen, "Thermally controlled widening of droplet etched nanoholes," *Nanoscale Res. Lett.*, vol. 9, no. 1, pp. 1–8, 2014, doi: 10.1186/1556-276X-9-285.

[205] C. Heyn and D. E. Jesson, "Congruent evaporation temperature of molecular beam epitaxy grown GaAs (001) determined by local droplet etching," *Appl. Phys. Lett.*, vol. 107, no. 16, 2015, doi: 10.1063/1.4934218.

[206] P. Kratzer, E. Penev, and M. Scheffler, "First-principles studies of kinetics in epitaxial growth of III-V semiconductors," *Appl. Phys. A Mater. Sci. Process.*, vol. 75, no. 1, pp. 79–88, 2002, doi: 10.1007/s003390101057.

[207] E. Schöll and S. Bose, "Kinetic Monte Carlo simulation of the nucleation stage of the self-organized growth of quantum dots," *Solid. State. Electron.*, vol. 42, no. 7–8, pp. 1587–1591, 1998, doi: 10.1016/S0038-1101(98)00076-8.

[208] T. P. Schulze and P. Smereka, "Kinetic Monte Carlo simulation of heteroepitaxial growth: Wetting layers, quantum dots, capping, and nanorings," *Phys. Rev. B - Condens. Matter Mater. Phys.*, vol. 86, no. 23, pp. 1–38, 2012, doi: 10.1103/PhysRevB.86.235313.

[209] C. H. Chiu and Z. Huang, "Numerical simulation for the formation of nanostructures on the Stranski-Krastanow systems by surface undulation," *J. Appl. Phys.*, vol. 101, no. 11, 2007, doi: 10.1063/1.2743734.

[210] R. Bergamaschini, M. Salvalaglio, R. Backofen, A. Voigt, and F. Montalenti, "Continuum modelling of semiconductor heteroepitaxy: an applied perspective," *Adv. Phys. X*, vol. 1, no. 3, pp. 331–367, 2016, doi: 10.1080/23746149.2016.1181986.

[211] A. Kumar, L. Du, and D. Maroudas, "Modeling of quantum dot and nanoring pattern formation on pit-patterned semiconductor substrates," *Mater. Res. Express*, vol. 5, no. 8, p. 86303, 2018, doi: 10.1088/2053-1591/aad263.

[212] A. V. Osipov, "Kinetic model of vapour-deposited thin film condensation: nucleation stage," *Thin Solid Films*, vol. 227, no. 2, pp. 111–118, 1993, doi: 10.1016/0040-6090(93)90027-M.

[213] S. A. Kukushkin and A. V Osipov, "Thin-film condensation processes," *Physics-Uspekhi*, vol. 41, no. 10, pp. 983–1014, 1998, doi: 10.1070/pu1998v041n10abeh000461.

[214] A. Ishii, K. Fujiwara, and T. Aisaka, "Dynamics of In atom during InAs/GaAs(0 0 1) growth process," *Appl. Surf. Sci.*, vol. 216, no. 1-4 SPEC., pp. 478–482, 2003, doi: 10.1016/S0169-4332(03)00410-0.

[215] K. Fujiwara, A. Ishii, and T. Aisaka, "First principles calculation of Indium migration barrier energy on an InAs(001) surface," *Thin Solid Films*, vol. 464–465, pp. 35–37, 2004, doi: 10.1016/j.tsf.2004.06.062.

[216] H. J. V. Tyrrell, "The origin and present status of fick's diffusion law," *J. Chem. Educ.*, vol. 41, no. 7, pp. 397–400, 1964, doi: 10.1021/ed041p397.

[217] E. G. Seebauer and C. E. Allen, "Estimating surface diffusion coefficients," *Prog. Surf. Sci.*, vol. 49, no. 3, pp. 265–330, 1995, doi: 10.1016/0079-6816(95)00039-2.

[218] C. Ratsch and A. Zangwill, "Equilibrium theory of the Stranski-Krastanov epitaxial morphology," *Surf. Sci.*, vol. 293, no. 1–2, pp. 123–131, 1993, doi: 10.1016/0039-6028(93)90250-N.

[219] S. W. Ellaway and D. A. Faux, "Effective elastic stiffnesses of InAs under uniform strain," *J. Appl. Phys.*, vol. 92, no. 6, pp. 3027–3033, 2002, doi: 10.1063/1.1500421.

[220] V. G. Dubrovskii, "Transition from thermodynamically to kinetically controlled regime of nucleation in a materially open system," *J. Phys. Condens. Matter*, vol. 16, no. 39, pp. 6929–6940, 2004, doi: 10.1088/0953-8984/16/39/025.

[221] Vladimir G. Dubrovskii and V. G. Dubrovskii, *Nucleation theory and growth of nanostructures*. Berlin: Springer, 2014.

[222] A. B. E. Placidi, F. Arciprete, R. Magri, M. Rosini, A. Vinattieri, L. Cavigli, M. Gurioli, E. Giovine, L. Persichetti, M. Fanfoni, F. Patella, *InAs Epitaxy on GaAs(001): A Model Case of Strain-Driven Self-assembling of Quantum Dots*. 2012.

[223] D. Gerlich, "Elastic constants of single-crystal indium arsenide," *J. Appl. Phys.*, vol. 34, no. 9, p. 2915, 1963, doi: 10.1063/1.1729833.

[224] J. S. Kim, M. Kawabe, and N. Koguchi, "Fabrication of highly aligned nano-hole/trench structures by atomic force microscopy tip-induced oxidation and atomic hydrogen cleaning," *J. Cryst. Growth*, vol. 262, no. 1–4, pp. 265–270, 2004, doi: 10.1016/j.jcrysgro.2003.10.020.

[225] Y. Nakata, "Interference laser processing," *Adv. Opt. Technol.*, vol. 5, no. 1, pp. 29–38, 2016, doi: 10.1515/aot-2015-0060.

[226] D. Wang, Z. Wang, Z. Zhang, Y. Yue, D. Li, and C. Maple, "Effects of polarization on four-beam laser interference lithography," *Appl. Phys. Lett.*, vol. 102, no. 8, 2013, doi: 10.1063/1.4793752.

[227] H. Saito, K. Nishi, and S. Sugou, "Shape transition of InAs quantum dots by growth at high temperature," *Appl. Phys. Lett.*, vol. 74, no. 9, pp. 1224–1226, 1999, doi: 10.1063/1.123506.

[228] V. G. Dubrovskiĭ *et al.*, "Dependence of Structural and Optical Properties of QD Arrays in an InAs/GaAs System on Surface Temperature and Growth Rate," *Semiconductors*, vol. 38, no. 3, pp. 329–334, 2004, doi: 10.1134/1.1682338.

[229] R. Parvizi, "Electronic coupling of single lateral strained InGaAs quantum dot molecule based on nanohole structure," *Phys. B Condens. Matter*, vol. 482, pp. 51–57, 2016, doi: 10.1016/j.physb.2015.12.011.

[230] Y. Chen and J. Washburn, "Structural transition in large-lattice-mismatch heteroepitaxy," *Phys. Rev. Lett.*, vol. 77, no. 19, pp. 4046–4049, 1996, doi: 10.1103/PhysRevLett.77.4046.

[231] E. C. Le Ru, J. Fack, and R. Murray, "Temperature and excitation density dependence of the photoluminescence from annealed InAs/GaAs quantum dots," *Phys. Rev. B - Condens. Matter Mater. Phys.*, vol. 67, no. 24, pp. 1–12, 2003, doi: 10.1103/PhysRevB.67.245318.

[232] K. M. Cha, I. Horiuchi, K. Shibata, and K. Hirakawa, "Size-limiting effect of site-controlled inas quantum dots grown at high temperatures by molecular beam epitaxy," *Appl. Phys. Express*, vol. 5, no. 8, pp. 3–5, 2012, doi: 10.1143/APEX.5.085501.

[233] T. Ishikawa, S. Kohmoto, S. Nishikawa, T. Nishimura, and K. Asakawa, "Site control of InAs quantum dots on GaAs surfaces patterned by in situ electron-beam lithography," *J. Vac. Sci. Technol. B Microelectron. Nanom. Struct.*, vol. 18, no. 6, p. 2635, 2000, doi: 10.1116/1.1322039.

[234] H. Lee, J. A. Johnson, J. S. Speck, and P. M. Petroff, "Controlled ordering and positioning of InAs self-assembled quantum dots," *J. Vac. Sci. Technol. B Microelectron. Nanom. Struct.*, vol. 18, no. 4, p. 2193, 2000, doi: 10.1116/1.1306281.

[235] C. Somaschini, S. Bietti, S. Sanguinetti, N. Koguchi, and A. Fedorov, "Self-assembled GaAs/AlGaAs coupled quantum ring-disk structures by droplet epitaxy," *Nanotechnology*, vol. 21, no. 12, 2010, doi: 10.1088/0957-4484/21/12/125601.

[236] A. Stemmann, C. Heyn, T. Köppen, T. Kipp, and W. Hansen, "Local droplet etching of nanoholes and rings on GaAs and AlGaAs surfaces," *Appl. Phys. Lett.*, vol. 93, no. 12, pp. 1–4, 2008, doi: 10.1063/1.2981517.

[237] C. Heyn, T. Bartsch, S. Sanguinetti, D. Jesson, and W. Hansen, "Dynamics of mass transport during nanohole drilling by local droplet etching," *Nanoscale Res. Lett.*, vol. 10, no. 1, 2015, doi: 10.1186/s11671-015-0779-5.

[238] X. L. Li and G. W. Yang, "Growth mechanisms of quantum ring self-assembly upon droplet epitaxy," *J. Phys. Chem. C*, vol. 112, no. 20, pp. 7693–7697, 2008, doi: 10.1021/jp801528r.

[239] C. Haase and H. Stiebig, "Thin-film silicon solar cells with efficient periodic light trapping texture," *Appl. Phys. Lett.*, vol. 91, no. 6, 2007, doi: 10.1063/1.2768882.

[240] A. Y. Vorobyev and C. Guo, "Antireflection effect of femtosecond laser-induced periodic surface structures on silicon," *Opt. Express*, vol. 19, no. S5, p. A1031, 2011, doi: 10.1364/oe.19.0a1031.

[241] Z. M. Zhao, O. Hulko, T. S. Yoon, and Y. H. Xie, "Initial stage of InAs growth on Si (001) studied by high-resolution transmission electron microscopy," *J. Appl. Phys.*, vol. 98, no. 12, 2005, doi: 10.1063/1.2149164.

[242] H. Döscher, B. Borkenhagen, G. Lilienkamp, W. Daum, and T. Hannappel, "III-V on silicon: Observation of gallium phosphide anti-phase disorder by low-energy electron microscopy," *Surf. Sci.*, vol. 605, no. 15–16, pp. L38–L41, 2011, doi: 10.1016/j.susc.2011.05.002.

[243] C. K. Sun *et al.*, "Optical investigations of the dynamic behavior of GaSb/GaAs quantum dots," *Appl. Phys. Lett.*, vol. 68, no. 11, pp. 1543–1545, 1996, doi: 10.1063/1.115693.

[244] H. Born, L. Müller-Kirsch, R. Heitz, A. Hoffmann, and D. Bimberg, "Radiative recombination in type II GaSb/GaAs quantum dots," *Phys. Status Solidi Basic Res.*, vol. 228, no. 3, pp. 1–4, 2001, doi: 10.1002/1521-3951(200112)228:3<R4::AID-PSSB99994>3.0.CO;2-H.

[245] M. Geller, C. Kapteyn, L. Müller-Kirsch, R. Heitz, and D. Bimberg, "450 meV hole localization in GaSb/GaAs quantum dots," *Appl. Phys. Lett.*, vol. 82, no. 16, pp. 2706–2708, 2003, doi: 10.1063/1.1569413.

[246] M. Geller, C. Kapteyn, L. Müller-Kirsch, R. Heitz, and D. Bimberg, "Hole storage in GaSb/GaAs quantum dots for memory devices," *Phys. Status Solidi Basic Res.*, vol. 238, no. 2, pp. 258–261, 2003, doi: 10.1002/pssb.200303023.

[247] A. Marent *et al.*, "106 years extrapolated hole storage time in GaSb/AlAs quantum dots," *Appl. Phys. Lett.*, vol. 91, no. 24, pp. 14–17, 2007, doi: 10.1063/1.2824884.

[248] T. D. Bennett, D. J. Krajnovich, C. P. Grigoropoulos, P. Baumgart, and A. C. Tam, "Marangoni mechanism in pulsed laser texturing of magnetic disk substrates," *J. Heattrans.*, vol. 119, no. 3, pp. 589–596, 1997.

[249] Y. Nakata, T. Okada, and M. Maeda, "Nano-sized hollow bump array generated by single femtosecond laser pulse," *Japanese J. Appl. Physics, Part 2 Lett.*, vol. 42, no. 12 A, 2003, doi: 10.1143/jjap.42.l1452.

[250] Y. Lu, S. Theppakuttai, and S. C. Chen, "Marangoni effect in nanosphere-enhanced laser nanopatterning of silicon," *Appl. Phys. Lett.*, vol. 82, no. 23, pp. 4143–4145, 2003, doi: 10.1063/1.1581387.

[251] T. Tavera, N. Pérez, A. Rodríguez, P. Yurrita, S. M. Olaizola, and E. Castaño, "Periodic patterning of silicon by direct nanosecond laser interference ablation," *Appl. Surf. Sci.*, vol. 258, no. 3, pp. 1175–1180, 2011, doi: 10.1016/j.apsusc.2011.09.062.

[252] J. Z. Li, J. Bai, C. Major, M. Carroll, A. Lochtefeld, and Z. Shellenbarger, "Defect reduction of GaAs/Si epitaxy by aspect ratio trapping," *J. Appl. Phys.*, vol. 103, no. 10, p. 106102, 2008.

[253] Q. Li, K. W. Ng, and K. M. Lau, "Growing antiphase-domain-free GaAs thin films out of highly ordered planar nanowire arrays on exact (001) silicon," *Appl. Phys. Lett.*, vol. 106, no. 7, p. 072105, 2015.

[254] M. A. Kamarudin *et al.*, "GaSb quantum dot morphology for different growth temperatures and the dissolution effect of the GaAs capping layer," *J. Phys. D. Appl. Phys.*, vol. 43, no. 6, 2010, doi: 10.1088/0022-3727/43/6/065402.

[255] M. DeJarld, L. Yan, M. Luengo-Kovac, V. Sih, and J. Millunchick, "Structural differences between capped GaSb nanostructures grown by Stranski-Krastanov and droplet epitaxy growth modes," *J. Appl. Phys.*, vol. 121, no. 3, 2017, doi: 10.1063/1.4973795.

[256] T. Kawazu, T. Mano, T. Noda, and H. Sakaki, "Optical properties of GaSb/GaAs type-II quantum dots grown by droplet epitaxy," *Appl. Phys. Lett.*, vol. 94, no. 8, pp. 1–4, 2009, doi: 10.1063/1.3090033.

[257] T. Nakai, S. Iwasaki, and K. Yamaguchi, "Control of GaSb/GaAs quantum nanostructures by molecular beam epitaxy," *Japanese J. Appl. Physics, Part 1 Regul. Pap. Short Notes Rev. Pap.*, vol. 43, no. 4 B, pp. 2122–2124, 2004, doi: 10.1143/JJAP.43.2122.

[258] Y. Wang *et al.*, "Photoluminescence investigation of type-II GaSb/GaAs quantum dots grown by liquid phase epitaxy," *Infrared Phys. Technol.*, vol. 91, pp. 68–71, 2018, doi: 10.1016/j.infrared.2018.03.023.

[259] D. Alonso-Álvarez, B. Aĺn, J. M. García, and J. M. Ripalda, "Optical investigation of type II GaSbGaAs self-assembled quantum dots," *Appl. Phys. Lett.*, vol. 91, no. 26, pp. 89–92, 2007, doi: 10.1063/1.2827582.

[260] E. R. Glaser, B. R. Bennett, B. V. Shanabrook, and R. Magno, "Photoluminescence studies of self-assembled InSb, GaSb, and AlSb quantum dot heterostructures," *Appl. Phys. Lett.*, vol. 68, no. 25, pp. 3614–3616, 1996, doi: 10.1063/1.115747.

[261] P. D. Hodgson *et al.*, "Blueshifts of the emission energy in type-II quantum dot and quantum ring nanostructures," *J. Appl. Phys.*, vol. 114, no. 7, 2013, doi: 10.1063/1.4818834.

[262] Y. S. Chiu, M. H. Ya, W. S. Su, and Y. F. Chen, "Properties of photoluminescence in type-II GaAsSb/GaAs multiple quantum wells," *J. Appl. Phys.*, vol. 92, no. 10, pp. 5810–5813, 2002, doi: 10.1063/1.1513200.

[263] T. T. Chen *et al.*, "Unusual optical properties of type-II InAs Ga As0.7 Sb0.3 quantum dots by photoluminescence studies," *Phys. Rev. B - Condens. Matter Mater. Phys.*, vol. 75, no. 3, pp. 5–8, 2007, doi: 10.1103/PhysRevB.75.033310.